# PROGRESS IN RESEARCH

## APRIL 1, 2015 - MARCH 31, 2016

**Prepared By**

**The Cyclotron Institute Staff**

**Texas A&M University**

**College Station, TX 77843-3366**

**Phone: (979) 845-1411**
**Fax: (979) 845-1899**

**Web: http://cyclotron.tamu.edu**

**June 2016**

# TABLE OF CONTENTS

## SECTION I: NUCLEAR STRUCTURE, FUNDAMENTAL INTERACTIONS AND ASTROPHYSICS

## SECTION II: HEAVY ION REACTIONS

## SECTION III: NUCLEAR THEORY

## SECTION IV: SUPERCONDUCTING CYCLOTRON, INSTRUMENTATION AND RIB UPGRADE

## SECTION V: PUBLICATIONS

## SECTION VI: APPENDIX

# Introduction
## April 1, 2015 – March 31, 2016

Progress in research and operations at the Texas A&M Cyclotron Institute is summarized in this report for the period April, 1, 2015 through March 31, 2016. The format follows that of previous years. Sections I through III contain reports from individual research projects. Operation and technical developments are given in Section IV. Section V lists the publications with Cyclotron Institute authors and outside users and the Appendix gives additional information including talks presented by members of the Institute during the past year. Once again, the full volume of this year's Progress in Research is available only on our web site (http://cyclotron.tamu.edu). *Since most of the contributions presented here are truly reports on progress in research, results and conclusions should not be quoted from the report without the consent of the authors.*

We are pleased to announce that we have successfully hired three new tenure track faculty. Dr. Gregory Christian and Dr. Ania Kwiatkowski are both outstanding young experimentalists that relocated from TRIUMF to join Texas A&M in the fall. Additionally Dr. Jeremy Holt, an excellent theorist from the INT joined us in January.

The K500 provided a record 6,400 hours of beam for both science and radiation effects testing. The K150 cyclotron provided a record 3,800 hours of beam on target. The list of beams from the K150 included protons (strip extracted), $^{4}$He, $^{6}$Li, $^{7}$Li, $^{22}$Ne, $^{26}$Mg, $^{27}$Al, $^{28}$Si, and $^{32}$S. As the light ion guide (LIG) continues to progress toward eventual production of radioactive beams, we tried an exercise on how to re-accelerate and transport weak beams. Using $^{16}$O$^{3+}$ ions as the pilot beam, we have accelerated and transported much weaker $^{86}$Rb$^{16+}$ ions from the CBECR ion source and through the K500 cyclotron and then to the MARS spectrometer. The intense oxygen beam was used to tune the injection line and the K500 cyclotron (set for 14 MeV/nucleon) and the beam transport to MARS, and then a simple shift of the K500 RF frequency, by +56 kHz, was all that was needed to bring the Rb beam to the MARS target. We hope to do the same when the radioactive $^{64}$Ga ions are identified after the CBECR ion source.

As in previous reports, I include here some highlights of work carried out over the past year.

- A good candidate for a state analogous to the $^{12}$C Hoyle in $^{16}$O has been identified via the thick target inverse kinematic measurement of $^{20}$Ne + alpha at an excitation energy of 15 MeV.

- The Heavy Elements Group has reported the first extraction of a metal (indium) using a deep eutectic solvent, which may have both fundamental and practical applications.

- The neutron-proton equilibration in dynamically-deformed atomic nuclei has been measured on a sub-zeptosecond timescale and shown to follow first-order kinetics with a mean equilibration time of 0.3 zs.

- Collective effects were shown to have a significant influence on fusion-evaporation reactions, and may substantially affect the likelihood of discovering the next new element.

- The first direct measurement of the $E_r \sim 450$ keV resonance in the $^{19}$Ne(p,γ)$^{20}$Na reaction put past uncertainties related to the resonance properties to rest and significantly improved constraints on the production of $^{19}$F in classical novae.

- Precise (±~1%) measurements of K-shell internal conversion coefficients (ICCs) for $E3$ and $M4$ transitions for a range of nuclei, $48 \leq Z \leq 78$, have demonstrated the need to include the K-shell vacancy in the theory used to calculate ICCs and have supported use of the "frozen orbital" approximation.

- The astrophysically important reaction rates for the s-process neutron source reactions $^{13}$C(α,n) and $^{22}$Ne(α,n) have been constrained by measuring alpha asymptotic normalization coefficients of the near threshold states in $^{17}$O and $^{26}$Mg using the sub-Coulomb ($^{6}$Li,d) alpha-transfer reactions.

- A long standing discrepancy in the structure of $^{9}$He has been resolved by the measurement of narrow (~100 keV) states in the low energy spectrum of $^{9}$He and that the spectrum is dominated by a broad 1/2+ states located at ~3 MeV above the neutron decay threshold.

- The astrophysical factor and reaction rates of the synthesis of primordial (Big Bang) $^{6}$Li isotopes were calculated with high accuracy and confirmed by recent LUNA (Italy) experiment.

- The scaling energies of the giant monopole resonances in $^{40}$Ca, $^{56}$Ni, $^{60}$Ni and $^{68}$Zn were found to agree nicely with HF-RPA calculations using SkM* ($K_{NM}$=216.6 MeV) while those for $^{44}$Ca, $^{54}$Fe, $^{58}$Ni, $^{64}$Zn and $^{90}$Zr agreed with calculations using the KDE0v1 interaction ($K_{NM}$=227.5 MeV), suggesting a need to go beyond the HF-RPA in calculating these excitations with possible implications for the resultant value for $K_{NM}$.

- Within the Born approximation, we have shown that the microscopic mean-field based RPA projected (one-body) transition density provides a good approximation for the hadron excitation cross section of isoscalar giant monopole obtained using the energy-average double transition density, which is not the case for the semi-classical collective model transition density.

- We have carried out HF based RPA calculations of isoscalar giant resonances of multipolarities L=0 – 3 for the Zr and Mo isotopes for over 30 commonly employed Skyrme-type interactions and compared with experimental data, obtaining good agreement for the energies of the monopole (L=0) and the dipole (l=1) but not for L= 2 and 3.

- We have extracted from realistic chiral nuclear interactions the quadratic, quartic, and sextic terms in the isospin-asymmetry expansion of the free energy of nuclear matter at finite temperature, from second-order many-body perturbation theory.

- The spectral functions resulting from the implementation of the Massive Yang-Mills approach for vector and axial vector mesons in vacuum exhibit a tendency toward chiral restoration whereby both a1 and rho mesons broaden while the a1 mass approaches the free rho mass; this is consistent with the phenomenology of dilepton production in heavy-ion experiments.

- Using an in-medium T-matrix approach to calculate the free energy of a heavy quark-antiquark pair in the quark-gluon plasma reveals an underlying interaction potential which retains a long-range string force in medium, suggestive for a strongly coupled medium with important consequences for the heavy-flavor transport coefficient.

- Preliminary simulations to investigate a hybrid EBIT/Penning trap for nuclear lifetime measurements of highly charged ions indicate switching between modes effectively acts as evaporative cooling.

- We have made the first measurement of fusion cross sections in laser produced plasma for the $d+d \rightarrow n+{}^3He$ and $d+{}^3He \rightarrow p+\alpha$ reactions.

- We have investigated the competition of Bosons and Fermions in nuclear dynamics using quantum fluctuations and Landau's approach.

- The spinodal instability of baryon-rich quark matter has been studied in the linear response theory using the Polyakov-Nambu-Jona-Lasinio model, which has added to the understanding of how unstable modes in the quark matter lead to large density fluctuations in a relativistic heavy ion collision.

- A hybrid model based on quark recombination and string fragmentation has been devised for the hadronization of perturbative parton showers in jets, which reproduces results from pure string fragmentation and can be easily generalized to include partons from an ambient medium.

Institute scientists remain active in a number of collaborative research efforts around the world. Major programs include: mass measurements using the Penning Trap at the University of Jyväskylä; continued work with the STAR collaboration at RHIC; measurements of beta decays with the TRINAT collaboration at TRIUMF; ANASEN at MSU; and participation in the SAMURAI collaboration at RIBF in Tokyo, Japan.

I am indebted to Dr. Y.-W. Lui for assembling this report.

S.J. Yennello
June 4, 2016

# SECTION I

# NUCLEAR STRUCTURE, FUNDAMENTAL INTERACTIONS AND ASTROPHYSICS

# Isoscalar E0, E1, and E2 strength in $^{44}$Ca, $^{54}$Fe, and $^{64,68}$Zn

J. Button, Y.-W. Lui, D.H. Youngblood, X. Chen,[1] G. Bonasera, and S. Shlomo
[1]*Department of Radiation Oncology, Medical College of Wisconsin, Milwaukee, Wisconsin*

The giant resonance region from 10 MeV < $E_x$ < 62 MeV in $^{44}$Ca, $^{54}$Fe, $^{64}$Zn, and $^{68}$Zn has been studied with inelastic scattering of 240 MeV α particles at small angles, including 0°. Between 70 and 105% of the expected isoscalar E0 strength has been identified below $E_x$ = 40 MeV for each of the nuclei. A majority of the Energy Weighted Sum Rule was identified for E0 and E2 (≈70%), and nearly half was identified for E1. Between 70 and 104% of the E1 strength has been identified while 60% of E2 strength in $^{54}$Fe and $^{68}$Zn and 120% of the strength in $^{64}$Zn have been identified. The techniques used for the experiments, data analysis, and DWBA calculations are described in Ref. [1] and references therein. The strength distributions are compared with the predictions from HF-RPA calculations with the KDE0v1 interaction [2--5] and are shown in Figs. 1-4 for the respective nuclei.

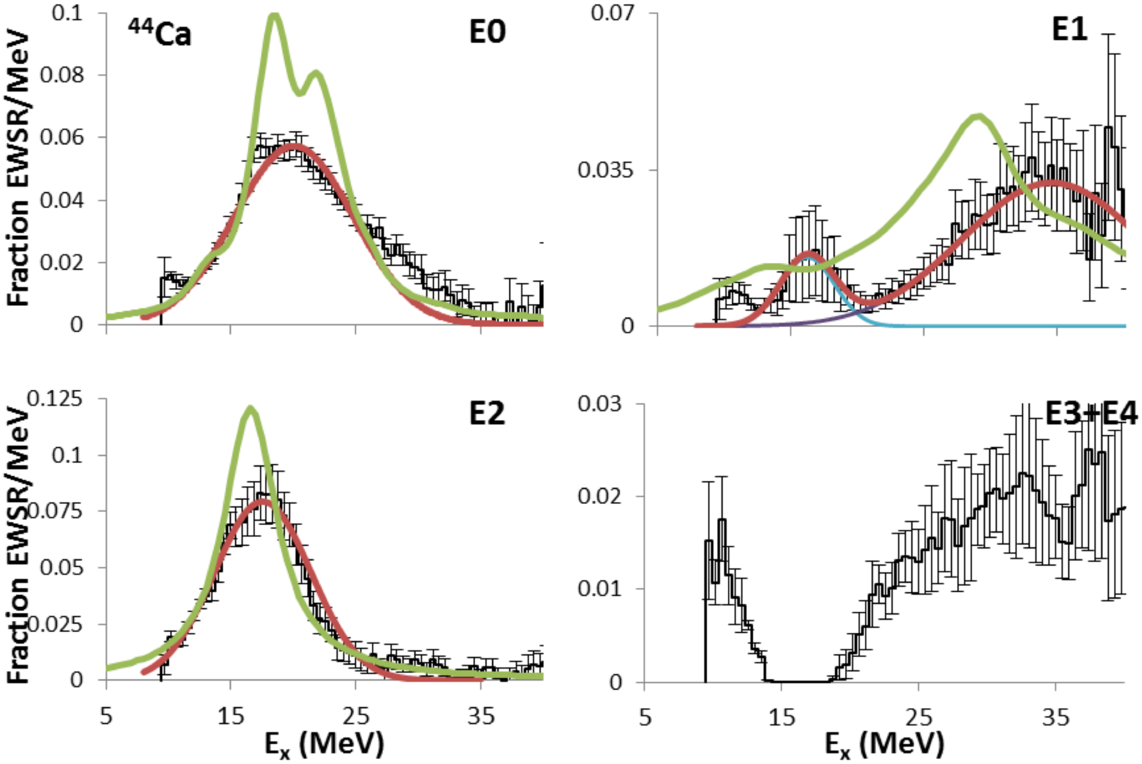

**FIG. 1.** Strength distributions obtained for 44Ca are shown by the histograms. Error bars represent the uncertainty based on the fitting of the angular distributions and different choices for the continuum. Gaussian fits to the E1 distributions for the individual peaks (blue and purple) and their sum (red) are shown. The green lines are the strength distributions obtained with the HF-RPA calculations using the KDE0v1 interaction, smeared to more closely represent the data.

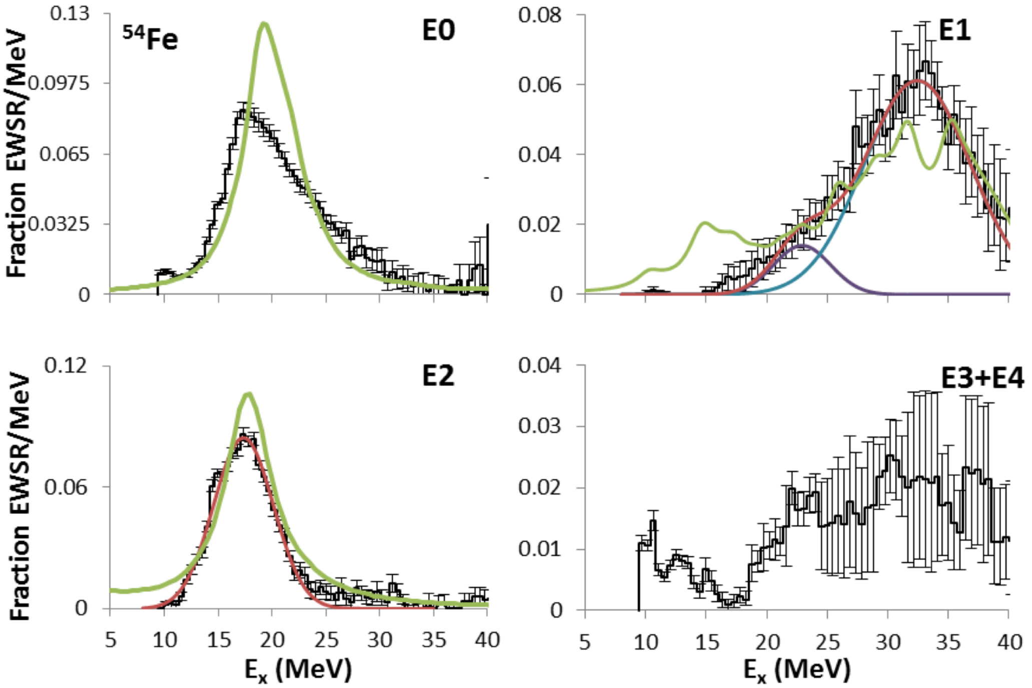

**FIG. 2.** Strength distributions obtained for $^{54}$Fe are shown by the histograms. Error bars represent the uncertainty based on the fitting of the angular distributions and different choices for the continuum. For E1, two Gaussian fits for the low component (purple, smooth line) and high component (blue line) are shown as a sum (red line). A single Gaussian fit is shown for E2. The green lines are the strength distributions obtained with the HF-RPA calculations using the KDE0v1 interaction, smeared to more closely represent the data.

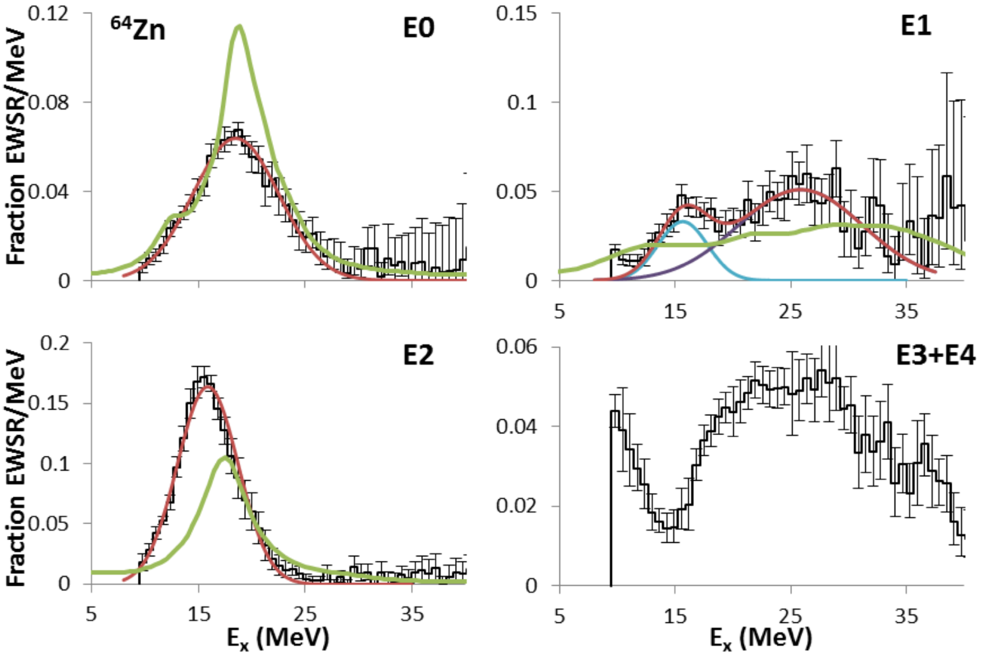

**FIG. 3.** Strength distributions obtained for $^{64}$Zn are shown by the histograms. Error bars represent the uncertainty based on the fitting of the angular distributions and different choices for the continuum. The green lines are the strength distributions obtained with the HF-RPA calculations using the KDE0v1 interaction, smeared to more closely represent the data. The smooth red lines show Gaussian fits.

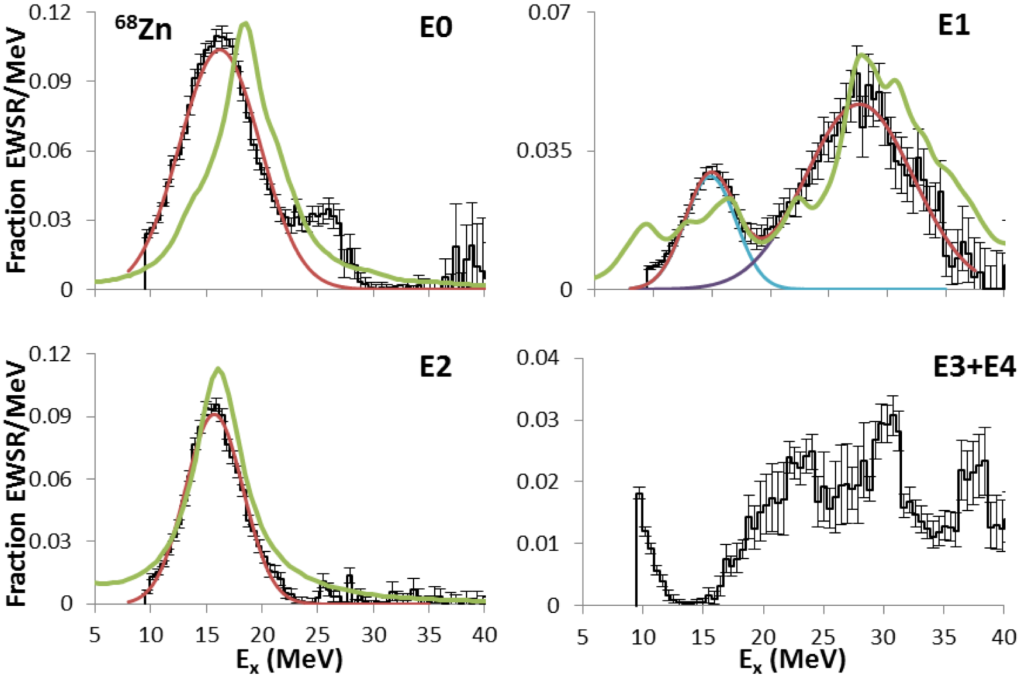

**FIG. 4.** Strength distributions obtained for $^{68}$Zn are shown by the histograms. Error bars represent the uncertainty based on the fitting of the angular distributions and different choices for the continuum. The red, smooth lines show Gaussian fits. The green lines are the strength distributions obtained with the HF-RPA calculations using the KDE0v1 interaction, smeared to more closely represent the data.

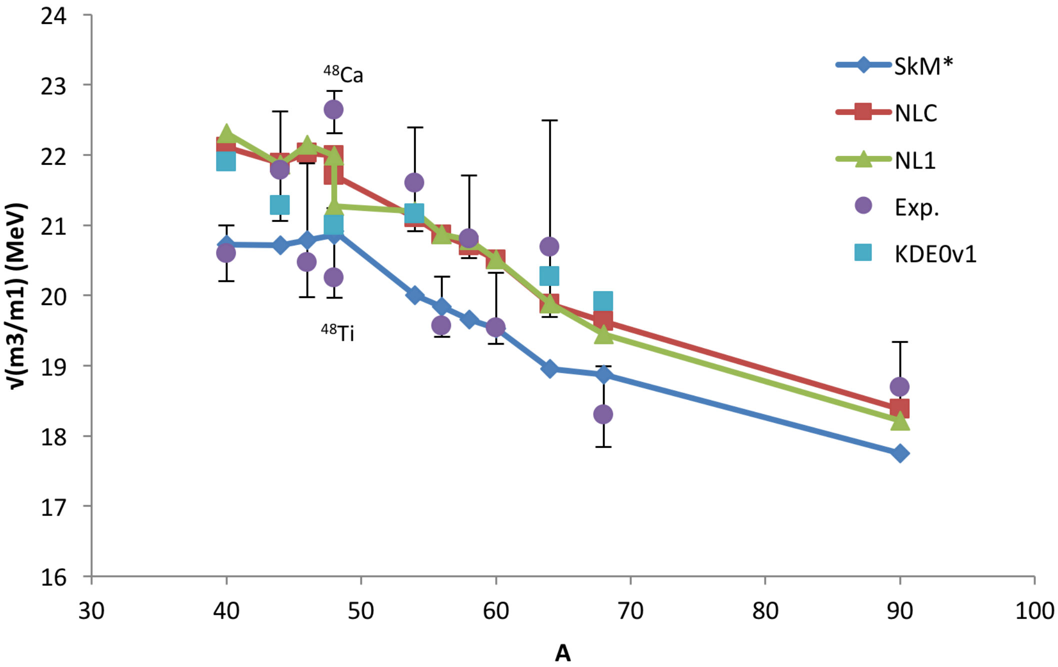

**FIG. 5.** Experimental GMR energies (represented by solid circles) are compared with values calculated by RMF parameterizations [7] (red squares and green triangles) and Skyrme non-relativistic parameterization [6] (blue diamonds). The error bars on the data include systematic errors. The light blue squares are the values obtained from the KDE0v1 interaction. The experimental energies for $^{40,48}$Ca from Ref. [8]; $^{46,48}$Ti from Ref. [9], $^{56}$Fe, $^{58}$Ni, and $^{60}$Ni from Ref. [10]; and $^{90}$Zr from Ref. [11] are included.

A comparison of the experimental values of the scaling model energy for E$_{\mathrm{GMR}}$ $\left(\sqrt{\frac{m_3}{m_1}}\right)$ with the values calculated from Nayak's [6] calculation based on the SkM*(K$_{\mathrm{NM}}$=216.6 MeV), and Chossy and Stocker's [7] calculations based on NLC (K$_{\mathrm{NM}}$=224.5 MeV) and NL1 (K$_{\mathrm{NM}}$=211.1 MeV) non-relativistic and relativistic parameter sets are included in Fig. 5. The $^{54}$Fe and $^{64}$Zn experimental values agree within the uncertainty with the NLC and NL1 values. The experimental value for $^{68}$Zn agrees within uncertainty with the SkM* value and is ~ 1.5 MeV below those calculated with the NLC and NL1 parameter sets. Interestingly, the energies of the GMR in six nuclei ($^{40}$Ca, $^{46,48}$Ti, $^{56}$Fe, $^{60}$Ni, and $^{68}$Zn) agree with the SkM* value, while those in six other nuclei ($^{44,48}$Ca, $^{54}$Fe, $^{58}$Ni, $^{64}$Zn, and $^{90}$Zr) agree with the NLC and NL1 values.

[1] D.H. Youngblood, Y.-W. Lui, J. Button, G. Bonasera, and S. Shlomo, Phys. Rev. C **92**, 014318 (2015).

[2] D.H. Youngblood, Y.-W. Lui, J. Button, M.R. Anders, M.L. Gorelik, M.H. Urin, and S. Shlomo, Phys. Rev. C **88**, 021301 (2013).

[3] M.R. Anders, S. Shlomo, T. Sil, D.H. Youngblood, and Y.-W. Lui, Phys. Rev. C **87**, 024303 (2013).

[4] M. Dutra, O. Lourenço, J.S. Martins, A. Delfino, J.R. Stone, and P. Stevenson, Phys. Rev. C **85**, 035201 (2012).

[5] P. Stevenson, P. Goddard, J. Stone, and M. Dutra, arXiv preprint arXiv:1210.1592 (2012).

[6] R.C. Nayak, J.M. Pearson, M. Farine, P. Gleissl, and M. Brack, Nucl. Phys. **A516**, 62 (1990).

[7] T.v. Chossy and W. Stocker, Phys. Rev. C **56**, 2518 (1997).

[8] D.H. Youngblood, Y.-W. Lui, and H.L. Clark, Phys. Rev. C **63**, 067307 (2001).

[9] Y. Tokimoto, Y.-W. Lui, H.L. Clark, B. John, X. Chen, and D.H. Youngblood, Phys. Rev. C **74**, 044308 (2006).

[10] Y.-W. Lui, D.H. Youngblood, H.L. Clark, Y. Tokimoto, and B. John, Phys. Rev. C **73**, 014314 (2006).

[11] D.H. Youngblood, H.L. Clark, and Y.-W. Lui, Phys. Rev. Lett. **82**, 691 (1999).

# Superallowed beta decay

J.C. Hardy, I.S. Towner, V.E. Iacob, H.I. Park, N. Nica, M. Bencomo, T. Eronen, V. Horvat, and L. Chen

Superallowed $0^+ \rightarrow 0^+$ beta decay between T=1 analogue states has been a subject of continuous and often intense study for five decades. The *ft* values of such transitions are nearly independent of nuclear-structure ambiguities and depend uniquely on the vector part of the weak interaction. Their measurement gives us access to clean tests of some of the fundamental precepts of weak-interaction theory, and, over the years, this strong motivation has led to very high precision being achieved in both the experiments and the theory used to interpret them. We have a major program at the Cyclotron Institute to study superallowed beta decay.

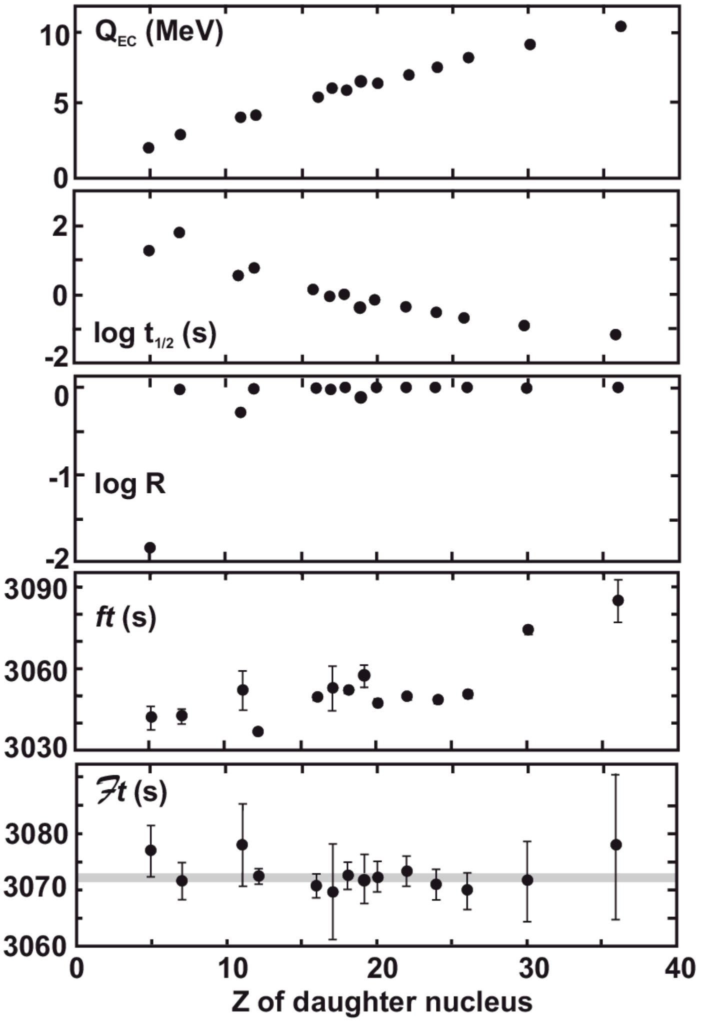

**FIG. 1.** Results of the most recent survey of 14 precisely measured superallowed $0^+ \rightarrow 0^+$ β transitions [1]. The parents of these trans-itions are $^{10}$C, $^{14}$O, $^{22}$Mg, $^{26m}$Al, $^{34}$Cl, $^{34}$Ar, $^{38m}$K, $^{38}$Ca, $^{42}$Sc, $^{46}$V, $^{50}$Mn, $^{54}$Co, $^{62}$Ga and $^{74}$Rb. The top three panels present the average $Q_{EC}$, log $t_{1/2}$ and log $R$ values for each transition. The bottom two panels give the corresponding *ft* and $\mathcal{F}t$ values. The shaded horizontal line in the bottom panel is the average $\mathcal{F}t$ value for all transitions. Where no error bars are visible, they are smaller than the data point.

To obtain the *ft* value for any transition, three quantities must be measured: the half-life $t_{1/2}$ of the parent, the $Q_{EC}$ value for the transition of interest, and the branching ratio *R* for that transition. Our most recent complete survey of world data on these superallowed decays, published in 2015 [1], provides a critical evaluation of all the experimental data and final *ft* values obtained from the averaged results, to which radiative and isospin-symmetry-breaking corrections have been applied in order to derive a final set of "corrected ft values", denoted $\mathcal{F}t$ for 14 transitions known to ~0.1% precision (see Fig. 1). Excellent consistency among the average $\mathcal{F}t$ values for all 14 transitions – an expected consequence of the conservation of vector current (CVC) – confirms the validity of the correction terms; and our recent measurement of $^{38}$Ca decay [2, 3], which closely compares a pair of mirror superallowed transitions with $A = 38$, further supports that validity.

The resultant average $\mathcal{F}t$ value, when combined with the muon lifetime, yields the up-down quark-mixing element of the Cabibbo-Kobayashi-Maskawa (CKM) matrix, $V_{ud} = 0.97417(21)$, a result that is consistent with, but more precise than, values we have obtained in previous analyses of superallowed β decay. The unitarity test on the top row of the matrix becomes $|V_{ud}|^2 + |V_{us}|^2 + |V_{ub}|^2 = 0.99978\ (55)$ if the Particle Data Group recommended value for $V_{us}$ is used. However, recent lattice QCD calculations, not included yet in the PDG evaluation, have introduced some inconsistency into kaon-decay measurements of $V_{us}$ and $V_{us}/V_{ud}$ . In ref. [1], we have examined the impact of these new results on the unitarity test and conclude that there is no evidence of any statistically significant violation of unitarity. Finally, from the $\mathcal{F}t$-value data we also set limits on the possible existence of scalar interactions.

This result is not only a significant verification of the standard model but the uncertainty quoted on the sum provides a tight limit on any possible new physics beyond the standard model, such as right-hand currents, extra *Z* bosons or supersymmetric models. In short, superallowed $0^+ \rightarrow 0^+$ beta decay provides a high-profile application of nuclear-physics measurements to the study of fundamental symmetries, a subject of vital interest to both nuclear and particle physicists. Although much has already been achieved in this field by nuclear physicists, improvements are still possible. Reducing the uncertainty on the unitarity sum – and, with it, the scope for new physics – remains the primary goal of our research program.

Our approach follows from the observation [1] that the second largest contributor to the uncertainty in $V_{ud}$ is the theoretical uncertainty in the nuclear-structure-dependent corrections, $\delta_{NS}$ and $\delta_C$, used in the derivation of the $\mathcal{F}t$ values. Though these corrections are only of order 1%, their effect is very significant: The bottom two panels of Fig. 1 show the result of applying the nuclear-structure-dependent corrections, $\delta_{NS}$ and $\delta_C$ (together with $\delta'_R$, which is nearly independent of *Z*). Obviously they act very well to remove the considerable "scatter" in *ft* values apparent in the second panel from the bottom, replacing it with the consistent set of corrected $\mathcal{F}t$ values appearing in the bottom panel. Since these corrections were determined [4] completely independently of the superallowed decay data, this consistency in $\mathcal{F}t$ values is already a powerful validation of these calculated corrections, but obviously the remaining uncertainty still influences the final result for $V_{ud}$.

Even though the 2015 survey [1] included more than 222 individual measurements relating to 14 precisely known *ft* values, it is still possible for well selected experiments to make real improvements in the validation tests of the nuclear-structure-dependent correction terms. At TAMU we are currently focusing on adding to the *ft*-value list new superallowed transitions, selected from amongst those with *large* calculated corrections. If the *ft* values measured for cases with large calculated corrections also turn into corrected $\mathcal{F}t$ values that are consistent with the others, then this must verify the calculations' reliability for the existing cases, which have smaller corrections. We are studying decays from $T_z$ = -1 parent nuclei, which consistently have higher predicted structure-dependent correction terms than the well-known $T_z$ = 0 cases.

Of particular importance are the four $T_z$ = -1 parent nuclei – $^{26}$Si, $^{34}$Ar, $^{38}$Ca and $^{42}$Ti – whose decays are mirrors to well-known superallowed decays from $T_z$ = 0 parents. Specifically, the mirror-decay pairs are $^{26}\text{Si} \rightarrow {}^{26m}\text{Al} \rightarrow {}^{26}\text{Mg}$, $^{34}\text{Ar} \rightarrow {}^{34}\text{Cl} \rightarrow {}^{34}\text{S}$, $^{38}\text{Ca} \rightarrow {}^{38m}\text{K} \rightarrow {}^{38}\text{Ar}$ and $^{42}\text{Ti} \rightarrow {}^{42}\text{Sc} \rightarrow {}^{42}\text{Ca}$. Their importance stems from our observation that the ratio of mirror *ft* values for such cases is very sensitive to the model used to calculate the small isospin-symmetry-breaking corrections $\delta_{NS}$ and $\delta_C$. The details have been described in our report on the first measurement of a mirror pair, with *A* = 38 [2]. Until very recently, none of the $T_z$ = -1 parent decays was known precisely enough to provide a statistically significant constraint on the correction terms via the ratio of mirror *ft* values, but we are now well on our way to rectifying this situation.

After a long period of incremental upgrades to our experimental techniques, we succeeded in pushing our precision in branching-ratio measurements close to ±0.1%, our ultimate goal. This is crucial for the characterization of $T_z$ = -1 parent decays, which – unlike $T_Z$ = 0 decays – exhibit a number of strong Gamow-Teller branches that compete with the superallowed Fermi branch. A demonstration of our success in this endeavor is our measurement of the superallowed branching ratio for the decay of $^{38}$Ca ($t_{1/2}$ = 444 ms) to a precision of ±0.2%, where that precision was actually limited by counting statistics, not systematics [2, 3]. An important aspect of these decays is the possibility of weak beta decays to highly excited states in the daughter, which are too weak to be observed individually but in total could constitute sufficient strength to affect the branching ratio obtained for the superallowed branch. These have been investigated theoretically for $^{34}$Ar and $^{38}$Ca decay, and found to be negligibly small [3, 5].

To our knowledge, this is the most precise direct branching-ratio measurement ever made for a short-lived beta emitter. It also provides the first mirror pair of $0^+ \rightarrow 0^+$ superallowed emitters ($^{38}$Ca and $^{38}$K$^m$) that is precise enough to distinguish meaningfully between the Saxon-Woods-based radial-overlap correction, $\delta_{C2}$, and the one based on Hartree-Fock radial wave functions. It favors the former over the latter, but we must await results from the other mirror pairs before we can be confident of the verdict. We are now well embarked on the measurement of the remaining three accessible pairs. We have already made a measurement of the branching ratio for the superallowed decay of $^{34}$Ar, which is being prepared for publication; and we have also re-measured its half-life [6]. In addition, we have made a successful measurement of the $^{26}$Si beta-decay branching ratios, which is under analysis as the thesis project of M. Bencomo [7]. Finally we have made an initial measurement of the half-life of $^{42}$Ti [8], which is also now under analysis. Likely a follow-up measurement will be required for us to achieve the precision we seek.

Our 2015 survey incorporated 20 superallowed transitions [1], which we deemed to be all those that were likely to be accessible in the near future. By the time the survey was published our prediction had already been proven wrong by the publication from GSI of a new measurement of the half-lives and Gamow-Teller branching ratios for the β decays of $^{42}$Ti, $^{46}$Cr, $^{50}$Fe and $^{54}$Ni. Although the $^{42}$Ti superallowed transition was included in our survey, the other three were not. Consequently we have published an addendum to our 2015 survey [9], in which we extended the same evaluation of world data to the three new superallowed parents [10], and we also included calculations of the correction terms [11] required to understand the results. These decays are not yet known precisely enough to contribute to the determination of $V_{ud}$, but all the required information is now available for the time when more precise measurements are available.

We are also endeavoring to improve our data acquisition techniques for half-life measurements by a variety of means, including the addition of a TDC-based approach, and a digital-pulse-analysis system. The TDC system has already proved very useful in disentangling a problem with our $^{42}$Ti measurement [8], and the digital system is currently being upgraded to increase its gain so as to avoid rate-dependent threshold effects [8]. We continue to test both these new systems while continuing to rely on our tried-and-true analog system to provide our primary data. We also continue to refine our measurement techniques [12] and to explore potential improvements in the statistical handling of our data [13].

[1] J.C. Hardy and I.S. Towner, Phys. Rev. C **91**, 025501 (2015).

[2] H.I. Park, J.C. Hardy, V.E. Iacob, M. Bencomo, L. Chan, V. Horvat, N. Nica, B.T. Roeder, E. Simmons, R.E. Tribble and I.S. Towner, Phys. Rev. Lett. **112**, 102502 (2014).

[3] H.I. Park, J.C. Hardy, V.E. Iacob, M. Bencomo, L. Chen, V. Horvat, N. Nica, B.T. Roeder, E. McCleskey, R.E. Tribble and I.S. Towner, Phys. Rev. C **92**, 015502 (2015).

[4] I.S. Towner and J.C. Hardy, Phys. Rev. C **77**, 025501 (2008).

[5] I.S. Towner and J.C. Hardy, *Progress in Research,* Cyclotron Institute, Texas A&M University (2014-2015), p. III-49.

[6] V.E. Iacob *et al.*, *Progress in Research,* Cyclotron Institute, Texas A&M University (2015-2016), p. I-14.

[7] M. Bencomo *et al.*, *Progress in Research,* Cyclotron Institute, Texas A&M University (2015-2016), p. I-10.

[8] H.I. Park *et al.*, *Progress in Research,* Cyclotron Institute, Texas A&M University (2015-2016), p. I-17.

[9] I.S. Towner and J.C. Hardy, Phys. Rev. C **92**, 055505 (2015).

[10] J.C. Hardy and I.S. Towner, *Progress in Research,* Cyclotron Institute, Texas A&M University (2015-2016), p. I-18.

[11] I.S. Towner and J.C. Hardy, *Progress in Research,* Cyclotron Institute, Texas A&M University (2015-2016), p. III-22.

[12] V.E. Iacob and J.C. Hardy, *Progress in Research,* Cyclotron Institute, Texas A&M University (2015-2016), p. IV-43.

[13] V. Horvat and J.C. Hardy, *Progress in Research,* Cyclotron Institute, Texas A&M University (2015-2016), p. IV-45.

## Superallowed β-decay branching ratio measurement of $^{26}$Si

M. Bencomo, J.C. Hardy, V.E. Iacob, H.I. Park, L. Chen, V. Horvat, N. Nica, B.T. Roeder, A. Saastamoinen, R.E. Tribble, and I.S. Towner

We have acquired data, which we are currently analyzing, on the branching ratio for the superallowed $0^+ \rightarrow 0^+$ $\beta^+$ emitter $^{26}$Si (Fig. 1). Since the $Q_{EC}$ [1] value and half-life [2] have already been measured, the branching ratio will allow us to determine the *ft* value. This would be the second pair of mirror superallowed transitions from a $T_Z$ = -1 parent, $^{26}\mathrm{Si} \rightarrow {}^{26m}\mathrm{Al}$ and $^{26m}\mathrm{Al} \rightarrow {}^{26}\mathrm{Mg}$. Our previous measurement of the mirror transitions, $^{38}\mathrm{Ca} \rightarrow {}^{38m}\mathrm{K}$ and $^{38m}\mathrm{K} \rightarrow {}^{38}\mathrm{Ar}$, showed that the ratio of mirror *ft* values is very sensitive to the model used to calculate the small isospin symmetry-breaking correction required to extract $V_{ud}$. In calculating this correction, two alternative models were used, one based on Woods-Saxon (WS) radial wave functions and the other on Hartree-Fock (HF), with the experimental results from the first pair favoring Woods-Saxon [3]. In an effort to determine if this conclusion is supported more generally, we continue this type of work with $^{26}$Si.

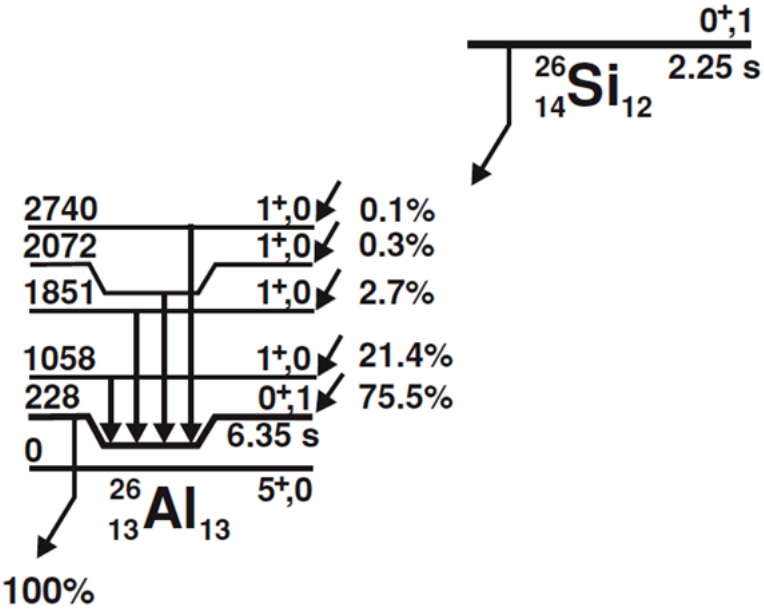

**FIG. 1.** Decay scheme of $^{26}$Si showing only those features of relevance to the superallowed β decay. All energies in keV. Data taken from Ref. [4].

Last year, we reported [5] the experimental procedure followed in the measurement, which used the Momentum Achromat Recoil Separator (MARS) along with the fast tape transport system. It was also reported, how the analysis for this particular isotope was to be carried out, with the branching ratios to the $1^+$ states in $^{26m}$Al being determined and then subtracted from 100% to yield the superallowed branching ratio. Corrections to the branching ratio were mentioned but none had been done at the time. These small corrections need to be made in order to determine the branching ratio precisely. Most of the corrections have now been made:

*Random coincidences* - We need to make sure that every *β-γ* coincidence involves a *γ*-ray and *β* particle from the same decay event. Because of the way data are collected and stored event-by-event we are able to remove random coincidences by gating on the prompt peak in the β-γ time-difference spectrum. The result is a β-coincident γ-ray spectrum only including events that correspond to the decay of $^{26}$Si.

*Parent fraction* - As data are being collected $^{26}$Si is decaying into $^{26m}$Al, which itself decays into $^{26}$Mg. This means that the number of *β*-singles we detect during the counting period includes both the decay of the parent nucleus and a fraction of the decay of the daughter. This is important since we need to determine the total number of β-singles that correspond to $^{26}$Si. As a necessary control, we record the number of $^{26}$Si ions deposited in the tape as a function of time during each cycle. Knowing this, along with the half-life of both $^{26}$Si and its daughter $^{26m}$Al, we can determine the activities of both and obtain a ratio. It was determined that 57.13% of the β-singles recorded were produced by the decay of $^{26}$Si.

*Real Coincidence summing* - With $\beta^+$ decay we have annihilation radiation being recorded by the HPGe detector in addition to the β-delayed γ rays. One of the 511 keV gammas from annihilation and an 829-keV gamma from the 1058 keV state, for example, can reach the detector simultaneously, creating a 1340-keV peak in our spectrum (see Fig. 2). This sum peak steals counts from the peak of interest; therefore a correction (~2.6%) has to be applied to the 829-keV peak to correct for this loss.

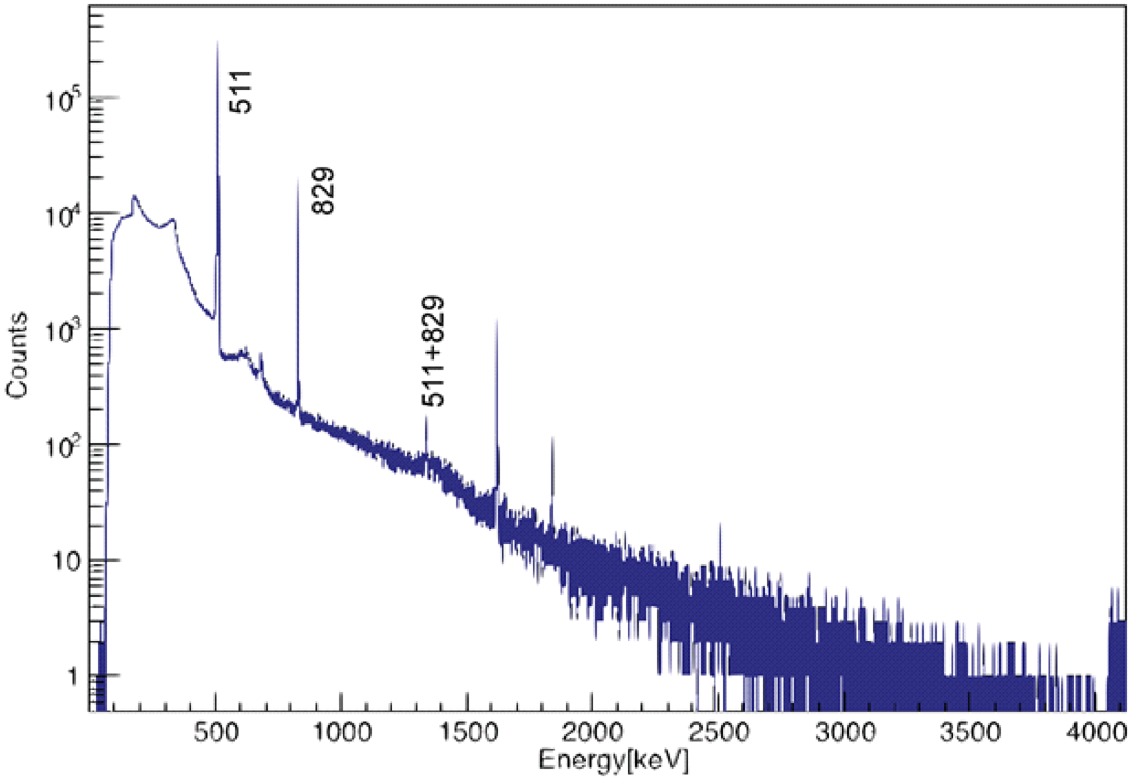

**FIG. 2.** Spectrum of β-delayed γ rays coincident with beta particles from the decay of $^{26}$Si. Peaks are labeled according to their energy in keV. The '511+829' peak is a result of coincidence summing between a 511-keV γ ray from annihilation and an 829-keV γ ray**.**

*Impurities* - Just as the decay from the daughter contributes to the beta singles rate, so impurities can also contribute, albeit at a much smaller scale. First, we need to determine which of the impurities that we observe at the focal plane of MARS actually get implanted in the tape by running calculations that use SRIM software. With this result, we can use the known half-lives of the contaminants to determine their contributions, usually a small fraction of a percent. In this measurement, the two contaminants that could potentially be implanted in the tape are $^{23}$Mg and $^{24}$Al. However, with the thickness of the Al degraders used during the experiment (146.05 μm), we determine that no impurities were implanted during the experiment (see Fig. 3).

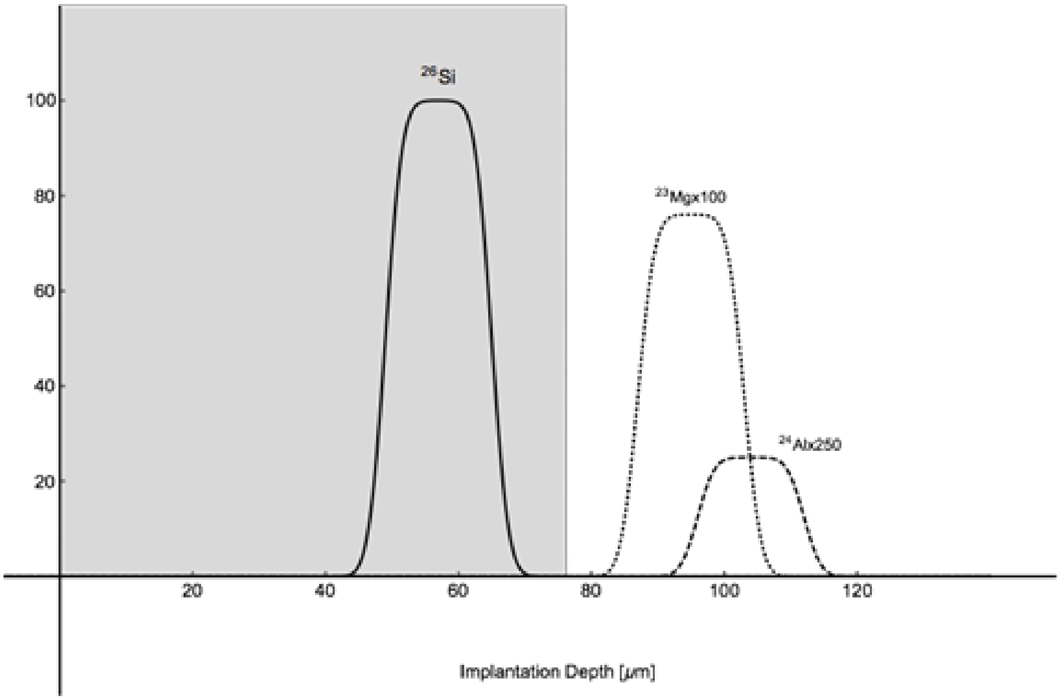

**FIG. 3.** Illustration of calculated implantation profiles in Mylar for the $^{26}$Si beam and those impurities with similar ranges. All beams enter from the left. The shaded region corresponds to the actual thickness of our collection tape. Those ions within the shaded region are collected in our sample, all others are not.

*Dead time* - This refers to the time during which the electronics are busy processing a signal from the detector. The dead time for *β* processing is small, ~450 ns. The *γ*–ray detection on the other hand is much slower and the dead time depends on the rate of coincident and singles *γ* rays. This correction is still in progress.

[1] T. Eronen *et al.*, Phys. Rev. C **79**, 032802(R) (2009).

[2] V.E. Iacob, J.C. Hardy, A. Banu, L. Chen, V.V. Golovko, J. Goodwin, V. Horvat, N. Nica, H.I. Park, L. Trache, and R.E. Tribble. Phys. Rev. C **82**, 035502 (2010).

[3] H.I. Park *et al.*, Phys. Rev. Lett. **112**, 102502 (2014).

[4] J.C. Hardy and I.S. Towner, Phys. Rev. C **91**, 025501 (2015).

[5] M. Bencomo *et al.*, *Progress in Research,* Cyclotron Institute, Texas A&M University (2014-2015), p. III-49.

# The half life of $^{34}$Ar

V.E. Iacob, J.C. Hardy, M. Bencomo, L. Chen, V. Horvat, N. Nica, H.I. Park,
B.T. Roeder, and A. Saastamoinen

Currently, precise *ft*-values measured for superallowed $0^+ \rightarrow 0^+$ $\beta$ transitions provide the most accurate value for $V_{ud}$, the up-down quark mixing element of the Cabibbo-Kobayashi-Maskawa (CKM) matrix [1]. This enables the most demanding test of CKM unitarity, a basic tenet of the Standard Model. Recently it has been shown [2] that further improvements in precision are possible if the *ft* values for pairs of mirror $0^+ \rightarrow 0^+$ transitions can be measured with 0.1% precision or better. The decays of $^{34}$Ar and $^{34}$Cl are members of such a mirror pair, but so far the former has not been known with sufficient precision. In the 10 years since the publication of our result for the half-life of $^{34}$Ar [3], we have improved significantly our acquisition set-up and our analysis techniques: We have added features [4] and refinements that allow a better control of the acquired data and thus lead to increased accuracy and precision in the final result.

We report here an experiment aiming to improve the half-life of $^{34}$Ar. The experiment detected positrons as in Ref. [3] but with improved controls. The total decay spectrum is presented in Fig. 1; it contains more than $3\times10^8$ combined $^{34}$Ar and $^{34}$Cl decays. The main difficulty in this type of measurement is caused by the decaying daughter nucleus, in this case $^{34}$Cl, whose half-life is about twice that of $^{34}$Ar.

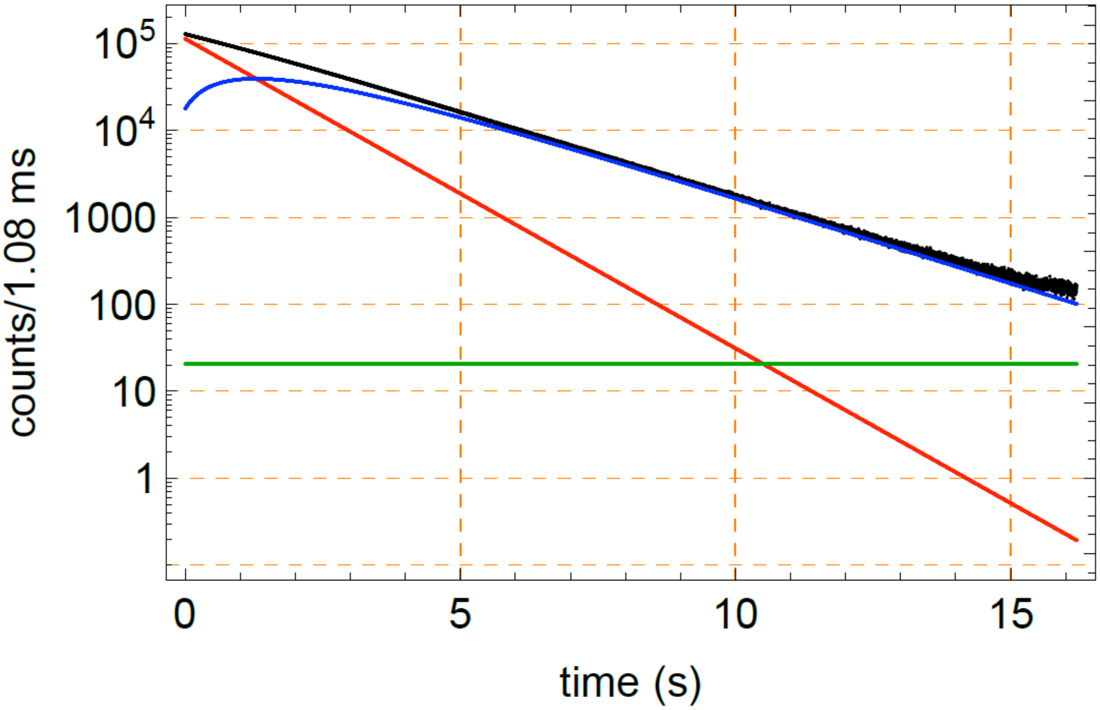

**FIG. 1.** Total decay spectrum observed in the decay of $^{34}$Ar. There is a total of more than $3\times10^8$ events in the spectrum distributed over 15,000 time channels, each 1.08 ms wide. The total spectrum (black) is decomposed into its contributors: $^{34}$Ar (red), $^{34}$Cl (blue) and background (green).

This almost completely obscures the $^{34}$Ar contribution to the total spectrum since we detect positrons and are thus unable to differentiate between parent and daughter decays. The case is illustrated in Fig. 1 which contains, along with the total decay spectrum, the individual contributions of the two nuclear decays.

We solved this problem [3] by using a restricted fit that makes use of the parent-daughter link involved in the decay. However, at the time of our previous measurement [3] we did not recognize the importance of the small difference in detection efficiency between the two decays, which have slightly different end-point energies. This is because the low-energy cut-off has a smaller effect on decay spectra with higher end-point energies than it does on lower energy decays. The result in our case is a slightly higher detection efficiency for the $^{34}$Ar decay. Fig. 2 illustrates this point by presenting the energy distribution of the positrons emitted by the two nuclei along with the detection efficiency curve. The inset zooms in on the low energy region relevant for the cut-off effect. For the particulars of our detector, this amounts to $\varepsilon_{Cl}/\varepsilon_{Ar} = 0.9996$.

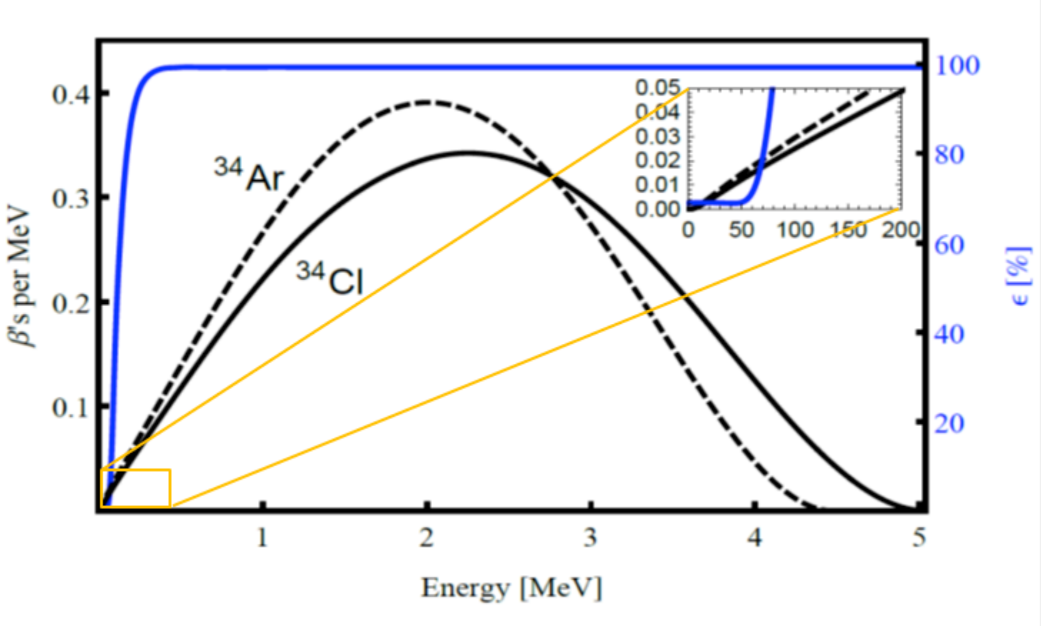

**FIG. 2**. Energy distribution of the positrons emitted in the decay of $^{34}$Ar (solid line, black) and $^{34}$Cl (dashed line, black). The detection efficiency (solid line, blue) is superimposed to illustrate the cut-off effect; the efficiency units are given in the right vertical axis. The inset zooms in the energy region relevant to the cut-off; the energy axis in the inset is given in keV's.

When included in the fit, this difference in detection efficiencies increases the half-life of $^{34}$Ar. The preliminary result obtained from the thorough analysis of about one third of the total statistics gives for this increase a value of 1.5 σ relative to the result in Ref. [3].

[1] J.C. Hardy and I.S. Towner, Phys. Rev. C **91**, 025501 (2015).

[2] H.I. Park, J.C. Hardy, V.E. Iacob, M. Bencomo, L. Chan, V. Horvat, N. Nica, B.T. Roeder, E. Simmons, R.E. Tribble, and I.S. Towner, Phys. Rev. Lett. **112**, 102502 (2014).

[3] V. Iacob *et al.*, Phys. Rev. C **74**, 055502 (2006).

[4] V.E. Iacob, *et al.*, *Progress in Research*, Cyclotron Institute, Texas A&M University (2008-2009), p. V-43.

# Studies towards the precise measurement of the half-life of $^{42}$Ti

H.I. Park, J.C. Hardy, V.E. Iacob, V. Horvat, M. Bencomo, L. Chen, N. Nica,
B.T. Roeder, and A. Saastamoinen

Two years ago [1], we reported a successful test measurement of the half-life of $^{42}$Ti, which employed a digital-waveform-analysis system. Then last year [2], we added a comparative study of our digital and standard analogue systems based on off-line measurements on calibration sources. The results from the on-line measurement showed that the $^4$He($^{40}$Ca, 2n)$^{42}$Ti reaction would provide approximately 2000 particles/s of $^{42}$Ti with 300 nA of primary $^{40}$Ca beam at 32 MeV/nucleon. It was also demonstrated that, with extraction slits on the MARS recoil spectrometer set tight, we could deposit $^{42}$Ti samples near the back of the collection tape and thus obtain quite pure $^{42}$Ti nuclei by letting most produced impurities pass through the tape without stopping. However, the off-line comparative study reached the unfavorable conclusion that the gain of the digital system was likely insufficient to permit us to detect the lowest energy beta particles, thus compromising half-life measurements by introducing a potentially rate-dependent threshold.

These findings were used to optimize the experimental conditions for a full-fledged measurement of the half-life of $^{42}$Ti, which we conducted in the summer of 2015. Compared with our test measurement, we replaced the digital system with our standard analogue electronics and also ran a TDC-based system in parallel to take data from the proportional gas counter. This arrangement allowed us to independently record absolute time information event by event under the same well-controlled conditions. More importantly, the use of an additional, separate method for taking data from the proportional gas counter offers a means to test for possible systematic effects in the measurement, as well as an opportunity to improve our data-acquisition techniques for all half-life measurements.

Unfortunately, our ongoing data analysis has revealed an unexpected problem. By comparing our standard analogue technique with the TDC-based approach, we found a time delay between the beginning of each count period as defined by the fast tape-transport system and the actual start time when data were recorded with our standard analogue system. This was a feature we had introduced for our branching-ratio measurements and had inadvertently left connected for the half-life measurement. Moreover, the time delay itself was apparently malfunctioning since it was found to vary with time (likely as a function of temperature in the cave). Having identified the cause, we could extract the time delay of the standard analogue system cycle-by-cycle based on the absolute time recorded from the TDC-based system. This made it possible to adjust the time base of the $^{42}$Ti decay spectra.

Our next step is to independently determine the $^{42}$Ti half-life from the data sets of the two systems and to test for the consistency of their results. All these studies will bring us one step closer to achieving a precise measurement of the $^{42}$Ti half-life.

[1] H.I. Park *et al.*, *Progress in Research*, Cyclotron Institute, Texas A&M University (2013-2014), p. I-23.

[2] H.I. Park *et al.*, *Progress in Research*, Cyclotron Institute, Texas A&M University (2014-2015), p. IV-79.

# Survey of world data for the superallowed decays of $^{42}$Ti, $^{46}$Cr, $^{50}$Fe, and $^{54}$Ni

J.C. Hardy and I.S. Towner

At regular intervals over more than four decades, we have published critical surveys of world data on superallowed $0^+ \rightarrow 0^+$ Fermi β transitions and their impact on weak-interaction physics, with the last survey appearing in February 2015 [1]. In all, 20 transitions were included in this most-recent survey, of which 18 had a complete set of data, comprising in each case the $Q_{EC}$ value, half-life and branching ratio. Of those 18, all but 4 had been measured to high precision. Our justification for including 20 cases, some of which were incomplete or poorly known was that we deemed these 20 cases to encompass all those that were likely to be accessible to precision measurements in the near future.

By the time the survey was published, our prediction had already been proven wrong: In January 2015, Molina *et al.* [2] reported a measurement of the half-lives and Gamow-Teller branching ratios for the β decays of $^{42}$Ti, $^{46}$Cr, $^{50}$Fe and $^{54}$Ni. Although the $^{42}$Ti transition was included in our survey, those of $^{46}$Cr, $^{50}$Fe and $^{54}$Ni were not. In fact, the $Q_{EC}$ values for the three latter transitions are still poorly known and even the new measurements of the half-lives and branching ratios have yet to reach the precision required to contribute meaningfully to any standard-model tests. Nevertheless, Molina *et al.* have convincingly demonstrated that these nuclei are indeed accessible and potentially amenable to more precise measurements.

As a result, we produced and published [3] an addendum to our 2015 survey, in which we extended the same evaluation of world data to the three new superallowed transitions and we also evaluated the correction terms required to understand the results, taking the opportunity to update results for $^{42}$Ti to incorporate new information. The correction-term calculations are described elsewhere in this report [4]. Here we focus on the survey of world data.

We surveyed world data using exactly the same methods as in our 2015 survey [1] and, for consistency, we displayed the results in a similar tabular format even though relatively few references are involved. For details of the measured results and the publications in which they appeared the reader is referred to Ref. [3]. In Table I, we present the average world-data results together with the corrected $\mathcal{F}t$ values derived using the calculated correction terms [4].

**Table I.** World data average results for the decays of $^{42}$Ti, $^{46}$Cr, $^{50}$Fe, and $^{54}$Ni.

| Parent nucleus | $f$ | Partial half-life $t$ (ms) | $ft$ (s) | $\mathcal{F}t$ |
|---|---|---|---|---|
| $^{42}$Ti | 7130.5±1.4 | 433 ± 12 | 3090 ± 88 | 3096 ± 88 |
| $^{46}$Cr | 10660±150 | 292.6 ± 9.1 | 3120 ± 110 | 3130 ± 110 |
| $^{50}$Fe | 14950±600 | 204.8 ± 4.5 | 3060 ± 140 | 3080 ± 140 |
| $^{54}$Ni | 21850±670 | 144.9 ± 2.3 | 3170 ± 110 | 3180 ± 110 |

Since the comparison of mirror pairs of $0^+ \rightarrow 0^+$ transitions has been shown [5] to be a valuable method for testing the isospin-symmetry-breaking corrections, we also tabulated the predicted *ft*-value ratios for the four mirror pairs, of which $^{42}$Ti, $^{46}$Cr, $^{50}$Fe and $^{54}$Ni are the most neutron deficient parents. These predicted ratios, presented here in Table 2, provide ample motivation for future high-precision measurements.

**Table II.** Calculated ratios $ft^a/ft^b$ for four mirror doublets.

| Decay pairs *a;b* | $\delta_R{}^b - \delta_R{}^a$ (%) | $\delta_C{}^b - \delta_C{}^a$ (%) | $ft^a/ft^b$ |
|---|---|---|---|
| $^{42}$Ti → $^{42}$Sc; $^{42}$Sc → $^{42}$Ca | 0.296 (30) | -0.265 (25) | 1.00564 (39) |
| $^{46}$Cr → $^{46}$V; $^{46}$V → $^{46}$Ti | 0.165 (10) | -0.140 (82) | 1.00305 (83) |
| $^{50}$Fe → $^{50}$Mn; $^{50}$Mn → $^{50}$Cr | 0.120 (20) | 0.005 (43) | 1.00115 (47) |
| $^{54}$Ni → $^{54}$Co; $^{54}$Co → $^{54}$Fe | 0.143 (30) | -0.020 (85) | 1.00163 (90) |

With future experimental precision at the ~0.1 % level, it would become possible to test the corrections for these pairs in the way we first demonstrated in Park *et al*. [5] for the mirror superallowed decays of $^{38}$Ca and $^{38m}$K. Particularly attractive is the mass-42 mirror pair, for which the *ft*-value ratio is expected to differ from unity by nearly 0.6%.

[1] J.C. Hardy and I.S. Towner, Phys. Rev. C **91**, 025501 (2015).

[2] F. Molina *et al.,* Phys. Rev. C **91**, 014301 (2015).

[3] I.S. Towner and J.C. Hardy, Phys. Rev. C **92**, 055505 (2015).

[4] I.S. Towner and J.C. Hardy, *Progress in Research,* Cyclotron Institute, Texas A&M University (2015-2016) p. III-22.

[5] H.I. Park *et al.,* Phys. Rev. Lett. **112**, 102502 (2014) and Phys. Rev. C **92**, 015502 (2015).

# United States nuclear structure data program (USNDP) and evaluated nuclear structure data file (ENSDF) at Texas A&M University

N. Nica[1] and J.C. Hardy
[1] *Under contract with Brookhaven National Laboratory*

Since 2005 we have been an important partner in the nationwide United States Nuclear Data Program (USNDP), which is part of the Nuclear Structure and Decay Data (NSDD) international nuclear data-evaluation network. USNDP is in fact the main part of the NSDD network, making the greatest effort in completion of the goals of the nuclear-structure data evaluation communities. Nuclear data evaluation is a national-interest activity financed by DOE, through which relevant nuclear-science results in virtually all world publications are retrieved and put together in a large Evaluated Nuclear Structure Data File (ENSDF) database according to general polices, a set of rules that make possible a standard approach through which the data are uniformly evaluated.

This activity is carried by a relatively small group of professionals located mostly in national institutes but also hosted by a few universities. The nuclear data network is the nodal point for the wide dissemination of nuclear knowledge to many users, from those in basic science to those engaged in commercial applications in American and international businesses. The output is published in the Nuclear Data Sheets, an Elsevier publication, and also is disseminated by different on-line databases, which can be retrieved at the NNDC site (http://www.nndc.bnl.gov), IAEA Vienna's site (http://www-nds.iaea.org), and other locations.

In the 11 years that the Cyclotron Institute of Texas A&M has been involved, we have completed the evaluation of mass chains covering a large part of the nuclear chart. We have published in Nuclear Data Sheets the superheavy $A$=252 mass chain [1]; the very data-rich mid-mass chains, $A$=140 [2], $A$=141 [3], $A$=147 [4] and $A$=148 [5]; the relatively lighter chains, $A$=97 [6] and $A$=84 [7]; and, in collaboration with B. Singh and a group of authors from McMaster University, Canada, we also published the $A$=77 [8], $A$=37 [9], $A$=36 [10], and $A$=34 [11] chains. Another big mass chain, $A$=157, was published in Nulear Data Sheets [12] at the beginning of 2016. Two more, $A$=140 and $A$=158, have been submitted and are currently undergoing review. Our total effort is 0.67 FTE per year.

In January 2016 we started a new evaluation of $A$=155, a mass chain that had previously been evaluated twelve years before. The chain consists of isotopes of Ce, Pr, Nd, Pm, Sm, Eu, Gd, Tb, Dy, Ho, Er, Tm, Yb, Lu, Hf, and Ta, a total of 16 isobars. About 190 papers relating to these nuclei have been published since June 2004 when the previous evaluation ended, of which about 70 are experimental studies. This work is in progress.

[1] N. Nica, Nucl. Data Sheets **106**, 813 (2005).
[2] N. Nica, Nucl. Data Sheets **108**, 1287 (2007).
[3] N. Nica, Nucl.Data Sheets **122**, 1 (2014).
[4] N. Nica, Nucl. Data Sheets **110**, 749 (2009).
[5] N. Nica, Nucl. Data Sheets **117**, 1 (2014).
[6] N. Nica, Nucl. Data Sheets **111**, 525 (2010).

[7] D. Abriola *et al.*, Nucl. Data Sheets **110**, 2815 (2009).
[8] B. Singh and N. Nica, Nucl. Data Sheets **113**, 1115 (2012).
[9] J. Cameron, J. Chen, B. Singh, and N. Nica, Nucl. Data Sheets **113**, 365 (2012).
[10] N. Nica, J. Cameron, and B. Singh, Nucl. Data Sheets **113**, 1 (2012).
[11] N. Nica and B. Singh, Nucl. Data Sheets **113**, 1563 (2012).
[12] N. Nica, Nucl.Data Sheets **132**, 1 (2016).

# Tests of internal-conversion theory with precise γ- and x-ray spectroscopy: The case of $^{125m}$Te

N. Nica, K. Ofodile, J.C. Hardy, V.E. Iacob, and M.B. Trzhaskovskaya[1]
[1]*Petersburg Nuclear Physics Institute, Gatchina RU-188300, Russia*

Internal conversion is an important component of most nuclear decay schemes. In order to balance decay schemes correctly, one needs to know the internal conversion contribution to each transition as expressed by its internal conversion coefficient (ICC). Nevertheless, ICCs are only rarely measured; instead they are taken from tabulations. As a result, calculated ICCs are essential input to every decay scheme, except those for the lightest nuclei. Unfortunately, over the decades, tabulated ICC values have differed significantly from one calculation to another by a few percent. Although for many applications such differences can be tolerated, transitions used in critical calibrations require very precise and accurate ICC values, precision that has simply been impossible to guarantee at the one-percent level or below.

In order to correct for this deficiency one can only seek guidance from measured ICCs that have sufficient precision to distinguish among the various calculations. However, as recently as about a decade ago, when a survey of measured ICCs was made by Raman et al. [1], there were only five published ICC values with precision of the order of ±1%, not enough to make any definitive conclusion possible. At that time, one aspect of the ICC calculations remained a particular concern. The final-state electron wave function must be calculated in a field that adequately represents the remaining atom. But should that representation include the atomic vacancy created by the conversion process? Some calculations included it and some did not.

Thus the problem of measuring ICCs at the ±1% precision level became critical and, with our very precisely efficiency-calibrated HPGe detector [2], we found ourselves in a position to be able to address it. Consequently, over the past decade we have been measuring a series of ICCs [3] covering a wide range of atomic numbers, $50 \leq Z \leq 78$. So far, all these results have indicated that the atomic vacancy should be taken into account in the calculations. The most recent case, the 109.3-keV $M4$ transition depopulating $^{125m}$Te, is reported here. We selected it because previous measurements of its $\alpha_K$ value disagreed with theory, whether or not the vacancy was accounted for.

The total intensity of an electromagnetic transition is split between γ-ray emission and electron conversion, which can take place in several atomic shells and subshells, and is followed by the corresponding x rays. If only $K$-shell conversion is considered, then one can use the following formula to determine the $K$-shell conversion coefficient, $\alpha_K$:

$$_K \quad _K = \frac{N_K}{N} \quad \frac{\quad}{_K}, \tag{1}$$

where $\omega_K$ is the fluorescence yield, which we take from Ref. [4]; $N_K$ and $N_\gamma$ are the respective peak areas of the $K$ x rays and the γ ray; and $\varepsilon_K$ and $\varepsilon_\gamma$ are the corresponding detector absolute efficiencies.

The transition of interest here is the 109.3-keV, *M4* transition in $^{125}$Te, which depopulates the 144.8-keV, 57.4-day isomeric state. The measurement is complicated by the fact that the *M*4 transition is followed by a 35.5-keV, *M1+E2* transition to the stable ground state. (The *E2* admixture, $\delta = 0.031(3)$ is small.) With a large value of $\alpha_K(35.5) = 11.64$[*], the *K* x rays from the conversion of the 35.5-keV transition constitute about 60% of the total strength of the tellurium *K* x-ray peaks in the spectrum. Thus, to achieve precision on the strength of K x rays attributable to the 109.3-keV transition, which is required to apply Eq. (1), a very precise detector efficiency is required at 35.5 keV γ-ray energy, as well as at 109.3 keV and at 28.0 keV, the weighted average energy of the tellurium *K* x rays.

Our detection efficiency for the 109.3-keV γ ray is known to within ±0.15% relative precision but, as described in Ref. [2], the original detector calibration was only established with that precision at energies above 50 keV. Accordingly, a special investigation was required to determine efficiency values below 50 keV, a task made especially difficult by the scattered radiation that becomes increasingly difficult to distinguish from the total-energy peak as the γ-ray energy decreases [3]. We obtained efficiencies at two different energies. The first, at 22.6 keV, was obtained with a standard $^{109}$Cd source, which produces an 88-keV γ ray and 22.6-keV silver *K* x rays. The second, at 34.1 keV, came from the decay of locally made $^{139}$Ba, which yields 165.9-keV γ rays and 34.1-keV lanthanum *K* x rays. For both sources the relative intensities of their γ and x rays are well known so this allowed the low energy data to be connected to the higher-energy data, for which our detector efficiencies were well established. We quote the efficiencies at the lower energies with an uncertainty of ±1%.

A $^{125m}$Te radioactive source was prepared from 99.9%-enriched $^{124}$Te, which was in the form of a thin disk 0.5 μm thick and 17 mm in diameter electroplated on a 10-μm thick pure Al backing. The source was activated by thermal neutrons for 24 h at the Nuclear Science Center TRIGA reactor of Texas A&M University to produce a very pure $^{125m}$Te radioactive source, which we measured for several days. The spectra were carefully searched for impurities but no major impurities were detected.

Because of the contribution from the 35.5-keV transition to the x-ray peak, our result, $\alpha_K(109.3) = 187.2(58)$, is rather less precise than in our previous measurements but it is quite sufficient to refute the previous measurements, 166(9) and 166(11), and confirm the theoretical ICC calculation. Furthermore, it clearly shows a preference for the theory that includes the vacancy, which yields $\alpha_K = 186$, over the calculation that ignores the vacancy, which yields $\alpha_K = 179$ but the experimental uncertainty prevents that discrimination from being conclusive.

[1] S. Raman *et al.*, Phys. Rev. C **66**, 044312 (2002).

[2] J.C. Hardy *et al.*, Appl. Radiat. Isot. **56**, 65 (2002) ; R.G. Helmer *et al.*, Nucl. Instrum. Methods Phys. Res. **A511**, 360 (2003); R.G. Helmer *et al.*, Appl. Radiat. Isot. **60**, 173 (2004).

[3] N. Nica *et al.*, Phys. Rev. C **70**, 054305 (2004); Phys. Rev. C **71**, 054320 (2005); Phys. Rev. C **75**, 024308 (2007), Phys. Rev. C **77**, 034306 (2008), Phys.Rev. C **80**, 064314 (2009); Phys.Rev. C **89**, 014303 (2014), Phys. Rev. C **93**, 034305 (2016); J.C.Hardy *et al.*, Appl.Radiat.Isot. **87**, 87 (2014).

[4] E. Schönfeld and H. Janssen, Nucl. Instrum. Methods Phys. Res. **A369,** 527 (1996).

---

[*] Average value calculated with the interpolator code BrIcc (http://bricc.anu.edu.au) of 11.68 (including vacancy, "frozen orbital" approach) and 11.60 (excluding vacancy).

[5] M. Sainath and K. Venkataramaniah, Nuova Cim., A **111**, 223 (1998); M. Sainath, K. Venkataramaniah, and P.C. Sood, Phys. Rev. **C** 58, 3730 (1998).

# Precise measurement of $\alpha_K$ and $\alpha_T$ for the 150.8-keV *E*3 transition in $^{111}$Cd: Test of internal-conversion theory

N. Nica, J.C. Hardy, V.E. Iacob, H.I. Park, T.A. Werke, C.M. Folden III, L. Pineda, and
M.B. Trzhaskovskaya[1]
[1] *Petersburg Nuclear Physics Institute, Gatchina RU-188300, Russia*

Last year, we reported [1] on a measurement of the internal conversion coefficients (ICC), $\alpha_K$ and $\alpha_T$, for the 150.8-keV *E*3 transition in $^{111}$Cd. At that time, analysis was incomplete and only preliminary results were presented. In the meantime, the analysis has been completed and the results published [2]. Since the experimental details were described last year [1], we focus here on the analysis.

The decay scheme of the 48.5-min isomer in $^{111}$Cd is shown in Fig. 1. The presence of a second transition in cascade with the *E*3 transition of interest might be expected to present a problem for our measurement but, in fact, because the conversion coefficients for the higher energy *E*2 transition are much smaller, it does not seriously degrade the uncertainty on $\alpha_K$ and it actually offers a further advantage: the opportunity to measure $\alpha_T$ as well as $\alpha_K$ for the *E*3 transition.

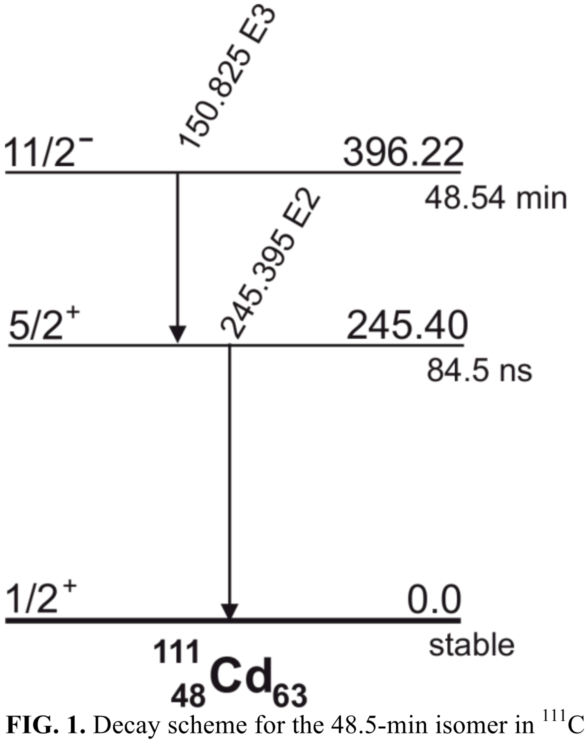

**FIG. 1.** Decay scheme for the 48.5-min isomer in $^{111}$Cd.

In simple cases with a single transition that can convert in the *K* shell the value of $\alpha_K$ is given by

$$\alpha_K = (N_K/N_\gamma)(\varepsilon_\gamma/\varepsilon_K)(1/\omega_K) , \tag{1}$$

where $\omega_K$ is the fluorescence yield, $N_K$ and $N_\gamma$ are the total number of observed *K* x rays and γ rays, respectively; and $\varepsilon_\gamma$ and $\varepsilon_K$ are the corresponding photopeak detection efficiencies.

In the case of $^{111m}$Cd decay there are two transitions involved that both can contribute to the *K* x ray peaks. However, there is no side feeding of the intermediate state so we can make use of the fact that the total transition intensities must be equal. Thus, we can extract the $\alpha_K$ value for the 150.8-keV transition, by using a modified version of Eq. (1): *viz.*

$$\alpha_{K150} = (N_K/N_{\gamma150})(\varepsilon_{\gamma150}/\varepsilon_K)(1/\omega_K) - \alpha_{K245}\,(N_{\gamma245}/N_{\gamma150})(\varepsilon_{\gamma150}/\varepsilon_{\gamma245})\ , \tag{2}$$

where the subscripts 150 and 245 on a quantity denote the transition – either the 150.8-keV or 245.4-keV one – to which the quantity applies. Furthermore, we can determine $\alpha_{T150}$ via the equation

$$(1 + \alpha_{T150})\,(N_{\gamma150}/\varepsilon_{\gamma150}) = (1 + \alpha_{T245})\,(N_{\gamma245}/\varepsilon_{\gamma245})\ . \tag{3}$$

In analyzing our data, we took the *N* values from our spectra and the γ-ray efficiencies from our well-established HPGe detector calibration [3]. The *K* x-ray efficiency, $\varepsilon_K$, we took from a calibration we made more recently with a $^{109}$Cd source [4]. Our two ICC results appear in the top line of Table I, where each can be compared with two theoretical values, one that was calculated without accounting for the atomic vacancy and one that included the vacancy in the "frozen orbital" (FO) approximation.. Clearly the result for $\alpha_K$ agrees well with the calculation that incorporates the vacancy. This is consistent with all our previous measurements of $\alpha_K$.

**Table I.** Comparison of the measured $\alpha_K$ and $\alpha_T$ values for the 150.853(15)-keV *E*3 transition from $^{111m}$Cd with calculated values based on two different theoretical models. Shown also are the percentage deviations Δ from the experimental value, calculated as (experiment-theory)/theory.

| **Model** | $\boldsymbol{\alpha_K}$ | **Δ(%)** | $\boldsymbol{\alpha_T}$ | **Δ(%)** |
|---|---|---|---|---|
| Experiment | 1.449(18) | | 2.217(26) | |
| Theory | | | | |
| No vacancy | 1.425(1) | +1.7(12) | 2.257(1) | -1.8(12) |
| Vacancy FO | 1.451(1) | -0.1(12) | 2.284(1) | -2.9(12) |

Our $\alpha_T$ result does not lead to such a simple conclusion: It is lower than both calculations, with the worst disagreement (~2.5σ) being with the FO calculation. One possible explanation [2] arises from the fact that the 150.8-keV transition is hindered by a factor of $10^4$ relative to the single-particle Weisskopf estimate. Under such conditions, one could expect to encounter "penetration", which is a dynamic effect associated with the change from transition electromagnetic potentials used for a point nucleus to transition potentials required for a realistic finite-sized nucleus. For unhindered electric transitions, the penetration effect is not significant, but it may reach several percent for magnetic transitions. The effect is included in our ICC calculations by an approximation based on the surface-current model but it is done uniformly with all nuclei and all transitions. For strongly hindered transitions, the penetration effect can become more important, giving rise to non-negligible nuclear matrix elements in the expressions for the ICCs. In this way these particular ICCs become dependent on nuclear structure details and nuclear transition dynamics. It is plausible that this can explain our results; certainly a no more definitive explanation is possible.

[1] N. Nica *et al.*, *Progress in Research,* Cyclotron Institute, Texas A&M University (2014-2015), p I-62.
[2] N. Nica, J.C. Hardy, V.E. Iacob, T.A. Werke, C.M. Folden III, L. Pineda, and M.B. Trzhaskovskaya, Phys. Rev. C **93**, 034305 (2016).
[3] J.C. Hardy *et al.*, Appl. Radiat. Isot. **56**, 65 (2002) ; R.G. Helmer *et al.*, Nucl. Instrum. Methods Phys. Res. **A511**, 360 (2003); R.G. Helmer *et al.*, Appl. Radiat. Isot. **60**, 173 (2004).
[4] N. Nica, J.C. Hardy, V.E. Iacob, M. Bencomo, V. Horvat, H.I. Park, M. Maguire, S. Miller, and M.B. Trzhaskovskaya, Phys. Rev. C **89**, 014303 (2014).

# Preliminary measurement of the superallowed *β*-branching ratio of $^{10}$C

T. Eronen, J.C. Hardy, V. Iacob, H.I. Park, M. Bencomo, L. Chen, V. Horvat,
N. Nica, B.T. Roeder, and A. Saastamoinen

$^{10}$C is one of the superallowed $0^+ \rightarrow 0^+$ $\beta$ emitters that can be used to test the Standard Model of Particle Physics [1]. It is the $V_{ud}$ matrix element of the Cabibbo-Kobayashi-Maskawa (CKM) quark mixing matrix that can be derived from the superallowed $\beta$ emitters, and $V_{ud}$ is a key component used in testing the unitarity of the matrix.

There are three experimental quantities that are required with high precisionin order for a superallowed $\beta$ decay to contribute to these studies. These are the half-life ($t_{1/2}$), branching ratio (BR) and the total decay energy ($Q_{EC}$). In addition, a few theoretical corrections of order 1% are needed to correct for radiative and isospin-symmetry-breaking effects. Combined, a comparative half-life value, denoted $\mathcal{F}t$, is obtained for each transition. The average of $\mathcal{F}t$ values for the 14 transition currently known with high precision yields the world-average $\mathcal{F}t$ value that is used for testing the Standard Model.

For $^{10}$C, all the three experimental quantities have already been measured with quite high precision, but the branching ratio has a fractional uncertainty three times that of the half-life and the $Q_{EC}$-value of the transition, as can be seen from Fig. 1. Thus, any improvement in the precision of the branching ratio alone would directly translate into an improvement in the $\mathcal{F}t$ value for $^{10}$C. The current branching ratio value of 1.4646(19)% derives primarily from two twenty-year-old measurements [2, 3].

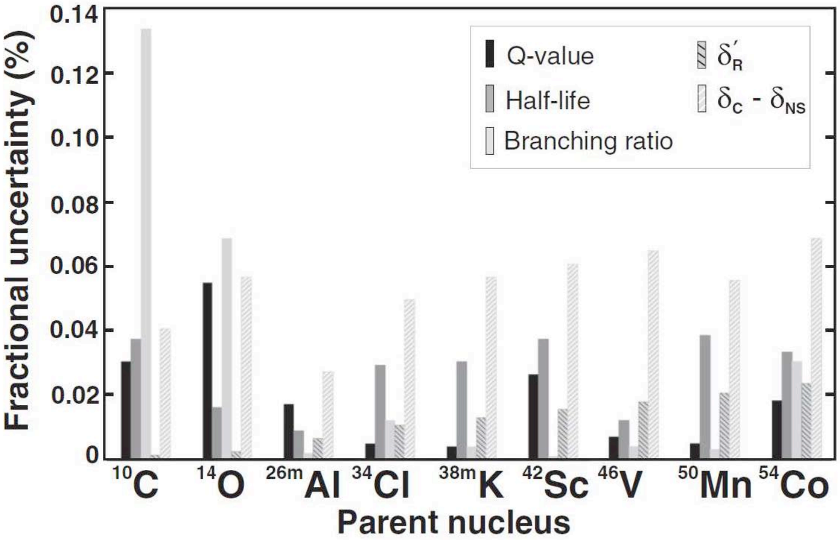

**FIG. 1.** Fractional uncertainties of experimental and theoretical quantities for some of the superallowed $\beta$ transitions used to test the unitarity of the CKM matrix. Clearly the branching ratio of $^{10}$C needs to be improved if it is to be equivalent to the rest of the quantities. This figure is from Ref. [1].

More interesting than just the precision of the $\mathcal{F}t$ value itself is its relationship to the world average of $\mathcal{F}t$ values for transitions in heavier nuclei, since the $^{10}$C transition is the most sensitive to the possible presence of a scalar current. Currently the $\mathcal{F}t$ value for $^{10}$C is slightly higher than the world average $\mathcal{F}t$ value, with an error bar that just about touches the world average value's error bar. If a more precise $\mathcal{F}t$ value of $^{10}$C were found to deviate with greater statistical significance, it would be a signal for the existence of a scalar current.

A project to improve the superallowed $\beta$ branching ratio of $^{10}$C was initiated at the Cyclotron Institute of Texas A&M University in the Fall of 2015. One week of beam time was used in November 2015 to produce $^{10}$C via the $^{1}$H($^{10}$B,n)$^{10}$C reaction. In this preliminary investigation, we measured the branching ratio using the $\beta - \gamma$ coincidence setup that has been specifically developed here for extremely high-precision branching-ratio measurements. It includes a germanium detector that has been calibrated to 0.15% relative absolute efficiency [4] and a thin scintillator for detecting positrons. The angular coverage of the germanium detector is about 1% and the scintillator about 40%. The setup has already been used several times for other branching ratio measurements, (e.g. see Ref. [5]).

The decay scheme of $^{10}$C is relatively simple, as seen in Fig. 2. In principle the superallowed branching ratio can be obtained directly from a ratio of the observed rate for the 1022-keV $\gamma$ ray relative to the rate for the 718-keV $\gamma$ ray, but in practice there are several important systematics effects that need to be carefully taken into account.

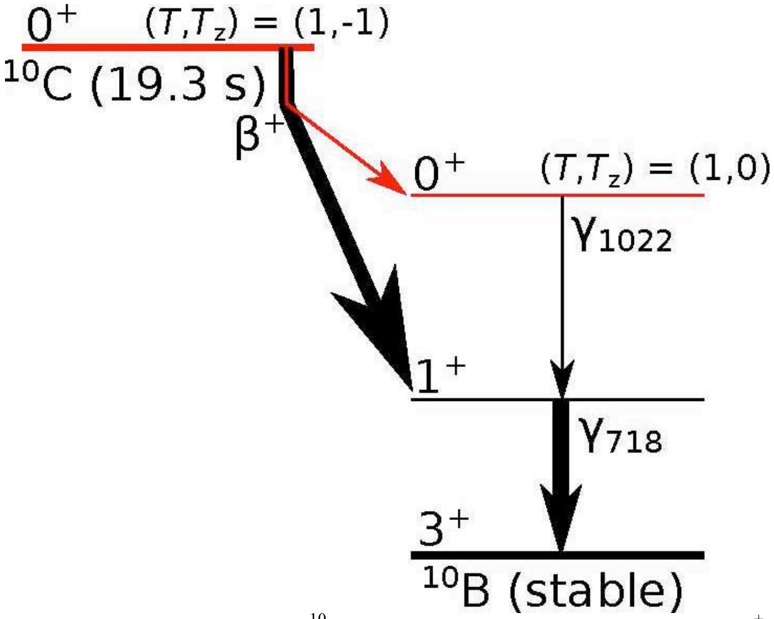

**FIG. 2.** Decay scheme of $^{10}$C. Most of the decays populate the $1^+$ state directly, with only a small fraction of about 1.5% proceeding through the superallowed transition to the $0^+$ state. The two decay paths merge at the 718 keV level, so there is a 718 keV $\gamma$ emitted in every decay. The superallowed transition is marked in red.

## Pileup of detector signals

To get enough statistics for the weak superallowed branch (the 1022 keV γ-ray line), a sufficient decay rate is needed in a limited beam-time period. High rate, however, increases the chance of detector signals piling up. This is especially troublesome for the 1022-keV γ-ray peak since 511-keV photons originating from positron annihilation can pile up at that energy, causing interference with the relatively weak γ-ray peak. With the decay rates during our first measurement the fraction of pileup counts of the whole peak was determined to be 5-10%. Separate studies to characterize the 511+511 keV pileup are ongoing.

## Positron detection efficiency

The endpoint energy of the emitted positrons in the $0^+ \rightarrow 0^+$ branch is rather low, about 1 MeV, whereas the endpoint energy for the $0^+ \rightarrow 1^+$ branch is about 2 MeV. These energies are so significantly different that the scintillator's detection efficiencies for the two transitions differ by more than 10%. The energy dependence of the scintillator's efficiency is now being characterized with sources and Monte Carlo simulations.

## Gamma detection efficiency

The germanium detector has been extensively efficiency-calibrated with both Monte Carlo simulations and sources [4]. To confirm these results for our specific energies – 718 and 1022 keV – we are using sources with similar energies.

Analysis of the data collected in the November 2015 run is ongoing. Another run is needed to obtain sufficient statistics in the 1022 keV peak. In November, we maximized the production rate by using all the available beam intensity. Unfortunately isotopically enriched $^{10}$B was not available for use in the ion source at that time, leaving a potential boost of ×5 for the future. The rate should be not too high, though, to swamp the 1022 keV peak with pileups rather than the 1022-keV γ rays we seek to measure.

[1] J.C. Hardy and I.S. Towner, Phys. Rev. C **91**, 025501 (2015).

[2] G. Savard *et al.*, Phys. Rev. Lett. 74, 1521 (1995).

[3] B. Fujikawa *et al.*, Phys. Lett. B **449**, 6 (1999).

[4] R. Helmer *et al.*, Nucl. Instrum. Methods Phys. Res., **A511**, 360 (2003).

[5] H.I. Park *et al.*, Phys. Rev. Lett. **112**, 102502 (2014).

# Clustering in $^{10}$Be

S. Upadhyayula, G.V. Rogachev, E. Koshchiy, E. Uberseder, V.Z. Goldberg, J. Hooker,
H. Jayatissa, C. Hunt, and B. T. Roeder

There is a strong experimental evidence that some states in $^{10}$Be exhibit molecular-like α:2n:α configuration [1,2,3]. Theoretically these exotic structures can be explored microscopically in the antisymmetrized molecular dynamics plus Hartree-Fock approach [4] or in Molecular Orbital model [5]. Based on these theoretical studies, it appears that the 6.179 MeV $0^+$ state in $^{10}$Be has a pronounced α:2n:α configuration with an α-α inter-distance of 3.55 fm. This is 1.8 times more than the corresponding value for the $^{10}$Be ground state. The $2^+$ at 7.542 MeV in $^{10}$Be is believed to be the next member of this rotational band [6]. The state at 10.2 MeV was identified as a $4^+$ member [1, 3]. The algebraic model [7] predicts that a $6^+$ state at around 13 MeV is the terminating member of this band. It would be of paramount importance to identify this $6^+$ state experimentally and to conclusively establish the complete α:2n:α rotational band. This would become the most striking and well established case of molecular-like configurations in nuclei and an important step towards better understanding of clustering phenomena in atomic nuclei.

We performed an experiment to search for the $6^+$ state in $^{10}$Be at around 13 MeV excitation energy in the excitation function for $^6$He+α scattering. The Cyclotron Institute Momentum Achromat Recoil Separator (MARS) facility was used to generate a secondary $^6$He beam at 7.0 MeV/u from the production reaction of $^7$Li(d,$^3$He). The sketch of the experimental setup is shown in Fig. 1. The scattering chamber consisted of three forward silicon detectors to measure the total energy of the recoil α's. A

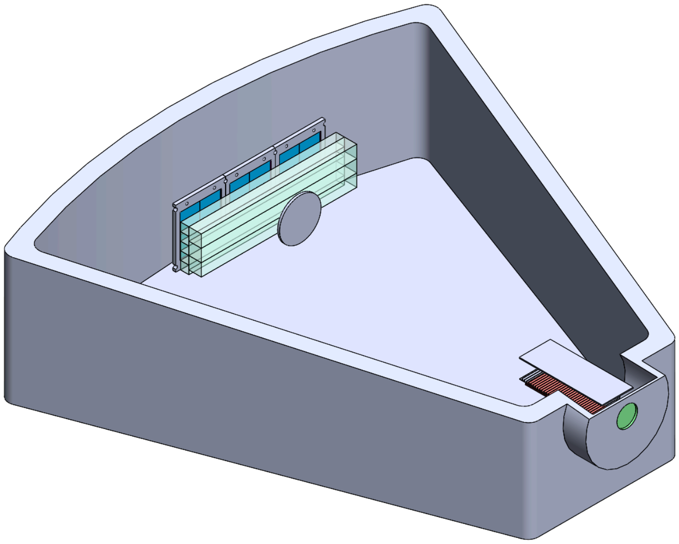

**FIG. 1.** Sketch of the experimental setup to measure the 6He+α excitation function around 13 MeV of $^{10}$Be excitation energy.

position sensitive proportional counter located just before the silicon detectors and consisted of eight cells, in two layers, was used for particle identification and scattering angle reconstruction. A windowless ionization chamber for overall normalization and beam contaminant identification was installed at the entrance to the gas filled scattering chamber. There was a removable disk just before the proportional counter cells to avoid permanently damaging the silicon detector located on the beam axis and to reduce the trigger rate by stopping 95% of the $^6$He ions not interacted with α particles. The setup was optimized to measure elastic and inelastic $^6$He+α scattering at the lowest laboratory angles possible

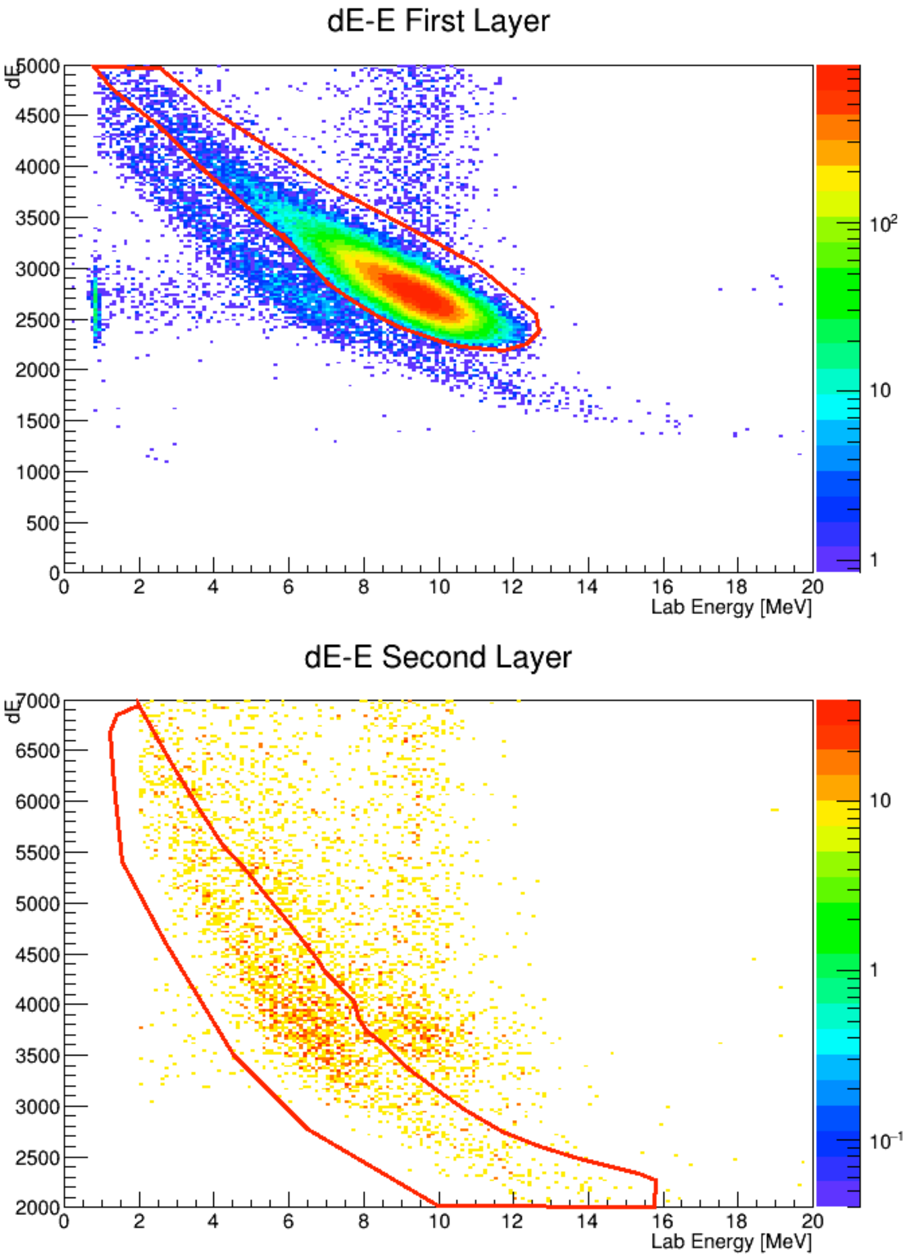

**FIG. 2.** dE-E spectrum for the first and second layers of the position sensitive proportional counter and an off-center silicon detector.

(closest to $180^o$ in c.m.) where the $6^+$ state has maximum cross section (but decreases sharply for smaller c.m. angles). A mixture of 95% Helium gas with 5% $CO_2$ was used as a target. We also used a scintillator placed before the entrance window to degrade the beam energy to achieve the desired energy range. This was used in conjunction with the ionization chamber for particle identification of the secondary beam.

The scattering of $^6$He+α was measured over a few angles close to $180^0$ c.m. to search for the $6^+$ state of the highly deformed cluster band in $^{10}$Be. Using the proportional counter, we were able to achieve good particle separation and select for the recoil α particles in spite of a significant background from the $^6$He ions. We have achieved strong background reduction by gating on the alpha-particles in the dE-E 2D spectrum in the second layer of wires after it was anti-gated on the $^6$He in the first layer of the wires, as shown in Fig. 2. A distinct peak of α particles is clearly visible in Fig. 3 and could be a result of a resonance in the $^6$He+α excitation function which we were looking for! Moreover, the energy of this peak corresponds to the excitation energy close to 13 MeV under the assumption that alpha decay of this state predominantly populates the first excited state in $^6$He, the $2^+$ at 1.8 MeV. Further analysis is now under way in order to investigate if any source other than the $^6$He+α inelastic scattering can result in similar spectrum.

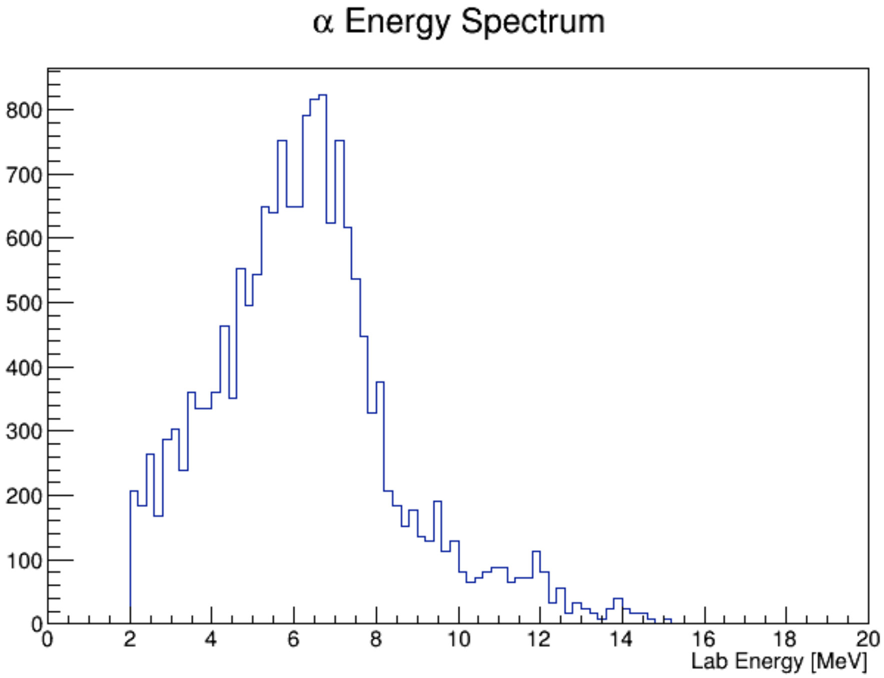

**FIG. 3.** Spectrum of α particles measured by the off-center Si detectors. The peak at 7 MeV may be a result of a resonance in the 6He+α inelastic scattering, or alternatively a result of random coincidence with the α+t events (see text for details).

[1] M. Freer *et al.*, Phys. Rev. Lett. **96**, 042501 (2006).
[2] M. Milin *et al.*, Phys. At. Nucl. **69**, 1360 (2006).
[3] D. Suzuki *et al.*, Phys. Rev. C **87**, 054301 (2013).
[4] A. Doté, H. Horiuchi, and Y. Kanada-Enýo, Phys. Rev. C **56**, 1844 (1997).

[5] N. Itagaki and S. Okabe, Phys. Rev. C **61**, 044306 (2000).
[6] A.N. Kuchera *et al.*, Phys. Rev. C **88**, 054615 (2011).
[7] R. Wolsky *et al.*, Phys. At. Nucl. **73**, 1405 (2010).

# Study of the $^{32}S(\alpha,\gamma)^{36}Ar$ reaction rate important for X-ray bursts nucleosynthesis

M.L. Avila,[1] G.V. Rogachev, E. Uberseder, E. Koshchiy, J. Hooker, C. Hunt, H. Jayatissa,
S. Upadhyayula, C. Magana, V.Z. Goldberg, B.T. Roeder, A. Saastamoinen,
A. Spiridon, M. Dag, M.L. Avila,[1] and D. Santiago-Gonzales[2]
[1]*Argonne National Laboratory, Argonne, Illinois*
[2]*Department of Physics, Louisiana State University, Baton Rouge, Louisiana*

X-ray bursts (XRBs) are thermonuclear flashes that occur in the envelope of a neutron star accreting mass from a companion star [1]. Type I X-ray bursts are the most frequent type of thermonuclear stellar explosions in the galaxy. The bursts are characterized by a sudden rise of the X-ray luminosity followed by an exponential decay, typically lasting from 10 seconds to several minutes with a recurrence time of hours to days. The abundance flow and nucleosynthesis of XRBs are related to the temperature and density conditions and the interplay of charged-particle reactions and $\beta$ decays. The main thermonuclear runaway is driven by the rp-process and the $\alpha$p-process, where proton- or $\alpha$-particle induced reactions on stable and radioactive nuclei occur using H and He accreted onto the surface of the neutron star. A recent study of the nucleosynthesis and nuclear processes important for type I X-ray bursts was published in Ref. [1]. This study identified about 30 nuclear reactions as the main sources of uncertainty in XRB nucleosynthesis, particularly because for most of these reactions there is no experimental rate information available. Thus, measuring the key reactions outlined in Ref. [1] will help to constrain the predictions of nucleosynthesis and light curves in XRBs.

One of the critical reactions identified in Ref. [1] is the $^{32}S(\alpha,\gamma)^{36}Ar$ reaction. A variation in the rates of this $\alpha$ capture process was found to affect the final yields of at least three isotopes around $A\approx30$. Little experimental information exists for the states near the $\alpha$ and proton thresholds in $^{36}Ar$ located at 6.64 MeV and 8.5 MeV, respectively. Several attempts have been made to measure these near-threshold states in $^{36}Ar$ [2,3]. A study by Ref. [2] was performed to investigate the influence of the SCl reaction cycle in explosive hydrogen burning that may occur in a variety of scenarios such as novae, type II supernovae, and X-ray bursts. In that work, states near the proton threshold in $^{36}Ar$ were studied using the $^{35}Cl(^{3}He,d)^{36}Ar$, $^{32}S(^{6}Li,d)^{36}Ar$, $^{32}S(\alpha,\gamma)^{36}Ar$, $^{35}Cl(p,\gamma)^{36}Ar$, and $^{35}Cl(p,\alpha)^{32}S$ reactions. However, the measurement of the $^{32}S(^{6}Li,d)^{36}Ar$ reaction suffered from low statistics, preventing the authors from measuring deuteron angular distributions. Therefore, only proton partial widths were measured and no spectroscopic information for the $\alpha$ channel was obtained. Although they were able to determine rates for the $^{35}Cl(p,\gamma)^{36}Ar$ reaction, the authors of [2] concluded that additional experimental work is needed in order to determine the (p,$\alpha$) rates. In Ref. [3], the $^{35}Cl(^{3}He,d)^{36}Ar$ reaction was used to study states near the proton threshold, but only upper limits for the relative $\alpha$ widths were obtained. It is clear that additional experimental information, especially about the $\alpha$ channel, is needed for the reaction rate calculations of the $^{32}S(\alpha,\gamma)^{36}Ar$ and the $^{32}S(\alpha,p)^{35}Cl$ reactions.

The Asymptotic Normalization Coefficient (ANC) technique has been shown to be successful for measuring $\alpha$ partial widths of sub-threshold states and near-threshold resonances using the $\alpha$ -transfer reaction ($^{6}Li$,d) [4-7]. It can be used to extract $\alpha$ partial widths of excited states in order to study $\alpha$-particle induced reactions. Moreover, using this approach at sub-Coulomb energies is a very powerful technique for studies of astrophysically important reaction rates since the results are practically model independent. This technique was first suggested in Ref. [4] and was later verified in Ref. [5] using the reaction $^{16}O(^{6}Li,d)^{20}Ne$ as a benchmark. It has also been successfully applied to study the $^{13}C(\alpha,n)^{16}O$ and $^{12}C(\alpha,\gamma)^{16}O$ reactions [6,7].

We propose to measure the spins and ANCs of the near-threshold states in order to extract the α partial widths using the α-transfer reaction $^{32}S(^{6}Li,d)^{36}Ar$ in inverse kinematics. Only states of natural parity that are strongly populated in α-transfer reactions are important for the $^{32}S(\alpha,\gamma)^{36}Ar$ reaction. Assuming a temperature of 1 GK, the Gamow window for this reaction covers the energy range of 1.5-2.5 MeV above the α-threshold with a peak at about 2 MeV. This corresponds to an excitation energy range of 8.14-9.2 MeV. Based on the work carried out in [2], where the $^{32}S(^{6}Li,d)^{36}Ar$ reaction was studied, we expect to populate the states at 8.28, 8.5, 8.68, 8.91, 9.12 and 9.24 MeV. It is important to note that in the work of [2] measurements of states below 8.28 MeV were not possible due to $^{16}O$ contaminations in the sulfur target. Since we will use inverse kinematics, the problem with this contaminant will be avoided. The aim of our study is to measure the spins and ANCs of these near-threshold states in the energy range of 8-9.2 MeV and obtain the α partial widths, important for the $^{32}S(\alpha,\gamma)^{36}Ar$ and $^{32}S(\alpha,p)^{35}Cl$ reaction rate calculations. This measurement will help to better constrain predictions of nucleosynthesis and light curves in XRBs.

## I. EXPERIMENT

We choose to measure the $^{32}S(^{6}Li,d)^{36}Ar$ reaction in the MDM spectrometer, capitalizing on the excellent resolution that can be achieved. An important point of using inverse kinematics is that we will avoid the difficulties associated with the use of sulfur targets such as contaminants and target deterioration effects that complicate measurements in normal kinematics. This experiment would utilized the α-transfer reaction $^{32}S(^{6}Li,d)^{36}Ar$ at sub-Coulomb energies to study states in $^{36}Ar$ in the excitation energy range of 8-9.2 MeV. The states that we are interested in are separated by more than 120 keV, and are thus can resolved in our experiment that has resolution of better than 100 keV. The $^{32}S$ beam energy was 1.4 MeV/u and the $^{6}LiF$ targets thicknesses were between 20-35 μg/cm$^2$ on 5-10 μg/cm$^2$ C foil. The idea was to impinge the $^{32}S$ beam on the $^{6}LiF$ target and to measured the deuterons at 0º in the MDM spectrometer in coincidence with α-particles measured with a silicon array (covering an angular range of about 10º-60º in the lab) positioned in the scattering chamber. This way we are able to determine the spin and ANC of the states simultaneously.

We performed DWBA calculations to estimate the cross sections assuming a small spectroscopic factor of 0.1. Since the spin of the states are not known we performed the calculations using different momentum transfer, in order to estimate a lower limit of the expected rates. We estimated a conservative cross section of about 10 μb/sr. Therefore, we requested a $^{32}S$ beam intensity of 30pnA in order to achieve significant statistics in 6 days.

To perform this experiment we adopted the following plan:

1. To measure Rutherford scattering at 6º on $^{197}Au$ to calibrate the Faraday cup.
2. Measure $^{6}Li$+ $^{32}S$ elastic scattering in order to determine the $^{6}LiF$ thickness more precisely.
3. To measure the energy of the beam from the field settings.
4. To perform a wire position calibration.

5. Then to position the MDM spectrometer at 0º for the physics measurement.

For step 1 we started with low intensities of $^{32}$S (about 50 pA). We successfully calibrated the Faraday cup by comparing the Rutherford scattering cross section and the reading in the Faraday cup. We found that Faraday cup reading was consistent with Rutherford scattering cross section. To proceed to step 2 we requested an increase on the $^{32}$S beam intensity however we were not able to increase the beam intensity any further. Since the beam intensity was too low we were not able to proceed. IT was later found that the beam intensity was low due to poor vacuum condition in the beam line leading to the MDM spectrometer. Several vacuum leaks have been eliminated since the time of experiment and vacuum has been improved by one order of magnitude. We plan to repeat this experiment after we verify the intensity of at least 10 pnA can be achieved for the 1.4 MeV/u $^{32}$S beam.

[1] A. Parikh *et al.*, The Astrophys. J. Supplement Series **178**, 110 (2008).
[2] C. Iliadis *et at.*, Nucl. Phys. **A571**, 132 (1994).
[3] J.G. Ross *et al.*, Phys. Rev. C **52**, 1681 (1995).
[4] C.R. Brune *et al.*, Phys. Rev. Lett. **83**, 4025 (1999).
[5] M.L. Avila *et al.*, Phys. Rev. C **90**, 042801 (2014).
[6] M.L. Avila *et al.*, Phys. Rev. C **91**, 048801 (2015).
[7] M.L. Avila *et al.*, Phys. Rev. Lett. **114**, 071101 (2015).

# Structure of $^{10}$N via $^{9}$C+p resonance scattering

J. Hooker, G.V. Rogachev, V.Z. Goldberg, E. Koshchiy, E. Uberseder, H. Jayatissa,
C. Hunt, and B. Roeder

The new capabilities of rare isotope beams developed three decades ago allowed the discovery of unusually large matter radii in some exotic nuclei by Tanihata *et al.* [1] and opened a new era in nuclear physics. The most famous example is $^{11}$Li which has a nuclear matter root mean square radius as large as that of $^{208}$Pb. This is due to the two-neutron halo of $^{11}$Li where the wave function of two valence neutrons extends far beyond the $^{9}$Li core. An important role in explaining the halo structure of $^{11}$Li was played by three-particle models that describe $^{11}$Li as a $^{9}$Li-n-n system. These models rely on accurate knowledge of neutron-$^{9}$Li interaction, that can be established from the known states in $^{10}$Li. However, in spite of much effort (see [2-8] and references therein), uncertainty in spin-parity assignments and excitation energies of some low-lying states in $^{10}$Li still remains. Even less is known about the mirror nucleus $^{10}$N. Only one experiment that claimed observation of the ground state of $^{10}$N has been done. A broad resonance at 2.6(4) MeV with a width of 2.3(16) MeV was identified using the multi-nucleon transfer reaction $^{10}$B($^{14}$N,$^{14}$B)$^{10}$N [9]. The goal of this work is to provide a spin-parity assignment for the ground state and search for the excited states in this exotic, proton drip-line nitrogen isotope - $^{10}$N.

States in $^{10}$N, including the ground state, were populated in resonance elastic scattering of $^{9}$C on protons. The rare isotope beam of $^{9}$C was produced by recoil spectrometer MARS using $^{10}$B(p,2n) reaction. The excitation function for the $^{9}$C+p elastic scattering was measured using a new time projection chamber, which is shown in Fig. 1. Preliminary results of lower excitation energies indicate the presence

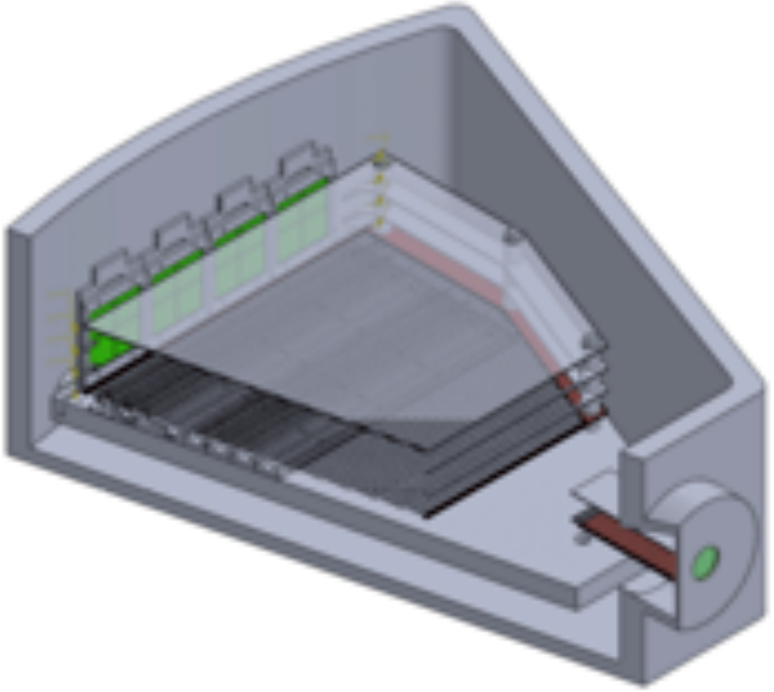

**FIG. 1.** The layout of the time projection chamber TexAT-P1.

of a broad s-wave state at an energy of 2.25 MeV with a width of 1.5 MeV are were already reported in 2015 Cyclotron Annual Report [10].

The analysis of the higher energy region is complicated by the fact that the high energy protons (>12 MeV) punch through the 1 mm Si detector and do not deposit all of its energy. The difficulty is to distinguishing protons in the spectrum that have 'punch-through' the silicon detectors from those that have not as well as reconstructing all of the 'punch-through' events correctly. The approach we have taken is to develop a realistic simulation in Geant4 (GEometry ANd Tracking) and use these results to aid in our analysis. The simulation includes all components of the experimental setup. Other factors are taken into consideration in the simulation such as the beam energy spread from the velocity filters in MARS and the resolution in both the position and timing, due to drifting of electrons in the gas, for the proportional counter wires.

The first step to using this simulation was to reconstruct the energy of 'punch-through' events. By simulating protons through a silicon detector at many different energies and angles, we are able to safely find the means and standard deviations of the distribution of energies that provide the signals we see in the silicon array. The results of the reconstruction can be found in Fig. 2. As shown in the figure, most events are reconstructed within an error of 1 MeV but improvements can be made.

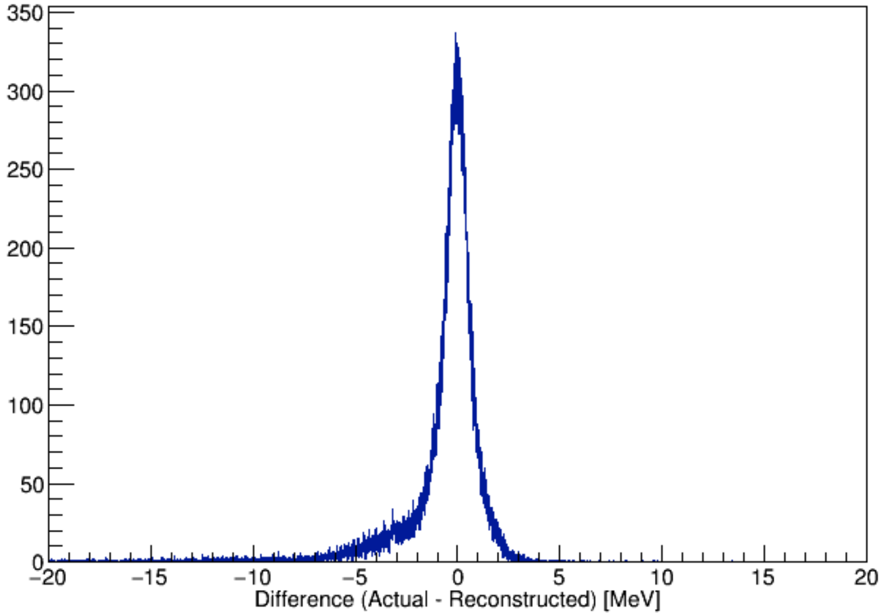

**FIG. 2.** The difference of the actual proton energy of 'punch-through' events and the reconstructed proton energies using the simulation.

The next step into extracting the full excitation function is to be able to distinguish 'punch-through' events from those that do not. Unfortunately, that cannot be done by only using the energy deposited in the proportional counter cells and the Si detectors. Other means must be used. One of the variables we can extract from our position sensitive wires is the location of the reaction vertex. This is done by tracking of the protons using time projection chamber. Since 'punch-through' events come from a higher C.M. energy of interaction, the vertex should be occurring closer to the entrance of the chamber than those that are low C.M. energy. As shown in Fig. 3., there is a difference in the vertex position for those higher energy events as expected. Of course a small overlap still present and statistical methods have to be implemented for excitation function reconstruction.

Due to complications that are mostly related to the punch-through events analysis of this data is still in progress, but we expect to finalize the project in the Summer of 2016.

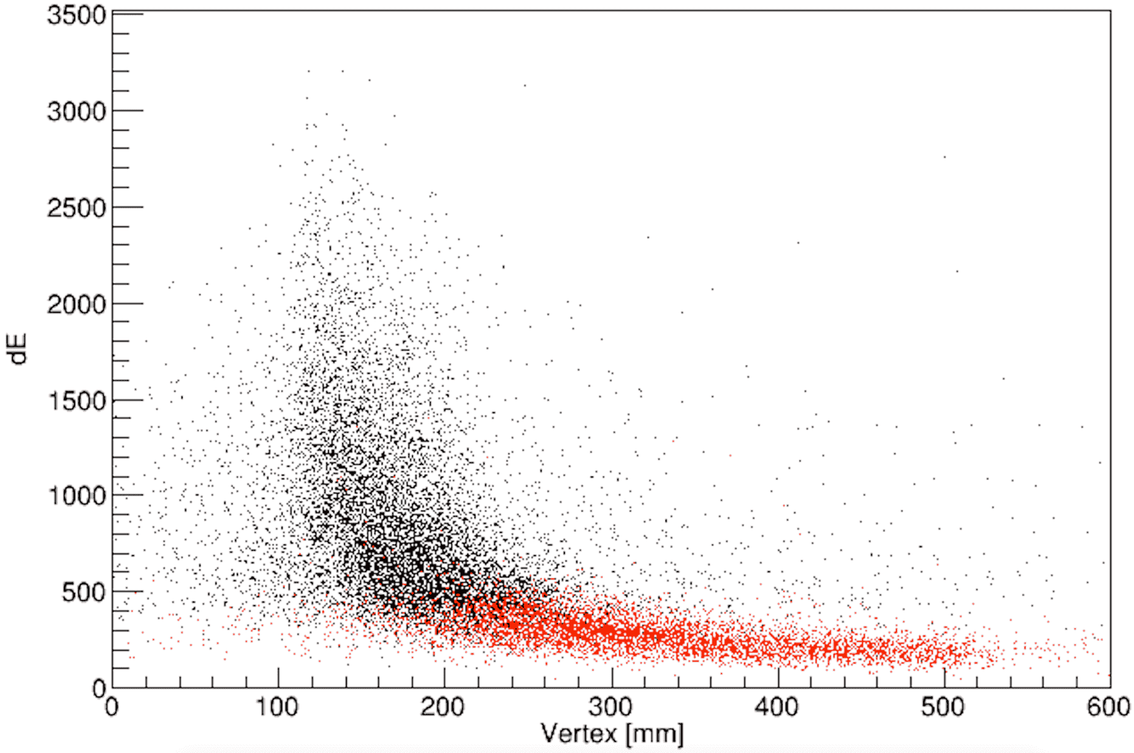

**FIG. 3.** Energy deposited in the proportional counter wire (dE) vs. the reconstructed vertex position. Black points are events that are not 'punch-through' events and red points are 'punch-through' events.

[1] I. Tanihata, H. Hamagaki, O. Hashimoto *et al.*, Phys. Rev. Lett. **55**, 2676 (1985).
[2] H.G. Bohlen, B. Gebauer, M. von Lucke-Petsch *et al.*, Z. Phys. A **344**, 381 (1993).
[3] B.M. Young, W. Benenson, J.H. Kelley *et al.*, Phys.Rev. C **49**, 279 (1994).
[4] M. Zinser, F. Humbert, T. Nilsson *et al.*, Phys. Rev. Lett. **75**, 1719 (1995).
[5] J.A. Caggiano, D. Bazin, W. Benenson *et al.*, Phys. Rev. C **60**, 064322 (1999).
[6] P. Santi, J.J. Kolata, V. Guimaraes *et al.*, Phys. Rev. C **67**, 024606 (2003).
[7] H. Jeppesen, F. Ames, U.C. Bergmann *et al.*, Nucl. Phys. **A738**, 511 (2004).
[8] B.A. Chernyshev, Yu.B. Gurov, V.S. Karpukhin *et al.*, Eur. Phys. J. A **49**, 68 (2013).
[9] A. Lepine-Szily, J.M. Oliveira, V.R. Vanin *et al.*, Phys. Rev. C **65**, 054318 (2002).
[10] G.V. Rogachev, J. Hooker *et al.*, *Progress in Research*, Cyclotron Institute, Texas A&M University (2014-2015), p. I-22.

# Progress in the studies of low energy reactions by the TTIK method

A.K. Nurmukhanbetova,[1] N.A. Mynbayev,[1] V.Z. Goldberg,[2] G.V. Rogachev,[2] M.S. Golovkov,[3]
D. Nauryzbayev,[1] A. Rakhymzhanov,[1] A. Tikhonov,[1,4] and R.E. Tribble[2]
[1] *National Laboratory Astana, Nazarbayev University, Astana, Kazakhstan*
[2] *Cyclotron Institute, Texas A&M University, 77843 3366, Texas, USA*
[3] *Joint Institute for Nuclear Research, Dubna, 141980 Russia*
[4] *School of Science and Technology, Nazarbayev University, Astana, Kazakhstan*

An interest and achievements in detailed description of nuclear processes in stars stimulated new studies of nuclear reactions, especially resonance reactions, at low energies. The new data are needed on resonance interaction of rare as well as conventional beams. The needed measurements at low energies are difficult because of (1) low cross sections, and also because (2) of low energies of the detected particles. Inverse kinematics of the TTIK method [1,2] is an important factors to make the measurements easier.

DC-60 cyclotron was built in Astana (Kazakhstan) in 2006 [3]. The facility is capable of providing intense heavy ion beams from Lithium to Xenon in the energy range of 0.35–1.77 MeV/nucleon. Since 2010 groups from the Cyclotron Institute and the Nazarbayev University (Astana) initiated a joint program of an investigation of low energy resonance reactions of the special nuclear physics and astrophysics interest by the TTIK method. In this technique the incoming ions are slowed in the target gas (usually, methane or helium) and the light recoils (usually protons or α particles) are detected from a scattering event. These recoils emerge from the interaction with the beam ions and hit Si detector array located at forward angles while the beam ions are stopped in the gas, as $p$ and $\alpha$ have smaller energy losses than the scattered ions. The TTIK approach provides for continuous excitation function as a result of slowing down the beam. Due to straggling effects, the energy and angular spread of the incoming beam increases as the ion traverses the scattering chamber.

The TTIK method cannot compete with the classic approach in the energy resolution of the excitation functions. The best cm resolution of the TTIK method is about 20 keV while it is an order of magnitude better for the conventional classic measurements. However, there are advantages of the TTIK method which are predominantly important in our case.

1. *The $180^0$ degree (cm) measurements are simple.*

The TTIK measurements are easy at $180^0$ degree ($0^0$ in lab. system) because the beam are stopped in the target before the detectors, and the detected energy of light recoils is relatively high due to high energy of the center of mass; for instance, for elastic scattering, the laboratory energy of scattered protons at zero degree, E~4Ecm (we neglected the mass of the proton to the mass of the heavy ion).

2. *Clean measurements with low abundance isotopes.*

There are well known difficulties of measurements when targets are low natural abundance isotopes (especially when elements are gases). It is difficult to separate the effect from the background related with admixtures of other isotopes, and these difficulties grow at low energy. On the contrary, there are no such difficulties in reverse kinematics because a cyclotron makes the perfect separation of the needed ions from a source material.

3. *High efficiency of the method.*

The whole excitation function is measured using a single energy of the cyclotron, the beam is slowed down and stopped using thick targets. Therefore, this method is the favorite approach to study resonance reactions with low intensity rare beams [4]. Due to high efficiency of the method and large cross sections for the resonance scattering, the main features of the excitation functions for exotic nuclei can be obtained with reasonable counting statistics and energy resolution. We additionally use the high efficiency as a possibility to improve time resolution of the beam for an application of the Time of Flight method (TF) with start signal provided by RF of the cyclotron. We are using TF to identify particle mass (as usual, by their velocities) and also to identify the different excitations in the same two particle final state processes (see details below). At low energy beams, the number of possible reaction channels is restricted, and due to low velocities TF can play an important role in the identification of the process without the deterioration of the energy resolution.

Fig.1 demonstrates $0^0$ ($180^0$ cm) E-T spectrum obtained by bombarding the chamber filled by pure hydrogen with 1.8MeV/A $^{15}$N beam. There are several loci corresponding to various channels of the reaction. Two loci corresponding to decay of the resonance states in $^{16}$O to the ground and the first excited states in $^{12}$C are evident at higher energies of the particles. The TTIK approach enabled us to observe α particle of the decay of the states at 12.4 and 12.9 MeV which had not been observed before because of the low energy of the particles. Intensive α particle decay to the first excited state in $^{12}$C is well below the Coulomb barrier and evidences for the unnatural parity of the resonance levels in $^{16}$O.

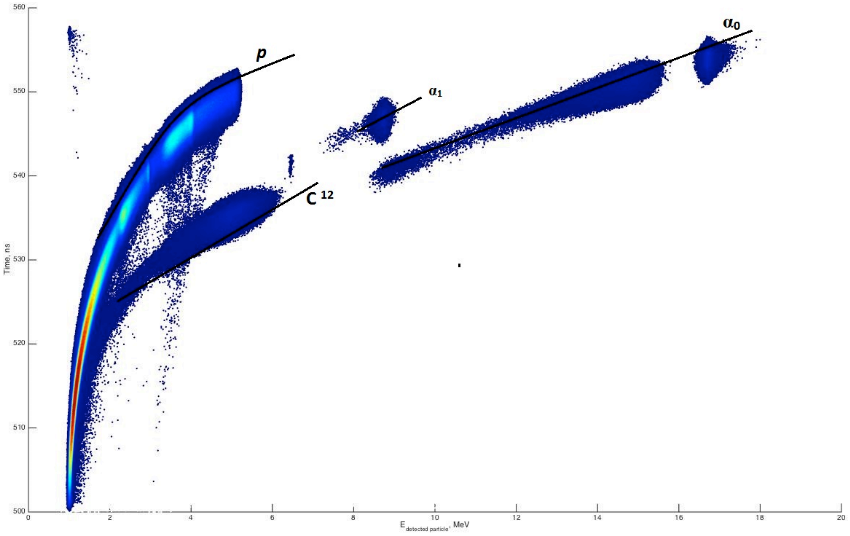

**FIG. 1.** $180^0$ Time of Flight-Energy plot for the products of $^{15}$N+p interaction.

At lower energies there is a loci corresponding to $^{12}$C moving in forward direction after the $^{16}$O decay into α +$^{12}$C. This curve is shifted relative to that of the α particle mainly because of the $^{12}$C high energy loss. The observation both products of the decay of the same resonance eliminate many uncertainties of the experimental conditions. An at the lowest energies one can see protons of the elastic scattering.

[1] K.P Artemov *et al.*, Sov. J. Nucl. Phys. **52**, 406 (1990).
[2] G.V. Rogachev *et al.*, AIP Conf. Proc. **1213**, 137 (2010).
[3] B. Gikal *et al.*, Phys. Part. Nucl. Lett. **7**, 642 (2008).
[4] V.Z. Goldberg *et al.*, Phys. Lett. B **692**, 307 (2010).

# Direct observation of α particle decay of the $^{16}$O levels close to $^{15}$N+p threshold: Do we understand the nature of the isospin mixture in $^{16}$O levels?

D.Nauryzbayev,[1] V.Z. Goldberg, G.V. Rogachev, N. Mynbayev,[1] A. Rakhymzhanov,[1] A. Nurmukhanbetova,[1] I. Ivanov,[2] S. Kozin,[2] and A. Tikhonov[1,3]
[1]*National Laboratory Astana, Nazarbayev University, Astana, Kazakhstan*
[2]*Institute of Nuclear Physics at Astana, Astana, Kazakhstan*
[3]*School of Science and Technology, Nazarbayev University, Astana, Kazakhstan*

The nucleus $^{16}$O plays a key role for the evolution of baryonic matter in our universe. Its pronounced α-cluster structure is responsible for the closing of the CN cycle through the $^{15}$N(p,α)$^{12}$C reaction, controlling the stellar hydrogen burning in massive main sequence stars and determines the strength of the $^{12}$C(α,γ )$^{16}$O reaction that defines the $^{12}$C/$^{16}$O ratio in stellar helium burning, which in turn influences the burning sequence during late stellar evolution, the ignition conditions of thermonuclear supernovae, and, last but not least, the formation of organic life on habitable planets such as Earth [1].

The reaction $^{15}$N(p,$\gamma_0$)$^{16}$O is of particular importance for modeling the CNO bi-cycle as it competes with the reaction $^{15}$N(p,α)$^{12}$C. A very important contribution to the (p, $\gamma_0$) process is a resonant contribution from the two $1^-$ levels in $^{16}$O at $E_x$ = 12.45 and 13.09 MeV. These two levels are mixed in the isospin. The T=1 admixture to the lower level at 12.45 is mainly responsible for its γ width. There are two more pairs of the same spin (J=2,3) levels which are also isospin mixed (see Fig.1). Because of the importance of the $^{16}$O structure for nuclear physics and astrophysics the levels in question were thoroughly investigated in different reactions [1]. The isospin mixing was evaluated using γ widths (inhibited for T=0 transitions) or α particle decay to the ground state in $^{12}$C (forbidden for T=1 states) and estimated as ~20% [1]. Direct α particle decay to the first excited state in $^{12}$C was observed only for the 13.3 MeV state over 50 years ago [2]. As a development of the TTIK method for low energy reactions in Astana [3], we observed various modes of decay of $^{16}$O levels in the excitation region of 12.3-13.5 MeV [3]. These levels were populated in resonance $^{15}$N+p reactions, using beam of $^{15}$N and extended hydrogen gas target. Fig. 2 presents the 180$^0$ cm excitation spectra for different exit channels of the reaction. The data on the decay α widths for the T=0 and T=1 levels in

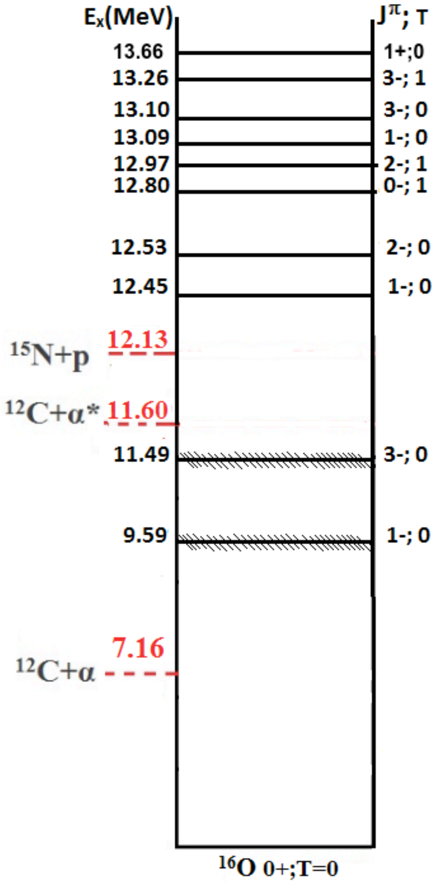

**FIG. 1.** Scheme of relevant levels in $^{16}$O.

question are given in Table I. These data summarize our preliminary analysis and that of Ref. [1]. The single particle, limit for the α widths, $\Gamma_{\alpha 1sp}$, was obtained in Woods-Saxon potential with parameters $r_0=1.23\ fm$ ($R= r_0 x 12^{1/3}$); $r_{0C}= 1.31 fm$; $a=0.65 fm$; The depth of real part well was changed to fit the binding energy.

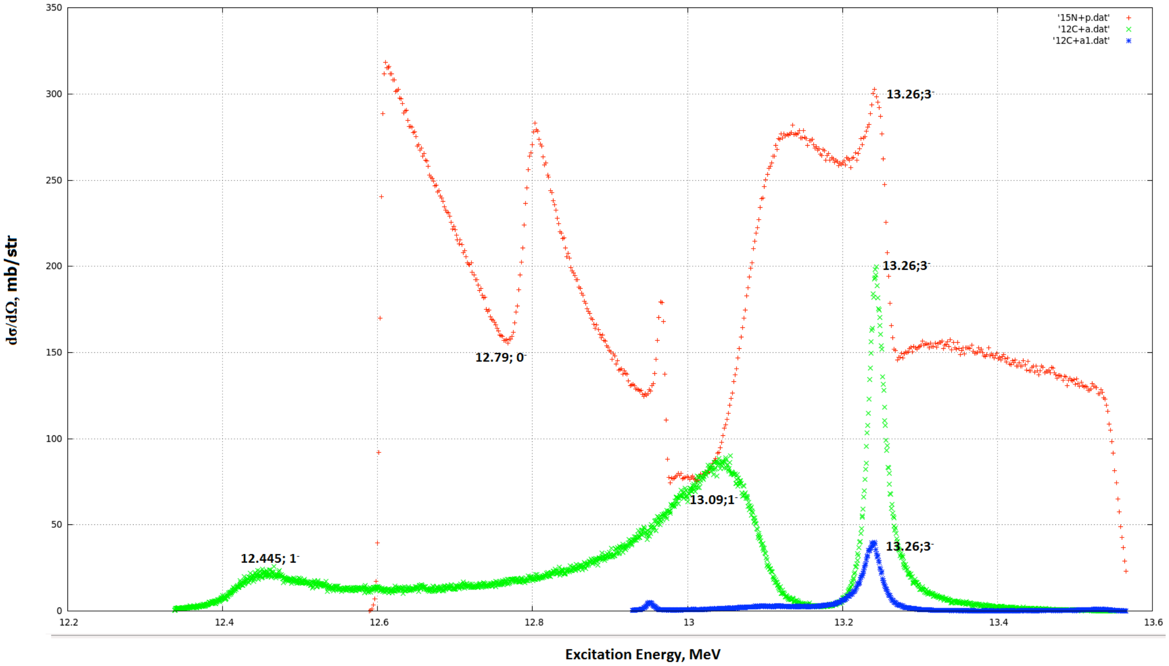

**FIG. 2.** Excitations functions for different channels of $^{15}$N+p reaction red line : p+$^{15}$N ; green: α+ $^{12}C_{gr}$; blue α +$^{12}$C*.

As it seen from Table I the reduce width for forbidden α decay of the T=1, $1^-$ state is even larger than that of the T=0 state. It is also seen that the isospin mixture for states with spin 2 and 3 is well over ~20% which was claimed before. It is difficult to explain the found large reduced width of the T forbidden decay. Indeed, one may consider the levels in question as manifestation of a simple shell model p1/2-d5/2 configuration. The relatively small reduced widths for α decay to the $^{12}$C ground state (for the $1^-$ ,$3^-$, T=0 states) can be understood as a result of the presence of well known broad α cluster states at 9.6 and 11.6 MeV, and the 20% mixture of T=1 and T=0 states (as a result of the similar structure and close excitation energies. However, $1^-$, $2^-$, $3^-$ states with large reduced widths for the decay to the first excited state in $^{12}$C are unknown in $^{16}$O. One can consider the present results as a motivation for the search. The presence of 1+ level with the corresponding reduced width of 18% (Table I) can be considered as a sign of the perspective for the search.

**Table I.** Decay of levels in $^{16}$O to the first excited state in $^{12}$C.

| $J^{\pi}$ ;T | $E^*_{16O}$ (MeV) | $\Gamma_{\alpha 1\ exp}$ (keV) | $\Gamma_{\alpha 1\ sp}$ (keV) | $\gamma_{\alpha 1}$ (%) |
|---|---|---|---|---|
| $1^-$; 0 | 12.44 | 0.030 | 18.5 | 1.6 |
| $2^-$; 0 | 12.53 | 0.092 | 29.0 | 3.2 |
| $0^-$; 1 | 12.80 | | | |
| $2^-$; 1 | 12.97 | 0.300 | 160.0 | 1.9 |
| $1^-$; 1 | 13.09 | 0.580 | 255.0 | 2.3 |
| $3^-$; 0 | 13.13 | 20.900 | 330.0 | 6.3 |
| $3^-$; 1 | 13.26 | 10.300 | 420.0 | 2.4 |
| $1^+$; 0 | 13.66 | 59.000 | 325.0 | 18.0 |

[1] R.J. deBoer *et al.*, Phys. Rev. C **87**, 015802 (2013).

[2] S. Bashkin, R.R. Carlson, and R.A. Douglas, Phys. Rev. **114**, 1543 (1959).

[3] A.K. Nurmukhanbetova *et. al.*, *Progress in Research*, Cyclotron institute, Texas A&M University (2015-2016), p. I-41.

# Alpha-cluster states in N≠Z nuclei: $^{17}$O

A. Kock, A. Nurmukhanbetova,[1] V.Z. Goldberg, G.V. Rogachev, E. Uberseder,
N. Mynbayev,[1] and D. Nauryzbayev[1]
[1]*National Laboratory Astana, Nazarbayev University, Astana, Kazakhsta*

Interest to clustering phenomena in atomic nuclei, especially in light nuclei, has grown steadily over the last few decades. This can be attributed to the realization of the important role that cluster degrees of freedom play in nuclear structure. In addition, the dramatic influence of clustering phenomena on the astrophysically important reaction rates adds urgency to the goal of achieving better understanding of clustering in nuclei. Significant theoretical progress has been achieved in this field. It is no longer necessary to introduce clusters "a priory", instead clustering emerges naturally as a result of microscopic calculations such as AMD [1], FMD [2], Lattice EFT [3], Greens Function Monte Carlo [4], CNCIM [5] and others. Qualitatively all theoretical approaches are in agreement that clustering is an important ingredient in understanding of nuclear structure. The challenge is to achieve quantitative understanding, which is not possible without detailed experimental information on nuclear clusters.

In this report we focus on clustering aspects of nuclear structure in $^{17}$O. An interest to this nucleus is twofold. First, the $^{13}$C(alpha,n) is an important neutron source reaction for the s-process - the slow neutron capture nucleosynthesis process responsible for the origin of half of all chemical elements heavier than Iron. This reaction proceeds through the population of excited states in $^{17}$O and cluster structure has a direct influence on the corresponding reaction cross section. Second, $^{17}$O provides a convenient test bench to study an interplay between cluster and single particle degrees of freedom. Its neutron decay threshold is 2 MeV below the alpha decay threshold and therefore nucleon decays can be studied simultaneously with alpha-decays. Also, since cluster structure of $^{16}$O is well studied experimentally it becomes possible one can trace the dynamical change in cluster structure due to one extra nucleon. This and also an opportunity to obtain information on the cluster structure of the mirror nucleus $^{17}$F using the $^{13}$N+alpha reaction are the attractive features of $^{17}$O a cluster structure in light nuclei case study.

Here we present data on the α cluster structure in $^{17}$O where the lowest nucleon decay is by neutrons and equal to 4.14 MeV, while the α–particle decay threshold is 6.36 MeV. The considerations are mainly based on the results of the very comprehensive ***R*** matrix analysis of the $^{13}$C(α, n)$^{16}$O reaction and the $^{13}$C(α, α)$^{13}$C elastic scattering in the work of Heil et al., [6], and on the new results of the $^{13}$C+ α resonance scattering [7] and on the $^{13}$C($^{6}$Li,d) experiment[8]. We characterized the alpha-cluster properties of the states above the alpha particle decay threshold by $SF=\Gamma_{\alpha\ exp}/\Gamma_{\alpha\ calc}$ , where $\Gamma_{\alpha\ calc}$ is the single alpha particle width calculated in the α-core potential. To normalize SFs we calculated these values for the well known states of the alpha-cluster bands in $^{16}$O.

Fig.1 shows the distribution of the α cluster strength in $^{17}$O in comparison with the known structure in $^{16}$O. One can see a very complicated structure in $^{17}$O with an alpha-cluster strength shared among several levels with the same spin. It is interesting that only the lowest *l=0, 1, 2* levels in $^{17}$O can be easily related with a simple and clear cut classical picture of bands with alternative parities. There is no simple explanation of the drastic change in the structure of the complicated presumably multipartical (alpha-cluster) as a result of extra low bound nucleon.

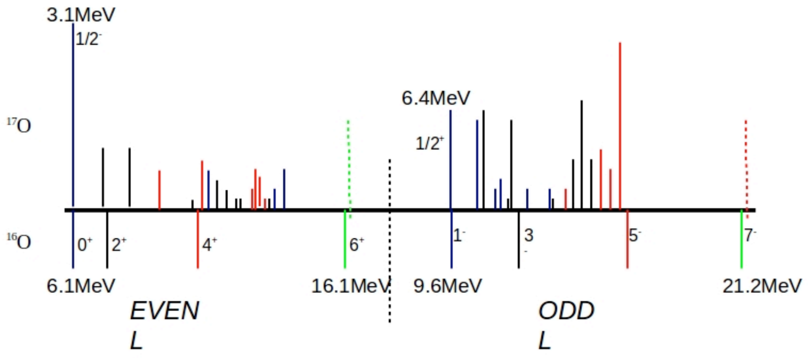

**FIG. 1.** Alpha-cluster levels in $^{16}$O and $^{17}$O.

[1] Y. Sugawa, M. Kimura, and H. Horiuchi, Prog. Theor. Phys. **106**, 1129 (2001).

[2] H. Feldmeier and J. Schnack, Prog. Part. Nucl. Phys. **39**, 343 (1997).

[3] E. Epelbaum, H. Krebs, T.A. Lahde, D. Lee, and Ulf-G. Meißner, Phys. Rev. Lett.**109**, 252501 (2012).

[4] R. Wiringa, S.C. Pieper, J. Carlson, and V.R. Pandharipande, Phys. Rev. C **62**, 014001 (2000).

[5] A. Volya, and Y. Tchuvilśky, Phys. Rev. C **91**, 044319 (2015).

[6] M. Heil *et al.*, Phys. Rev. C **78**, 025803 (2008).

[7] N.A.Mynbayev *et al.*, J. Expt. Theo. Phys. **119**, 663 (2014).

[8] M.L. Avila *et al.*, Phys. Rev. Lett. **114**, 071101 (2015).

# Experimental study of astrophysically important $^{22}$Ne(α,n)$^{25}$Mg reaction via $^{22}$Ne($^{6}$Li,d)$^{26}$Mg reaction performed at sub-Coulomb energies

H. Jayatissa, G.V. Rogachev, E. Uberseder, E. Koshchiy, J. Hooker, C. Hunt,
S. Upadhyayula, C. Magana, V.Z. Goldberg, B.T. Roeder, A. Saastamoinen,
A. Spiridon, M. Dag, M.L. Avila,[1] and D. Santiago-Gonzales[2]
[1]*Argonne National Laboratory*
[2]*Department of Physics, Louisiana State University*

The $^{22}$Ne(α,n)$^{25}$Mg reaction is a very important reaction for nuclear astrophysics as a source of neutrons for the *s*-process that is responsible for the formation of about half the elements heavier than Iron [1]. The weak component of the s-process occurs in massive stars ($M>10M_o$), where the $^{22}$Ne(α,n)$^{25}$Mg reaction is the dominant neutron source during the helium burning and the carbon-shell burning phases [2].

The direct measurement of the $^{22}$Ne(α,n)$^{25}$Mg reaction at energies that cover Gamow window energy range cannot be done at present because the cross section is prohibitively small. Hence, we conducted series of experiments that allowed us to develop a technique to constrain the $^{22}$Ne(α,n)$^{25}$Mg reaction and other astrophysically relevant α-capture reactions using low energy beams from K150 cyclotron and MDM spectrometer.

First, we investigated the well-studied reaction $^{12}$C($^{6}$Li,t)$^{15}$O [3]. This was the test run to verify detection of Z=1 ions in the MDM focal plane detector (Oxford) and determine energy resolution. This reaction was carried out using a beam of 72 MeV $^{6}$Li ions and a self-supporting $^{12}$C target with a thickness of 45 μg/cm$^{2}$. The reaction products were separated using the MDM spectrometer placed at $4.95^0$ from the beam axis, and the tritons, populating the known states of $^{15}$O (namely 12.84 MeV and 15.05 MeV), were observed by the focal plane detector (Oxford). The spectrum of tritons is shown Fig. 1. It is very similar to that measured in [3] and it was found that the energy resolution was better than 80 keV.

After the completion of this experiment, the Ni-Cr proportional counter wires inside the Oxford Detector were replaced with the new set of slightly thinner wires made out of stablohm-675, which resulted in better position resolution for the particle trajectories.

In order to constrain the $^{22}$Ne(α,n)$^{25}$Mg reaction, the α-capture reaction of $^{22}$Ne($^{6}$Li,d)$^{26}$Mg was carried out at sub-Coulomb energies. We used a 1.0 MeV/u beam of $^{22}$Ne ions and a $^{6}$LiF target of thickness 30 μg/cm$^{2}$ made on a 10 μg/cm$^{2}$ $^{12}$C backing. The MDM spectrometer was set at $5^0$ relative to the beam axis. The magnetic field settings of the spectrometer were set to cover the deuteron energies populating the 10.6 MeV – 11.5 MeV excitation energy range of the $^{26}$Mg nucleus. For the recoil deuterons, the focal plane of the MDM spectrometer was positioned very close to the 3rd proportional counter wire of the Oxford detector. The raw position spectrum of this wire (Fig. 2) depicts the various states of $^{26}$Mg that were observed in this experiment. It is clear from Fig. 2 that while statistics was not sufficient for conclusive results, the states in $^{26}$Mg have been populated. In particular, we observed about 50 events that correspond to the known 11.3 MeV state in $^{26}$Mg [4] (raw position 0.3 in Fig. 2) that plays

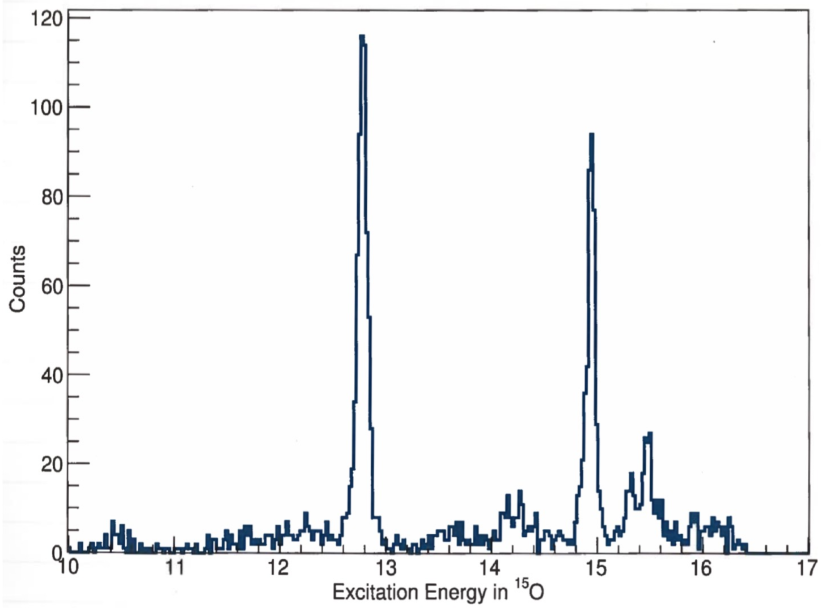

**FIG. 1.** The spectrum of tritons from the $^{12}C(^{6}Li,t)^{15}O$ reaction measuredby the MDM spectrometer and Oxford detector. The two strongest peaks are the known 12.84 MeV and 15.05 MeV states in $^{15}O$.

an important role in the $^{22}Ne(\alpha,n)^{25}Mg$ reaction at astrophysical energies. Hints of the lower lying states (raw position >0.3 in Fig. 2), that may be even more important, have been observed. Better statistics has to be accumulated however. At the time of this writing, an experiment that featured a factor of 10 better

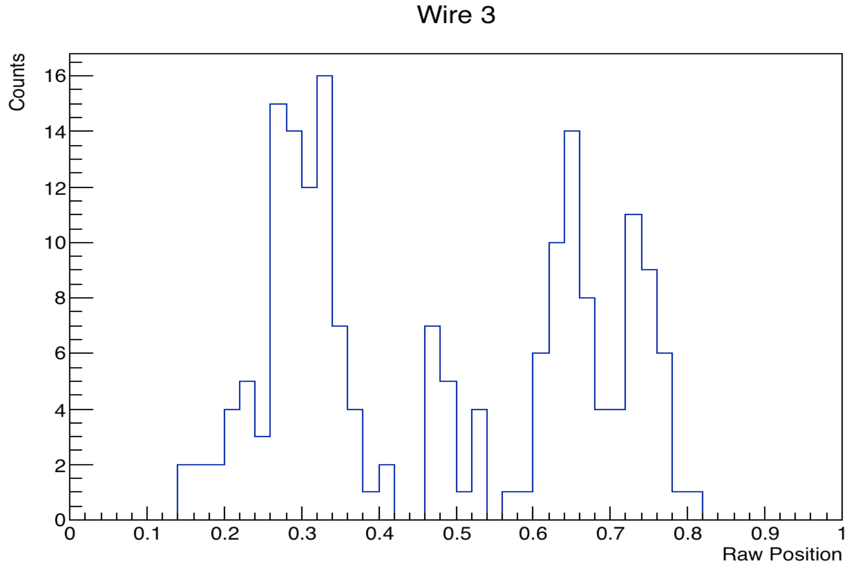

**FIG. 2.** 3rd wire raw position of deuterons from the $^{6}Li(^{22}Ne,d)^{26}Mg$ reactions. The strong leftmost peak is a known 11.3 MeV states in $^{26}Mg$ [4].

statistics has been performed in April. The analysis is currently underway. We believe that we will be able to dramatically reduce the uncertainties for the $^{22}$Ne(α,n)$^{25}$Mg reaction cross section at low energies when the analysis is complete.

[1] M. Jaeger *et al.*, Phys. Rev. Lett. **87**, 202501 (2001).
[2] F. Kappeler *et al.*, Rev. Mod. Phys. **83**, 157 (2011).
[3] H.G. Bingham *et al.*, Phys. Rev. C **11**, 1913 (1975).
[4] M. Jaeger *et al.*, Phys. Rev. Lett. **87**, 202501 (2001).

# Direct measurement of the $E_r$ = 457 keV resonance in the astrophysical $^{19}$Ne($p$, $\gamma$)$^{20}$Na reaction

G. Christian, R. Wilkinson,[1] G. Lotaty,[1] W.N. Catford,[1] D. Connolly,[2] D.A. Hutcheon,[2]
D. Jedrejcic,[3] A. Lennarz,[2] C. Ruiz,[2] and U. Greife[3]
[1]*University of Surrey, Surrey, United Kingdom*
[2]*TRIUMF, Vancouver, Canada*
[3]*Colorado School of Mines, Golden, Colorado*

Classical novae occur in binary systems consisting of a compact white dwarf and a main-sequence companion. The white dwarf accretes hydrogen-rich material onto its surface, resulting in thermonuclear runaway. Two broad types of novae exist depending on the underlying composition of the white dwarf: carbon-oxygen (CO), and oxygen-neon (ONe). The more massive ONe novae reach significantly higher peak temperatures (T ~ 0.4 GK), resulting in synthesis of nuclei up to the Si – Ca mass region [1, 2]. In a detailed study of different nova models [3], it was found that the significant detection of $^{19}$F in nova ejecta was one of only four isotopic signatures of an underlying ONe white dwarf. Hence it is crucial that both the production and destruction of $^{19}$F in classical novae be fully understood. The production of $^{19}$F in ONe novae occurs through the reaction chain $^{17}$O($p$, $\gamma$)$^{18}$F($p$, $\gamma$)$^{19}$Ne($\beta^+$)$^{19}$F. However, this may be bypassed at higher temperatures through the alternative reaction path $^{19}$Ne($p$, $\gamma$)$^{20}$Na($\beta^+$)$^{20}$Ne. As a result, a precise determination of the $^{19}$Ne($p$, $\gamma$)$^{20}$Na reaction rate is important for understanding $^{19}$F generation in ONe classical novae.

At nova temperatures, the $^{19}$Ne($p$, $\gamma$)$^{20}$Na reaction rate is thought to be dominated by a single resonance at $E_r \sim 450$ keV, populating an excited state in $^{20}$Na with $E_x \sim 2640$ keV. The strength of this resonance has been investigated in multiple experiments over the past 20 years, and it still subject to debate. Early ($^3$He, $t$) measurements [4, 5] generated conflicting $1^+$ and $3^+$ assignments for the $^{20}$Na excited state corresponding to the $E_r \sim 450$ keV resonance. A later attempt at a direct measurement of the $^{19}$Ne($p$, $\gamma$)$^{20}$Na reaction [6] established an upper limit on the resonance strength of 15 meV, suggesting a $1^+$ spin-parity for the corresponding $^{20}$Na state but not ruling out a $3^+$ assignment. Most recently, a detailed $^{20}$Mg $\beta$-decay study at the Texas A&M Cyclotron Institute established a log *ft* lower limit of 6.9 on the branch to the $E_x \sim 2640$ keV state in $^{20}$Na, firmly establishing the state as $3^+$. Additionally, high-resolution measurements of the $^{20}$Na proton separation threshold [8] and the excitation energy of the resonance in question [9] established a resonance energy of 457(3) keV, around 10 keV higher than previously thought. This suggests that the direct measurement of Ref. [6] failed to observe the resonance as a consequence of running on the wrong beam energy.

In order to resolve this situation, we have undertaken another direct measurement of the $E_r$ = 457(3) keV resonance in $^{19}$Ne($p$, $\gamma$)$^{20}$Na, armed with updated knowledge of the resonance energy. This measurement was performed at the TRIUMF radioactive beam facility in Vancouver, Canada. We produced a beam of $^{19}$Ne ions using the ISOL technique, impinging 500 MeV protons onto a high-power SiC production target. The $^{19}$Ne ions were then post-accelerated to a laboratory energy of ~490 AkeV before impinging onto a windowless, recirculating gas target filled with ~8 torr of $H_2$. The beam energy was chosen to place the 457 keV resonance approximately in the center of the gas target. The overall $^{19}$Ne beam current was $\sim 5\times10^6$ particles/second.

The $^{20}$Na recoils resulting from $^{19}$Ne($p$, $\gamma$)$^{20}$Na were sent through the DRAGON recoil mass separator [10], where they were separated from unreacted beam and other reaction products by means of two successive pairs of magnetic and electric dipoles. Since it acts as both a charge and mass filter, only ions in the 6$^{+}$ charge state were transmitted through DRAGON. Particles reaching the DRAGON focal plane were detected in a pair of microchannel plates (MCPs) and an ionization chamber segmented into four anode regions. In coincidence, the $\gamma$ rays resulting from $^{19}$Ne($p$, $\gamma$)$^{20}$Na were detected in an array of bismuth-germinate (BGO) scintillators surrounding the target. Recoil/$\gamma$-ray coincidences were separated from a background of "leaky" $^{19}$Ne beam arriving at the focal plane in random coincidence with room $\gamma$ rays by analyzing the time of flight between the two MCPs ("MCP TOF") and between the $\gamma$ ray signal and the upstream MCP ("separator TOF"), as well as the ionization chamber energy loss signals.

Figure 1 shows a plot of total energy loss in the ionization chamber vs. energy lost in the first (upstream) anode. The events denoted by red stars also appear clustered in plots of separator vs. MCP TOF. They are clearly well separated from the other loci in the ion chamber $E$-$\Delta E$, giving conclusive evidence that these events correspond to $^{20}$Na recoils. Overall, ten preliminary coincidence recoils were identified based on this analysis of the separator–MCP TOF and the ion chamber $E$-$\Delta E$ signals. Based on this and the preliminary coincidence detection efficiency of 15%; charge state fraction of 45%; integrated beam current of $2\times10^{12}$ particles; and $^{19}$Ne+$H_2$ stopping power of $4.3\times10^{-15}$ eV/cm$^2$, we calculate a preliminary resonance strength of $\omega\gamma$ = 30 meV for the $E_r$ = 457 keV resonance in $^{19}$Ne($p$, $\gamma$)$^{20}$Na. Additionally, the location of the resonance in the extended DRAGON gas target is consistent with the most recent resonance energy determination of 457(3) keV. The preliminary strength value deduced from the present measurement is significantly larger than the upper limit of 15 meV established in the previous

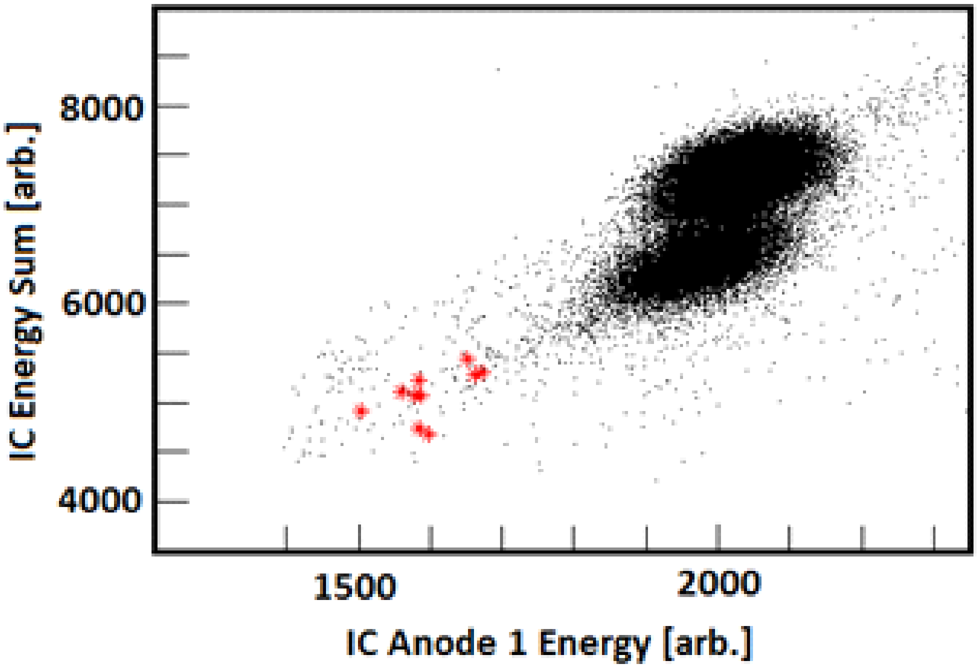

**FIG. 1.** Ionization chamber total energy loss vs. energy loss in the first anode. The events denoted by red stars also appear clustered in MCP vs. Separator TOF and correspond to $^{20}$Na recoils.

attempt at a direct measurement [6]. This gives conclusive evidence that the resonance is indeed $3^+$ as suggested in Ref. [7]. The analysis of this experiment is ongoing; future efforts will focus on finalizing the resonance strength measurement and on extracting an independent measurement of the resonance energy from the $\gamma$-ray hit pattern in the BGO array [11]. Following completion of the analysis, we will integrate our results into nova model calculations, examining the influence of our measurement on the predicted synthesis of $^{19}$F in ONe classical novae.

[1] J. Jose, M. Hernanz, and C. Iliadis, Nucl. Phys. **A777**, 550 (2006).
[2] J. Jose, M. Hernanz, S. Amari, K. Lodders, and E. Zinner, Astrophys. J. **612**, 414 (2004).
[3] J. Jose and M. Hernanz, Astrophys. J. **494**, 680 (1998).
[4] L.O. Lamm *et al.*, Nucl. Phys. **A510**, 503 (1990).
[5] N.M. Clarke *et al.*, J. Phys. G **19**, 1411 (1993).
[6] R.D. Page *et al.*, Phys. Rev. Lett. **73**, 3066 (1994).
[7] J.P. Wallace *et al.*, Phys. Lett. B **712**, 59 (2012).
[8] C. Wrede *et al.*, Phys. Rev. C **81** 055503 (2010).
[9] M.S. Smith *et al.*, Nucl. Phys. **A536**, 333 (1992).
[10] D.A. Hutcheon *et al.*, Nucl. Instrum. Methods Phys. Res. **A498**, 190 (2003).
[11] D.A. Hutcheon *et al.*, Nucl. Instrum. Methods Phys. Res. **A689**, 70 (2012).

# High-precision mass measurements and in-trap branching ratio measurements at TITAN, TRIUMF

C. Andreiou,[1] J.C. Bale,[2,3] B.R. Barquest,[2] M. Brodeur,[4] T. Brunner,[5] U. Chowdhury,[2,6] S. Ettenauer-Malbrunot,[7] J. Even,[2] A. Finlay,[2,3] D. Frekers,[8] A.T. Gallant,[2,3] G. Gwinner,[5] J. Kelly,[4] R. Klawitter,[2,9] B.A. Kootte,[2,5] A.A. Kwiatkowski,[10] D. Lascar,[2] K.G. Leach,[11] E. Leistenschneider,[2,3] A. Lennarz,[2,8] H. Savajols,[12] B.E. Schultz,[4] R. Schupp,[2,6] D.A. Short,[1,2] and J. Dilling[2,3]

[1]*Simon Fraser University, Burnaby, British Columbia, Canada*
[2]*TRIUMF, Vancouver, British Columbia, Canada*
[3]*University of British Columbia, Vancouver, British Columbia, Canada*
[4]*University of Notre Dame, Notre Dame, Indiana*
[5]*McGill University, Montreal, Quebec, Canada*
[6] *University of Manitoba, Winnipeg, Manitoba, Canada*
[7]*CERN, Geneva, Switzerland*
[8]*Westfälische Wilhems-Universität Münster, Münster, Germany*
[9]*University of Heidelberg, Heidelberg, Germany*
[10]*Cyclotron Institute, Texas A&M University, College Station, Texas*
[11]*Colorado School of Mines, Golden, Colorado*
[12]*GANIL, Caen, France*

Four experiments for TRIUMF's Ion Trap for Nuclear and Atomic Science (TITAN) [1] were scheduled at ISAC-TRIUMF. TITAN comprises three on-line ion traps for high-precision measurements. The Measurement PEnning Trap (MPET) combines electrostatic and magnetic fields to trap ions in a small volume. We measure the cyclotron frequency and thus determine the mass using the Time-Of-Flight Ion-Cyclotron-Resonance (TOF-ICR) technique on radioactive ions with lifetimes as short as 9 ms. The masses are then used to probe nuclear structure, investigate nucleosynthesis, improve the nuclear-physics foundation of neutrino physics, or test fundamental symmetries. To prepare the beam, a linear RadioFrequency Quadrupole (RFQ) ion trap is used to accumulate, cool, and bunch the hot radioactive ion beam (RIB). An Electron Beam Ion Trap (EBIT) can be used to charge breed the beam, thereby improving the achievable precision or reducing beam time requirements. The Helmholtz configuration of the magnet and seven radially placed ports and windows also allow optical access to the trapping volume; seven SiLi detectors are used to measure x-rays from the highly charged ions (HCI). The detectors are part of the TITAN Electron Capture (TITAN-EC) sub-program, wherein the branching ratio of odd-odd intermediate nuclides are measured to benchmark the nuclear matrix elements of two-neutrino double-β decay. Normalization can be done with an in-line PIPS detector or with a germanium detector; the latter is used when the electron beam is used to increase the radial confinement of the radioactive ions.

Decay spectroscopy experiments are encompassed under the approval proposal S1066. In November, the desired species was $^{110}$Ag, which was delivered with overwhelming amounts of $^{110}$In to make it impossible to achieve the science objectives, which were to verify and to improve the precision of the 1965 value [2]. The data taken is under analysis by D.A. Short for his Master's thesis at Simon Fraser University.

The two radioactive mass-measuring experiments focused on nuclides near the neutron dripline to investigate the rapid-neutron-capture or *r*-process which is believed to occur in supernovae and neutron-star mergers and to be the source of elements heavier than iron. S1466 and S1373, "Shell quenching of N=82 shell gap studied through mass measurements of the r-process waiting point $^{130}$Cd nucleus" and "Precise mass measurements of Sr and Rb isotopes in the vicinity of the r-process path," were thus scheduled sequentially.

Immediately preceding the experiments, a storm caused a site-wide power outage lasting several hours. As a result, several cryogenic systems for the accelerators had to be warmed up and then re-cooled; the ISAC target received substantial thermal shock (decreasing yields); and, the TITAN efficiencies reduced by worsened vacuum and smaller transport efficiencies. These consequences and the loss of beam time reduced the achievable scope of the experiments. The cadmium yields had fallen an order of magnitudes from before and after the power outage; they were insufficient to tune through the RFQ and tune the TITAN system. Based on yield measurements of rubidium and strontium isotopes, we could only be able to re-confirm previous measurements [3,4] and perform none of heavier isotopes. We focused on measuring an isomer in $^{98}$Rb; however, the maximum charge state which could be used with the experimental system under these circumstances led to insufficient precision to resolve the isomer from the ground state.

S1445, "High precision mass measurements for the determination of $^{74}$Rb's *Q*-value," focused on preparations for the high-precision mentioned in the title ($\delta Q/Q \sim 10^{-9}$) and could not be performed due to a conflict in the beam schedule. The nuclide $^{74}$Rb is the heaviest superallowed $0^+ \rightarrow 0^+$ $\beta$ emitter, and its short half-life and low production yield pose substantial challenges. This preparatory experiment was envisaged to investigate the charge breeding with krypton from the OfflLine Ion Source (OLIS) under beam-time conditions and ensure the expected gains due to the high charge states could be realized.

[1] J. Dilling, P. Bricault, M. Smith, and H.-J. Kluge, The proposed TITAN facility at ISAC for very precise mass measurements on highly charged short-lived isotopes, Nucl. Instrum. Methods Phys. Res. **B204**, 492 (2003).

[2] L. Frevert, R. Schneberg *et al.*, Zeit. f. Phys. **182**, 439 (1965).

[3] V.V. Simon, T. Brunner, U. Chowdhury, B. Eberhardt, S. Ettenauer, A.T. Gallant, E. Mané, M.C. Simon, P. Delheij, M.R. Pearson, *et al.*, Penning-trap mass spectrometry of highly-charged, neutron-rich Rb and Sr isotopes in the vicinity of A = 100, Phys. Rev. C **85**, 064308 (2012).

[4] R. Klawitter, A. Bader, M. Brodeur, U. Chosdhury, A. Chaudhuri, J. Fallis, A.T. Gallant, A. Grossheim, A.A. Kwiatkowski, D. Lascar, K.G. Leach, A. Lennarz, T.D. Macdonald, J. Pearkes, S. Seeraji, M.C. Simon, V.V. Simon, B.E. Schultz, and J. Dilling, Mass measurements of neutron-rich Rb and Sr isotopes, Phys. Rev. C **93**, 045807 (2016).

# Towards nuclear lifetime measurements of highly charged radioactive ions: Development of a hybrid EBIT-Penning ion trap

A.A. Kwiatkowski, M.R. Morrison, and R. Steinbrügge

Radioactive decay was discovered more than a century ago, and yet it is not fully understood despite its crucial role in stellar nucleosynthesis, investigations of the neutrino, and fundamental symmetries. Additional questions arise when we consider the non-terrestrial conditions in stars, where the hot and dense conditions can lead to partial or full ionization. This change in charge state can alter the available decay channels. For example, orbital electron capture (EC) is forbidden in bare ions and suppressed in hydrogen-like ions. Thus, radionuclides like $^{7}$Be which is part of the *pp*-chain in the sun can become extremely long lived. In the reverse process, bound-state β decay can cause terrestrially stable nuclides to become unstable when highly charged. These two processes alone can alter the course of stellar evolution, which in turn affects the nucleosynthesis of elements heavier than iron and cosmology.

Four principle challenges present themselves in the lifetime measurements of highly charged ions (HCI): the production of the desired – predominantly radioactive – species, charge breeding to the high charge states, storage compatible with the expected half-lives, and a compatible detection scheme. Tape stations and most traditional nuclear decay spectroscopy techniques are unfeasible such measurements since HCI must be stored in vacuum. As such, we propose a hybrid ion trap which combines the charge-breeding capabilities of an electron beam ion trap (EBIT) with the mass-spectrometry techniques of a Penning trap at the Cyclotron Institute.

The upgrades under development at the Cyclotron Institute, namely the light and heavy ion guides, will provide low-energy radioactive (singly charged) ions to the trap. The EBIT is the only means to charge breed low-energy beams to bare, hydrogen-like, and helium-like charge states necessary. These are achieved through successive electron impact of the nuclides by electrons in a high-energy beam. In Penning traps, the Fourier-Transform Ion-Cyclotron-Resonance (FT-ICR) technique is used for ultra-high-precision mass spectroscopy and *g*-factor measurements, will allow for precise identification of both the desired nuclide and the desired charge state, and can be adapted for lifetime measurements. The proposed system will share the beam cooler and buncher of the TAMUTRAP system [1].

A Penning trap relies on a strong, uniform magnetic field for radial confinement and a quadrupolar electrostatic field for axial confinement. An EBIT unites a cylindrical Penning trap with an electron beam. The use of a 7-Tesla superconducting solenoid magnet (JASTEC JMTB-7.0T/96/SS) is under negotiation from TRIUMF (Vancouver, Canada). A cylindrical Penning trap design was chosen based on those of SHIPTRAP [2] (GSI, Darmstadt, Germany) and TAMUTRAP [1]. It was then adapted to be an EBIT with the addition of cylindrical electrodes similar to the designs of the FLASH [3] and TITAN [4] (sister) EBITs. The field and ion trajectories were simulated in SIMION 8.1 [5]. These simulations indicate that switching between EBIT and Penning trap modes, i.e. turning off the electron beam and changing the trapping potential, acts as evaporative cooling. To reduce these losses we are investigating different trap geometries and trapping potentials.

Charge-breeding simulations were performed with CBSIM [6] and CHASER [7] with electron beam energies up to 100 keV. The maximum beam energy is limited by the available space in the experimental hall. Due to the $Z$ (proton number) dependence in charge breeding, the heaviest element which could be fully ionized is mercury [8], which is beyond the lanthanides which are the heaviest nuclides of interest. The simulations indicate 1% of heavy beams will populate the bare charge state when the product of the electron current density $J$ and the charge breeding time $t$, $Jt$ equals 80000 $A{\cdot}s/cm^2$. The ratio will allow other charge states to be cleaned with standard Penning-trap-mass-spectrometry techniques [9] with an allowance to clean the ionized background gas as well. The $Jt$ is feasible with standard cathodes and the expected beam compression due to the 7 T magnetic field and the terrestrial and expected half-lives of the radionuclides of interest.

[1] M. Mehlman, P.D. Shidling, R. Burch, E. Bennett, B. Fenker, and D. Melconian, Status of the TAMUTRAP facility and initial characterization of the RFQ cooler/buncher, Hyper. Interact. **235**, 77 (2015).

[2] M. Block, D. Ackermann, D. Beck, K. Blaum, M. Breitenfeldt, A. Chaudhuri, A. Dömer, S. Eliseev, D. Habs, S. Heinz, *et al.*, The Ion-trap facility SHIPTRAP, Eur. Phys. J. A **25**, 49 (2005).

[3] S.W. Epp, J.R. Crespo López-Urritia, M.C. Simon, T. Baumann, G. Brenner, R. Ginzel, N. Buerassimova, V. Mäckel, P.H. Mokler, B.L. Schmitt, H. Tawara, and J. Ullrich, X-ray laser spectroscopy of highly charged ions at FLASH, J. Phys. B **43**, 194008 (2010).

[4] A. Lapierre, M. Brodeur, T. Brunner, S. Ettenauer, A.T. Gallant, V.V. Simon, M. Good, M.W. Fröse, J.R. Crespo López-Urritia, P. Delheij, S. Epp, R. Ringle, S. Schwarz, J. Ullrich, and J. Dilling, The TITAN EBIT charge breeder for mass measurements on highly charged short-lived isotopes: First online operation, Nucl. Instrum. Methods Phys. Res. **A624**, 54 (2010).

[5] D. Manura and D. Dahl, SIMION (R) 8.0 User Manual, Scientific Instrument Services, Inc. Ringoes, NJ 08551, http://simion.com/, January 2008.

[6] R. Becker, O. Kester, and Th. Stöhlker, Simulation of charge breeding for trapped ions, J. Phys. Conf. Ser. **58**, 443 (2007).

[7] J.S. Kim, L. Zhao, J.A. Spencer, and E.G. Evstatiev, Electron-beam-ion-source (EBIS) modeling progress at FAR-TECH, Inc., AIP Conf. Proc. **1640**, 44 (2015).

[8] G.C. Rodrigues, P. Indelicato, J.P. Santos, P. Patté, and F. Parente, Systematic calculation of total atomic energies of ground state configurations, At. Data Nucl. Data Tables **86**, 117 (2004).

[9] V.S. Kolhinen, S. Kopecky, T. Eronen, U. Hager, J. Hakala, J. Huikari, A. Jokinen, A. Niminen, S. Rinta-Antila, J. Szerypo, and J. Äustö, JYFLTRAP: a cylindrical Penning trap for isobaric beam purification at IGISOL, Nucl. Instrum. Methods Phys. Res. **A528**, 776 (2004).

# Elastic scattering of $^{32}$S on $^{13}$C

M. Dag, R. Chyzh, B.T. Roeder, A. Saastamoinen, A. Spiridon, R.E. Tribble,
J. Hooker, C. Hunt, H. Jayatissa, C. Magana, S. Upadhyayula, and J. Button

In the previous work, elastic scattering channel $^{13}$C($^{26}$Mg,$^{26}$Mg)$^{13}$C and the single neutron transfer channel $^{13}$C($^{26}$Mg,$^{27}$Mg)$^{12}$C measurements were performed with the purpose of extracting the parameters of the optical model potentials that were needed for DWBA calculations to determine the asymptotic normalization coefficient (ANC) for the $^{26}$Mg + n → $^{27}$Mg system, and consequently calculating the astrophysical reaction rate for $^{26}$Si(p,gamma)$^{27}$P from ANC [1]. It is shown below on Fig. 1 shows the angular distribution of the cross-section in the center-of-mass system for the elastic scattering of $^{26}$Mg on $^{13}$C.

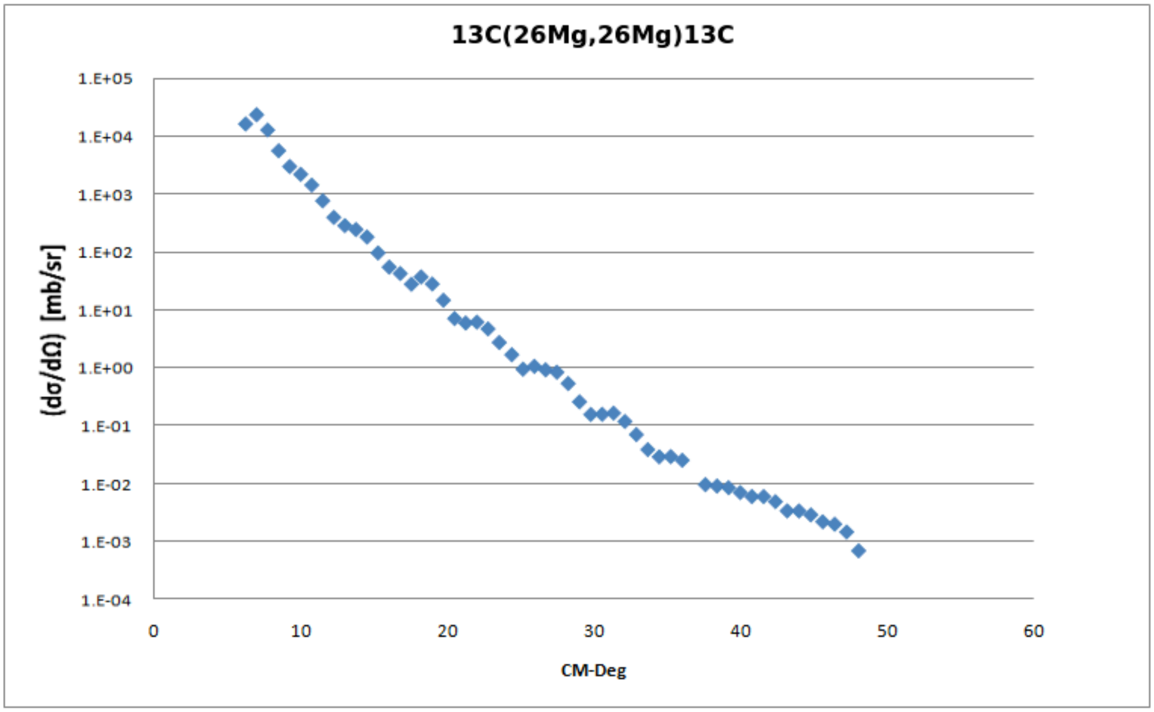

**FIG. 1.** The angular distribution of the cross-section in the center-of-mass system for the elastic scattering of $^{26}$Mg on $^{13}$C.

Subsequently, the elastic scattering of $^{28}$Si on $^{13}$C experiment was carried out to better understand the optical model parameters that are needed for $^{26}$Mg and other systems in this mass region [2]. The angular distribution of the cross-section in the center-of-mass system for the elastic scattering of $^{28}$Si on $^{13}$C is shown below on Fig. 2.

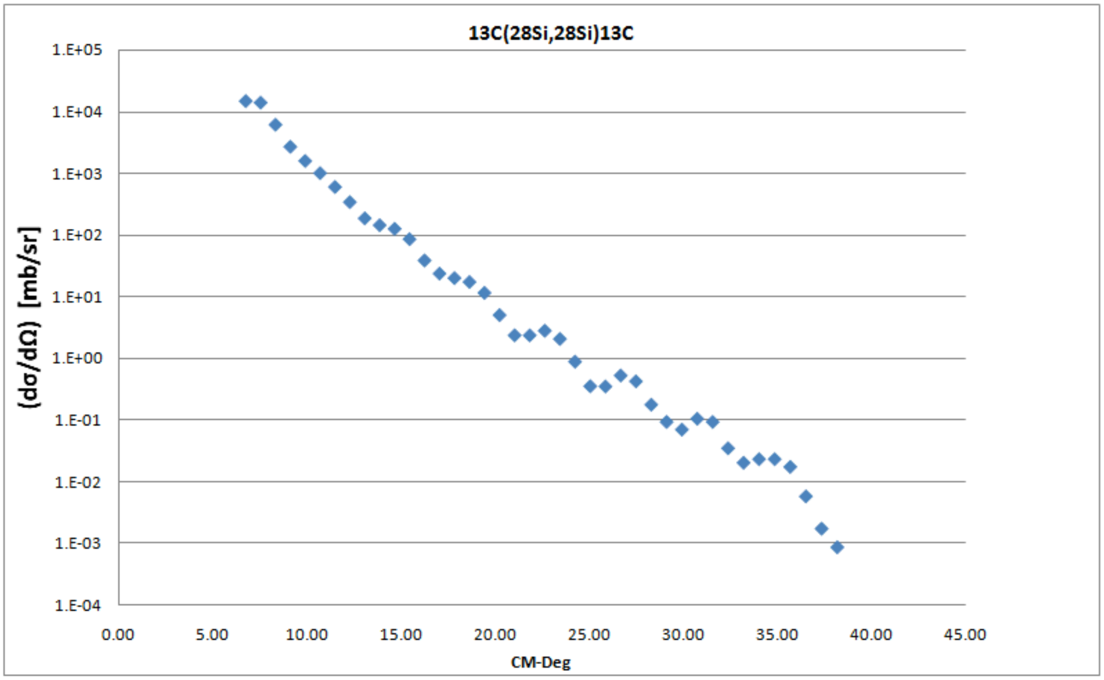

**FIG. 2. :** The angular distribution of the cross-section in the center-of-mass system for the elastic scattering of $^{28}$Si on $^{13}$C.

In this follow-up experiment conducted at Texas A&M Cyclotron Institute, a beam of 334 MeV $^{32}$S ions from the K150 cyclotron impinged on a $^{13}$C target in the chamber of the MDM spectrometer. Reaction products were separated using the multipole-dipole-multipole (MDM) spectrometer, and observed with the help with the recently updated Oxford detector. Elastic scattering of $^{32}$S on $^{13}$C was measured from 2$^{o}$ to 14$^{o}$ in the lab frame (corresponding to 6$^{o}$ – 50$^{o}$ in the center-of-mass frame). The angular distribution of the cross-section in the lab system for the elastic scattering can be seen in Fig. 3.

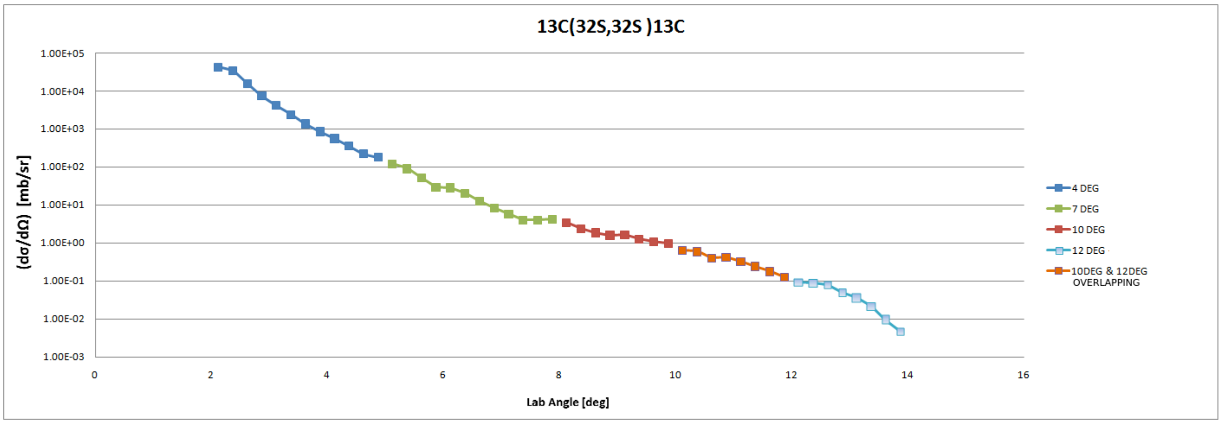

**FIG. 3. :** The angular distribution of the cross-section in the center-of-mass system for the elastic scattering of $^{32}$S on $^{13}$C.

Due to the insufficient residual energy of the particles left in the scintillator, which is placed behind the back window of Oxford detector where the reaction products stop, and a gradual loss in observed particles in the scintillator with a larger angle related to decreasing cross section, it was difficult to obtain data at lab angles larger than $12^{o}$. Hence, in order to overcome this issue, a second Micromegas pad was placed between wire 2 and 3 in the Oxford detector, as shown in Fig. 4, to increase the quality of identification as well as to obtain more data at larger angles by stopping the reaction products in the area right below Micromegas placed between wire3 and 4 [3].

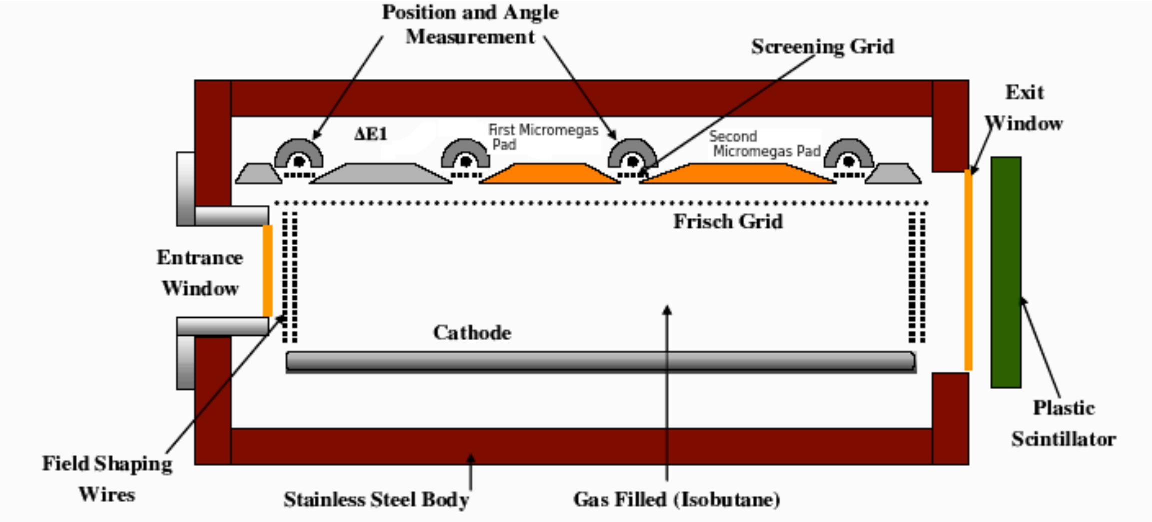

**FIG. 4.** Side View of newly upgraded Oxford detector.

New measurements of the elastic scattering of both $^{28}$Si and $^{32}$S on $^{13}$C at larger lab angles will be performed with newly upgraded Oxford detector. New experiments are already scheduled and will be conducted in May 2016.

[1] M.Dag *et al.*, *Progress in Research*, Cyclotron Institute, Texas A&M University (2013-2014), p. I-40.
[2] M.Dag *et al.*, *Progress in Research*, Cyclotron Institute, Texas A&M University (2014-2015), p. I-28.
[3] A. Spiridon *et al.*, *Progress in Research*, Cyclotron Institute, Texas A&M University (2014-2015), p. IV-45.

# Prototype Penning trap of TAMU-TRAP facility

E. Bennett, B. Fenker, M. Mehlman, D. Melconian, J. Patti, and P.D. Shidling

A prototype cylindrical Penning trap has been designed and fabricated to demonstarate the trapping of stable ions from the offline ion source. The dimension of prototype trap is half the dimension of the planned Penning trap for measuring the beta-neutrino correlation parameter, $a_{\beta\nu}$, in T=2 superallowed β-delayed proton decays. More details about the planned Penning trap is discussed in previous annual reports [1,2]. The electrode structure of the trap is both tunable and orthogonalized, which allows for a near quadrupole electric field at the trap center, a feature necessary for performing precision mass measurements.

The TAMUTRAP prototype Penning trap will also be used to perform mass measurements. Penning trap determine the mass '$m$' of a trapped ion of charge state '$q$' by measuring its cyclotron frequency

$$\omega_c = \frac{q}{m}B,$$

in a magnetic field '$B$'. In the trap the ions are confined in three-dimensions by overlaying a quadrupolar potential and a magnetic field. The motion in a Penning trap is not a simple cyclotron motion($\omega_c$) but a combination of three harmoic eignemotions, an axial oscillation ($z$) and two circular motion commonly referred to as magnetron ($\omega_-$) and reduced cyclotron ( $\omega_+$) motions. The mass of the trapped ions can be determined by performing independent measurements of the eigenfrequencies and a determination of the true cyclotron frequency via the relation :

$$\omega_c = \omega_+ + \omega_-.$$

To measure the cyclotron frequency of a stored ion, it is necessary to drive the ions motion at a sum, or difference, of two eigenfrequencies with an external oscillating electric field (quadrupole radiofrequency (RF) field). At TAMUTRAP, a quadrupolar driving field in the radial plane will be applied. For this purpose one of the electrode is four-fold segmented as indicated in Fig. 1.

Fig. 1 shows the prototype cylindrical Penning trap system of TAMUTRAP facility. The superconducting magnet has a homogeneous (to better than 2 ppm) region at the center, where the trap will be placed. The inner diameter of the trap is 90 mm and a length of about 166 mm, and consists of seven electrodes: a pair of end caps, a pair of end electrodes, a pair of compensation electrodes and one ring electrode. The end caps have a hole of diameter 5 mm for loading and ejecting the ions from the trap. To apply the RF-fields as required for the exciation of the ion motion, the ring electrode is azimuthally divide into four segments. The four-fold segmented ring electrode offers the possibility to excite the trapped ions by a quadrupole RF field. The pair of compensation electrodes are used to compensate for higher-order electric field components. The trap geometry is both tunable and orthogonalized, which allows for a near quadrupole electric field at the trap center. All the trap electrodes are made of oxygen-free high conductivity (OFHC) copper, and are gold-plated to avoid oxidization

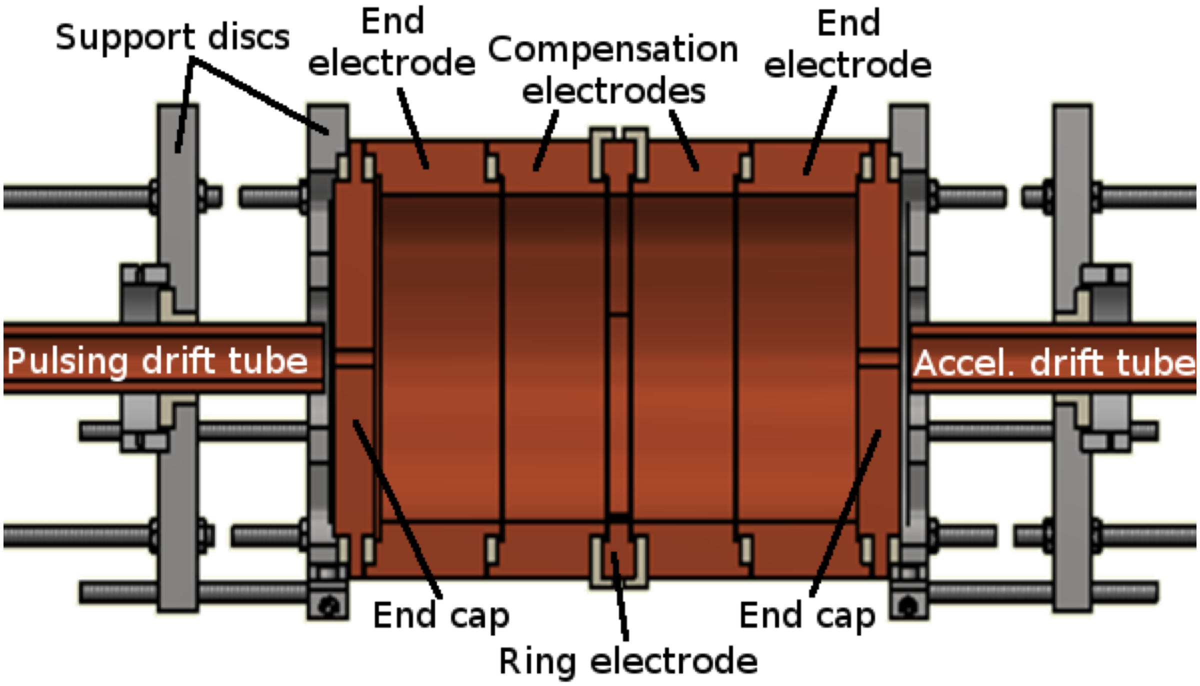

**FIG. 1.** Prototype cylindrical Penning trap system.

which would distort the electric field. The insulators between the electrodes are made of aluminium oxide ($Al_2O_3$) and the distance between two electrodes is 0.5 mm. The elements are mounted on 12 mm thick disc (labelled "Support disc" in Fig.1) made of high strength Aluminum (7075 grade). The disc has two titanium wheels at $45^0$ from the centre. The wheels are used to rail the Penning trap system into the beampipe tube which is inside the magent bore. The tube is made of 316 L stainless steel with low susceptibility and no magnetic enclosures in order to maintain the high homogeneity of the magnetic field. The alignment of the Penning trap with respect to the magnetic-field axis will be performed by electron gun method and is discussed in other report.

As mentioned earlier, the mass of an ion is determined via its cyclotron frequency. At TAMUTRAP facility, we plan to measure the cyclotron frequency by the time-of-flight ion cyclotron resonance method (TOF-ICR). It is a destructive detection method and can be used for single or a low number of stored ions in the trap. This is of particular advantage for very short-lived radioactive ions where the nuclear decay anyhow limits the storage and observation time in the trap.

The injection optics of TAMUTRAP Penning trap system consists of einzel lens, x-y steerer, and a pulsing drift tube. The ion bunches at energy 2.5 keV are guided using the combination of einzel lens and an x-y steerer into the pulsing drift tube with a length of $l = 400$ mm and put at a potential of 2.4 kV. While the ion bunches fly through the tube, its voltage is pulsed to the ground potential. This lowers the ion energy from 2.5 keV to about 100 eV for an efficient capture in the cylindrical Penning trap. Einzel lens and x-y steerer are installed outside the magnet where the strength of the magnetic-field is around 200 Gauss. The pulsing drift tube is placed in strong magnetic field. The gap between the pulsing drift tube and the end cap is around 5 mm. The extraction optics consists of a 13 mm inner diameter drift tube with a length of l = 400 mm to accelerate the ion while they are in the strong magnetic field region. Since the magnetic field gradient in this region is small, no radial kinetic energy change occurs. Thus, no significant effect on the time-of-flight spectra will be observed by varying the drift tube potential. After the ion undergoes sequence of excitation in the center of the trap, the ions will be axially released as an ion pulse from the trap through an accelerating drift tube. Their individual time of flight will be recorded by a MCP detector. A DEL MAR Microchannel Plate Detector (MCP-MA series) with two microchannel plates and a single metal anode readout will be installed about 0.8 m from the center of the trap (about 20 cm from the end of the magnet) where the strength of the magnetic field is around 200 Gauss.

The Penning trap system has been assembled and we are currently installing it in the superconducting solenoid. The electronics to apply an external RF field to the segmented ring electrode of the Penning trap has been built and tested up to 6 MHz. All the parts and electronics essential to couple the Penning trap system to the beam line have been fabricated and tested. We expect to demonstrate trapping of stable ions before the end of the summer of 2016.

[1] M.Mehlman *et al.*, Nucl. Instrum. Methods Phys. Res. **A712**, 11 (2010).

[2] R.S. Behling *et al.*, Progress in Research, Cyclotron Institute, Texas A&M University (2011-2012), p. V-40**.**

# TRINAT Status – Precision polarization and beta-asymmetry

D. Melconian and TRINAT Collaboration

The TRINAT collaboration seeks to make precision measurements angular correlations in the positron decay of $^{37}$K which confine and cool with a magneto-optical trap. Measurements with a relative uncertainty of <1.0% can constrain physics beyond the standard model with complementary uncertainties to direct searches at high-energy colliders. Alternatively, correlation coefficient measurements at this level of precision can be used to derive a value of $V_{ud}$, the top-left element of the CKM matrix independent of the most precise determination using pure-Fermi super-allowed decays [1]. We expect our current data set, collected in 2014, to measure the beta-asymmetry, i.e. the correlation between the spin of the parent nucleus and the momentum of the outgoing positron, to $\Delta A/A \leq 0.5\%$ . When complete, this will be the most precise measurement of this parameter in any nucleus and have comparable precision the measurements in the neutron.

Critical to this measurement is a precise determination of the degree of polarization of the parent nuclei. We use the technique of optical pumping to select the atomic sublevel with maximum projection of nuclear angular momentum along the quantization axis. We monitor the total population of unpolarized and partially polarized atoms by photoionizing atoms after excitation by the optical pumping light and detecting the resulting photoions by accelerating them onto a microchannel plate detector with an electric field. As atoms accumulate in the fully-polarized state, they are no longer available to be photoionized and the rate of photoionization decreases as shown in Fig. 1. The contribution to the average nuclear polarization from the atoms that are not fully polarized is modeled using the density matrix [2]. Our analysis makes a precise measurement of the degree of polarization of the optical pumping light [3] and fits a magnetic field transverse to the optical pumping axis to the experimental data, shown as the red curve. With coherent population trapping accounted for in the theoretical model and deliberately avoided in the experiment, this accounts for all of the possible mechanisms leading to less-than-perfect polarization. The final results we obtained with this method are $P = +0.9913(7)(5)$ and $P = -0.9912(6)(5)$

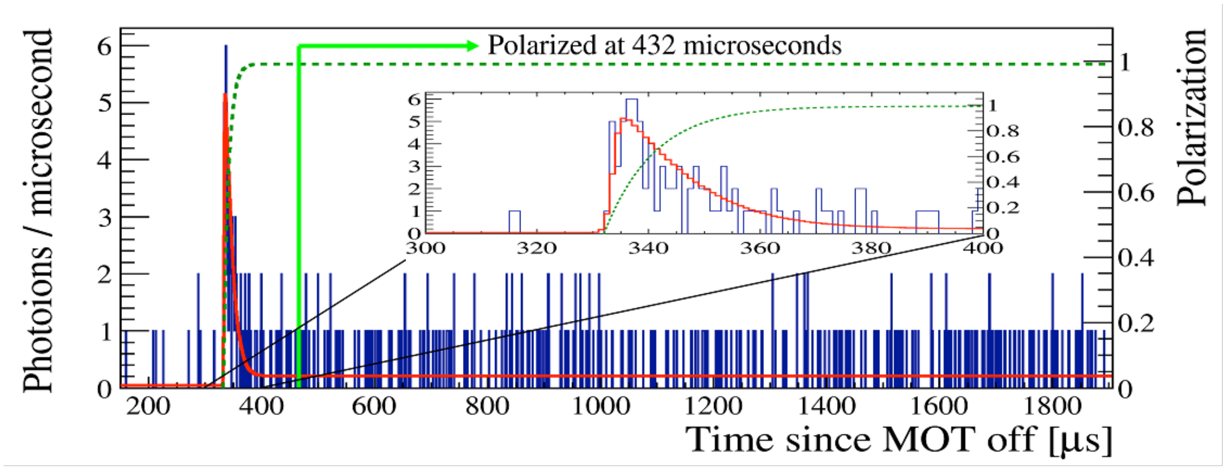

**FIG. 1.** Time spectrum of photoions used to determine the cloud polarization. The optical pumping light is turned on at 350μs, and are polarized in 82μs.

where the first uncertainty is statistical and the second systematic. The largest systematic uncertainty comes from an uncertainty in the initial distribution of the atoms amongst the possible sublevels. This result has been submitted for publication [4].

Furthermore, significant progress has been made towards the measurement of the asymmetry in the number of positrons detected along and against the nuclear polarization axis. At this point, all of the detectors have been characterized and the analysis cuts are in the process of being finalized. Although the data is still "blind" to prevent over- or under-fitting of the data, it agrees well with the experimental asymmetry predicted by a GEANT4 simulation that includes tracking the positron through the experimental geometry and ideally includes the effects of scattering off of the surrounding material.

Fig. 2 shows the energy spectrum from our plastic scintillator detectors which record the total energy deposited by the positron. Overlayed with the data is the GEANT4 simulation which is able to reproduce the spectrum. It is worth emphasizing that there is zero background included in this figure. This analysis, which is in its final stages, will make up Benjamin Fenker's Ph.D. thesis and will be complete this summer.

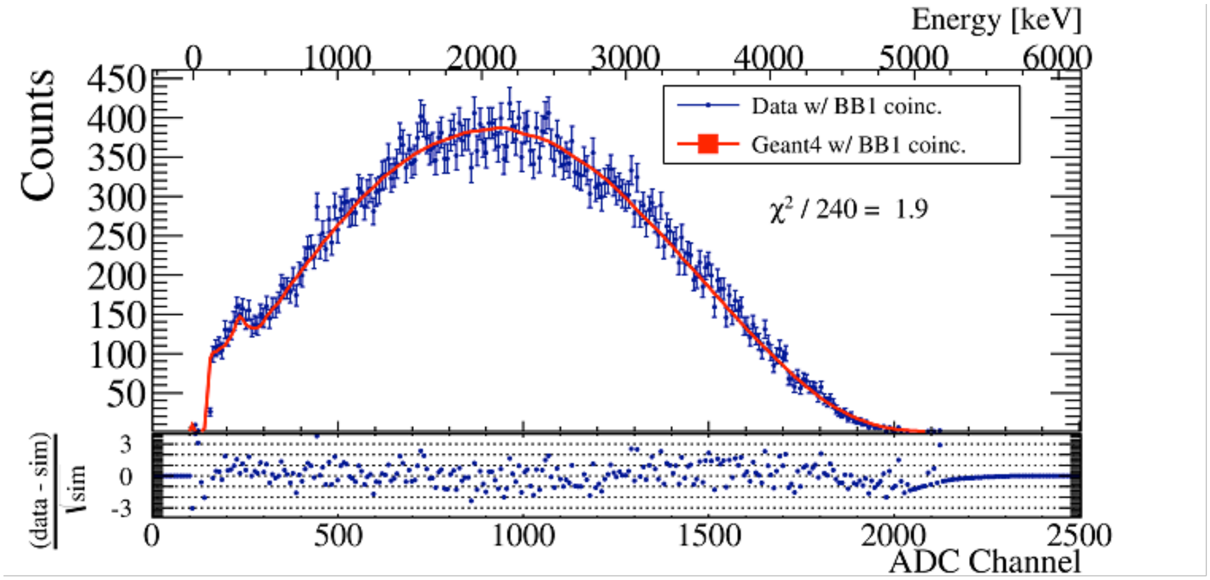

**FIG. 2.** Energy spectrum of the upper plastic scintillator and comparison to our Monte Carlo simulation (top). The residuals of the fit are shown below.

[1] O. Naviliat-Cuncic and N. Severijns, Phys. Rev. Lett., **102**, 142302 (2009).

[2] P. Tremblay and C. Jacques, Phys. Rev. A **41**, 1990 (1989).

[3] C.L. Warner, J.A. Behr, and A. Gorelov, Rev. Sci. Instrum., **85**, 113106 (2014).

[4] B. Fenker *et al.*, (2016), arXiv:1602.04526 [nucl-ex].

# A study of the contribution from non-perturbative effects to di-jet yields at forward rapidity

A. Poulsen,[1] Z. Chang, and C.A. Gagliardi
[1]*2015 REU student at Texas A&M from University of Dallas*

The STAR Collaboration has proposed to upgrade its forward calorimetry in order to perform a range of polarized proton and *p*+A studies in the 2020+ time frame [1]. One anticipated measurement will investigate the double-longitudinal spin asymmetry, $A_{LL}$, for forward di-jet production in *pp* collisions at $\sqrt{s}$ = 500 GeV to constrain the gluon polarization in the proton at very low $x$. Next-to-leading-order perturbative QCD calculations indicate that forward di-jets with transverse momenta $p_{T,1} >$ 8 GeV/*c* and $p_{T,2} >$ 5 GeV/*c* would provide very good sensitivity for gluons with $x \sim 10^{-3}$ [1], where existing data provide essentially no constraints [2,3]. However, the NLO pQCD calculations do not include possible background contributions from initial-state radiation, underlying event effects, and beam remnants that can create additional particles which appear as jets in the detector.

A PYTHIA study was performed to estimate the size of the background contributions that were absent in the NLO pQCD calculation. It found that, for ~20% of the di-jets that satisfy a back-to-back requirement ($|\Delta\varphi-\pi| < 1$), one or both of the observed jets arose from the various background effects. However, the background contributions end up nearly uncorrelated in $\Delta\varphi$. Thus, if the trigger is designed to accept di-jet events over a wide $\Delta\varphi$ range, for example $\Delta\varphi > \pi/2$, a simple subtraction will provide a clean di-jet sample suitable to determine the gluon polarization.

[1] E.C. Aschenauer *et al.*, “The RHIC Cold QCD Plan for 2017 to 2023: A Portal to the EIC”, arXiv:1602.03922.
[2] D. de Florian, R. Sassot, M. Stratmann, and W. Vogelsang, Phys. Rev. Lett. **113**, 012001 (2014).
[3] E.R. Nocera *et al.* (NNPDF Collaboration), Nucl. Phys. **B887**, 276 (2014).

# Spin physics with STAR at RHIC

Z. Chang, C.A. Gagliardi, M.M. Mondal, R.E. Tribble,
and the STAR Collaboration

Our group continues to play major roles in STAR investigations of both longitudinal and transverse spin phenomena in polarized *pp* collisions at RHIC. During the past year, we have been working to finalize several of the analyses that were discussed in last year's *Progress in Research*.

A major goal of the RHIC spin program is to determine the gluon polarization in the proton over a wide range of momentum fraction $x$. The longitudinal double-spin asymmetry, $A_{LL}$, for inclusive jet production is an ideal tool in this effort because the cross section is large and dominated by quark-gluon and gluon-gluon scattering processes, both of which have large partonic asymmetries. Our paper describing the final $A_{LL}$ results for inclusive jets at $\sqrt{s}$ = 200 GeV, based on data that STAR recorded during 2009, was published in *Physical Review Letters* this past year [1]. It was chosen to be an Editors' Suggestion article. The implication of the results, that the gluons in the proton with $x > 0.05$ have their spins preferentially aligned with the proton spin, was called "a significant breakthrough" in the 2015 NSAC Long-Range Plan.

As reported last year, we presented preliminary results at the SPIN 2014 conference in Beijing on $A_{LL}$ for inclusive jets at a higher beam energy, $\sqrt{s}$ = 510 GeV, based on data that STAR recorded during 2012. The higher beam energy extends the sensitivity to gluon polarization to lower $x$ gluons. Since then, we have been working to on the steps necessary to complete the final analysis.

The larger phase space for soft particle production at 510 GeV relative to 200 GeV produces a substantial increase in the underlying event (UE) activity. This can distort the jet finding, especially for low-$p_T$ jets. An additional concern is that the UE activity might itself have a spin asymmetry that could distort measurements of the jet $A_{LL}$. For the preliminary result, we required $p_T > 7.1$ GeV to minimize these systematic effects. We want to lower the $p_T$ cut-off for the final result further to enhance our sensitivity to low-$x$ gluon polarization. We also want to obtain a direct experimental estimate of the UE $A_{LL}$ to set a limit on its contribution to our measured jet asymmetries. A PYTHIA study showed that we could substantially reduce our sensitivity to UE contributions by implementing an "off-angle cone" subtraction procedure, similar to that used for *pp* collisions by ALICE [2]. Thus, we developed the tools necessary to match each reconstructed jet with the charged-particle tracks and calorimeter towers present in two cones at the same pseudorapidity as the jet, but offset azimuthally from the jet by $\Delta\varphi = \pi/2$. The STAR TPC and BEMC are symmetric under such a rotation, which makes this procedure particularly attractive. Furthermore, the procedure also provides an approximate subtraction of pile-up backgrounds, which are much larger in 510 GeV *pp* collisions than in 200 GeV collisions. We are now using the new tools both to subtract the UE and pile-up contributions and to measure the UE $A_{LL}$ for the first time. The tools that we developed will also be utilized to subtract combinatorial background for jet analyses in *p*+A collisions.

Preliminary measurements of pion azimuthal distributions in jets utilizing 500 GeV data that STAR recorded during 2011 indicated that the Perugia-0 tune that we've used for PYTHIA in previous

200 GeV analyses has shortcomings when applied to 500 GeV collisions. Therefore, our group, in collaboration with colleagues from University of Kentucky, undertook a study to find PYTHIA parameters that would simultaneously describe jet data at 200 and 500 GeV. We found that the Perugia-2012 tune provides a good description of the jets, but produces too much UE activity. Reducing the PARP(90) parameter from 0.24 (default for Perugia-2012) to 0.213 provides the best compromise between good jet and UE descriptions. The STAR Spin PWG has now adopted this combination for all on-going jet analyses.

We have now completed the reanalysis of the 2012 inclusive jet data with the off-axis cone subtraction implemented, and are about to start the production of the Monte Carlo embedding simulations required to calculate corrections for jet energy scale distortions and trigger and reconstruction bias. We will complete the final 2012 inclusive jet $A_{LL}$ analysis within the coming year.

In last year's *Progress in Research*, we described the first measurements of the "Collins effect" in transversely polarized *pp* collisions. The Collins effect involves the convolution of the quark transversity distributions in the proton with the Collins fragmentation function. The net result is to produce an azimuthally asymmetric distribution of charged pions within jets. During the past year, first calculations [3] of the Collins effect have been performed for STAR kinematics, as shown in Fig. 1. These calculations are based on global analyses of the Collins fragmentation function from $e^+e^-$ collisions and

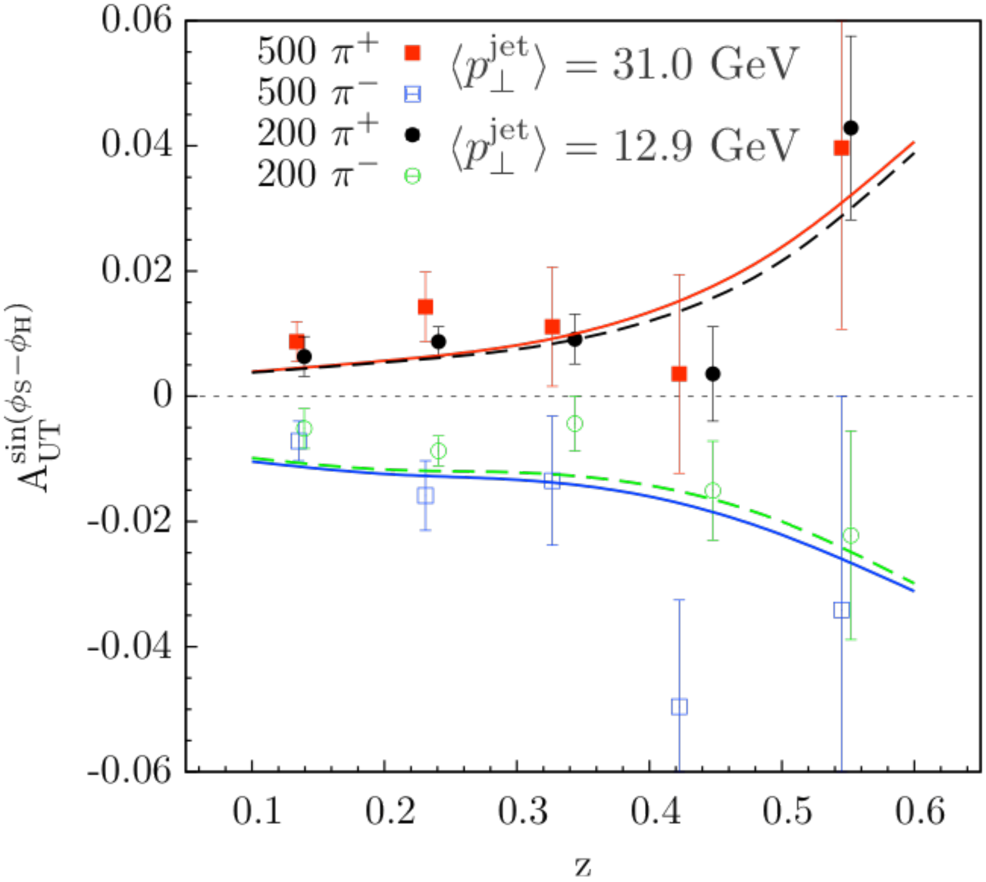

**FIG. 1.** A comparison of our preliminary measurement of the Collins effect in 200 and 500 GeV *pp* collisions with recent calculations from [3].

transversity extracted from semi-inclusive deep-inelastic scattering (SIDIS). The good agreement between the preliminary STAR results and the Collins effect calculations provide the first ever test of the predicted universality of the Collins effect for SIDIS and *pp* collisions. It's also important to recognize that the calculations do not include any TMD evolution effects for the Collins fragmentation function. $Q^2$ ~ 1000 GeV$^2$ for the 500 GeV STAR data, approximately two orders of magnitude larger than for the SIDIS data at the comparable $x$ value. This might indicate that TMD evolution effects are small, or perhaps they tend to cancel between the polarized numerator and the unpolarized denominator for asymmetry measurements like this.

For the preliminary analysis, we estimated the kaon, proton, and electron contaminations with simple 4-Gaussian fits to the measured TPC *dE/dx* distributions. We used the same procedure while preparing a first draft paper describing these results, together with collaborators from Lamar University, University of Kentucky, and Valparaiso University. The paper also described measurements of asymmetries in lower-$p_T$ jets. During the God-Parent Committee review of our draft, concerns were raised about similar particle identification procedures for a different STAR spin analysis. Although the concerns had not been directed toward analysis, we quickly realized that they could also apply to the lower-$p_T$ pions that we use to investigate gluon linear polarization. During the past year, we have developed far more sophisticated procedures for particle identification. The net result for the high-$p_T$ jets, relevant for the Collins effect measurement, is a substantial reduction in the systematic uncertainties at the expense of a small loss of statistics. We expect the same will be true for the lower-$p_T$ jets that provide information about gluon linear polarization, but that analysis is not quite complete yet. We are now writing a letter describing the Collins effect results, while working in parallel to complete the lower-$p_T$ jet analysis.

[1] L. Adamczyk *et al*. (STAR Collaboration), Phys. Rev. Lett. **115**, 092002 (2015).
[2] B. Abelev *et al*. (ALICE Collaboration), Phys. Rev. D **91**, 112012 (2015).
[3] Z. Kang *et al*., (to be submitted).

# SECTION II

# HEAVY ION REACTIONS

# First evidence of metal transfer into hydrophobic deep eutectic mixtures: Indium extraction from hydrochloric and oxalic acids

E.E. Tereshatov,[1] M.Yu. Boltoeva,[2,3] and C.M. Folden III[1]
[1]*Cyclotron Institute, Texas A&M University, College Station, Texas*
[2]*Université de Strasbourg, IPHC, Strasbourg, 67037 France*
[3]*CNRS, Strasbourg, 67037 France*

The near-critical and strategic metal, indium, has been successfully extracted from hydrochloric and oxalic acid media into quaternary ammonium- and menthol-based eutectic mixtures with carboxylic acids. This is the first report on metallic species transfer from aqueous solution into hydrophobic deep eutectic mixtures.

Transfer of indium was carried out from hydrochloric and oxalic acid solutions. Three DESs composed of quaternary ammonium chloride and fatty acids, namely decanoic and oleic acids, and ibuprofen provide very quick and efficient metal extraction in the range of 0.01 – 10.2 M HCl (Fig. 1) and $10^{-7}$ – 8x$10^{-1}$ M oxalic acid (Fig. 2) in the aqueous phase. The DES composed of DL-menthol and lauric acid extracts indium efficiently only from aqueous solutions with low acidity. Back-extraction of In from ammonium-based DESs has been performed using 0.1 M DTPA. The results provide an opportunity for valuable metallic species extraction from an aqueous phase by means of cheap and ecofriendly deep eutectic mixtures. A full publication on these results is currently under review.

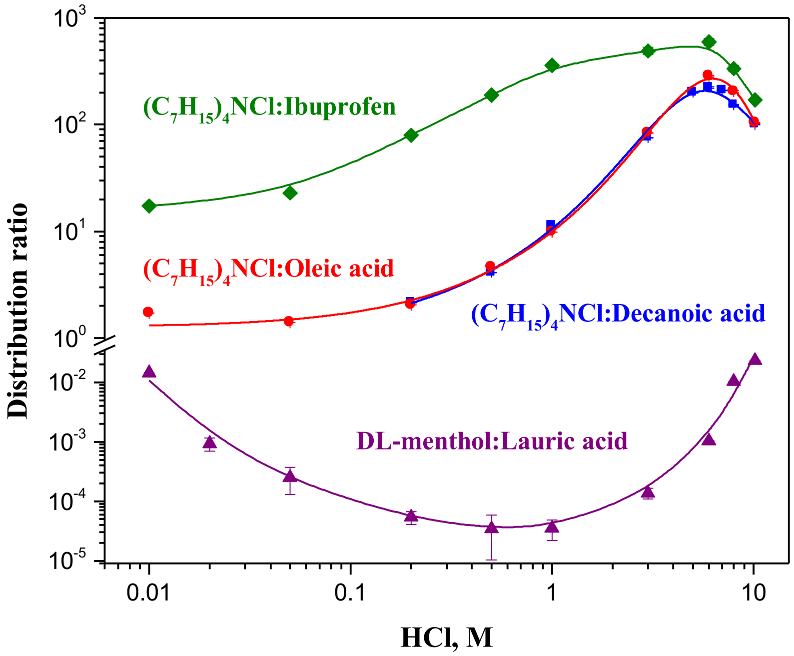

**FIG. 1.** Effect of aqueous hydrochloric acid concentration on the extraction efficiency of In into quaternary ammonium-based hydrophobic DESs. Lines are drawn to guide the eye.

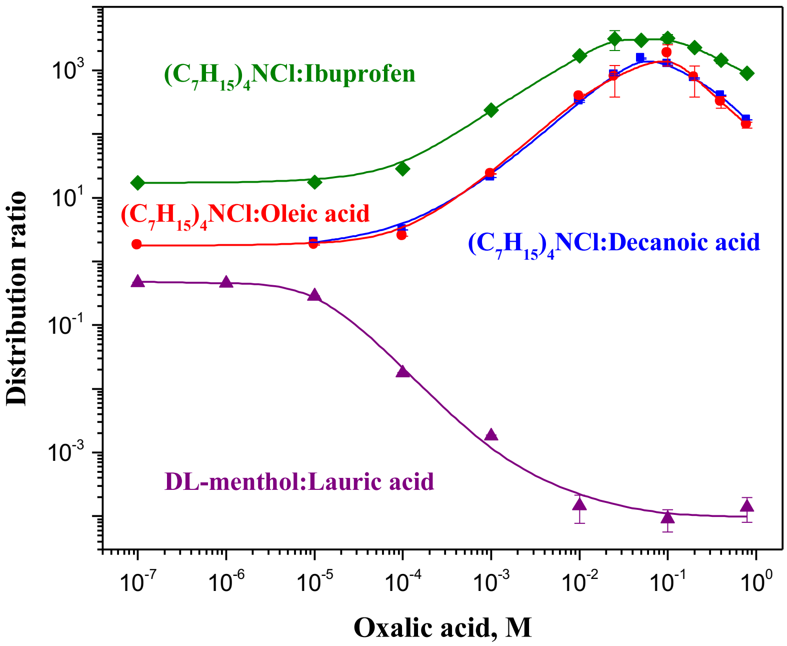

**FIG. 2.** Effect of oxalic acid concentration on the extraction of In into quaternary ammonium- and menthol-based hydrophobic DESs. The lines are drawn to guide the eye.

# Indium extraction with HDEHP in menthol-based deep eutectic solvent

M.F. Volia, E.E. Tereshatov, M.Yu. Boltoeva,[1, 2] and C.M. Folden III
[1]*Université de Strasbourg, IPHC, Strasbourg, 67037 France*
[2]*CNRS, Strasbourg, 67037 France*

The study of indium extraction by using liquid phase chemistry techniques has been ongoing in the Heavy Elements, Nuclear and Radiochemistry Group at the Cyclotron Institute of Texas A&M University. This study aims to contribute to the fundamental research on the chemistry of the superheavy elements, specifically element 113 (E113). E113 is the newest member of group 13 of the Periodic Table of Elements and its chemical properties have not yet been studied extensively. Based on theoretical predictions, this element is expected to be volatile [1]. A gas-phase chemistry experiment of E113 was conducted at the Joint Institute for Nuclear Research (JINR) in Dubna, Russia in an attempt to reveal its chemical properties. Although the result of that experiment was somewhat inconclusive, it was concluded that E113 is highly volatile and thus confirmed the theoretical predictions [2]. More experiments are required in order to provide more information about the chemical properties of E113. The study of homologs (other elements in the same group) is commonly employed to provide such information. Indium is the lighter homolog of E113, and our group has previously studied indium behavior in hydrochloric acid solutions by means of ion exchange and liquid-liquid extraction techniques [3]. In the current work, the performance of the liquid-liquid extraction (LLE) technique for indium extraction is developed and explored further. The description of experimental procedure and preliminary results are presented in the following paragraphs.

The LLE system in this work uses a deep eutectic solvent (DES) as the organic phase to substitute for conventional organic compounds. DESs are characterized by lower melting points compared to their individual constituents. They are prepared by mixing two components that act as hydrogen bond acceptor (HBA) and hydrogen bond donor (HBD), from which hydrogen bonds form and facilitate liquefaction of the final mixture [4]. DESs are generally believed to be biodegradable, thus they pose less hazard to environment compared to conventional solvents [5]. In this work, a DES comprised of DL-menthol and lauric acid was synthetized in our laboratory. DL-menthol and lauric acid which were originally solid at room temperature were mixed with molar ratio 2:1. The mixture was heated in a water bath at 90$^{o}$C until it formed a homogenous liquid phase. Subsequently, the solution was cooled down to room temperature, shaken for 5 minutes with a Vortex mixer at 3000 rpm, and centrifuged for 1 minute at 4400 rpm before usage.

Indium stock solution was prepared by adding an appropriate amount of radioisotope indium-111 (half-life 67.32 hours) in 0.2 M hydrochloric acid (HCl). The aqueous phase consists of 10 μL indium from the stock solution and 490 μL of HCl of various concentrations. Equal volumes of aqueous and organic phases (500 μL) were placed in a 5 mL polyethylene tube, shaken with a Vortex mixer for 5 minutes at 3000 rpm, and then centrifuged for 1 minute at 4400 rpm. After the centrifugation, 250 μL was drawn from each phase and subsequently assayed with a sodium iodide detector according to a technique described elsewhere [6]. The distribution of indium between the two phases (D) was calculated by taking the ratio of the activity in the organic phase to the activity in the aqueous phase. The result showed that indium was poorly extracted (D ≤ 1 in pH 1 – 6). In order to increase the extraction yield, a complexing agent was added into the organic phase as the extractant of indium.

In this work, an organophosphorus acidic extractant, namely di-(2-ethylhexyl)-phosphoric acid (HDEHP), was used as the complexing agent for indium. The structure of HDEHP is presented in Fig. 1.

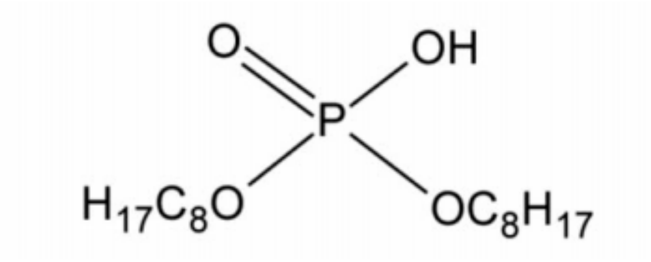

**FIG. 1.** Structure of HDEHP.

The organic phase for indium extraction with this system consists of 30% (v/v) HDEHP in DES menthol-lauric acid, and the extraction was done from HCl media. The effect of pH on indium extraction was investigated and the result is presented in Fig. 2. As can be seen from the figure, indium was extracted at pH > 0.6 and pH < 2.8 (D ≥ 10). Generally, the distribution ratios of indium extraction increase with increasing pH up to pH 2, and they decrease above this pH.

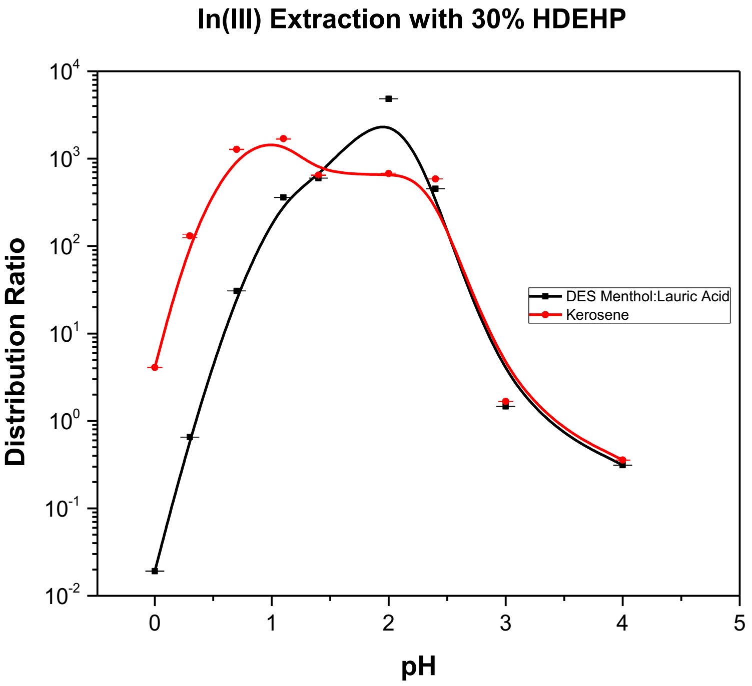

**FIG. 2.** Extraction of indium with HDEHP in DES menthol-lauric acid and kerosene. The lines are drawn to guide the eye.

Addition of HDEHP results in a significant increase in extraction yield. This leads to the conclusion that HDEHP is responsible for the extraction of indium from the aqueous phase to the organic phase. To check the effectiveness of DES menthol-lauric acid as the organic solvent, the extraction of indium into HDEHP with the DES menthol-lauric acid was compared with extraction into HDEHP with kerosene, a conventional organic solvent which is commonly used in LLE. In both systems, 30% (v/v) HDEHP was added to the organic phase. Based on the results in Fig. 2, the distribution ratios of indium extraction into HDEHP with kerosene are generally higher at pH below 1.1. As the pH increases, the extraction yield with kerosene decreases and reaches a plateau at pH 1.4 – 2.4. Beyond this pH range, the distribution ratios decrease with a similar trend as extraction with DES menthol-lauric acid. Based on these results, best extraction with kerosene and HDEHP was obtained at pH 1.1. Experiments are still ongoing to confirm this result. However, this preliminary result is a good indication that DES menthol-lauric acid can be a proper candidate to replace toxic and flammable organic solvents in LLE of metals.

[1] A. Türler and V. Pershina, Chem. Rev. **113**, 1237 (2013).
[2] S.N. Dmitriev, N.V. Aksenov, Y.V. Albin, G.A. Bozhikov, M.L. Chelnokov, V.I. Chepygin, R. Eichler, A.V. Isaev, D. E. Katrasev, V.Y. Lebedev, O.N. Malyshev, O.V. Petrushkin, L.S. Porobanuk, M.A. Ryabinin, A.V. Sabel'Nikov, E.A. Sokol, A.V. Svirikhin, G.Y. Starodub, I. Usoltsev, G.K. Vostokin, and A.V. Yeremin, Mendeleev Commun. **24**, 253 (2014).
[3] E.E. Tereshatov, M.Yu Boeltova, and C.M. Folden III, Solvent Extr. Ion Exch. **33,** 607 **(**2015).
[4] F. Pena-Pereira and J. Namieśnik, ChemSusChem. **7**, 1784 (2014).
[5] B.D. Ribeiro, C. Florindo, L.C. Iff, M.A.Z. Coelho, and I.M. Marrucho, ACS Sustainable Chem. Eng. **3**, 2469 **(**2015).
[6] E.E. Tereshatov and C.M. Folden, *Progress in Research*, Cyclotron Institute, Texas A&M University (2014-2015), p. IV-66; http://cyclotron.tamu.edu/2015 progress report/4 superconducting cyclotron and instrumentation/iv_66-74_a labview solution.pdf (accessed May 20, 2016).
[7] M. Regel-Rosocka, F.J. Alguacil, REVMETAL Revista de Metalurgia. **49**, 292 (2013).

# Thallium transfer from hydrochloric acid media into pure ionic liquids

E.E. Tereshatov,[1] M.Yu. Boltoeva,[2,3] V. Mazan,[2,3] M.F. Volia,[1,4] and C.M. Folden III[1]
[1]*Cyclotron Institute, Texas A&M University, College Station, Texas*
[2]*Université de Strasbourg, IPHC, Strasbourg, 67037 France*
[3]*CNRS, Strasbourg, 67037 France*
[4]*Department of Nuclear Engineering, Texas A&M University, College Station, Texas*

Pure hydrophobic ionic liquids are known to extract metallic species from aqueous solutions. Here, we report on the systematic investigation of thallium (Tl) extraction from aqueous hydrochloric acid (HCl) solutions into six pure fluorinated ionic liquids, namely imidazolium- and pyrrolidinium-based ionic liquids with *bis*(trifluoromethanesulfonyl)imide and *bis*(fluorosulfonyl)imide anions.

It has been shown that distribution ratios attributed to Tl(I) are below 1. In the case of Tl(III), surprisingly high extraction efficiencies and fast kinetics have been observed, and equilibrium has been reached in seconds. Bromine water (Fig. 1a) or chlorine water (Fig. 1b) was used to oxidize Tl(I) to Tl(III). It has been found that the Tl(III) extraction ability of ionic liquids in this work increases in the order $[C_2mim][Tf_2N]$ < $[C_3C_1pyrr][Tf_2N]$ < $[C_4mim][Tf_2N]$ < $[C_2mim][FSI]$ < $[C_3C_1mim][Tf_2N]$ < $[C_8mim][Tf_2N]$. The solubilities of the $[Tf_2N^-]$-based ionic liquids in water decrease in the same order. The highest distribution value of Tl(III) was approximately 2000 (Fig. 1a). The charge of the Tl(III)

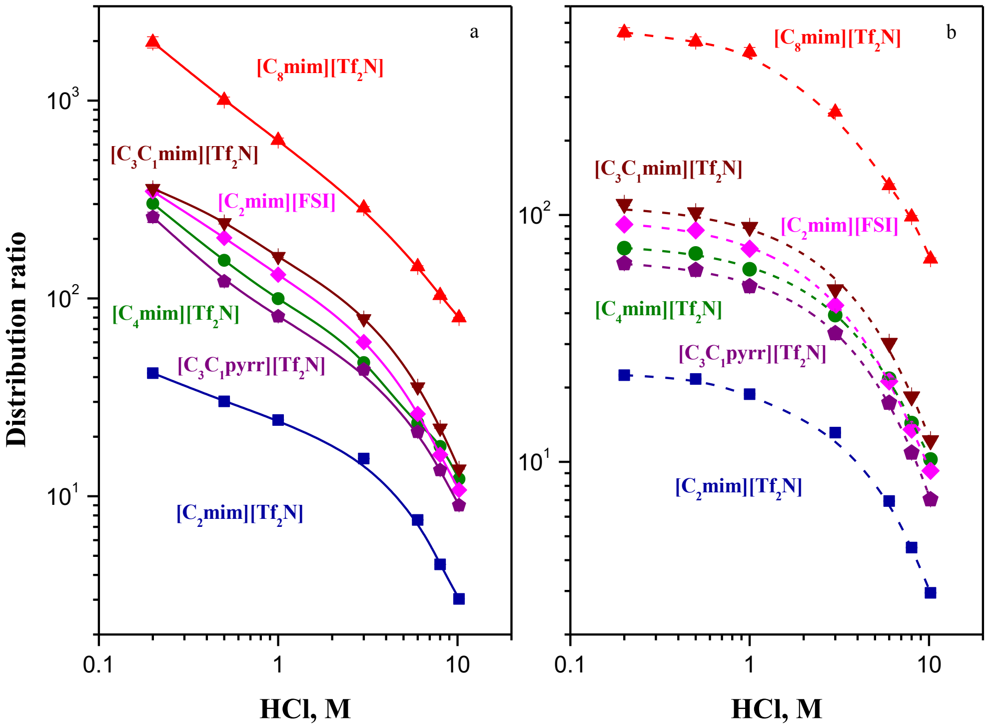

**FIG. 1.** Tl(III) extraction from HCl aqueous solutions into different ionic liquids: a) data with bromine water, b) data with chlorine water.

complexes has been determined by introduction of Li[$Tf_2N$] into the aqueous phase for experiments with [$Tf_2N^-$]-based ionic liquids. The measured data indicated that the extraction of Tl(III) proceeds mainly *via* ion pair complex formation with IL cations, and that the extracted metallic species are $TlCl_4^-$ in low acid concentrations and either $TlCl_5^{2-}$ or a mixture of $TlCl_4^-$ and $TlCl_6^{3-}$ in high acid concentrations in the presence of chlorine water. Tl(III) extraction is quantitative for initial metal concentrations up to $1 \times 10^{-3}$ M. Back-extraction of Tl(III) has been checked as a function of HCl concentration, and a successful decrease in distribution ratio values has been observed. In total, these results indicate that the use of pure ionic liquids for extraction of Tl from aqueous HCl solutions is feasible. A full publication on these results is available in Ref. [1].

[1] E.E. Tereshatov *et al.*, J. Phys. Chem. B **120**, 2311 (2016); doi:10.1021/acs.jpcb.5b08924

# Candidate for a state analogous the Hoyle state observed in $^{16}$O at about 15 MeV excitation energy using the thick target inverse kinematics technique

M. Barbui,[1] K. Hagel,[1] J. Gauthier,[1] S. Wuenschel,[1] R.T. deSouza,[2] S. Hudan,[2]
D. Fang,[3] and J.B.Natowitz
[1]*Cyclotron Institute, Texas A&M University, College Station, Texas*
[2]*Indiana University, Bloomington, Indiana*
[3]*Shanghai Institute of Applied Physics (SINAP), Chinese Academy of Sciences, Shanghai, China*

Searching for alpha cluster states analogous to the $^{12}$C Hoyle state in heavier alpha-conjugate nuclei can provide tests of the existence of alpha condensates in nuclear matter. Such states are predicted for $^{16}$O, $^{20}$Ne, $^{24}$Mg, $^{28}$Si etc. at excitation energies slightly above the multi-alpha particle decay threshold [1-3].

The Thick Target Inverse Kinematics (TTIK) [4] technique can be successfully used to study the breakup of excited self-conjugate nuclei into many alpha particles. The reaction $^{20}$Ne+α at 10 and 12 AMeV was studied at Cyclotron Institute at Texas A&M University. A picture of the experimental setup is shown in Fig. 1.

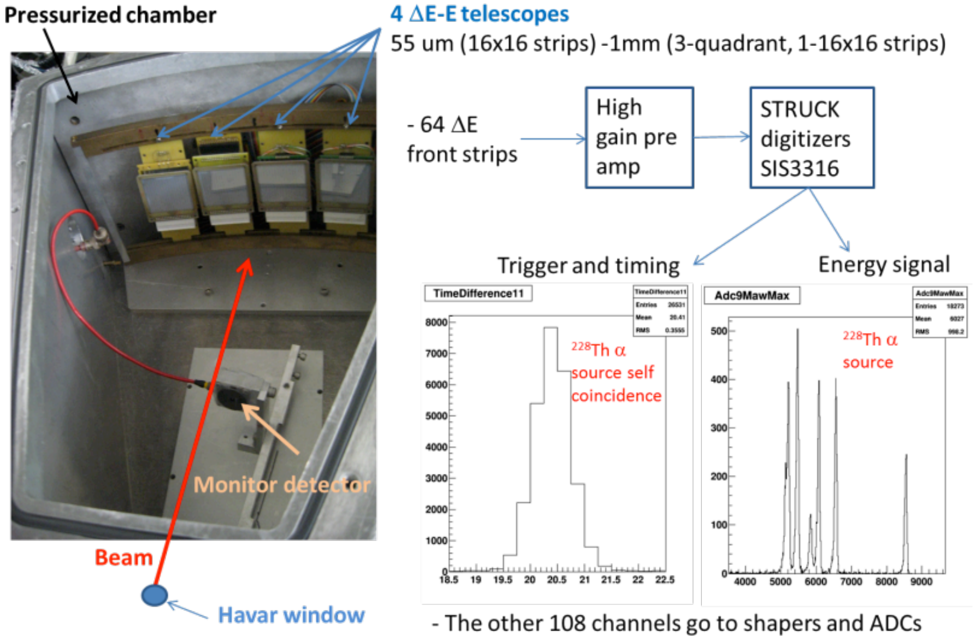

**FIG. 1.** Experimental setup and scheme of the electronics. Good energy and time resolution are obtained by using the STRUCK digitizers SIS3316.

The TTIK method was used to study both single α-particle emission and multiple α-particle decays. The analysis of the three α - particle emission data allowed the identification of the Hoyle state and other $^{12}$C excited states decaying into three alpha particles. Some results are reported in ref [5, 6] and compared with other data available in the literature. In this report, we summarize the results obtained from the analysis of the events with alpha multiplicity four. In order to minimize the contribution due to accidentals, only events in which the four alpha particles arrive to the detectors in a time window of 15 ns are selected. Due to the very low beam intensity used during this run we estimate one beam particle per beam burst.

The reconstruction of the position of the interaction point for alpha multiplicity four events is based on a recursive procedure using the reaction kinematics, energy and momentum conservation. This reconstruction is based on the assumption tof having, in the exit channel, $^{8}$Be in the ground state (undetected), and $^{16}$O (with enough excitation energy to decay into 4 alpha particles). The preliminary analysis of these events shows very promising results.

Fig. 2 shows the reconstructed excitation function of $^{16}$O. The peak at around 15 MeV is a good candidate for Hoyle state analogous in $^{16}$O; the other peaks correspond to known states in $^{16}$O.

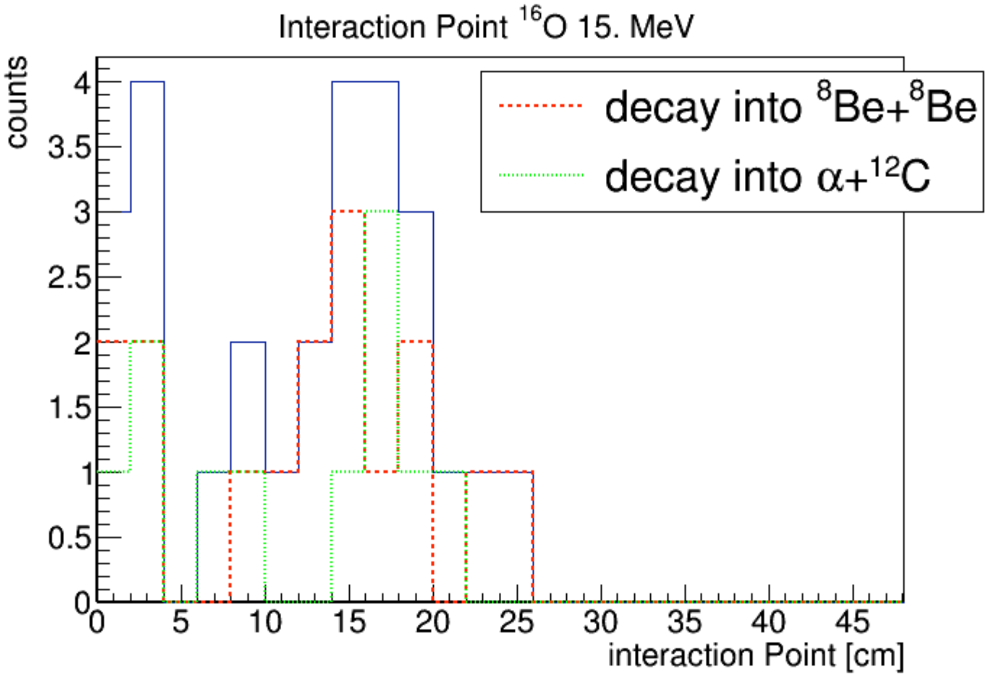

**FIG. 2.** Reconstructed excitation energy of $^{16}$O obtained from the events with multiplicity 4. The arrows mark the position of known states in $^{16}$O decaying into alpha particles [7,8].

Funaki *et al.* [9] predicted a state in $^{16}$O at 15.1 MeV (the state) with the structure of the "Hoyle" state in $^{12}$C coupled to an alpha particle. Our peak is very close to this prediction. Kokalova *et al.* suggest that the signature for multi-alpha condensed states would be the decay of the excited system into pieces that are condensates themselves, ie. $^{8}$Be$_{gs}$, $^{12}$C$_{Hoyle}$ , etc.[10]. A total of 33 events were found in the 15 MeV peak. We further analyzed these events to determine wether they decay by two $^{8}$Be in the ground state or an alpha-particle and a $^{12}$C in the Hoyle state. The events decaying into two $^{8}$Be were identified looking for two couples of alpha particles with relative energy less than 180 keV. The events decaying with one alpha and a $^{12}$C only have one couple of alpha particles with relative energy less than 180keV. 17 events were found to decay into two $^{8}$Be and 16 events into alpha plus $^{12}$C in the Hoyle state. A monte carlo simulation of the two decay modes shows that the detection efficiency of our experimental setup is 45% for the first case and 40% for the latter. This indicates that within the experimental errors the events in the 15 MeV peak equally decay into the two possible decay branches. According to ref. [10] this is a signature for an alpha condensate state.

The position of the reconstructed interaction point for the events in the 15 MeV peak is reported in Fig. 3.

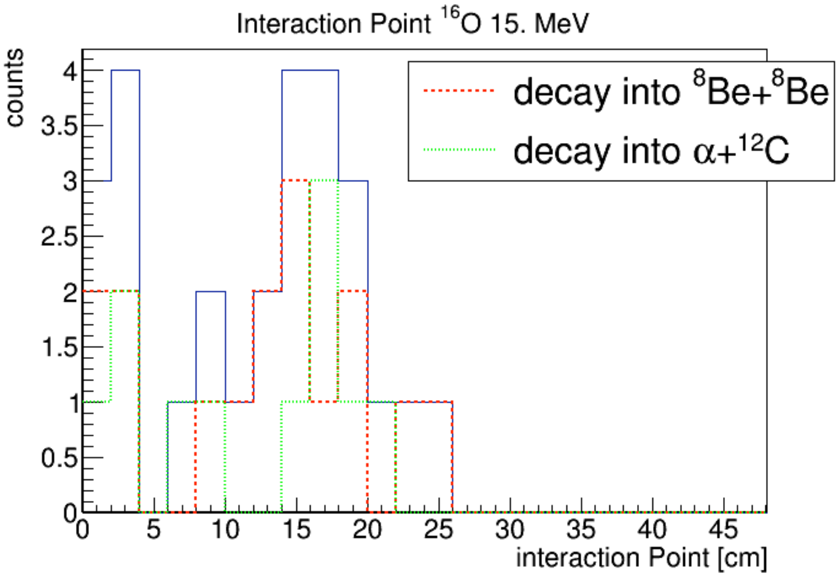

**FIG. 3.** Reconstructed interaction point for events in the 15MeV peak. Blue solid line: all events; red dotted line: events decaying into two $^8$Be; green line: events decaying into alpha plus $^{12}$C Hoyle state.

The left panel in Fig. 4 shows the reconstructed position of the interaction point as a function of the measured kinetic energy of the $^{16}$O, after energy loss correction. The right panel shows the kinetic energy of the undetected $^8$Be as a function of the kinetic energy of the $^{16}$O at the interaction point. It is clear from this picture that the energy of the two alphas from the undetected $^8$Be would be too low to be identified in the telescopes with the deltaE-E technique.

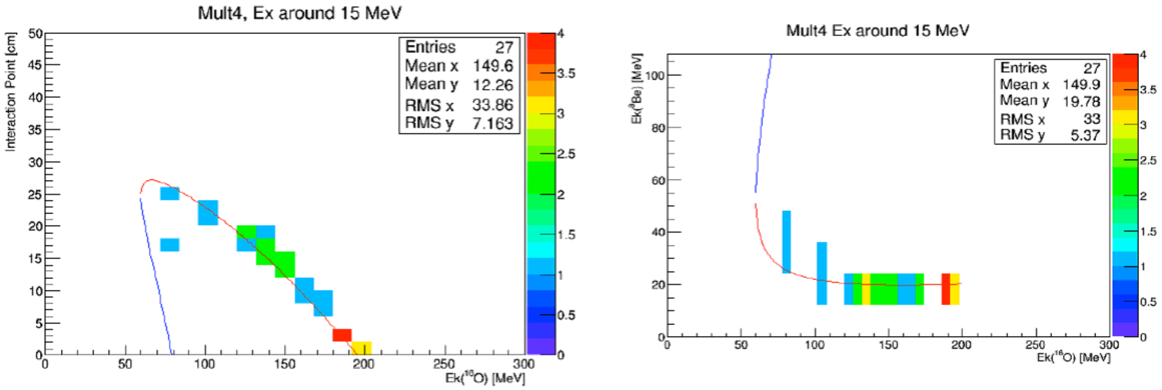

**FIG. 4.** Events in the 15 MeV peak. Left panel: reconstructed interaction point versus kinetic energy of the decaying $^{16}$O after energy loss correction. Right panel: Calculated kinetic energy of the undetected $^8$Be as a function of the kinetic energy of the $^{16}$O. In both panels, the lines show the corresponding kinematic calculation.

The data analysis is still in progress to finalize the result. Higher statistics is necessary to reduce the statistical error.

[1] K. Ikeda, N. Takigawa, and H. Horiuchi, Prog. Theor, Phys. Suppl. Extra Number **E68**, 464 (1968).
[2] W. von Oertzen, M. Freer, and Y. Kanada-Eńyo, Phys. Rep. **432**, 43 (2006).
[3] C. Beck, EPJ Conference Series **436**, 012014 (2013).
[4] K. Artemov *et al.*, Sov. J. Nucl. Phys. **52**, 406 (1990).
[5] M. Barbui *et al.*, Eur. Phys. J. Web of Conferences **66**, 03005 (2014).
[6] M. Barbui *et al.*, Eur. Phys. J. Web of Conferences **117**, 07013 (2016).
[7] M. Freer *et al.*, Phys Rev C **51**,1682 (1995).
[8] E.G. Adelberger *et al.*, Nucl. Phys. **A143**, 97 (1970).
[9] Y. Funaki *et al.*, Phys. Rev. Lett. **101** 082502 (2008).
[10] Tz. Kokalova *et al.*, Phys. Rev. Lett. **96**, 192502 (2006).

# Ternary fission fragment yield analysis in $^{124}$Sn+$^{112,124}$Sn at 26*A* MeV

J. Gauthier, M. Barbui, X. Cao, K. Hagel, J.B. Natowitz, R. Wada, and S. Wuenschel

An analysis of the data set coming from 26*A* MeV $^{124}$Sn on $^{112}$Sn and $^{124}$Sn targets acquired by the NIMROD heavy ion detector [1] is underway. These data are being used to perform studies of the reaction products and thus the emission sources [2] in order to better characterize the charge and the isotopic yields of the fragments emitted in ternary fission processes [3] at high temperature and excitation energy. A better understanding of this phenomenon should help to improve the characterization of the reaction dynamics [4].

The initial analysis focuses on global features of the reaction. The data set is composed of 33 runs combining 26,000,000 events. The linearization [5] of those data is now completed [6] and the particle identifications have been generated for every detector. Fig. 1 shows the isotopic fractional yields from detected hydrogen to oxygen fragments for both $^{112}$Sn and $^{124}$Sn targets. As one should expect, the more neutron rich system tends to produce more neutron rich isotopes. The yields are also in very good agreement with previous measurements shown in reference [2].

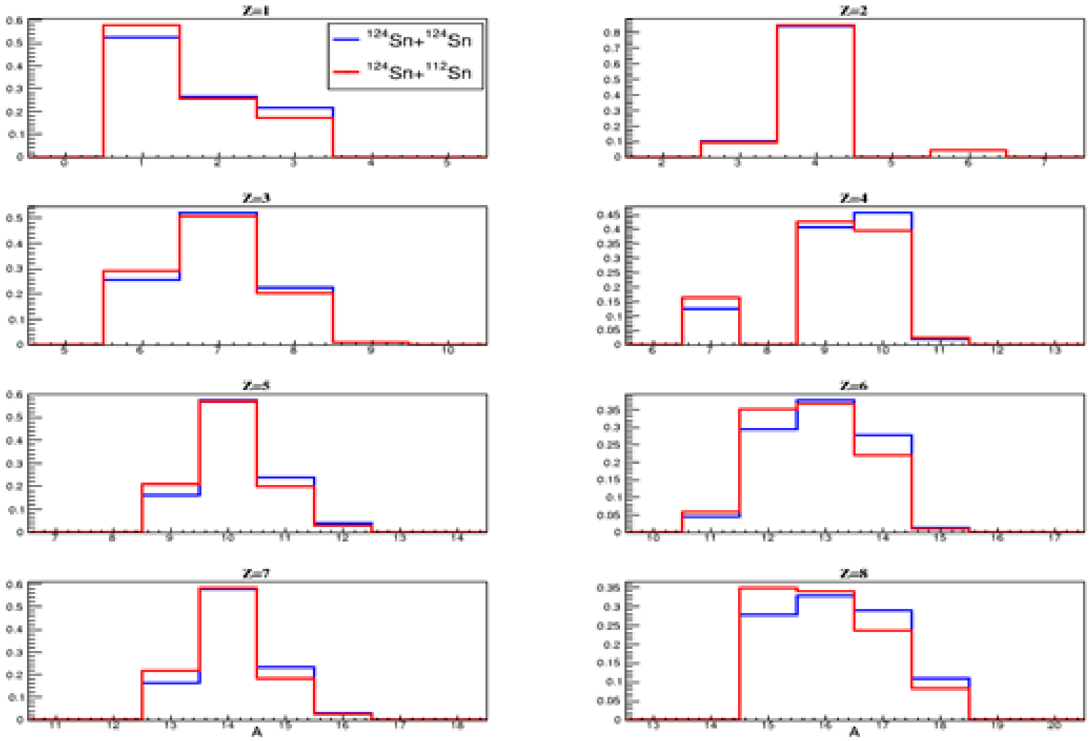

**FIG. 1.** Isotopic fractional yields up to Z=8 for $^{112}$Sn and $^{124}$Sn targets.

The Si-Si super telescope energy calibration using the punch through energy points and SRIM stopping power calculations [7] is also completed. Using the HIPSE (Heavy Ion Phase Space Exploration) event generator [8], we can compare the energy and velocity distributions as we can see in Fig. 2. The addition of the degrader foil introduces a much higher threshold than what we see in the experimental data. It has to be noticed that the upper Z cut in the experimental data is induced by detector gain saturation and not by a detection threshold.

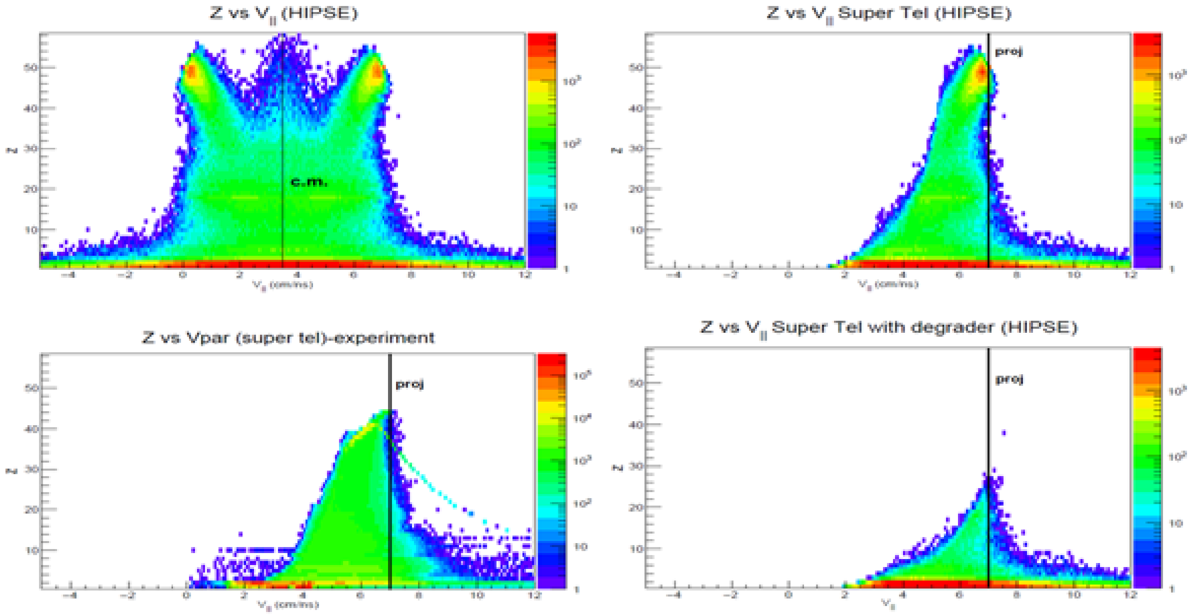

**FIG. 2.** HIPSE and experimental charge vs. parallel velocity comparison. Up-left: HIPSE not filtered. Up-right: HIPSE filtered.

Most of the experimental energy distributions match those of the HIPSE calculation very well especially for high Z fragments. Fig. 3 shows a sample of these energy comparisons for Z=17 to 23 in ring #3. Moreover, we have seen that experimental Z ratios and angular distributions are also in generally good agreement with the HIPSE generated data set.

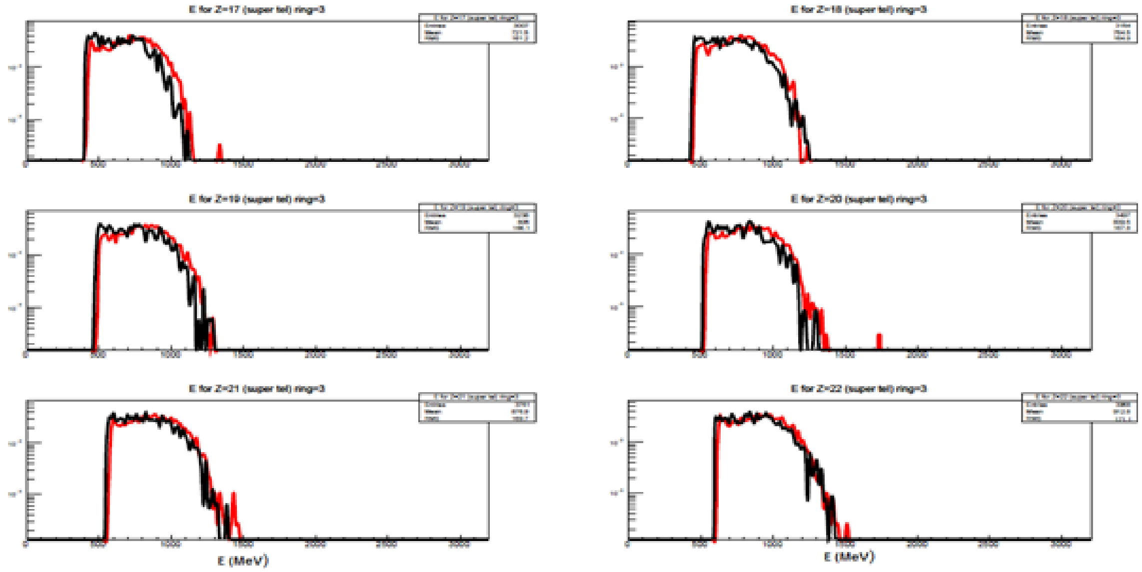

**FIG. 3.** Energy spectra for 16<Z<23 in Si-Si-CsI(Tl) super telescopes (ring 3). The black line represents experimental calibrated energy, and the red line is for HIPSE filtered data.

In order to select only peripheral and mid-peripheral collisions, which is mandatory for this analysis, we used HIPSE to test some variables sensitive to the impact parameter [9]. As one can see in Fig. 4, a selection on the highest charge detected fragment ($Z_{max}$) combined to a parallel velocity cut on this fragment efficiently remove most of the central events while minimizing fluctuations that would occur with the use of other variables that require complete event detection (such as multiplicity, total transverse energy, flow angle, etc.).

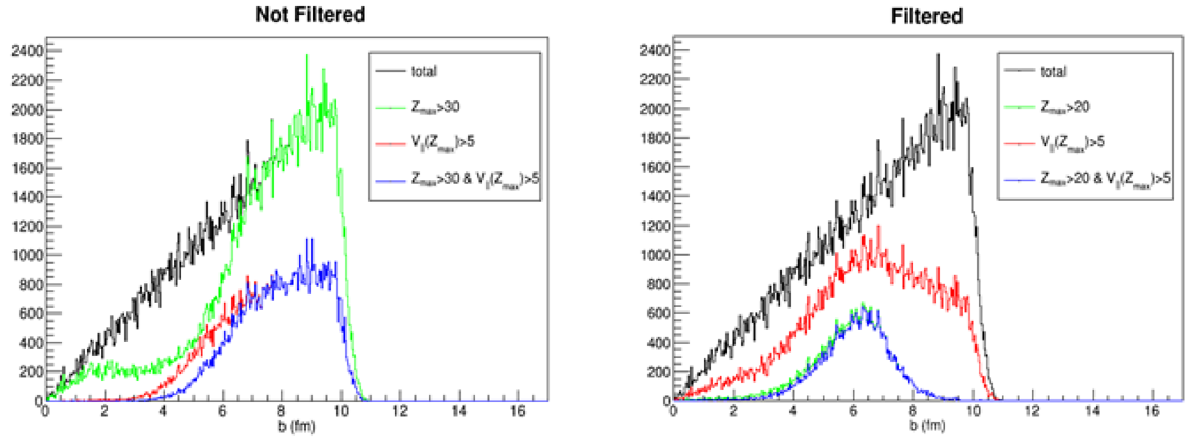

**FIG. 4.** Effect of $Z_{max}$ and $V_{||}(Z_{max})$ selection on the impact parameter (HIPSE data).

Parallel velocity will also be a useful tool for selecting emission sources and preliminary results show that the values given by the super telescopes are suitable. In Fig. 5, we can see multiplicity distributions and average parallel velocities as a function of the charge for fragments having a parallel velocity either lower or higher than 5 cm/ns and these results are in agreement with a forward projectile-like-fragment source and a mid-rapidity emission.

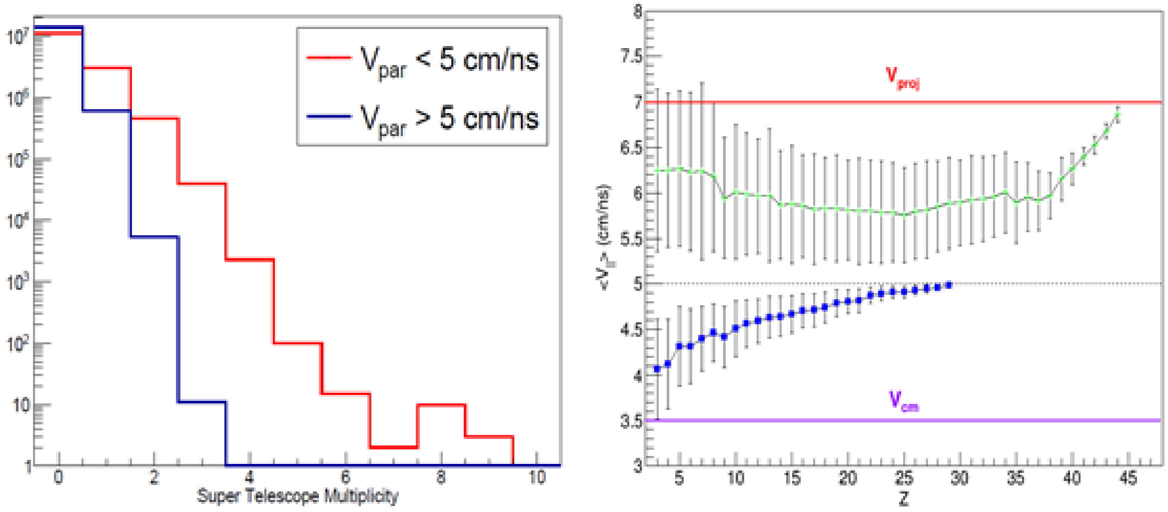

**FIG. 5.** Left: Multiplicity in the super telescopes for $V_{||} < 5$ (red) and $V_{||} > 5$ cm/ns (blue). Right: average parallel velocity as a function of Z for $V_{||} < 5$ (blue) and $V_{||} > 5$ cm/ns (green).

The next and final steps will be to complete the energy calibrations for the Si-CsI(Tl) telescopes and the light particles in the CsI(Tl) in order to be able to achieve a suitable emission source selection for every fragment of interest and then a good quality yield analysis. Analysis of ternary events will then proceed.

[1] R. Wada *et al.*, Nucl. Phys. News, **24**, 28 (2014).
[2] D.V. Shetty *et al.*, Phys. Rev. C **68**, 054605 (2003).
[3] S. Wuenschel *et al.*, Phys. Rev. C **90**, 011601, (2014).
[4] M.A. Famiano *et al.*, Phys. Rev. Lett. **97**, 052701 (2006).
[5] L.W. May *et al.*, *Progress in Research*, Cyclotron Institute, Texas A&M University (2007-2008), p. II-26.
[6] J. Gauthier *et al.*, *Progress in Research*, Cyclotron Institute, Texas A&M University (2014-2015), p. II-29.
[7] J.F. Ziegler *et al.*, Nucl. Instrum. Methods Phys. Res. **B268**, 11 (2010).
[8] D. Lacroix *et al.*, Phys. Rev. C **69**, 054604, (2004).
[9] J. Peter *et al*., Nucl. Phys. **A519**, 611 (1990).

## Searching for high-spin toroidal isomers in collisions induced by α-conjugate nuclei

X.G. Cao, K. Schmidt, E.-J. Kim, K. Hagel, M. Barbui, J. Gauthier, M. Huang, J.B. Natowitz,
R. Wada, S. Wuenschel, G.Q. Zhang, H. Zheng, N. Blando, A. Bonasera,
G. Giuliani, M. Rodrigues, C. Botosso, and G. Liu

Nuclei in the valley of stability are usually treated as a fluid made of nucleons with sphere-like geometry in their ground states. However, correlations between nucleons and cluster formation play more important roles in excited nuclei. For light excited α-conjugate (even-even N=Z) nuclei, the importance of α clusters is apparent in both theoretical calculations and experimental observables.

Wheeler suggested that nuclear liquid can assume toroidal shapes under certain conditions [1]. Wong et al. quantitatively discussed where the existence of a toroidal nucleus and its stability against sausage deformation [2, 3]. In light α-conjugate nuclei the α particle can be expected to be important in the toroidal configuration which leads to a reduced nuclear density. Heavy ion collisions induced by light α-conjugate nuclei may provide the appropriate conditions to access toroidal isomers with high angular momentum and excitation energy. The toroidal isomer may manifest itself by decaying into α particles or α-like fragments (where the α-like fragments refer to α, $^{12}$C, $^{16}$o, and $^{20}$Ne etc.). Therefore, an experimental exploration with special attention and methodology into observing α-like decays is indicated and very intriguing.

A series of experiments were carried out at Texas A&M University Cyclotron Institute with $^{40}$Ca and $^{28}$Si beams at 10, 25, 35 MeV/u provided by the K500 superconducting cyclotron incident on $^{28}$Si, $^{12}$C, $^{40}$Ca, and $^{181}$Ta targets [4], respectively. The combinations with different α-conjugate projectiles ($^{28}$Si and $^{40}$Ca) and targets ($^{12}$C, $^{28}$Si, and $^{40}$Ca) may favor population of different α cluster states. The reaction products were detected using a $4\pi$ array, NIMROD-ISiS (Neutron Ion Multidetector for Reaction Oriented Dynamics with the Indiana Silicon Sphere), which consisted of 14 concentric rings covering from $3.6^\circ$ to $167^\circ$ in the laboratory frame. In addition, the neutron ball surrounding the NIMROD-ISiS charged particle array provided information on average neutron multiplicities for different selected event groups. The preliminary analysis of parts of the raw data was accomplished by C. Bottosso, E-J Kim, and K. Schmidt *et al.* [4] and some interesting preliminary results about the α-like mass (Almass) emission have been obtained for $^{40}$Ca+$^{40}$Ca [5]. Here we focus on cluster decay from $^{28}$Si and check its dependence on $^{12}$C, $^{28}$Si and $^{181}$Ta targets [6].

For the $^{28}$Si+$^{12}$C reaction, a total of 17 million events were recorded and a significant proportion of events have significant alpha-like mass emission. Half a million events have Almass=28. There are 7 alpha-like decay channels with Almass=28 as shown in Fig. 1. For the most interesting event group: 7 α decay channels, more than 10 thousand events are obtained.

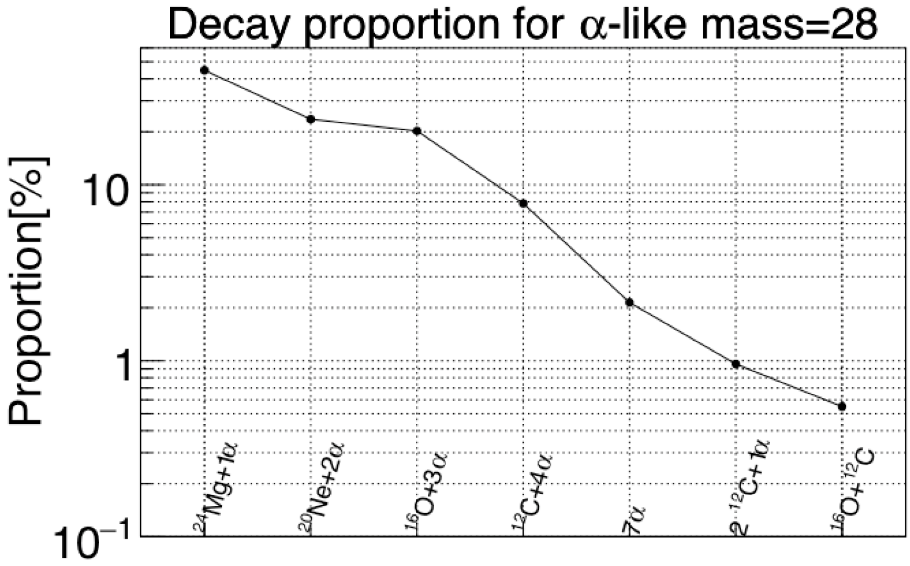

**FIG. 1.** The proportion of decay channels for Almass=28 from $^{28}$Si+$^{12}$C @ 35MeV/u.

The hierarchy effect, which refers to a correspondence between fragment mass and parallel velocity, was found for α-like fragments from $^{40}$Ca decay [5]. For most of the $^{28}$Si channels this hierarchy effect is also observed. The angles between α and heavier fragments are shown in Fig. 2. The αs tend to

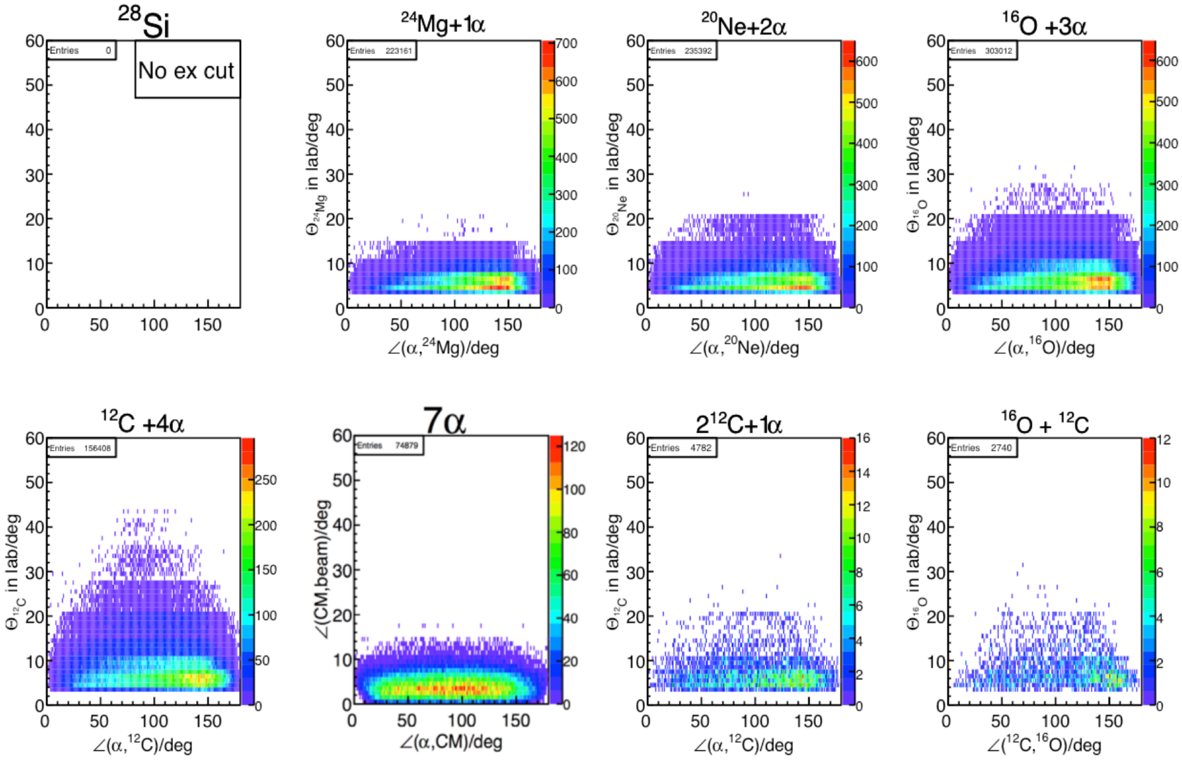

**FIG. 2.** The emission angle between α and heavier fragment for the α-like decay channels. For the 7 α channel, the angle is calculated between center-of-mass velocity and the velocity of α particles.

be emitted backward relative to the large fragment, indicating they mainly come from the neck region. This means absence of complete equilibrium of the α-like emission source.

In order to explore the configuration of the possible toroid formed in the dynamical stage, we utilize a shape analysis technique to diagnose the source shape in momentum space [7]. Shape analysis is a popular method to study emission patterns of sources, dynamical aspects of multifragmentation and collective flows of particles in relativistic heavy ion collisions. A tensor constructed on the momenta can be written as: $T_{ij} = \sum_{\nu=1}^{N} p_i^{\nu} p_j^{\nu}$, where N is the total nucleon number, $p_i^{\nu}$ is the momentum component of $\nu^{\text{th}}$ nucleon in the center-of-mass and i refers to the Cartesian coordinate. The tensor can be diagonalized to reduce the event shape to an ellipsoid. The eigenvalues of the tensor: $\lambda_1$, $\lambda_2$, and $\lambda_3$, normalized by: $\lambda_1 + \lambda_2 + \lambda_3 = 1$ and ordered according to: $\lambda_1 \leq \lambda_2 \leq \lambda_3$ , can quantitatively give shape information of the events. The sphericity is defined as: $S = \frac{3}{2}(1 - \lambda_3)$, and coplanarity is defined as: $S = \frac{\sqrt{3}}{2}(\lambda_2 - \lambda_1)$. In the sphericity-coplanarity plane, the ideal rod, disk and sphere events exactly locate at the three vertexes of the triangle: (0,0) (3/4, $\sqrt{3}/4$), and (1,0), respectively. A schematic figure of shape analysis is shown by Fig. 3.

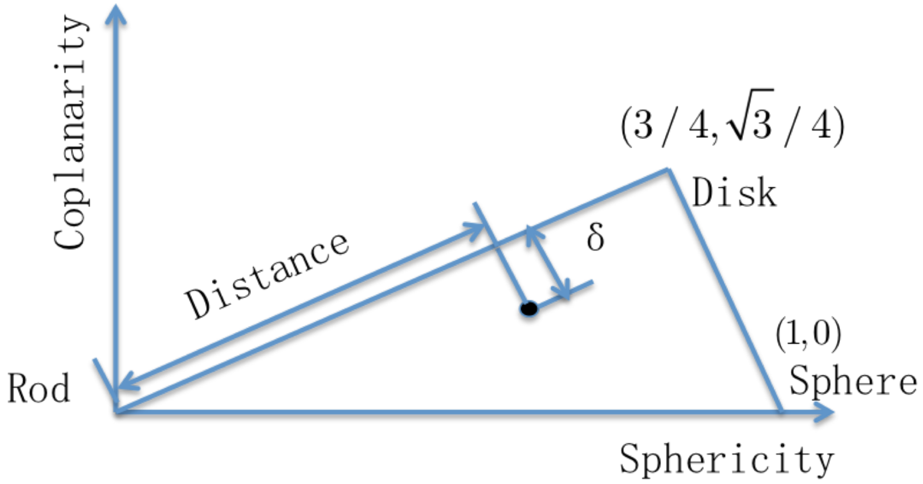

**FIG. 3.** A schematic figure illustrating the shape analysis method, where the δ and distance definitions are used in Fig. 5.

The results of the shape analysis are shown in Fig. 4. events. Two fragments will always have a rod shape in momentum space while three fragments can form a plane or rod shape. We can see there are always some events located around the disk point, which may be the toroidal candidates, especially for the 7 α channel.

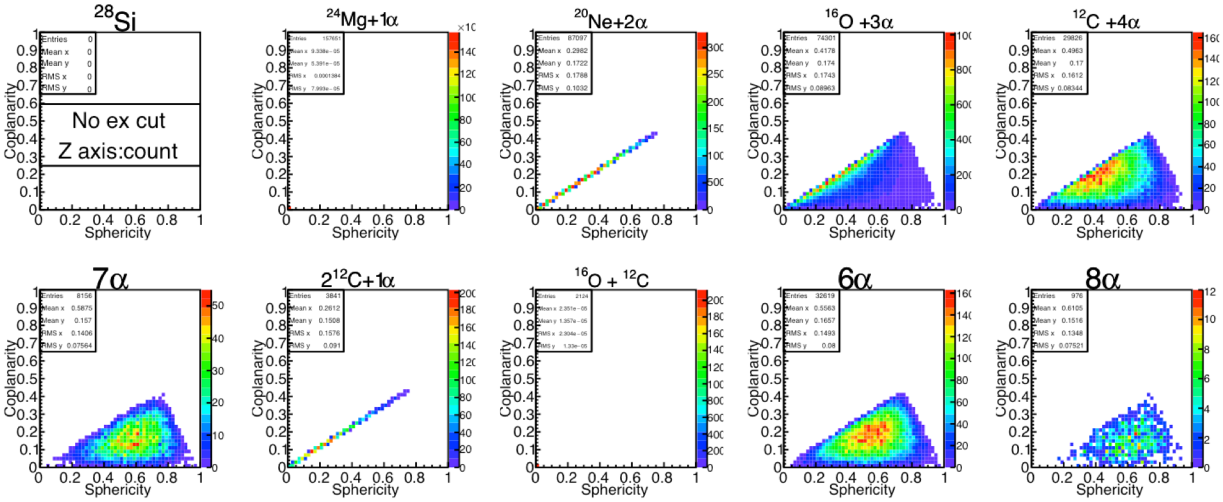

**FIG. 4.** Shape analysis of sources decaying by Almass.

We extract the excitation energy of source decaying by Almass by scanning around the rod-disk line. The extracted excitation energy is shown in Fig. 5, with cut labeled: $\delta \in [0,0.05]$ and $distance \in [0.4,0.6]$, where the $\delta$ and distance are defined in Fig. 3. For our most interesting channel: 7 α, there are several peaks near the 143.18 MeV energy predicted by Staszczak and Wong's [3]. They predicted this to be a 44 $\hbar$ $^{28}$Si isomer corresponding to a toroidal configuration. The 6 α and 8 α channels are included for comparison. For the 6 α channel, there are no obvious peaks. For the 8 α channel, at least one α would have to come from the target-like fragment (TLF). The statistics are low and this suggests that the 7 α we analyzed may be relatively free of contributions from decay of the target-like fragment (TLF).

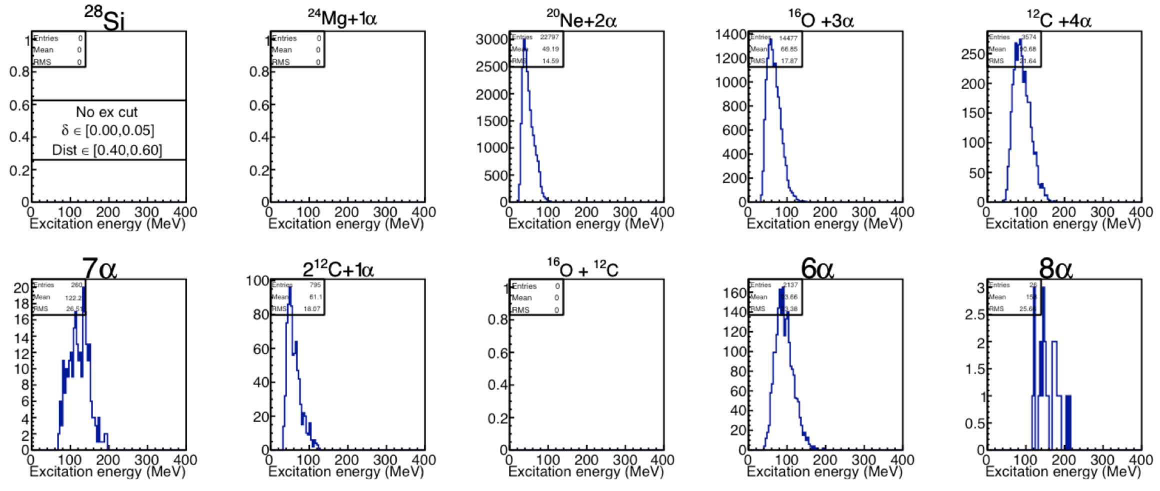

**FIG. 5.** Excitation energy of Almass source with cut on sphericity-coplanarity plane.

A determination of the angular momentum of Almass source is necessary to pin down the toroidal candidate. Such a determination is difficult. Antisymmetrized molecular dynamics (AMD) simulations are in progress.

Similar results are seen for the $^{28}$S+$^{28}$Si, and $^{28}$Si+$^{181}$Ta systems at 35MeV/u. However, the statistics for the $^{28}$Si+$^{181}$Ta reaction is much lower than for the other two systems.

[1] G. Gamow, Biography of Physics, Harper & Brothers Publishers, New York, 1961, 297 pp.
[2] C.Y. Wong, Phys. Lett. **41B**, 446 (1972); C.Y. Wong, Phys. Rev. C **17**, 331 (1978).
[3] A. Staszczak, C.Y. Wong, Phys. Lett. B **738**, 401 (2014).
[4] K. Schmidt *et al.*, *Progress in Research*, Cyclotron Institute, Texas A&M University (2010-2011), p. II-8; C. Bottosso *et al.*, *Progress in Research*, Cyclotron Institute, Texas A&M University (2008-2009), p.II-7.
[5] K. Schmidt *et al.*, *Progress in Research*, Cyclotron Institute, Texas A&M University (2011-2012), p. II-7; *Progress in Research*, Cyclotron Institute, Texas A&M University (2012-2013), p. II-17; *Progress in Research*, Cyclotron Institute, Texas A&M University (2013-2014), p. II-18.
[6] X.G. Cao *et al.*, *Progress in Research*, Cyclotron Institute, Texas A&M University (2014-2015), p. II-16.
[7] J. P. Bondorf *et al.*, Phys. Lett. B **240**, 28 (1990).

## Surveying deep inelastic multi-nucleon transfer for creation of super- and hyper-heavy elements

S. Wuenschel, M. Barbui, X. Cao, J. Gauthier, K. Hagel, S. Kowalski, Z. Majka, J.B. Natowitz,
K. Schmidt, Z. Sosin, R. Wada, A. Wieloch, and G. Zhang

Recent advances in the super heavy element experimental reaction program have followed two tracks. The first approach has been to employ the current active catcher array, composed of fast plastics, to acquire a better data set. The second approach has been to develop a second generation active catcher array. The new array design is the product of carefully studying the most interesting results in the existing data and the previous detector shortcomings.

In the first active catcher experiment, the data suffered from three major issues. First, the time required for the silicon detectors to generate a trigger exceeded the waveform recorded for the active catcher detectors. Secondly, the fast plastic detectors proved to be incapable of differentiating alpha particles from fission fragments and degraded beam. Finally, the high beam rate necessary for accessing the low cross sections for production of heavy and super heavy elements exceeded the capability of the passive bases and resulted in unstable gain in the photomultiplier tubes.

A second fast plastic based active catcher experiment was conducted in the Fall. This experiment was able to correct some of the previous issues. The times in the active catcher and silicon detectors were calibrated. This required changes in the silicon triggering behavior, but resulted in a well-defined region where exit peaks should be found in the the active catcher waveforms. Additionally, the active catcher detectors were better gain matched throughout the array. Finally, both high and low beam intensity runs were taken.

Throughout the last year, we have studied alternate detector materials for the active catcher array. We determined that Yttrium aluminum perovskite (YAP) is the most suitable replacement material. YAP is radiation hard, has light decay constants in the ns range, and has two components to its light output. The two components of the light output make pulse shape discrimination (PSD) possible. We have confirmed the suitability of YAP during two test runs. Fig. 1 depicts the PSD available in the proposed YAP/PMT/active base configuration. Fig. 2 depicts the time correlation of events leaving the active catcher and being observed in the IC-Si modules (x-axis). When plotted against the Si energy (y-axis), a band emerges that is correlated to the flight times of alphas from the active catcher to the Si detector.

A second generation active catcher array is currently under construction. It will employ 40 YAP/PMT/active base modules. These modules will provide the PSD necessary to differentiate alpha decay from alphas emitted during fission or as the result of scattered beam reactions with the active catcher. The addition of newly constructed active bases will provide a factor of ~1,000 in increased beam intensity relative to the previous bases before gain shifting occurs.

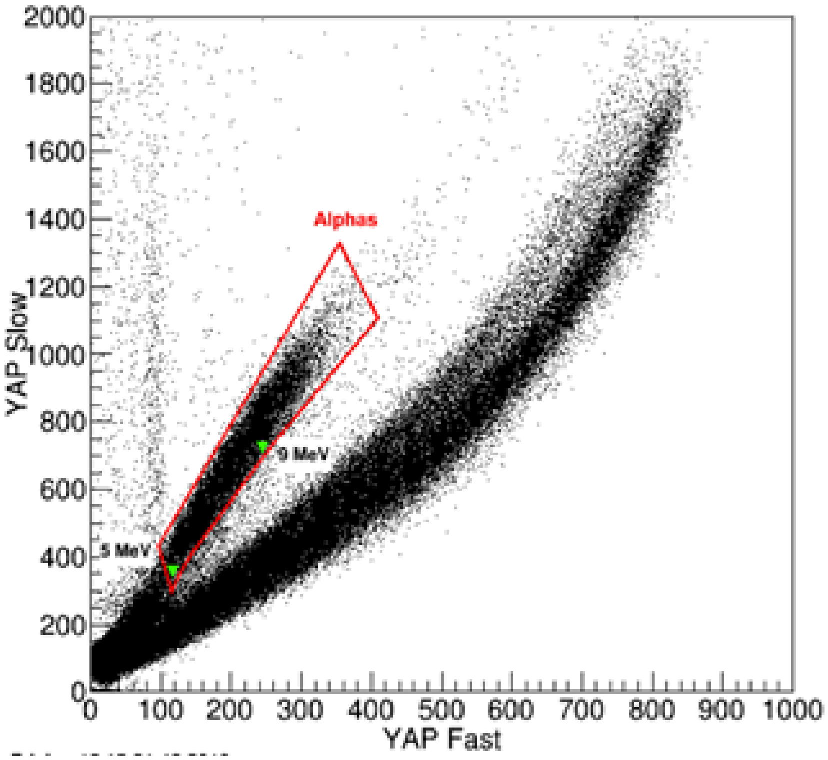

**FIG. 1.** YAP fast light output vs YAP slow light output. Approximate positions of Th228 alpha peaks are shown for reference.

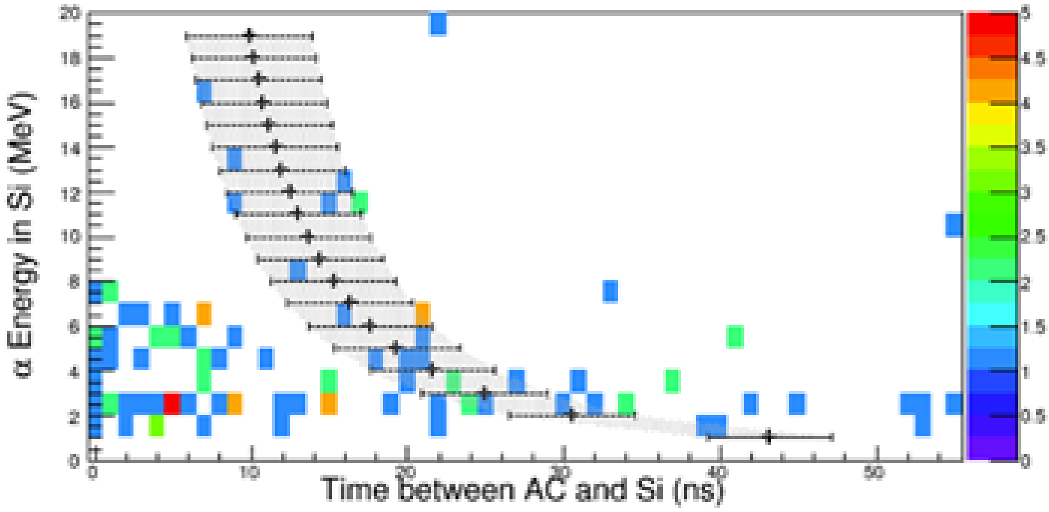

**FIG. 2.** The x-axis is the time difference between the signals observed in the active catcher module and the silicon module. The y-axis is the energy observed in the Si detector. The shaded region is the flight time (±4ns) for an alpha of a given energy.

Additionally, we have changed the waveform digitizers that will be used for the active catcher array. The new array will employ Struck SIS3316 digitizers (FADCs). These FADCs have a minimum 4ns bucket size but appropriate experimental conditions can reduce the the time resolution to ~1ns. These digitizers also offer new capabilities in triggering. The SIS3316 digitizers are capable of acquiring waveforms up to 32M samples long. This roughly translates to 1/8 s in wave form. Finally, the waveforms may be shifted to provide up to 64us of history prior to the trigger.

# Production mechanism of high energy protons at intermediate heavy ion collisions

R. Wada, X. Liu, W. Lin, and M. Huang

In experiments, high energy proton emission has been observed at intermediate heavy ion reactions. The energy of the ejected protons often exceeds more than 4 times of the incident beam energy per nucleon. Coniglione *et al.* reported the energetic proton emissions in $^{40}$Ar + $^{51}$V at 44 MeV/nucleon using the MEDEA detector array and compared the energy spectra to those of BNV calculations [1]. In their BNV, Fermi distribution with a sharp cut off is incorporated as the Fermi motion of the nucleons, neglecting the stability of the initial nuclei, and suggested that the Fermi motion is a possible origin for the observed high energy protons. Germain et al. reported high energy proton emissions in $^{36}$Ar + $^{181}$Ta collisions at 94 MeV/nucleon [2]. In the analysis, a BNV code is used to calculate the density of nucleons during the time evolution and collisions are made in a perturbed way, using the calculated nucleon density. Since they cannot reproduce the high energy proton spectra by the two collision process alone, they added a three body collision process in their calculation and concluded that the three-body collision term takes a significant role to reproduce the observed high energy proton spectra.

We report here the results of AMD simulations in which the Fermi motion is taken into account explicitly in the nucleon-nucleon collision process in addition to the fluctuation in the dynamical time evolution of the wave packets through a diffusion process which has been built in in the ordinal AMD. The modified code is called AMD-FM. In AMD, each nucleon is expressed by Gaussian distributions in coordinate and momentum space. The wave packets propagate in a given mean field by solving classically the Vlasov equation using the centroid of the Gaussian wave packet. The width of the Gaussian distribution is partially taken into account in the quantum branching, called a diffusion process. In addition to that, in AMD-FM, the momentum fluctuation is added as a Fermi boost in the collision process. When two nucleons are at the collision distance Sqrt($\sigma_{NN}$)/π, a momentum fluctuation along the Gaussian distribution is added for each nucleon as

$$\boldsymbol{P}_i = \boldsymbol{P}_i^0 + \Delta \boldsymbol{P}'_i \quad (i = 1, 2)$$

where

$$\begin{aligned} \Delta \boldsymbol{P}'_i &= \sqrt{\left(\frac{|\Delta \boldsymbol{P}_i|^2}{2M_0} - T_0\right) 2M_0}\,\frac{\Delta \boldsymbol{P}_i}{|\Delta \boldsymbol{P}_i|} \\ \Delta P_{i\tau} &= \hbar\sqrt{\nu}(rho/\rho_0)_i^{1/3} G(1) \end{aligned}$$

here $P_i^0$ is the centroid of the Gaussian distribution, and G(1) is a random number generated along the Gaussian distribution, with Σ = 1. $T_0$ ~ 10 MeV being the expectation value of the average energy of the Gaussian distribution and subtracted to avoid the double counting between the diffusion process and collision process.

First, we compare the experimental results of $^{40}$Ar+$^{51}$V at 44 A MeV with those of the ordinal AMD and CoMD calculations. The results are shown in Fig.1. In CoMD, a process is added to QMD to prevent the violation of the Pauli principle in the wave packet propagation in time in a stochastic manner.

Different from AMD, in CoMD the Fermi motion is explicitly taken into the initial ground state nuclei. When the initial nuclei are prepared, the momentum is assigned to each nucleon under a local Fermi Gas assumption with a sharp cut off momentum. In order to get the enough stability during calculations with a proper binding energy of these nuclei, the nuclei are further cooled by a friction method. Therefore the momentum distribution becomes much smaller values in the initial nuclei. In AMD, the centroid of the wave packet of the Gaussian distribution in the initial nuclei is set to nearly zero. This means that the initial nuclei are "frozen" and makes the initial nuclei stable in time. One should note that, in the results of AMD, the calculated spectra have slightly harder slopes than those of CoMD, even though the initial nuclei are ”frozen” in the AMD calculation. This enhancement is caused from the diffusion process discussed earlier.

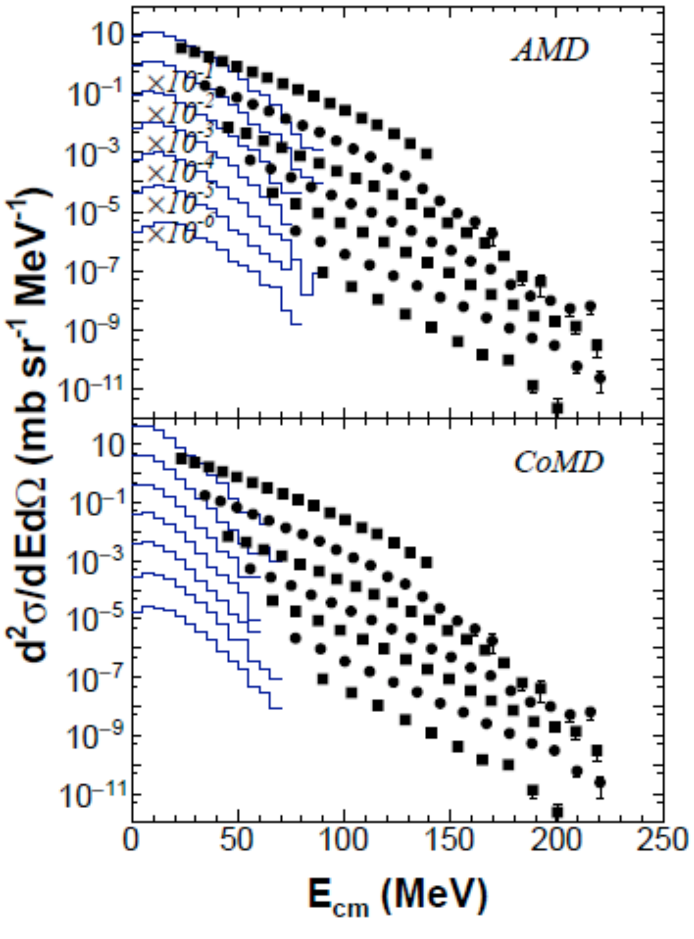

**FIG. 1.** The Center of Mass frame proton energy spectra of AMD (Top), CoMD (Bottom) in an absolute scale are compared with the experimentally observed inclusive data for 40Ar + 51V at 44 MeV/nucleon at θ = 72◦, 90◦, 104◦,116◦, 128◦, 142◦ and 160◦ from top to bottom. The experimental data are taken from Ref. [1].

Fig. 2 shows the comparisons between the experimental proton energy spectra and those of AMD-FM with b = 0−5fm in (a) and b = 0−9fm in (b) in an absolute scale. The experimental data are inclusive. A few hundred thousand events have been generated for AMD-FM calculation. No afterburner is used for this comparison. The results for b = 0 − 5fm can reproduce the experimental data pretty well. If we take the impact parameter range of b = 0 − 9fm, the calculated cross sections become about twice larger at four forward angles.

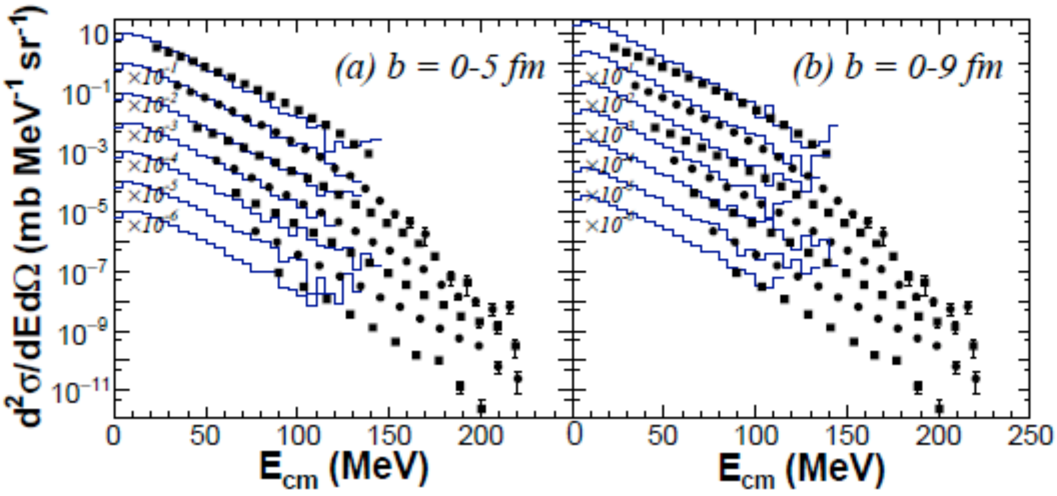

**FIG. 2.** Proton energy spectra of the AMD-FM calculation for b = 0 - 5fm (a) and b = 0 9fm (b) are compared in an absolute scale with the experimentally observed inclusive data of $^{40}$Ar + $^{51}$V at 44 MeV/nucleon. See also the figure caption of Fig.1.

This comparison confirms that, at 44 MeV/nucleon, the high energy protons are solely generated by the Fermi boost, which is characterized by the Gaussian distribution with sigma ~80 MeV/c.

It is interesting to extend the comparisons at higher incident energies. The high energy protons are generated at an early stage of the collisions where the nuclear density is high. If the three body collisions contribute, the contribution comes more significant at higher incident energy, because the three body collisions occur in proportion to the third power of the nuclear density whereas the two body collisions to the second power. In order to test the validity of AMD-FM at higher incident energies, the experimental data of $^{36}$Ar + $^{181}$Ta at 94 MeV/nucleon by Germain et al. [2] are used. The experimental data are inclusive, and therefore the impact parameter range of b = 0 − 9fm is used for the AMD-FM calculation. The calculated proton energy spectra with AMD-FM at 75° (red histogram) and 105° (green histogram) are plotted in Fig. 3 in the laboratory reference frame together with those of the experiment (full symbols) in an absolute scale. Though the statistic is still not enough for detailed comparisons, one can see that the slopes of the experimental energy spectra are well reproduced by AMD-FM for both of angles as well as the amplitudes. This comparison indicates that the high energy protons observed at 94 MeV/nucleon originates essentially from the co-play of the Fermi boost in the diffusion and collision processes. However, from this analysis, we cannot exclude the necessity of the three body collision term, but the contribution is small even if it contributes some.

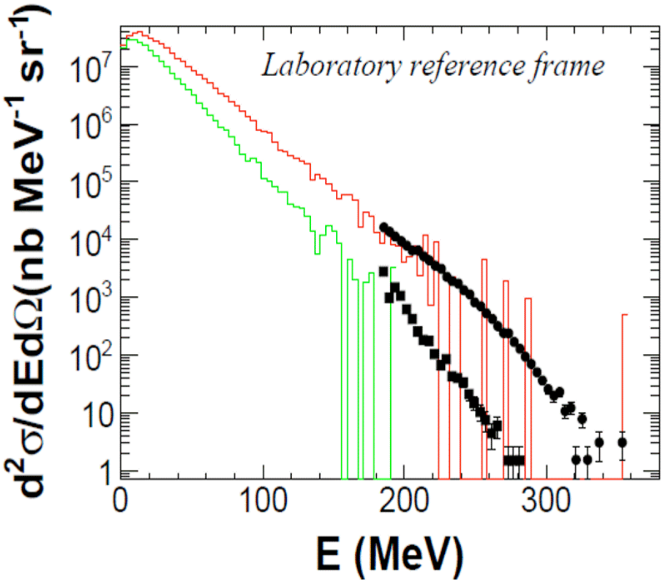

**FIG. 3.** Proton energy spectra of the AMD-FM calculation for b ≤ 9fm (histograms) are compared in an absolute scale with the experimentally observed inclusive data of $^{36}$Ar + Ta at 94 MeV/nucleon (dots) at 75° and 105° in the laboratory frame.

[1] R. Coniglione *et al.*, Phys. Lett. B **471**, 339 (2000).

[2] M. Germain *et al.*, Nucl. Phys. **A620**, 81 (1997).

# Total reaction cross section measurement and neutron density distribution in light stable and radioactive nuclei

R. Wada, W. Lin, P. Ren, I. Tanihata, and D.T. Tran

This experimental study aims to determine the neutron density distribution in light isotopes, especially very neutron rich isotopes. Such data would provide a mean not only to distinguish skin type and hallo type nuclei, but also enable to extract the parameters of their neutron density distribution.

Neutron density distribution of light exotic nuclei has been studied experimentally and theoretically in the last 30 years using total reaction cross section (TRCS) measurements. However, there are still large uncertainties, because the contributions from the halo or skin of neutron distributions in TRCS are rather small, and in order to eliminate such ambiguities, precise measurements with accuracy of an order of 1% are necessary.

The basic idea of this study based on the fact that the contribution of the nuclear matter distribution to TRCS depends on the incident energy. In order to illustrate this, we performed simple calculations, using the Glauber model. Fig. 1 shows the calculated ratios of TRCS of hypothetical skin- or halo-type $^{14}$C nucleus relative to that of $^{12}$C are shown as a function of the incident beam energy. When we use the same diffuseness parameter for $^{14}$C (we call it a skin type $^{14}$C) as $^{12}$C, the ratio stays flat from 10 – 1000 MeV/nucleon range. In Fig. 1, line (a) and line (b) show the absolute cross section increase in proportional to the RMS radius. On the other hand when we use a halo-type $^{14}$C with a larger diffuseness, then the ratio starts to increase below 100 MeV/nucleon as shown in line (c). This is because, at high energy regime, the total reaction cross section is determined mainly by the nuclear interaction near the

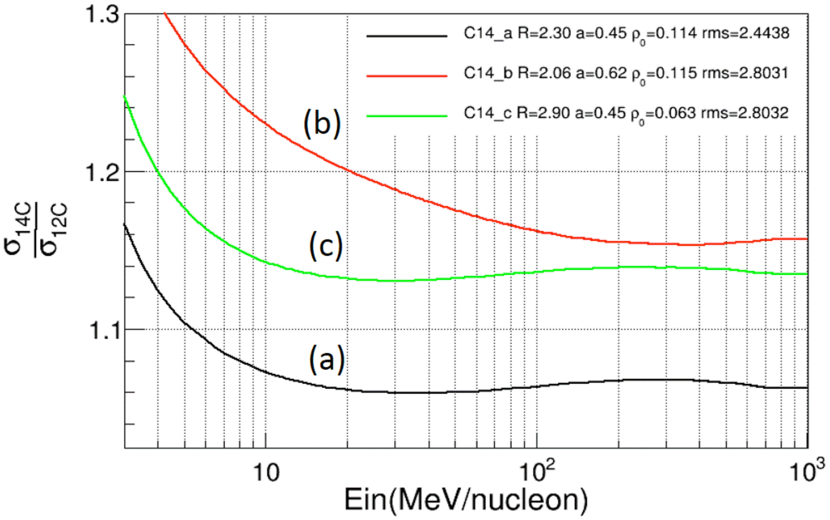

**FIG. 1.** Calculated ratios of the total reaction cross section of hypothetical skin- or halo-type $^{14}$C nucleus relative to that of $^{12}$C are shown as a function of the incident energy.

surface around the RMS radius, but at lower energy regime, the neutron distribution at large radius makes a notable contribution to TRCS because of nucleon-nucleon collisions. This exercise indicates that if one can measure the excitation function of TRCS below 100 MeV/nucleon with a sufficient accuracy, one can determine the neutron density distribution at larger radius experimentally. One should note that the increment of the TRCS at 100 MeV/nucleon and at 20 MeV/nucleon is an order of 5 % or less. Therefore in order to distinguish the differences, the accuracy of an order of 1 % is necessary for the TRCS measurements.

The first experiment was performed in 2014 at RCNP, Osaka University, in Japan, using the secondary beams. $^{22}$Ne beam were bombarded on $^{9}$Be target at F0 at 80 A MeV. The generated secondary beams were delivered to the detector system shown in Fig.2, using two dipole magnets between F1-F2 and F2-F3. The isotope identification of the incident isotopes before the target is performed by three time of flight measurements between PPACS and plastic detector and the energy loss in the Si detector right before the target. The identification of the isotopes after the target is made by MUSIC (MUlti-Sampling Ionization Chamber) and the energy is measured by NaI. MUSIC detector was used in order to avoid the channeling effect in Si detector, which often caused significant background for the isotope identification.

Typical particle identifications before the target and after the target are shown in Fig.3. TRCS. $\sigma_R$, is calculated by the following formula,

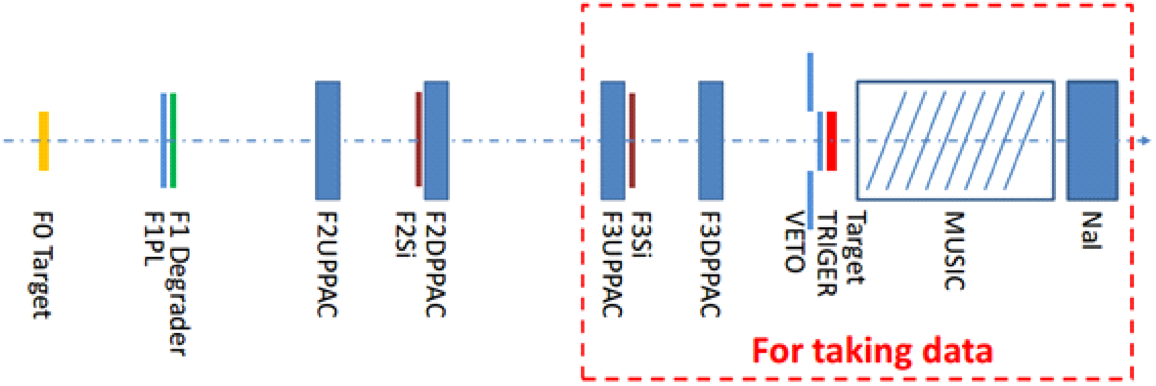

**FIG. 2.** Schematic view of the beam line and detector system.

$$\sigma_R = \frac{1}{t} ln\left[\frac{\gamma_0(1-P_{m0})}{\gamma(1-P_m)}\right]$$

$\gamma=N_{out}/N_{in}$ is with the target and $\gamma_0$ is that without the target. N is the number of isotope before the target (in) and after the target (out). t is the target thickness. $P_m$ *and* $P_{m0}$ are the correction factors for the inelastic scattering loss in the target and the elastic loss in the MUSIC chamber.

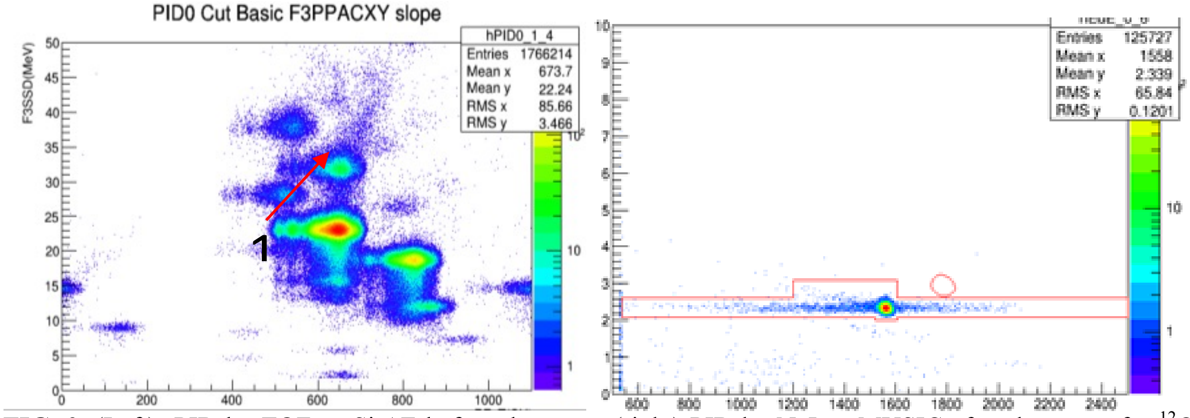

**FIG. 3.** (Left) PID by TOF vs Si-ΔE before the target (right) PID by NaI vs MUSIC after the target for $^{12}$C run.

The inelastic loss is evaluated by comparing the NaI energy spectra with and without the target runs as shown in the left panel of Fig.4. Blue histogram is the spectra with target and red one is without. Both spectra are normalize at the elastic peak. On the right the elastic loss is evaluated using 8 segments of the MUSIC chamber and NaI. ΔN is the counts difference between the two consecutive segments in the MUSIC chamber. The highest yield at ~ 5° is the difference between the last segment of MUSIC and NaI. The red curve is the predicted yields from the Rutherford (Mott) scattering. Further data analysis is underway.

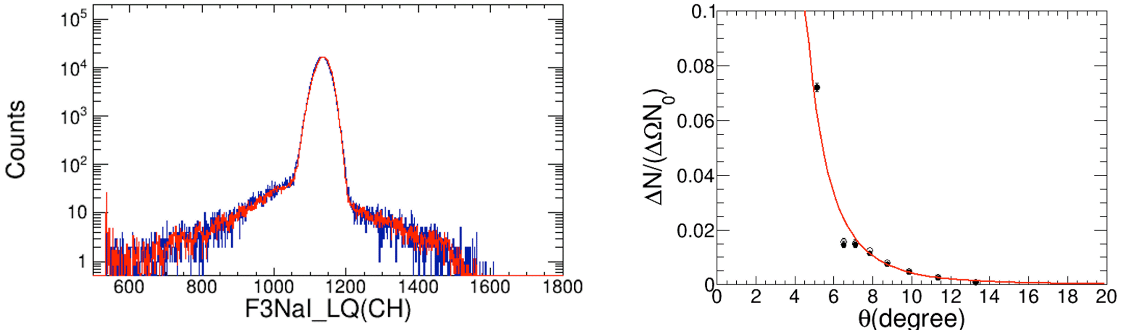

**FIG. 4.** (Left) Energy spectra with (blue) and without (red) target runs for *Pm* correction. (Right) Elastic scattering loss in the MUSIC chamber and NaI after the target for *Pm0* correction. Both are from $^{12}$C run.

# Dynamical transport model and freezeout concept at intermediate heavy ion reactions

R. Wada, X. Liu, W. Lin, and M. Huang

In the intermediate heavy ion collisions, intermediate mass fragments (IMFs) are copiously produced through a multifragmentation process. Isotope distribution of these IMFs, especially their widths, is mainly governed by the symmetry energy at the density and temperature of the fragment formation. In other words, the isotope distribution can be used as a probe for the density and temperature of the hot fragmenting nuclear matter through the symmetry energy.

To model the multifragmentation process, a number of different models have been developed in two distinct scenarios at this energy range. One is based on a transport model, in which nucleon propagation in a mean field and nucleon-nucleon collisions under Pauli-blocking are two main ingredients. No thermal or chemical equilibrium are assumed for IMF production. The other is based on a statistical multifragmentation under thermal and chemical equilibriums at a freezeout volume. These two modelings are quite different, but they can account reasonably well for many characteristic properties experimentally observed. In transport models, simulated events for a given reaction system show large fluctuations in space and time for the formation of IMFs. This large fluctuation causes difficulty in identifying a unique freezeout volume and time on an event by event basis. However, there are some evidences that statistical equilibrations are established before or at the time of the IMF production when the observables are averaged over many events.

In a series of our recent works [1-4], the isotopic yield ratio method has been applied to extract the density and temperature of the fragmenting source. In the present study, we apply the same method to AMD events in a wider incident energy range. AMD events are generated for central collisions (b = 0 fm) of $^{40}$Ca + $^{40}$Ca at 35, 50, 80, 100, 140, and 300 MeV/nucleon, using Gogny interactions having different density dependencies of the symmetry energy term, i.e., the standard Gogny interaction which has an asymptotic soft symmetry energy (g0), another with an asymptotic stiff symmetry energy (g0AS), and the other with an asymptotic superstiff symmetry energy (g0ASS). For each set of parameters, more than 10,000 events are generated up to t = 300 fm/c and IMFs are identified at that time with a coalescence technique with the radius of Rc = 5 in the phase space.

The extracted density and temperature values in the incident energy range of 35 to 300 A MeV are summarized in Fig. 1. The extracted density values (filled circles) are plotted together with the maximum density created during the collisions (open circles) in (a). The maximum density values are calculated at the origin of the center of mass system and normalized by the density of the initial nuclei at t = 0 fm/c . They increase monotonically from ρ/ρ0 ∼ 1.3 at 35 MeV/nucleon to ∼1.8 at 300 MeV/nucleon. On the contrary, the extracted density values for the fragmenting source distribute at ρ/ρ0 is ∼0.65 to 0.7. The extracted temperature values (red dots connected by lines) in (b) [and (c)] show also more or less a constant distribution, and T0 values of 5.9 to 6.5 MeV are obtained. These flat distributions of the extracted density and temperature values indicate that IMFs are in average formed at a later stage when the hot nuclear matter reaches at a “freezeout” volume by the expansion. This freezeout volume is not assumed in any transport models, but assumed generally in statistical multifragmentation models.

These results have been published in Phys.L Rev. C **92**, 014623 (2015).

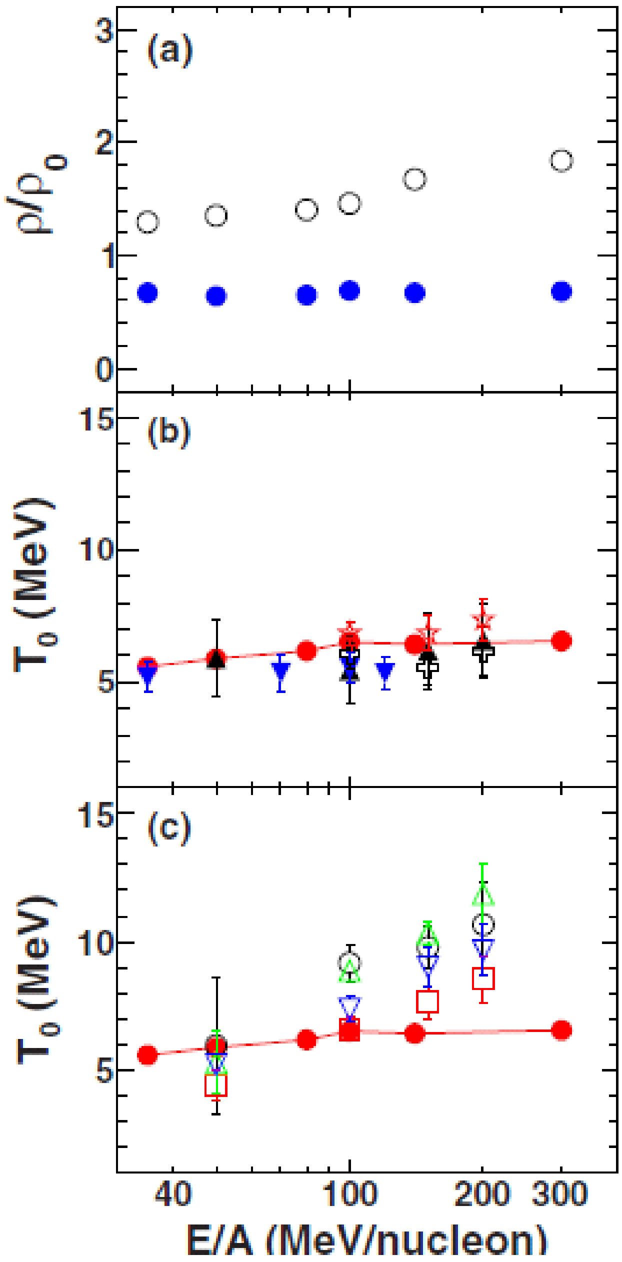

**FIG. 1.** (a) Extracted ρ/ρ0 values (filled circles) and the maximum ρ/ρ0 values (open circles) as a function of the incident energy. (b) Extracted T0 values from the final rounds (red dots connected by lines). Filled triangles (black) and filled inverted triangles (blue) are taken from Serfling et al. and Xi et al., respectively. Open cross and starts are the results from CLi and CC thermometer. (c) The extracted results and those of double ratio thermometers mostly related to the H and He isotopes except BeLi. Those are BeLi (black circles), Hedt (red squares), HeLi (green triangles), and tHeLiBe (blue inverted triangles).

[1] W. Lin *et al.*, Phys. Rev. C **89**, 021601(R) (2014).
[2] X. Liu *et al.*, Phys. Rev. C **90**, 014605 (2014).
[3] X. Liu *et al.*, Nucl. Phys. **A933**, 290 (2015).
[4] W. Lin *et al.*, Phys. Rev. C **90**, 044603 (2014).

# Chemical potential and symmetry energy for intermediate mass fragment production in heavy ion reactions near Fermi energy

X. Liu, W. Lin, M. Huang, R. Wada, J. Wang, A. Bonasera, Z. Chen, S. Kowalski, T. Keutgen, K. Hagel, L. Qin, J. B. Natowitz, T. Materna, P.K. Sahu, M. Barbui, C. Bottosso, and M.R.D. Rodrigues

Ratios of differential chemical potential values relative to the temperature, $\Delta\mu/T=(\mu_n-\mu_p)/T$, extracted from isotope yields of thirteen reaction systems at 40 MeV/nucleon are compared to those of a quantum statistical model to determine the temperature and symmetry energy values of the fragmenting system.

In a series of our recent works [1-4], the isotopic yield ratio method has been applied to extract the density, temperature, and symmetry energy of the fragmenting source. In the present study, the experimentally extracted $\Delta\mu/T$ values are compared with the Quantum statistical model [5] to determine the temperature and symmetry energy of the fragmenting system. The experimental $\Delta\mu/T$ values are extracted based on the Modified Fisher Model.

The experiment was performed at the K-500 superconducting cyclotron facility at Texas A&M University. The system studies are $^{64,70}$Zn and $^{64}$Ni beams were used to irradiate $^{58,64}$Ni, $^{112,124}$Sn, $^{197}$Au, and $^{232}$Th targets at 40 MeV/nucleon. 13 reaction systems were analyzed for the present work.

The experimentally observed $\Delta\mu/T$ values are shown in Fig.1 as a function of the Z/A value of the nucleon-nucleon system, which are evaluated from the moving source fit of all ejected particles, including neutrons. When fragments are emitted from the source, many of them are in excited states and cool by evaporation processes before they are detected. The sequential decay of these primary hot

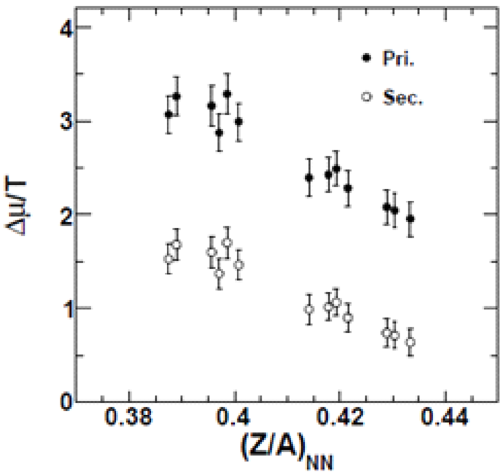

**FIG. 1.** Open circles: the $\Delta\mu/T$ values from the experimentally observed IMF yields from all 13 systems as a function of $(Z/A)_{NN}$. Full circles: the "primary" $\Delta\mu/T$ values with the sequential decay correction.

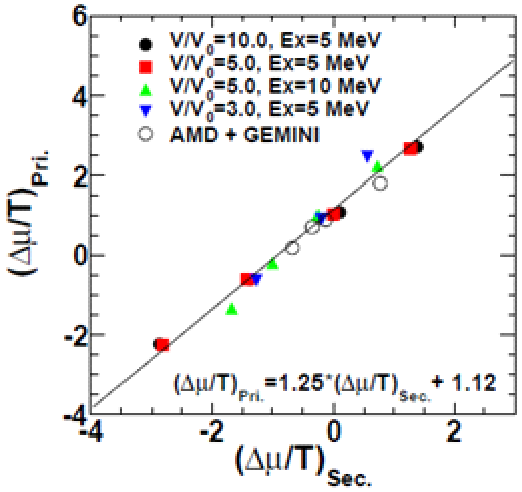

**FIG. 2..** Calculated primary $\Delta\mu/T$ vs secondary $\Delta\mu/T$. The results from the SMM calculations are shown by solid symbols and those from the AMD-GEMINI are shown by open circles.

fragments significantly alters the yield distribution and distorts the information in the primary yields. Here the statistical multifragmentation model (SMM) is employed to evaluate the effect. The evaluated primary Δμ/T and the secondary Δμ/T ratios are shown in Fig.2. For some of the systems, the values are calculated and plotted for AMD + Gemini calculations. The calculated ratio between $(\Delta\mu/T)_{pri}$ and $(\Delta\mu/T)_{sec}$ are well fit by a linear function as

$$(\Delta\mu/T)_{Pri.} = 1.25 \cdot (\Delta\mu/T)_{Sec.} + 1.12,$$

Using this relation, the primary Δμ/T values are calculated from the experimentally extracted values (secondary) and shown in Fig.3. These results are compared with the QSM calculations [5].

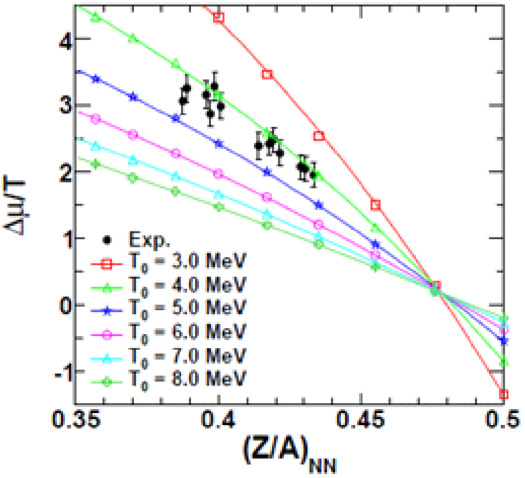

**FIG. 3.** The comparison between the Δμ/T values from the calculations with different temperature inputs from 3 - 8 MeV and the experimentally extracted primary ones. The curves are the results of polynomial fits to the calculated values for each given T value.

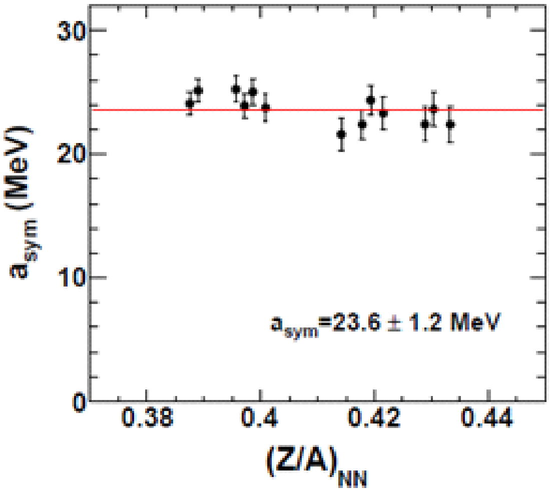

**FIG. 4.** The resultant symmetry coefficient values as a function of $(Z/A)_{NN}$. The line is the constant fit of the data points.

Within QSM, one cannot determine the density and temperature values uniquely from the experimental isotope yield ratios. In the present analysis, therefore, the source density of $\rho/\rho_0 = 0.65$ is used, which has been determined from the experimentally reconstructed primary hot isotope yields in the reaction system $^{64}$Zn+$^{112}$Sn in our previous studies [2,3]. The calculated results for different temperatures are shown together with the experimental ones in Fig.3. From these comparisons, T=4.3±0.4 MeV is extracted.

The differential chemical potential, Δμ, can be given as

$$\Delta\mu = 2 \cdot \frac{\partial(E_{total}/A)}{\partial\delta}.$$

When we approximate the total energy by a semi-classical mass formula, one can get

$$\Delta\mu = 4\delta a_{sym}(T,\rho) - a_c(\rho)A^{2/3}(1-\delta).$$

From the experiments, $\Delta\mu$ can be calculated as $\Delta\mu/T = T\bullet(\Delta\mu/T)$ from the primary $\Delta\mu/T$ values in Fig.3 and the NN- source temperature obtained above. Therefore $a_{sym}$ coefficient in the above formula can be rewritten as

$$a_{sym} = \frac{\Delta\mu + a_c(\rho)\cdot(\rho/\rho_0)^{1/3}A^{2/3}(1-\delta)}{4\delta}.$$

$a_c(\rho) = a_c(\rho_0) \bullet (\rho/\rho_0)^{1/3}$, where $a_c(\rho_0) = 0{:}67$ MeV is the Coulomb coefficient at the saturation density. The resultant $a_{sym}$ values are shown in Fig.4 as a function of (Z/A) of the NN source. From this figure $a_{sym}$= 23.6 ± 1.2 MeV is obtained.

The extracted T=4.3±0.4MeV and $a_{sym}$= 23.6 ± 1.2 MeV values are consistent to those of the previous work [3] where T=5.0±0.4MeV and $a_{sym}$= 23.1 ± 0.6 MeV are extracted together with $\rho/\rho_0$ = 0.65, using a self-consistent method from the experimental single reaction system of $^{64}$Zn+$^{112}$Sn at 40 A MeV.

[1] W. Lin *et al.*, Phys. Rev. C **89**, 021601(R) (2014).
[2] X. Liu *et al.*, Phys. Rev. C **90**, 014605 (2014).
[3] X. Liu *et al.*, Nucl. Phys. **A933**, 290 (2015).
[4] W. Lin *et al.*, Phys. Rev. C **90**, 044603 (2014).
[5] D. Hahn and H. Stöcker, Nucl.Phys. **A476**, 718 (1988).

# Characterizing neutron-proton equilibration in nuclear reactions with sub-zeptosecond resolution

A. Jedele, A.B. McIntosh, L. Heilborn, M. Huang, M. Youngs, A. Zarrella,
E. McCleskey, and S.J. Yennello

The density dependence of the asymmetry term is currently the largest uncertainty of the nuclear equation-of-state (EoS). These constraints can be probed using multi-nucleon exchange studies between the excited projectile-like fragment (PLF*) and the excited target-like fragment (TLF*). This neutron-proton (N-Z) equilibration is governed by the contact time between the colliding nuclei and the gradient of the potential driving the equilibration. Recently, N-Z equilibration within a single dynamically produced and deformed nuclear system has been observed [1-3]. The decaying PLF* has an angular distribution indicative of decay on a timescale shorter than its rotational period. The N-Z composition was observed to depend on the decay angle and thus on the lifetime, consistent with equilibration between regions of the decaying PLF*[4-8]. We present observations that the composition of the heaviest and second heaviest fragment evolve towards each other following first-order kinetics on a zeptosecond (zs) timescale.

We analyzed data from $^{70}$Zn+$^{70}$Zn, $^{64}$Zn+$^{64}$Zn, and $^{64}$Ni+$^{64}$Ni reactions at 35A MeV using the NIMROD array [3]. Events were sorted based on atomic number with charge-symmetric fragments sorted by mass. The heaviest fragment in each event was designated as **HF** and the second heaviest was designated as **LF**. To focus on N-Z equilibration in binary decays, events were required to have $Z_H \geq 12$ and $Z_L \geq 3$. A total Z cut of $Z \geq 21$ (70% of beam) and $Z \leq 32$ for all fragments was also included. Evidence that both fragments came from the PLF* comes from the velocity distribution, where the velocity of the $Z_H$ and $Z_L$ are centered above the center-of-mass velocity of the TLF* and PLF* (0.135 c). The decay angle (α) is the angle between the relative velocity ($v_{REL}$), defined as $v_H$-$v_L$, and the center-of-

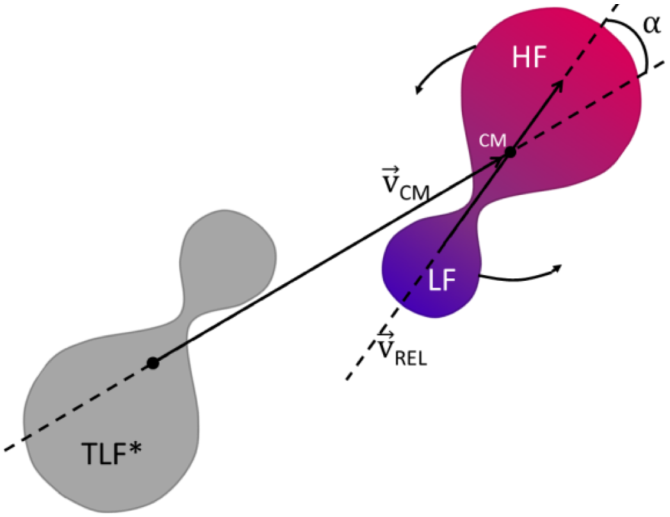

**FIG. 1.** Illustration of dynamical deformation and decay. The PLF* has rotated relative to the PLF*-TLF* separation axis ($\vec{\mathbf{v}}_{CM}$) and is about to break up into two fragments (HF and LF). The time the PLF* lives before breaking up is measured by the angle α. The color denotes the composition with blue (red) indicating relative neutron richness (deficiency).

mass velocity ($v_{CM}$) of the two fragments.

The angle α was calculated using the formula

$$\alpha = \cos^{-1}\left(\frac{\vec{v}_{REL}\cdot\vec{v}_{CM}}{\|\vec{v}_{REL}\|\|\vec{v}_{CM}\|}\right).$$

Aligned emission of the $Z_L$ in the backward direction (towards the target) corresponds to α=0°. Fig. 1 depicts α.

The angular distributions for some representative pairings of $Z_H$ and $Z_L$ are shown in Fig. 2. There are two distinct features present in all three pairings ($Z_H$=14, and $Z_L$=5, $Z_H$=14, and $Z_L$=7, $Z_H$=12 and $Z_L$=7). First, there is a flat distribution from cos(α) = -1 to cos(α) = 0, indicative of statistical decay. The slight increase in yield at cos(α) = -1 is consistent with a rotating PLF* source. Statistical decay is also evident between cos(α) = 0 and cos(α) = 1. However, the presence of a large yield peaked near cos(α) = 1 implies a second decay mechanism, specifically, dynamical decay. This finding is consistent with previous studies [4]. The strong presence of this mechanism for strongly aligned decay in which $Z_L$ is emitted in the backward direction indicates a timescale of dynamical binary splitting of the PLF* much shorter than its rotational period. As the pairings become more symmetric, the peak of the relative yield

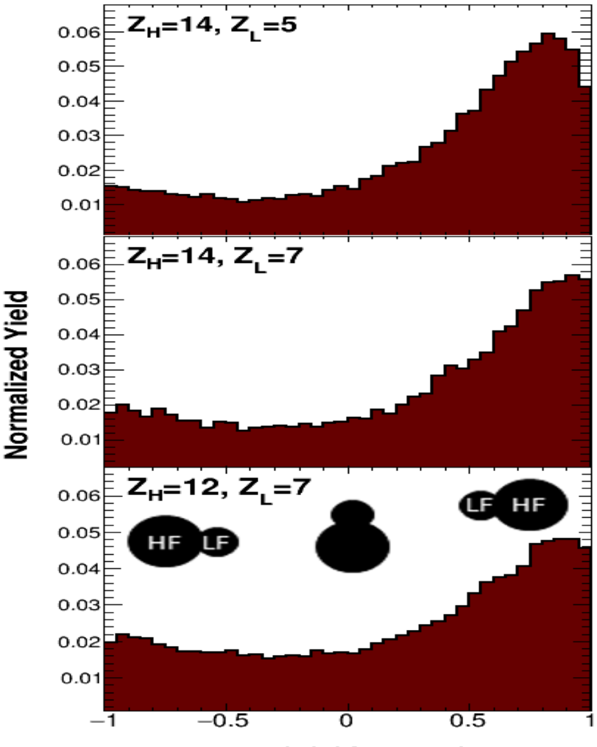

**FIG. 2.** Normalized angular distribution for representative $Z_H$ and $Z_L$ pairings. Emission of the lighter charged fragment in the backward direction (toward the target) corresponds to cos(α)=1.

for very strongly aligned backward decay decreases and broadens, suggesting a decrease in preference for immediate dynamical decay.

Next, the composition of **HF** and **LF** were examined as a function of angle. Fig. 3 depicts a maximum in the $\langle \Delta_L \rangle = \langle (N-Z)/A \rangle$ for $Z_L$ at α=0°. The composition decreases rapidly for small angles of rotation (α near 0°). As the angle increases, indicating a greater contact time, the composition levels off with most of the equilibration occurring by α=80°. A similar effect is seen in the composition of $Z_H$, however the composition starts off more neutron deficient. As the angle increases from 0° to 80°, the $\langle \Delta_H \rangle = \langle (N-Z)/A \rangle$ increases rapidly, followed by an leveling off by α=80°. This characteristic of the equilibration is consistent with first-order kinetics.

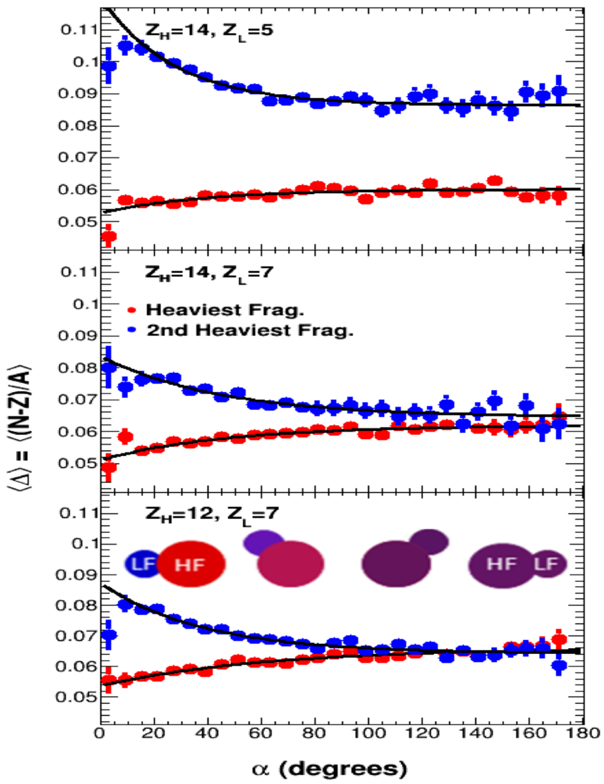

**FIG. 3.** Composition as a function of decay alignment showing equilibration for the same $Z_H$ and $Z_L$ pairings shown in Fig. 2. As the angle of rotation increases (α increases from 0°), the $\langle \Delta_L \rangle = \langle (N-L)/A \rangle$ initially decreases rapidly for $Z_L$ and increases for $Z_H$ before plateauing. The majority of equilibration occurs between 0° and ~80°.

Results are consistent with the statistical and dynamical decay mechanisms present. Due to its dynamical deformation and the presence of a velocity gradient, the PLF* tends to break apart rapidly into two fragments along the direction of its deformation. Material close to mid-velocity corresponds to fragments emitted from the neck region, which is neutron-rich [9]. If the two fragments promptly separate, the composition of **LF** will be neutron rich and **HF** will be relatively neutron poor. As the two fragments remain in contact, their densities will evolve towards each other. The asymmetries will do likewise, resulting in more similar values of $\langle \Delta_L \rangle$ and $\langle \Delta_H \rangle$.

Given the first-order kinetics picture, all $Z_H$ and $Z_L$ pairings were fit with an exponential of the form: $\langle\Delta\rangle= a+be^{-c\alpha}$. The resulting fits are shown as black lines on Fig. 3. Since the angle can be related to time, the parameter *c* can be used as a surrogate for the rate constant. The resulting fits for all 43 pairings are consistent within statistical uncertainty. The average parameter *c* was 0.03±0.01 per degree for $Z_H$ and 0.02±0.01 per degree for $Z_L$.

Next, the angle of rotation was correlated to the equilibration time through the equation:

$$t=\alpha/\omega$$

where $\omega$ is the angular frequency. The angular frequency is calculated using the equation:

$$\omega=(J\hbar)/I_{eff}$$

where J is the angular momentum and $I_{eff}$ is the moment of inertia. The moment of inertia was calculated assuming two touching spheres **HF** and **LF** of radius $r_H$ and $r_L$ respectively, rotating around their common center of mass:

$$I_{eff}=m_H r^2_{CM,H}+\tfrac{2}{5}m_H\, r^2_H+m_L r^2_{CM,L}+\tfrac{2}{5}m_L r^2_L$$

where $m_H$, $m_L$ correspond to the mass of **HF** and **LF**, respectively. $r_{H,CM}$ and $r_{L,CM}$ correspond to the center-of-mass radii of the $Z_H$ and $Z_L$. The angular momentum was obtained from GEMINI++ [10] simulations of the out-of-plane angular distribution of alpha particles. The width of the distribution (0.28), which is sensitive to the angular momentum, was recreated for L=10-50ħ for an excitation energy per nucleon of 0.8-1.2 MeV. The geometric mean of 22ħ was used for the calculations. The resulting timescales for all pairings analyzed ranged from 2 to 4 zs with an average timescale of $3\pm^{6}_{1}$ zs. The average rate constant was calculated to be 3 $zs^{-1}$, corresponding to a mean lifetime of equilibration of 0.3 zs. These results have been submitted to Phys. Rev. Lett.

[1] M.B. Tsang *et al.*, Phys. Rev. C **86**, 015803 (2012).
[2] M.B. Tsang *et al.*, Phys. Rev. Lett. **92**, 062701 (2004).
[3] Z. Kohley *et al.*, Phys. Rev. C **86**, 044605 (2012).
[4] A.B. McIntosh *et al.*, Phys. Rev. C **81**, 034603 (2010).
[5] S. Hudan *et al.*, Phys. Rev. C **86**, 02160 (2012).
[6] K. Brown *et al.*, Phys. Rev. C **87**, 061601 (2013).
[7] S. Hudan *et al.*, Eur. Phys. J. A **50**, 36 (2014).
[8] K. Stiefel *et al.*, Phys. Rev. C **90**, 061605 (2014).

# N-Z equilibration in target-like and projectile-like fragments

A. Jedele, A.B. McIntosh, L. Heilborn, A. Zarrella, and S.J. Yennello

Recent work has shown N-Z equilibration follows first-order kinetics within projectile-like fragments (PLF*) in symmetric $^{70}$Zn, $^{64}$Zn, and $^{64}$Ni reaction systems at 35A MeV. Due to the angular distribution indicative of a timescale of PLF* decay much shorter than its rotational period, the angle of rotation was used as a surrogate for time. We propose future experiments to examine the N-Z equilibration within the target-like fragments (TLF*) and PLF*.

Constrained Molecular Dynamics (CoMD) simulations were performed for $^{40,48}$Ca+$^{40}$Ca reaction systems at 10A and 15A MeV and for $^{64,70}$Zn+$^{40}$Ca reaction systems at 10A MeV. For each reaction system with the exception of $^{48}$Ca+$^{40}$Ca at 10A MeV, 10,000 events were analyzed. For each event, fragments were sorted based on atomic number. Fragments were sorted into two categories: fusion events and binary decay. Fusion events are considered events where the largest fragment had an atomic number of $Z \geq 30$ for $^{40,48}$Ca+$^{40}$Ca and $Z \geq 40$ for $^{64,70}$Zn+$^{40}$Ca and the second fragment has a $Z<10$. For the $^{40,48}$Ca+$^{40}$Ca reaction systems at 15A MeV, approx. 15% of all events were fusion events. The number of fusion events was 18-20% for the reaction systems at 10A MeV. For the binary decay events, the two biggest fragments were required to have a $Z>10$. The TLF* was designated as the fragment with the smaller velocity in the laboratory frame; the PLF* has a greater velocity. The average multiplicity for each reaction system, with the exception of the $^{48}$Ca+$^{40}$Ca at 10A MeV, was six. The $^{48}$Ca+$^{40}$Ca reaction system had an average multiplicity of five. However, the width of the distribution was greatest for the

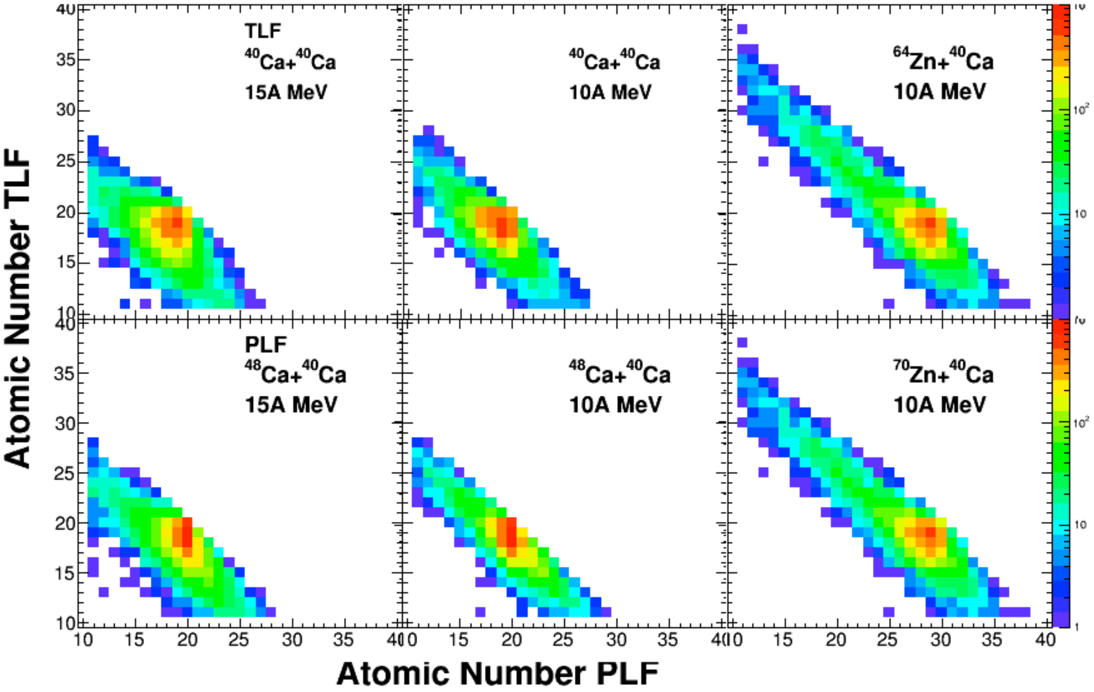

**FIG. 1.** The atomic number of the TLF* and the PLF* for all six reaction system. The neutron-poor systems are on the top row and the neutron-rich systems are on the bottom row. The largest yield corresponds to loss of 1-2 protons per fragment.

$^{40,48}$Ca+$^{40}$Ca reaction system at 15A MeV. The maximum for this system was 18. The $^{40,48}$Ca+$^{40}$Ca reaction system at 10A MeV has the smallest width and a maximum multiplicity of 14. The composition of the fragments was examined as seen in Fig. 1. The largest yield for each reaction system corresponded to loss of 1-2 protons per TLF* and PLF*. The spread in the Zn+$^{40}$Ca reaction is due to the 10 proton difference between Zn (Z=30) and Ca (Z=20). A similar trend was observed for the mass of the TLF* and PLF*. The yield was peaked on a loss of 3-4 nucleons.

Looking at the velocity distribution, the PLF* is located above center of mass velocity (v/c=0.07 for 10A MeV reaction systems and v/c=0.09 for 15A MeV reaction systems). The velocity of the TLF* is below the center of mass velocity. The majority of the TLF* and PLF* are located at v/c=0, which is the initial velocity of the target fragment, and at the beam velocity (v/c=0.15 for 10A MeV reaction systems and v/c=0.18 for 15A MeV reaction systems), respectively.

For detector design, the energy-angle correlation was examined. The results are shown in Fig. 2. There are two areas of concentration corresponding to the different fragments. For the PLF*, the majority lies between 0-10° with the range expanding slightly for the lower energy reaction systems. The grazing angle for the reactions at 10A MeV is 9° and 6° for the 15A MeV reactions. This presents a challenge for detector design since most of the PLF* fall within the grazing angle. The PLF* also has significantly

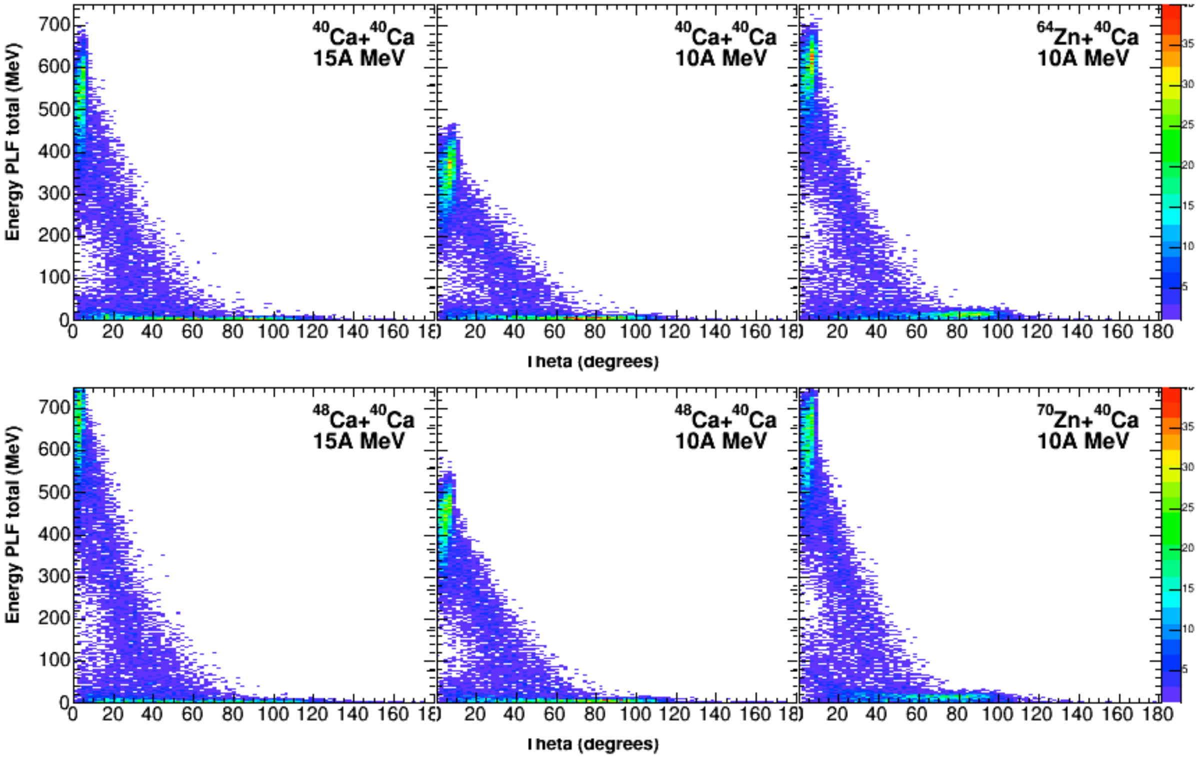

**FIG. 2.** Energy vs. theta. The top row corresponds to the neutron-poor reaction systems; bottom to the neutron-rich. The large concentration at high energy and small angles corresponds to the PLF*. The TLF* is located between 0-120° and under 50 MeV.

higher energy than the TLF* with energies around 9-14A MeV. The energy of the TLF* is below 10 MeV for the $^{40,48}$Ca+$^{40}$Ca at 15A MeV. For the lower energy systems, the TLF* increases in energy. However, most PLF* still have an energy below 10 MeV. By changing the projectile from Ca to Zn, the energy of the TLF* was increased to 20 MeV. This increases the likelihood of detecting the TLF*.

# Measurement of Kr+C @ 15, 25, 35 A MeV

A.B. McIntosh, L. Heilborn, M. Huang, A. Jedele, L. May, E. McCleskey, M. Youngs,
A. Zarrella, and S.J. Yennello

Previous research [1-3] has observed an asymmetry dependence of the nuclear caloric curve: increasing the neutron composition of an excited nucleus at a given excitation energy lowers its temperature. To independently verify this and to investigate this further, a new measurement was made. Beams of $^{78}$Kr and $^{86}$Kr impinged on a $^{12}$C target at beam energies of 15, 25, and 35 A MeV. Incomplete fusion of the entire Kr beam with a fraction of the carbon target dominates the cross section at these energies, though at the lowest energy there should be a measureable amount of complete fusion. The excited compound nucleus (CN) de-excites often by emitting light charged particles. The temperature of the emitting source is reflected in the emission patterns such as the kinetic energy spectra, momentum distributions and fluctuations, and yield ratios. The light charged particles are measured with the FAUST array between 1.6° and 45° relative to the beam axis. The position sensitive DADL detectors of the FAUST upgrade are used for this measurement. The CN evaporation residues are measured in the Quadrupole Triplet Spectrometer (QTS) where their time of flight (TOF), energy loss (ΔE), and total energy (E) is measured.

Fig. 1 shows the ΔE vs TOF distribution for heavy residues produced in reactions of $^{86}$Kr + $^{12}$C @ 25A MeV. Since the energy loss (ΔE) of a particle is proportional to $Z^2/v^2$, the bands of data observed

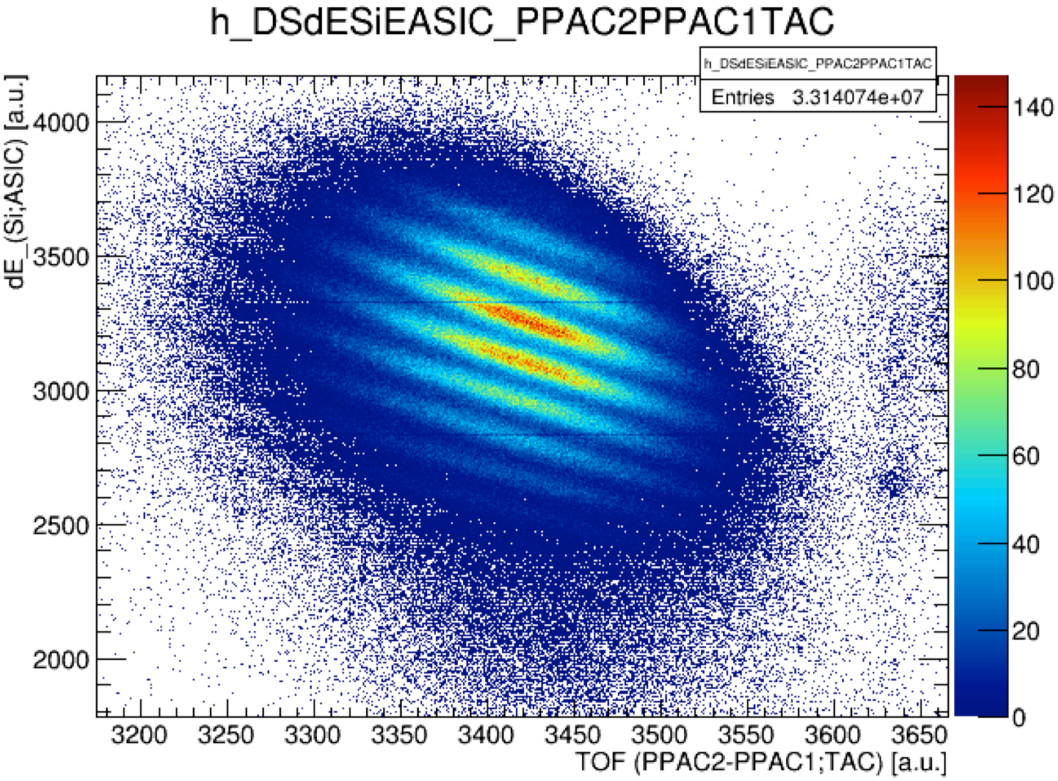

**FIG. 1.** Energy loss vs time of flight spectrum for evaporation residues measured in the QTS. Z resolution is obtained.

here correspond to different atomic numbers. Clearly unit Z resolution is obtained. Similarly, by correlating the total energy with the time of flight, mass information may be obtained. However, the single most important piece of data that can be obtained is the velocity, or more specifically the velocity damping. This contains information of how much of the carbon target fused with the projectile, which then determines the excitation energy and composition. The QTS was tuned significantly below the rigidity of the beam in the region where production cross-section for residues of interest maximized. The trigger for these events was at least one charged particle in FAUST, and with this trigger the yield of elastically scattered beam particles in the data stream is hugely suppressed. A small contribution of spurious events with a particle in FAUST and a beam particle in the QTS are observed (E=2640,ΔE=2700).

Fig. 2 shows a typical ΔE vs E distribution from FAUST. Isotopes of light charged particles can clearly be resolved.

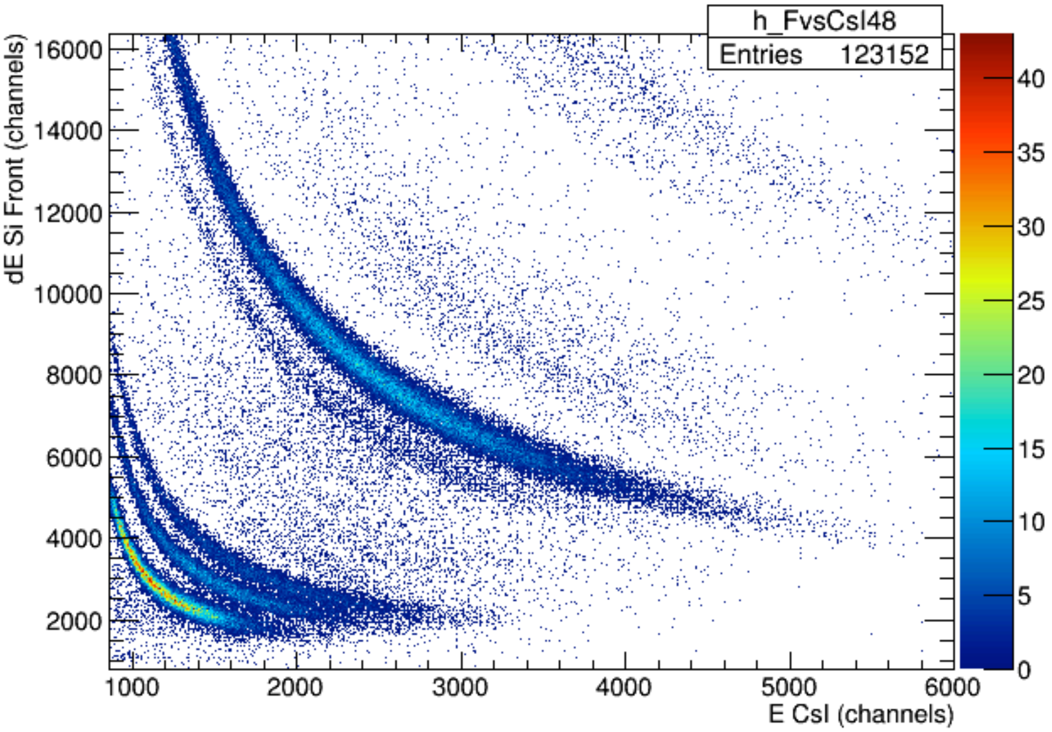

**FIG. 2.** ΔE (Si) vs E (CsI) in FAUST. Isotopes of Z=1 and Z=2 are clearly separable, and some Z=3 resolution can be seen as well.

The calibration of this data set is underway. Once complete, the data will be useful for other analyses in addition to that mentioned above. Correlation functions exploring the space-time properties of emitting source can be examined. These correlation functions may also allow us to study Coulomb and nuclear tidal forces acting on short-lived clusters. The evolution of the reaction mechanism with the incident beam energy may also be interesting and addressable in this data set.

This work is supported by the Department of Energy (DE-FG02-93ER40773) and the Welch Foundation (A-1266).

[1] A.B. McIntosh *et al.*, Phys. Lett. B **719**, 337 (2012).
[2] A.B. McIntosh *et al.*, Phys. Rev. C **87**, 034617 (2013).
[3] A.B. McIntosh *et al.*, Eur. Phys. J. A **50**, 35 (2014).

## Identifying requirements in the experimental design and analysis for isoscaling

M. Youngs, A.B. McIntosh, L. Heilborn, A. Jedele, L.W. May, E. McCleskey,
S.J. Yennello, and A. Zarrella

Isoscaling is a technique that has been used in many experiments to investigate bulk systematic trends in experimental results such as in multifragmentation [2-5], evaporation [6-8], deep inelastic collisions [8-10] and fission [11-12] experiments. The isoscaling behavior is also seen in the results of transport model calculations[13-14]. At its most basic level, isoscaling investigates the ratio of the number of particles of a given isotope emitted from two reactions as a function of proton and neutron number as such

$$R_{21} = \frac{\int \frac{dM_2}{dE}}{\int \frac{dM_1}{dE}} = C \exp(\alpha N + \beta Z). \quad (1)$$

This method of analysis is primarily used when the two reactions systems vary primarily between isospin content. We wished to investigate some of the differences between the light and heavy fragments in regards to isoscaling. To do so we used the thesis data taken by Z. Kohley and described in Reference [1]. This experiment detected fragments from both $^{64}$Zn+$^{64}$Zn and $^{70}$Zn+$^{70}$Zn (system 1 and 2 respectively in Equation (1)) at 35 MeV per nucleon using the 4π NIMROD array. This system was chosen due to the similar nature of the reaction and a relatively wide range in isospin content.

Many of the results of this analysis can be seen in Fig. 1. This figure shows the experimental isoscaling results for all detected particles on the left, projectile-like (PLF) fragments in the center and light emitted fragments on the right. For this analysis the PLF was determined to be the heaviest measured particle in an event. The emitted fragments are defined to be any particle that is not a PLF. Fig. 1 contains elements from boron (black circles on the left) through calcium (black squares on the right) as well as the fits to determine the value for α. The top row performs a global fit where all elements are used to find a single value while the bottom row fits each element individually.

The isoscaling analysis suggests that the ratio of these particles should be linear when plotted on a semi-log scale. This is actually a truncated form where there should also be higher order terms. A curvature in the data can be seen particularly for high Z elements showing this behavior. In order to reduce the effect of the higher orders and in order to compare our results to previous experimental results we limited our fits to only include the three most abundantly measured isotopes of any element. These are represented in Fig. 1 by the solid points, while the open points are provided as a demonstration of the effect. An identical treatment was performed to fit the β value for different isotopes of constant neutron number.

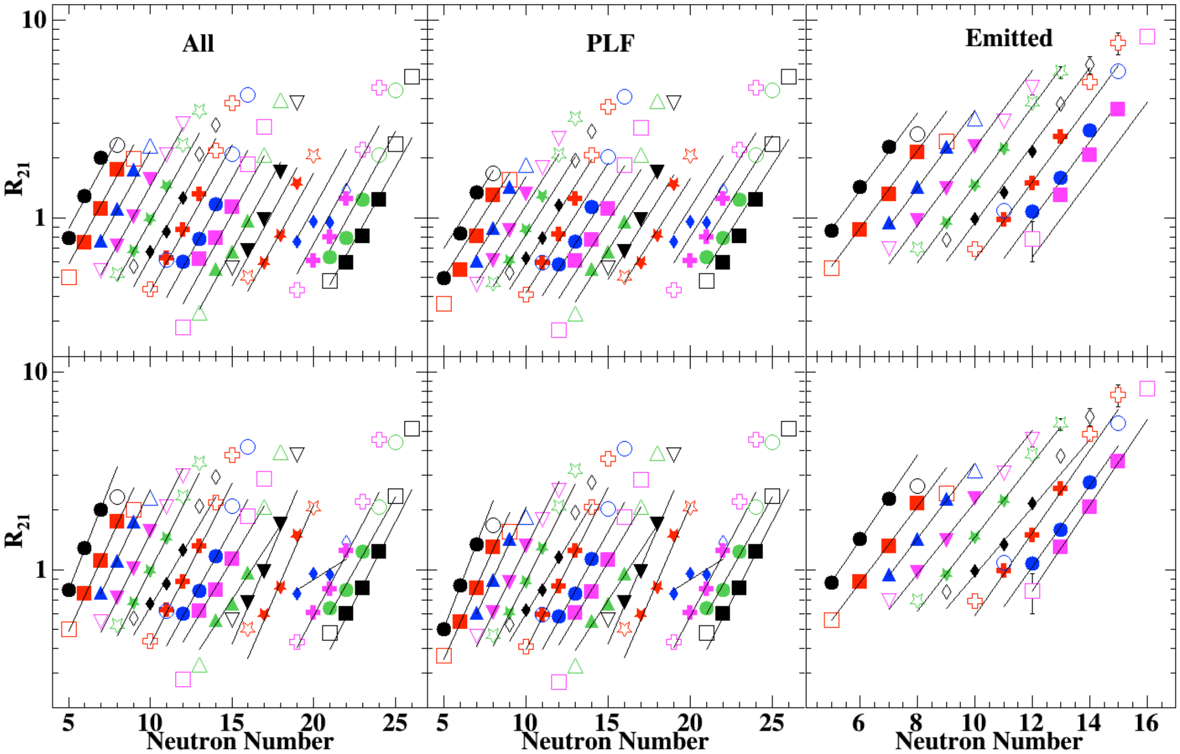

**FIG. 1.** The isoscaling ratios for all (left), projectile like (center), and light emitted (right) fragments with isoscaling fits included.

Naturally, the individual fits are better representations for each isotope however the global fit can still provide interesting information about the system as a whole. Fig. 2 shows the results of each of the

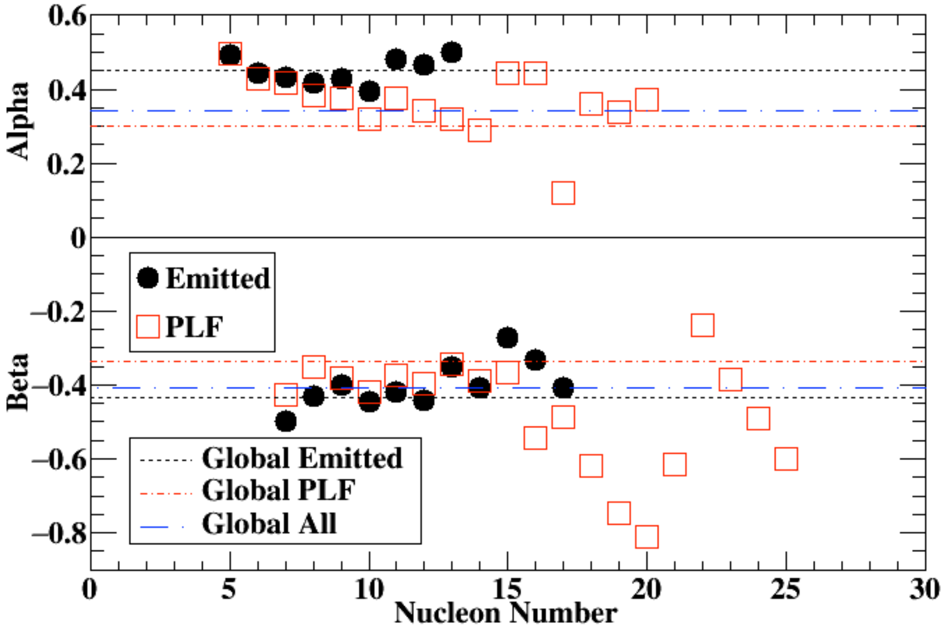

**FIG. 2.** The individual and global isoscaling parameters for emitted PLF and all fragments.

individual fits in comparison with the global fits. Interestingly, the emitted particles result in higher values of the $R_{21}$ value as well as α values than the PLF counterparts. Of particular interest is which type of particle dominates the global fits for the two isoscaling parameters. For the α parameter, the global fit for all particles is driven primarily by the PLF while the emitted fragments seem to dominate for the β parameter.

This difference leads us to an important distinction that needs to be made in the experimental design and analysis when isoscaling is intended to be used. In this experiment, due to the relatively small size of the zinc isotopes, it was quite possible to have isotopes in the range of carbon to oxygen, for example, be either a PLF or an emitted fragment in not insignificant quantities. Without the NIMROD array and the ability to discern the PLF on an event by event basis, our results would show isoscaling parameters for emitted particles that are affected by the PLF. This would provide inaccurate values for those parameters which can contribute to inaccurate results which derive from those values.

There are two ways that experiments can minimize this effect. An experiment can use a nearly 4π detector to identify as many of the fragments as possible to ensure the removal or particular selection of the PLF on an event by event basis. The other option would be to design the experiment using a rather large system and primarily detecting the PLF to make those comparisons, or by only analyzing a range of isotopes where the likelihood of those fragments being the PLF is quite low. These methods would either prevent or minimize cross contamination between the two types of particles in order to ensure as true a comparison as possible and receive the more accurate results.

[1] Z. Kohley, Ph.D. Thesis, Texas A&M University (2010).
[2] E. Geraci, Nucl. Phys. **A732**, 173  (2004).
[3] A. Le Fevre, Phys. Rev. Lett. **94**, 162701 (2005).
[4] D. Henzlova, arXiv:nucl-ex/0507003 (2010).
[5] H.S. Xu, Phys. Rev. Lett. **85**, 716 (2000).
[6] A.S. Botvina, Phys. Rev. C **65**, 044610 (2002).
[7] J. Brzychczyk, Phys. Rev. C **47**, 1553 (1993).
[8] M.B. Tsang, Phys. Rev. Lett. **86**, 5023 (2001).
[9] G.A. Souliotis, Phys. Rev. C **68**, 024605 (2003).
[10] V.V. Volkov, Phys. Rep. **44**, 93 (1978).
[11] W.A. Friedman, Phys. Rev. C **69**, 031601 (2004).
[12] M. Veselsky, Phys. Rev. C **69**, 044607 (2004).
[13] C.O. Dorso, Phys. Rev. C **73**, 044601 (2006).
[14] A. Ono, Phys. Rev. C **68**, 051601 (2003).

# Peculiar spin alignment of excited projectiles

D.E.M. Hoff,[1] J. Bromell,[1] K.W. Brown,[1] R.J. Charity,[1] J.M. Elson,[1] C.D. Pruitt,[1] L.G. Sobotka,[1,2]
T. Webb,[2] A. Saastamoinen,[3] and B. Roeder[3]
[1]*Department of Chemistry, Washington University in St. Louis, St. Louis, Missouri*
[2]*Department of Physics, Washington University in St. Louis, St. Louis, Missouri*
[3]*Cyclotron Institute, Texas A&M University, College Station, Texas*

In many nuclear reactions such as fusion, deep inelastic scattering and Coulomb excitation the total angular momentum of the resulting system is dominated by the entrance channel orbital angular momentum component. (If the target and projectile are both spin zero this is the only angular momentum.) In most reactions, the transfer of angular momentum from orbital to intrinsic spin of the reactants produces fragment spin alignment perpendicular to the beam axis. In such cases, i.e. exit channel fragments with their intrinsic spin largely aligned perpendicular to the beam axis, the fragments from sequential decay will exhibit a forward/backward focused angular distribution.

Recently reactions were observed for which the spin of excited $^7$Be* ($J^\pi = 7/2^-$) projectiles were strongly aligned with (not perpendicular to) the beam axis [1]. In other words, the fragments of the decay of the unbound $J^\pi = 7/2^-$ state were found largely transverse to the beam axis. In this previous work (at NSCL at 70 MeV/u), the peculiar angular distribution of $^7$Be* decay was for projectile excitation excited when the target, $^9$Be ($J^\pi = 3/2^-$), remaining in its ground state. To explain this effect a reaction mechanism was proposed that depended on the “molecular” structure of $^9$Be. $^9$Be is well described by an α-α backbone with a valence neutron in one of two doubly degenerate “π-orbitals”, analogous to molecular diatomic systems. In this reaction scenario, when the α-α backbone is aligned along the beam axis, the projectile could interact only with the distant valence neutron, flipping its spin (transfer of the neutron from one of the degenerate orbits to the other) and leaving the target in its ground state. Other orientations would more likely interact with α-α backbone, resulting in excitation and breakup of the target. This scenario would result in a net transfer of intrinsic spin from the target to the projectile along the beam axis.

To test this hypothesized reaction mechanism we studied the inelastic excitation of $^7$Li ($J^\pi = 3/2^-$) at 24 MeV/u, provided by the TAMU K500 cyclotron in August 2015, with three different targets: $^9$Be ($J^\pi = 3/2^-$), $^{12}$C ($J^\pi = 0^+$), and $^{27}$Al ($J^\pi = 5/2^+$). We expected to see a similar spin alignment phenomenon with the $^7$Li beam on a $^9$Be target as we observed at the NSCL with a $^7$Be beam. On the other hand, the ground state of $^{12}$C has zero spin, thus there can be no transfer of spin from target to projectile and while a spin-flip mechanism, with transfer of spin from target to projectile, is possible for the $^{27}$Al, “molecular” structure mediated reactions are irrelevant.

The experimental setup was mounted on a rail system inside the TECSA chamber at the end of the MARS line. The CAD representation of the apparatus is shown in Fig. 1. Mounted on the rail were

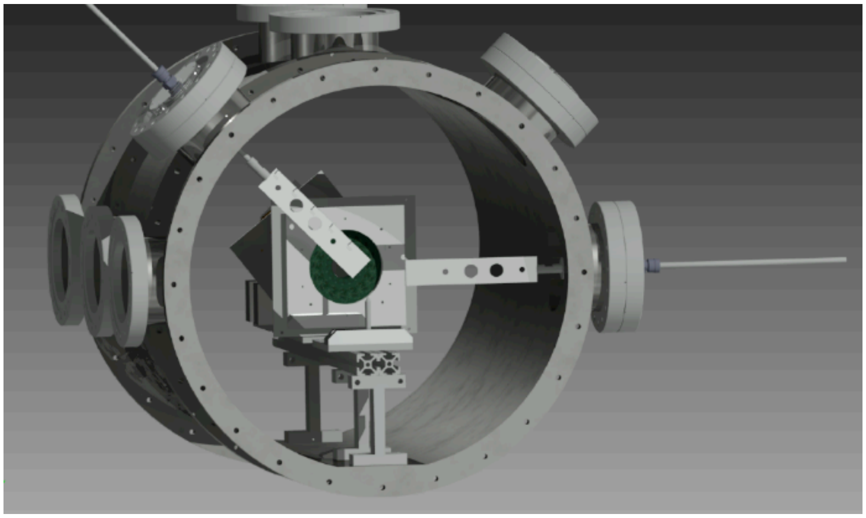

**FIG. 1.** CAD representation of the experimental setup in the TECSA chamber. Only the first of the annular Si telescopes can be seen from this downstream perspective.

two annular Si-CsI telescopes. We measured α-t coincidences to access the particle unbound states of $^7$Li. In particular, we looked at the first particle unbound state at 4.63 MeV ($J^\pi = 7/2^-$), the strong peak in the invariant mass spectrum shown in Fig. 2. One goal of this experiment was to improve the energy resolution (relative to ref. [1]) of the reconstructed target energy. In that prior work (at the NSCL), the FWHM of the ground-state peak was about 10 MeV. With our apparatus at TAMU, we were able to reduce this to under 3 MeV. This was enough to strongly bias the data set with events where the $^9$Be target stayed in its ground state (the first excited state of $^9$Be is at 1.7 MeV) and generate a clean data set

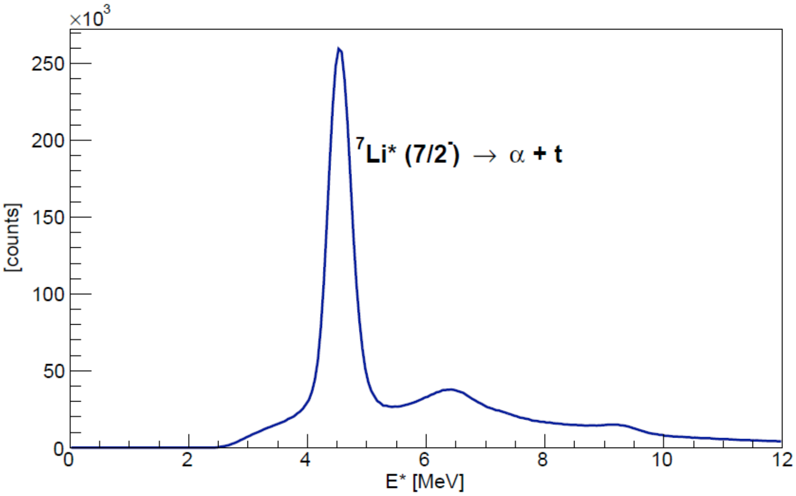

**FIG. 2**. Invariant mass excitation spectrum of $^7$Li.

where the $^{12}$C target stayed in its ground state. The reconstructed energies of the three targets are shown in Fig. 3.

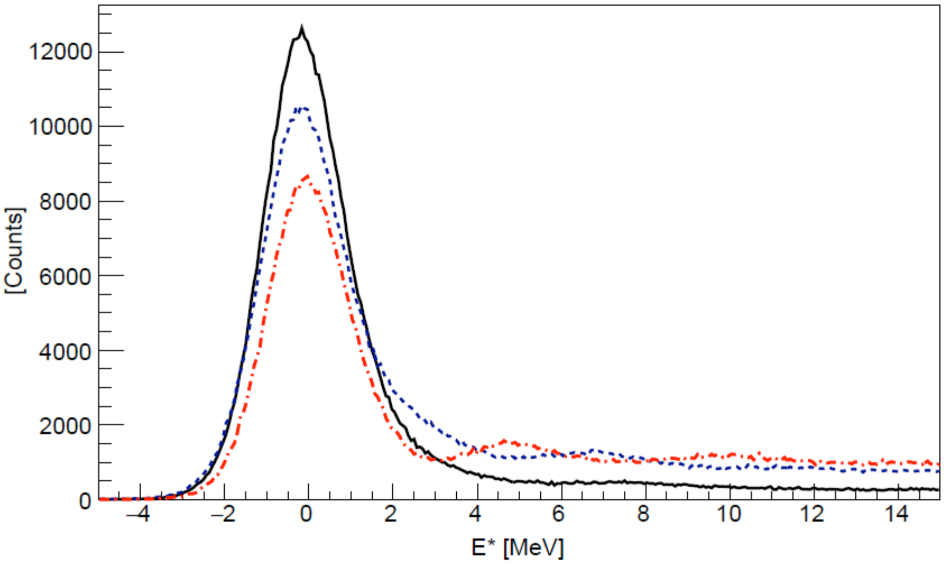

**FIG. 3.** Reconstructed target energy for $^{9}$Be (dash/blue), $^{27}$Al (solid/back), and $^{12}$C (dot-dash/red).

This experiment was also the first use of the latest HINP chip system [2]. The new chip features active dual-gains allowing for a dynamic range of 0.5-400 MeV. This new system also includes remote and distributed digitization allowing for faster readout.

By measuring the angle between the relative velocity of the fragments and the beam axis, $\psi$, we can extract information on the spin alignment of the excited projectile (see [1] for more details). It should be noted that the fragments found at $\psi$=90$^{o}$, or cos($\psi$)=0, are transverse decays. Fig. 4 shows the

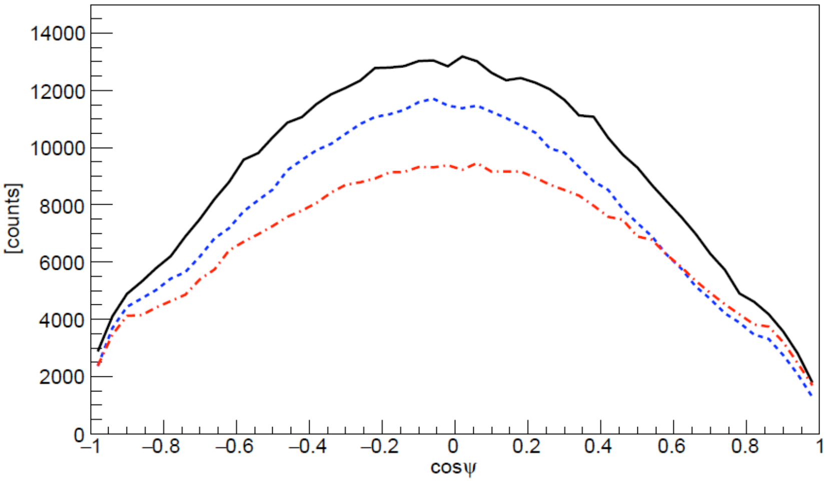

**FIG. 4.** cos($\psi$) distrbutions for the three different targets: $^{9}$Be (dash/blue), $^{27}$Al (solid/black), and $^{12}$C (dot-dash/red).

preliminary distributions for the three different targets: $^{27}$Al (solid/black), $^{9}$Be (dash/blue) and $^{12}$C (dot-dash/red). These were all generated by gating on the 4.63 state of $^{7}$Li and the target ground-state peak. These distributions do not include simulated efficiency corrections. However, the simulations done to date suggest that the shape of these angular distributions are largely independent of the efficiency for the detector. A significant position dependence of the CsI(Tl) light output was accounted for. At present we do not understand the asymmetry about $\cos(\psi)=0$, but it may be due to the inferred triton calibration, extrapolated from p and d data.

In all cases, the fragment decay distributions suggest a spin alignment of the excited $^{7}$Li projectile along the beam axis. This is inconsistent with our expectations and proposed reaction model. This peculiar decay, now observed for all targets, could find an explanation in the clustered structure of $^{7}$Li/$^{7}$Be. We are presently pursuing calculations from FRESCO in an attempt to understand this observed spin alignment, along the beam axis, that these reactions seem to produce.

[1] R.J. Charity *et al.*, Phys. Rev. C **91**, 024610 (2015).

[2] G. Engel *et al.*, Nucl. Instrum. Methods Phys. Res. **A573,** 418 (2007). The updated chip was designed as part of a RIKEN/TAMU/WU collaboration. A paper on this revised chip is in preparation.

# LLNL direct reactions experiments at TAMU-CI

J.T. Burke,[1] R.O. Hughes,[1] and R.J. Casperson[1]
[1]*Lawrence Livermore National Laboratory, Livermore, California*

Lawrence Livermore National Laboratory has two ongoing experimental setups at the Texas A&M Cyclotron Institute NeutronSTARS and Hyperion. Experiments in low energy nuclear physics reactions are conducted using the NeutronBall and a highly segmented charged particle detector array called STARS. Together the system is called NeutronSTARS and allows the direct detection of charged particles and neutrons from charged particle induced nuclear reactions. Similarly, Hyperion is a charged particle array surrounded by up to 14 HPGe Clover detectors which can detector gamma rays.

## NeutronSTARS

NeutronSTARS consists of a highly segmented (192 element) silicon telescope array, in vacuum target changer, a segmented (6 volumes) 3.5 ton pseudocumene scintillator doped with 0.4% Gd neutron detector and high speed digital and conventional VME based electronics readout system.

The NeutronSTARS detector system was installed on the NIMROD beam line at the Texas A&M University Cyclotron Institute (see Fig. 1), and a benchmark experiment was fielded in December 2015,

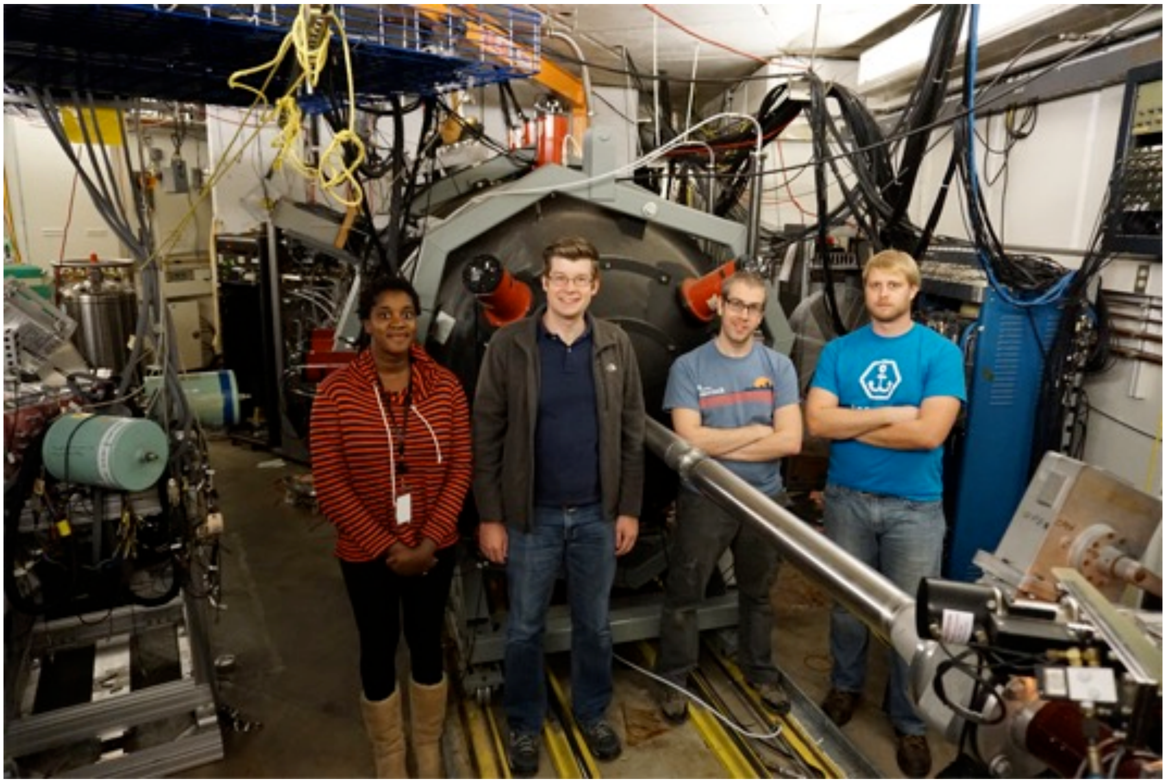

**FIG. 1.** NeutronSTARS detector system on a K150 Cyclotron beam line at Texas A&M Cyclotron Institute. The NeutronSTARS chamber is in the core of a 3.5 ton pseudocumene doped with ~0.4% of natural Gadolinium segmented detector tank. From left: Tomi Akindele (UC Berkeley PhD graduate student), Robert Casperson (LLNL staff member), Richard Hughes (LLNL post-doctoral researcher) and John Koglin (Lawrence Graduate Scholar/Penn State graduate student).

which involved an alpha particle beam incident on a $^{236}$U target. The purpose of the experiment was to reproduce the $^{235}$U(n,2n) cross section using the surrogate reactions $^{236}$U(α,α'2n) and $^{236}$U(α,α'f), along with the $^{235}$U(n,f) reference reaction in an internal ratio. This experiment is intended to validate the technique, and analysis of the experiment is underway. As a number of repairs were made to the array before the experiment, the array has been recalibrated using the $^{12}$C(α,α'γ) reaction, and spontaneous fission from a $^{252}$Cf source. The reaction on $^{12}$C is particularly useful, as it provides a 4.44 MeV gamma ray in coincidence with an alpha particle, and time gating can be used to isolate the signal. The $^{252}$Cf source provides a known number of neutrons with a fission fragment tag.

NeutronSTARS is currently being used to measure cross sections of previously unobtainable (n,2n) reactions using the surrogate ratio method. Oluwatomi Akindele, from the University of California Berkeley, will be using the array to obtain the data needed for her PhD thesis. A summer student from Oregon State University was also participated in the test runs of NeutronSTARS, namely Aaron Tamashiro. A graduate student from the Pennyslvania State University has also participated in the experiments at NeutronSTARS; Johnathan Koglin.

### Hyperion detector array

The Hyperion detector array was installed and commissioned at the Texas A&M Cyclotron Institute in the summer of 2015 (see Fig. 2). Hyperion is the largest gamma ray array owned and operated by the National Nuclear Security Agency. When fully instrumented it will hold up to 14 HPGe Clover detectors surrounding a central vacuum chamber where the targets are located. Hyperion has approximately a 12% photopeak efficiency at 150 keV and 3.5% at 1.0 MeV. Fully instrumented Hyperion will be a $4M detector array available to TAMU-CI and its collabroators for basic and applied science research.

Hyperion will be used to perform nuclear structure measurements, study the lifetimes of nuclear states, determine level densities and gamma ray strength functions and measure fundamental data to then use for surrogate reaction cross sections. All measurements use charged particle beams from the K150 Cyclotron at the Texas A&M Cyclotron Institute to induce low energy nuclear reactions.

Hyperion has been comissioned and performed two nuclear structure measurements since July 2015 before the Clover Share detectors had to be returned to the user community.

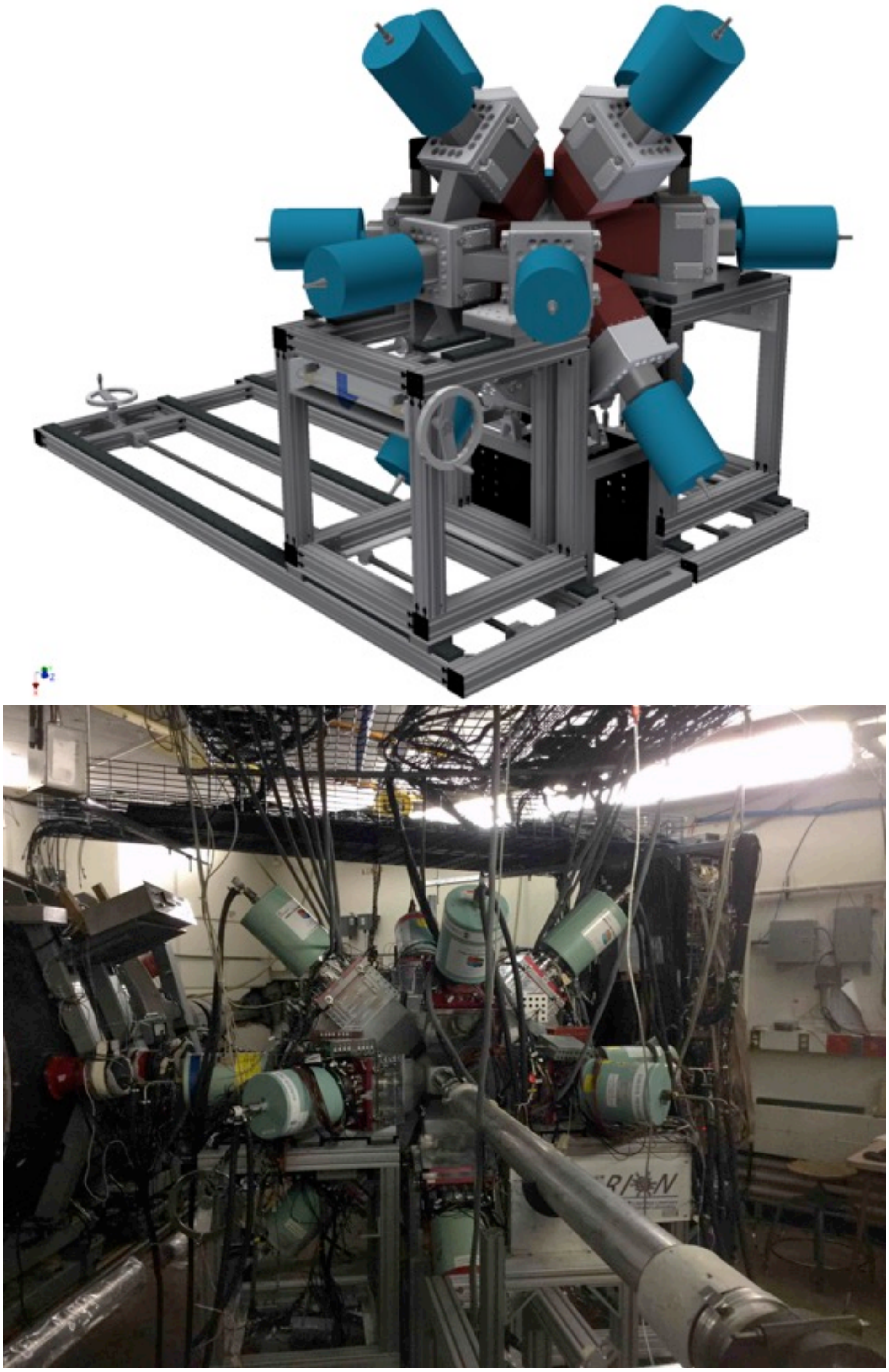

**FIG. 2.** Hyperion conceptual drawing in 2013 (above) and fully assembled with 13 HPGe Clovers from LLNL, the CloverShare program, the University of Richmond, and Texas A&M University (below).

# Toward understanding relativistic heavy-ion collisions with the STAR detector at RHIC

D.M. Anderson, Y. Liu, S. Mioduszewski, N. Sahoo, and the STAR Collaboration

The focus of this project is the study of high-energy heavy-ion collisions at the Relativistic Heavy Ion Collider (RHIC). Two valuable probes of the matter created in these collisions are direct-photon-triggered (jet) correlations and heavy-quarkonium production.

## Measurement of $\gamma$-Jet at low $z_T$ and high trigger $p_T$

Direct photons produced in hard collisions, early in the evolution of a heavy-ion collision, are promising probes [1], as they do not interact via the strong force. Jet correlations (of the recoiling parton) with a direct-photon trigger can give information about the parton energy loss in the medium. The correlations with a photon trigger are compared to those measured with a $\pi^0$ trigger because of the difference in expected surface biases. While direct photons are not affected by the medium and can originate from anywhere in the medium without bias, $\pi^0$ triggers are likely to be have a bias of production near the surface of the medium. Therefore, on average, one would expect that the away-side jet for a $\pi^0$ trigger has a larger path length to traverse and experiences larger energy loss than the away-side jet of a $\gamma^{dir}$ trigger. To enhance our sensitivity to the dependence on the path length through the medium, the measurement was extended to lower $z_T$ ($z_T$ is the ratio of the $p_T$ of the associated particle to the $p_T$ of the trigger particle, $z_T=p_{T,assoc}/p_{T,trig}$). To reach lower $z_T$, one can increase the trigger-particle $p_T$, which requires higher statistics, or lower the associated-particle $p_T$. To avoid the large uncertainties associated with background subtraction when lowering the associated-particle $p_T$, the trigger-particle, $p_T$, was increased to 12-20 GeV/c.

To measure the effect of the medium, Fig.1 shows the ratio of per-trigger yields $I_{AA}$, defined as the yield measured in Au+Au to that measured in p+p, as a function of $z_T$.

At low $z_T$ ($0.1<z_T<0.2$), both the suppression levels in $\pi^0$-triggered yields, $I_{AA}{}^{\pi^0}$, and in $\gamma^{dir}$-triggered yields, $I_{AA}{}^{\gamma_{dir}}$, appear to be less than at higher $z_T$. At high $z_T$, the suppression factor is approximately 3–5. The theory calculations, labeled Wang [3, 4] and Qin [5] describe the data for $\gamma^{dir}+h^{\pm}$ correlations. Since the model calculations do not include a redistribution of the lost energy to the low-$p_T$ jet fragments, the rise in $I_{AA}{}^{\gamma_{dir}}$ at low $z_T$ is likely due to the volume emission of the $\gamma^{dir}$ triggers (vs. surface emission of $\pi^0$ triggers). Also shown is the calculation for $I_{AA}{}^{\pi^0}$ [3, 4], which does not show the same rise at low $z_T$. However, within the measured uncertainties, there is no difference in the suppression of $\pi^0$-triggered yields and $\gamma^{dir}$-triggered yields, even at low $z_T$. This figure is included in the manuscript written by our group, which was recently submitted for publication [2]. It will be important to measure this more precisely with higher-statistics data (allowing for more systematic studies), in order to understand whether the rise is due to a redistribution of lost energy or effects of surface vs. volume emission trigger biases.

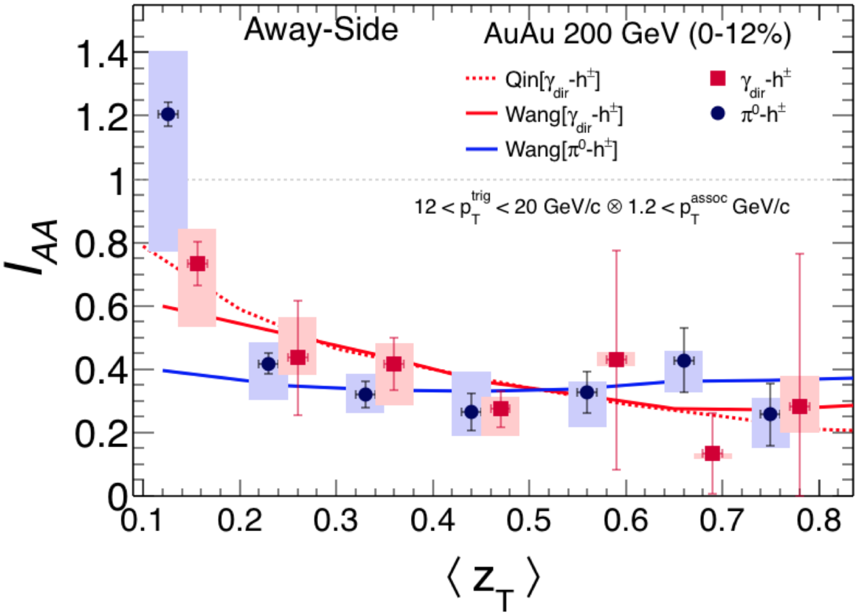

**FIG. 1.** $I_{AA}$ vs. $z_T$ for $\pi^0$-triggered away-side yields (blue) and $\gamma^{dir}$-triggered away-side yields (red) from Run-9 p+p and Run-11 central Au+Au data.

## Heavy Quarkonium Studies using the Muon Telescope Detector in STAR

The J/ψ has long been considered one of the most promising direct probes of deconfinement [6]. In order to quantify effects of deconfinement, cold nuclear matter effects (via p+A collisions) must be measured and disentangled [7].

We have been working on determining the trigger efficiency in Run-14 Au+Au collisions. We have done this for low-luminosity and mid-luminosity data separately. The high-luminosity data was not yet reconstructed when Y. Liu started this study, but it will also be analyzed soon. Shown in Fig. 2 (left panel) is the "Single-Muon" trigger efficiency, requiring an energy signal within a "trigger patch" (region) in the MTD, as a function of $p_T$, in the mid-luminosity data. It is found to approach 91% at high $p_T$.

The di-muon efficiency is also calculated and shown in Fig. 2 (right panel), as a function of the pair $p_T$, where $p_T^{pair} = \sqrt{(p_x^{\mu_1} + p_x^{\mu_2})^2 + (p_y^{\mu_1} + p_y^{\mu_2})^2}$. The measured di-muon efficiency agrees with a simple simulation of two uncorrelated muons, each having trigger efficiency as shown in the left panel of Fig. 2.

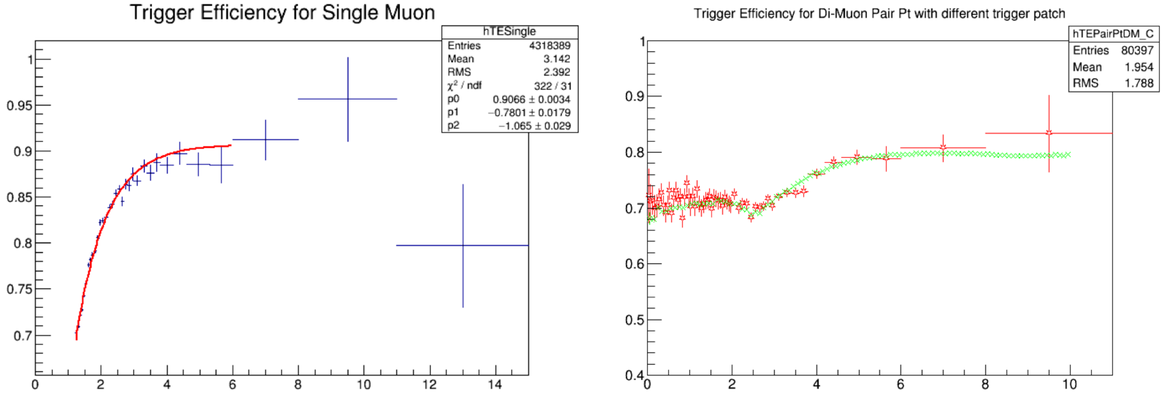

**FIG. 2.** (Left) Single-muon trigger efficiency in Run-14 Au+Au mid-luminosity data, as a function of $p_T$. The line is a fit to the data. (Right) Di-muon trigger efficiency in Run-14 Au+Au mid-luminosity collisions, as a function of pair $p_T$. The red are the measured data points, and the green is the simulated di-muon efficiency taking as input the $p_T$ distribution of muon candidates and the single-muon efficiency, as shown on the left panel.

Last summer's REU student calculated survival probabilities of background particles in the MTD (pions, proton, and kaons). He used a sample of simulated particles embedded into and reconstructed within Au+Au collision data. He found that for $p_T$>1.2 GeV, muons had a 20% efficiency of being detected and passing the particle-identification criteria, while pions, protons, and kaons had less than 0.3% probability of detection and survival of the selection criteria.

The effort that the group has invested in understanding the response of the MTD and the triggers using the MTD will be useful for the J/Ψ measurement.

[1] X.N. Wang, Z. Huang, and I. Sarcevic, Phys. Rev. Lett. **77**, 231 (1996).
[2] L. Adamczyk *et al.* (STAR Collaboration), arXiv:1604.01117 [nucl-ex].
[3] H. Zhang, J.F. Owens, E. Wang, and X.-N. Wang, Phys. Rev. Lett. **103**, 032302 (2009).
[4] X.-F. Chen, C. Greiner, E. Wang, X.-N. Wang, and Z. Xu, Phys. Rev. C **81**, 064908 (2010); X.-N.Wang, private communication.
[5] G.-Y Qin *et al*., Phys. Rev. C **80**, 054909 (2009).
[6] T. Matsui and H. Satz, Phys. Lett. B **178**, 416 (1986).
[7] R. Vogt, Phys. Rev. C **71**, 054902 (2005).

# SECTION III

# NUCLEAR THEORY

# Systematic analysis of hadron spectra in p+p collisions using Tsallis distribution

H. Zheng,[1] Lilin Zhu,[2] and A. Bonasera

[1]*Laboratori Nazionali del Sud, INFN, via Santa Sofia, 62, 95123 Catania, Italy*
[2]*Department of Physics, Sichuan University, Chengdu 610064, P. R. China*

Using the experimental data from the STAR, PHENIX, ALICE, and CMS programs on the rapidity and energy dependence of the pT spectra in p+p collisions, we show that a universal distribution exists. The energy dependence of temperature, T, and parameter, n, of the Tsallis distribution are also discussed in detail. A cascade particle production mechanism in p+p collisions is proposed [1].

Recently, the Tsallis distribution has attracted many theorists' and experimentalists' attention in high energy heavy-ion collisions. The excellent ability to fit the spectra of identified hadrons and charged particles in a large range of pT  up to 200 GeV/c is quite impressive. From the phenomenological view, there may be real physics behind the prominent phenomenology work, e.g. Regge trajectory for particle classification. p+p collision experiments have been performed and measured under different energies. Since p+p collision is very simple compared to nucleus-nucleus collision, the measurements of p+p collisions are used to understand the particle interaction, particle production mechanism and as a baseline for nucleus-nucleus collisions. Many efforts have been put to study the particle spectra produced in p+p collisions using Tsallis distribution. Different versions of the Tsallis distribution are used in the literature. The parameter T in the Tsallis distribution was interpreted as temperature. All of them can fit the particle spectra very well but they give different temperatures. We would like to study the connections and differences among different versions of the Tsallis distribution. We collected p+p collisions data with different $p_T$ ranges and different rapidity cuts from different experiment groups at RHIC and LHC and did a systematic study of the particle spectra using one of the Tsallis distributions.  We adopted

$$\left(E\frac{d^3N}{dp^3}\right)_{|N|<n} = A\left(1+\frac{E_T}{nT}\right)^{-n},$$

where $A$, $n$ and $T$ are fitting parameters. $E_T$ is the transverse energy of the particle.

We collect the spectra data for different particles with different $p_T$ ranges and different rapidity cuts from p+p collisions at 62.4, 200, 900, 2760, and 7000 GeV. In Fig. 1, we showed the prominent fitting power of the Tsallis distribution. This is for charged particles. As we can see, the excellent fitting can cover 15 orders of magnitude up to 200 GeV/c for $p_T$. This spectacular result was first shown by Wong et al [2]. After performing the systematic analysis of the particle spectra. We found that T is not dependent on the beam energy for pions, while for kaons and protons it increases with increasing energy. Furthermore, we notice that T is higher for the particle whose mass is larger. This is probably due to the particle produced time. In the cascade particle production mechanism, this result is perfectly understandable. The behavior of n for kaons is not the same as pions and protons, which is related to the

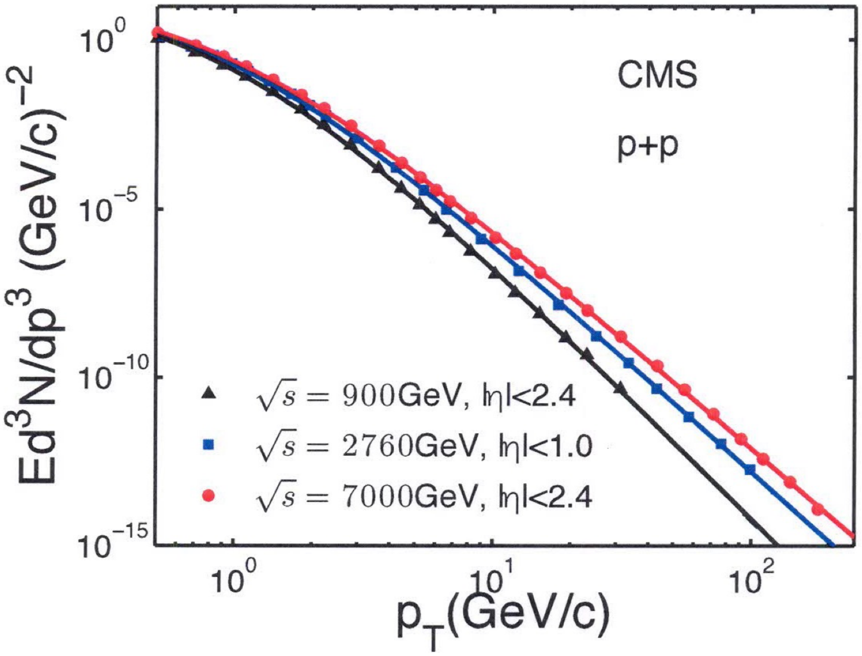

**FIG. 1.** Fitting results using the Tsallis distribution for charged particles in p+p collisions at 900, 2760, and 7000 GeV, respectively. Data are taken from CMS.

particle production process. From the properties of T and n, we get more information about particle production mechanism in p+p collision.

[1] H. Zheng, Lilin Zhu, and A. Bonasera, Phys. Rev. D **92**, 074009 (2015).
[2] Cheuk-Yin Wong and G. Wilk, Acta Phys. Pol. B **43**, 2047 (2012).

# Asymptotic normalization coefficients and radiative widths

A.M. Mukhamedzhanov and D.Y. Pang

The asymptotic normalization coefficient (ANC) is an important quantity in the calculation of radiative width amplitudes, providing limits on the radiative width. Here we present some examples showing the connection between the ANC and radiative width. In particular, the radiative width of the $E1$ transition $^{17}$F ($1/2^-$,$E_x$ = 3.104 MeV) to $^{17}$F ($1/2^+$,$E_x$ = 0.495 MeV) reported by Rolfs [1] is (1.2 ± 0.2) × $10^{-2}$ eV. Meanwhile the ANC for the first excited state in $^{17}$F puts a lower limit on the radiative width, which is (3.4 ± 0.50) ×$10^{-2}$ eV. Such a strong disagreement between the measured radiative width and the lower limit imposed by the ANC calls for a new measurement of this radiative width.

We discussed also the role of the ANC in determination of the radiative width for the capture to the bound state through the subthreshold resonance. In this case the radiative width is determined by the product of the squares of the ANCs for the subthreshold bound state and the final bound state. The presented cases require new more accurate measurements of the radiative width. Other examples are also considered.

The work was published in Phys. Rev. C **92**, 014625 (2015).

[1] C. Rolfs, Nucl. Phys. **A217**, 29 (1973).

# Improvement of the high-accuracy $^{17}O(p,\alpha)^{14}N$ reaction-rate measurement via the Trojan Horse method for application to $^{17}O$ nucleosynthesis

M.L. Sergi, C. Spitaleri, M. La Cognata, L. Lamia, R.G. Pizzone, G.G. Rapisarda,
X.D. Tang, B. Bucher, M. Couder, P. Davies, R. deBoer, X. Fang, L. Lamm, C. Ma,
M. Notani, S. O'Brien, D. Roberson, W. Tan, M. Wiescher, B. Irgaziev,
A. Mukhamedzhanov, J. Mrazek, and V. Kroha

The $^{17}O(p,\alpha)^{14}N$ and $^{17}O(p,\gamma)^{18}F$ reactions are of paramount importance for the nucleosynthesis in a number of stellar sites, including red giants (RGs), asymptotic giant branch (AGB) stars, massive stars, and classical novae. In particular, they govern the destruction of $^{17}O$ and the formation of the short-lived radioisotope $^{18}F$, which is of special interest for $\gamma$ -ray astronomy. At temperatures typical of the above-mentioned astrophysical scenario, T = 0.01–0.1 GK for RG, AGB, and massive stars and T = 0.1–0.4 GK for a classical nova explosion, the $^{17}O(p,\alpha)^{14}N$ reaction cross section is dominated by two resonances: one at about $E_R^{cm} = 65$ keV above the $^{18}F$ proton threshold energy, corresponding to the $E_X$= 5.673 MeV level in $^{18}F$, and another one at $E_R^{cm} = 183$ keV ($E_X$ = 5.786 MeV).We report on the indirect study of the $^{17}O(p,\alpha)^{14}N$ reaction via the Trojan Horse method by applying the approach recently developed for extracting the strength of narrow resonance at ultra low energies. The mean value of the strengths obtained in the two measurements was calculated and compared with the direct data available in literature. This value was used as input parameter for reaction-rate determination and its comparison with the result of the direct measurement is also discussed in the light of the electron screening effect.

The paper was published in Phys. Rev. C **91**, 065803 (2015).

## New approach to folding with the Coulomb wave function

L.D. Blokhintsev, A.S. Kadyrov, A.M. Mukhamedzhanov, and D.A. Savin

Due to the long-range character of the Coulomb interaction theoretical description of low-energy nuclear reactions with charged particles still remains a formidable task. One way of dealing with the problem in an integral-equation approach is to employ a screened Coulomb potential. A general approach without screening requires folding of kernels of the integral equations with the Coulomb wave. A new method of folding a function with the Coulomb partial waves is presented. The partial-wave Coulomb function both in the configuration and momentum representations is written in the form of separable series. Each term of the series is represented as a product of a factor depending only on the Coulomb parameter and a function depending on the spatial variable in the configuration space and the momentum variable if the momentum representation is used. Using a trial function, the method is demonstrated to be efficient and reliable.

The work was published in J. Math. Phys. **56**, 052102 (2015).

# The cosmological lithium problem revisited

C.A. Bertulani, A.M. Mukhamedzhanov, and Shubhchintak

We report a few recent attempts to find theoretical solutions by our group at Texas A&M University (Commerce & College Station). Our studies on the theoretical description of electron screening, the possible existence of parallel universes of dark matter, and the use of non-extensive statistics during the Big Bang nucleosynthesis (BBN) epoch. For the calculation of reaction rates in the BBN one assumes the validity of the Maxwell-Boltzmann (MB) distribution of velocities of the nuclei in a plasma. The effects of a non-extensive statistics for BBN has been used to make predictions for the abundances of light nuclei using the available experimental data of these reactions. We conclude that it is not possible to solve the lithium puzzle with use of a non-extensive statistics to calculate the reaction rates during the BBN. The departure from the Boltzman-Gibbs (BG) statistics in fact worsens the lithium problem by increasing its abundance.

Last but not least, we discuss possible solutions within nuclear physics realm. The impact of recent measurements of relevant nuclear reaction cross sections for the Big Bang nucleosynthesis based on indirect methods is also assessed. Although our attempts may not able to explain the observed discrepancies between theory and observations, they suggest theoretical developments that can be useful also for stellar nucleosynthesis.

# THM determination of the 65 keV resonance strength intervening in the $^{17}$O(p,α)$^{14}$N reaction rate

M.L. Sergi , C. Spitaleri, V. Burjan, S. Cherubini, A. Coc, M. Gulino, F. Hammache, Z. Hons, B. Irgaziev, G.G. Kiss, V. Kroha, M. La Cognata, L. Lamia, A.M. Mukhamedzhanov, R.G. Pizzone, S.M.R. Puglia, G.G. Rapisarda, S. Romano, N. de Séréville, E. Somorjai, and A. Tumino

The $^{17}$O(p,α)$^{14}$N reaction is of paramount importance for the nucleosynthesis in a number of stellar sites, including red giants (RG), asymptotic giant branch (AGB) stars, massive stars, and classical novae. We report on the indirect study of the $^{17}$O(p,α)$^{14}$N reaction via the Trojan Horse method by applying the approach recently developed for extracting the resonance strength of the narrow resonance at $E_R^{cm} = 65$ keV ($E_x$=5.673 MeV). The strength of the 65 keV resonance in the $^{17}$O(p,α)$^{14}$N reaction, measured by means of the THM, has been used to renormalize the corresponding resonance strength in the $^{17}$O + p radiative capture channel.

The work published in AIP Conference Proceedings **1645**, 392 (2015).

# Updated THM astrophysical factor of the $^{19}$F (p, α)$^{16}$O reaction and influence of new direct data at astrophysical energies

M. La Cognata, S. Palmerini, C. Spitaleri, I. Indelicato, A.M. Mukhamedzhanov,
I. Lombardo, and O. Trippella

Fluorine nucleosynthesis represents one of the most intriguing open questions in nuclear astrophysics. It has triggered new measurements which may modify the presently accepted paradigm of fluorine production and establish fluorine as an accurate probe of the inner layers of asymptotic giant branch (AGB) stars. Both direct and indirect measurements have attempted to improve the recommended extrapolation to astrophysical energies, showing no resonances. In this work, we will demonstrate that the interplay between direct and indirect techniques represents the most suitable approach to attain the required accuracy for the astrophysical factor at low energies, Ec.m. $\lesssim$ 300 keV, which is of interest for fluorine nucleosynthesis in AGB stars. We use the recently measured direct $^{19}$F(p, α)$^{16}$O astrophysical factor in the 600 keV $\lesssim$ $E_{c.m.}$ $\lesssim$ 800 keV. Energy interval to renormalize the existing Trojan Horse Method (THM) data spanning the astrophysical energies, accounting for all identified sources of uncertainty. This has a twofold impact on nuclear astrophysics. It shows the robustness of the THM approach even in the case of direct data of questionable quality, as normalization is extended over a broad range, minimizing systematic effects. Moreover, it allows us to obtain more accurate resonance data at astrophysical energies, thanks to the improved $^{19}$F( p, α)$^{16}$O direct data. Finally, the present work strongly calls for more accurate direct data at low energies, so that we can obtain a better fitting of the direct reaction mechanism contributing to the $^{19}$F( p, α)$^{16}$O astrophysical factor. Indeed, this work points out that the major source of uncertainty affecting the low-energy S(E) factor is the estimate of the non-resonant contribution, as the dominant role of the 113 keV resonance is now well established.

This work was published in the Astrophys. J. **805**, 128 (2015).

## Divergence of the isospin asymmetry expansion of the nuclear equation of state

C. Wellenhofer, J.W. Holt, and N. Kaiser

We have extracted [1] from realistic chiral nuclear interactions the quadratic, quartic, and sextic terms in the isospin-asymmetry expansion of the equation of state of nuclear matter at finite temperature,

$$F(T,\rho,\delta) \simeq \sum_{n=0}^{N} A_{2n}(T,\rho)\,\delta^{2n}\,, \tag{1}$$

from second-order many-body perturbation theory. In the bottom-right panel of Fig. 1, we observe that the quadratic coefficient $A_2$ describes well the global isospin asymmetry dependence from symmetric nuclear matter to pure neutron matter by comparing to the symmetry energy $F_{sym} = F(T,\rho,\delta=1) - F(T,\rho,\delta=0)$. The higher-order terms, however, are shown to be large and alternating in sign (see the top-right and bottom-left panels of Fig. 1) at low temperature and high density, indicating a divergent

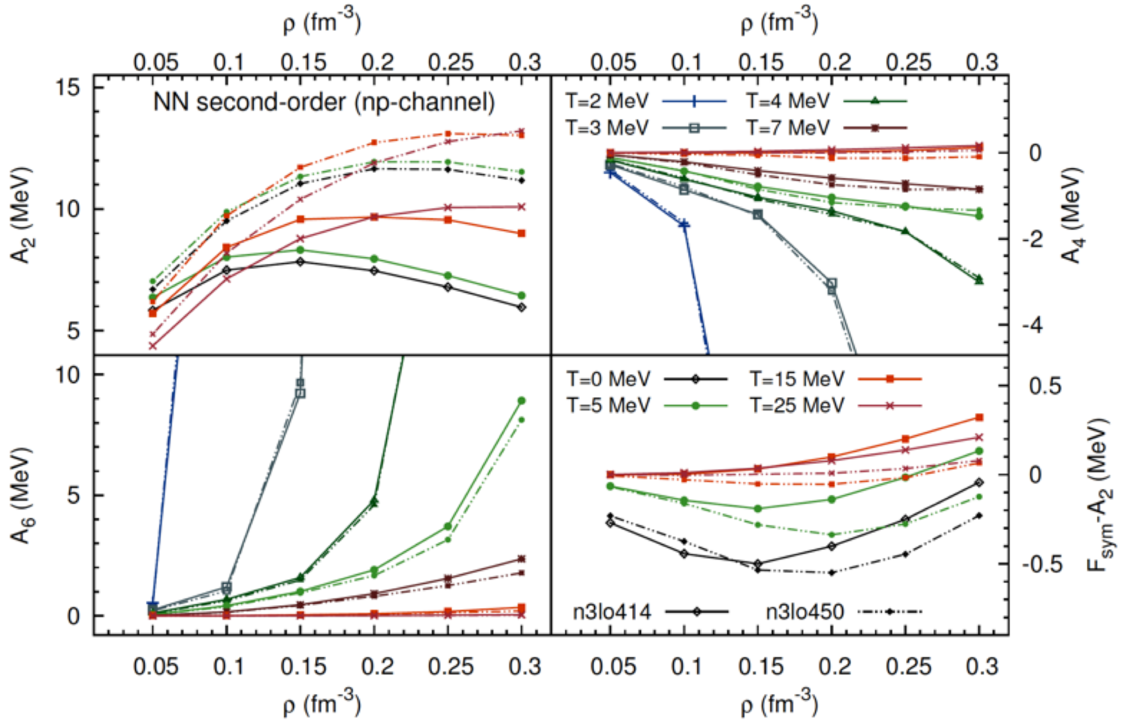

**FIG. 1.** Coefficients of the Maclaurin expansion for the isospin-asymmetry dependence of the nuclear equation of state as a function of temperature and density from two chiral nuclear force models. The difference between the nuclear symmetry energy $\boldsymbol{F_{sym}}$ and the $\boldsymbol{A_2}$ coefficient is shown in the bottom-right panel.

series incompatible with the traditional assumption in Eq. (1). In Ref. [2] it was shown that at zero temperature an *S*-wave contact interaction gives an additional logarithmic contribution to Eq. (1) when computed at second order in perturbation theory. Extracting this nonanalytic term leads to a significant improvement in the description of the free energy per particle at large isospin asymmetries. In future work these results will be used to study the crust-core transition density in neutron stars and the threshold density for the onset of direct URCA processes relevant for neutron star cooling.

[1] C. Wellenhofer, J.W. Holt, and N. Kaiser, Phys. Rev. C **93**, 055802 (2016).
[2] N. Kaiser, Phys. Rev. C **91**, 065201 (2015).

# Investigation of the energy-averaged double transition density of isoscalar monopole excitations in medium-heavy mass spherical nuclei

M.L. Gorelik,[1] S. Shlomo, B.A. Tulupov,[1,2] and M.H. Urin[1]
[1]*National Research Nuclear University «MEPhI», Moscow, 115409 Russia*
[2]*Institute for Nuclear Research, RAS, Moscow, 117312 Russia*

The study of properties of collective states in nuclei provides information on the bulk properties of nuclear matter. In particular, the interest in experimental and theoretical studies of high-energy particle-hole-type isoscalar monopole (ISM) excitations in medium-heavy mass nuclei is mainly due to the possibility of determining the nuclear matter incompressibility coefficient, a fundamental physical quantity essential for astrophysics and nuclear physics. The value of this coefficient depends on the mean energy of the strength distribution of the isoscalar giant monopole resonance (ISGMR), corresponding to the ISM external field $r^2Y_{00}$. To deduce this strength distribution from experimental data of ($\alpha$,$\alpha$')-inelastic scattering cross sections at small angles, it is usually assumed that the ISM strength is concentrated in the vicinity of the ISGMR and the properly normalized classical collective model transition density of the ISGMR can be used within the folding model distorted wave Born approximation (FM-DWBA). It is important to point out that the classical collective model one-body transition density is independent of the excitation energy.

We emphasize that in a microscopic approach, the input quantity for the analysis of the ($\alpha$,$\alpha$')-reaction cross section should be the energy-averaged double transition density (i.e. the energy-averaged product of energy dependent transition densities taken in different points). In a wide excitation-energy interval involving the ISGMR and its overtone, ISGMR2, this quantity is expected to be different from the product of the classical collective model transition densities, which is independent of excitation energy, or the product of microscopic transition densities, due to proper treatment of the shell structure of nuclei (i.e. the Landau damping) and also the spreading effect. In this work we apply the newly developed particle-hole dispersive optical model (PHDOM) to study properties of high-energy isoscalar monopole excitations in $^{208}$Pb. The PHDOM, as an extension of the continuum-RPA, accounts for the Landau damping, coupling of high-energy (p-h)-type states to the single-particle (s-p) continuum and to many-quasiparticle configurations (the spreading effect). The PHDOM allows one to describe the energy-averaged ISM double transition density at arbitrary (but high-enough) excitation energy and, in particular, to trace the change of this quantity from the ISGMR to ISGMR2.

In this work[1] we have carried out an investigation of the energy-averaged double transition density. The calculations were performed for ISM excitations in $^{208}$Pb. A wide excitation-energy interval is considered which includes the ISGMR and ISGMR2. The fractions of the energy-weighted sum-rule (EWSR) associated with the strength functions of these resonances, i.e. the energy-weighted strength functions divided by the corresponding EWSR, were analyzed. We also considered single p-h transition density obtained by various projections of the double p-h transition density, as well as the classical collective models transition densities, and investigate their applicability. This is done by considering the excitation cross sections with the Born approximation and comparing with the results obtained from the double p-h transition density. We add that it is important to carry out this test on the accuracy of the experimental analysis of cross sections before a reliable comparison between experimental data with theoretical prediction obtained using energy density functional.

To describe the properties of the ISGMR and ISGMR2, it is convenient to choose for the radial external fields the forms

$$V_{0,1}(r) = r^{2} and V_{0,2}(r) = r^{4} \qquad r^{2}, \tag{1}$$

respectively. To study possibilities of an appropriate factorization of the ISM double-transition-density radial dependence in a wide excitation-energy interval, we define the projected transition density,

$$_{V_0}(r, \quad) = \qquad (r,r', \quad)V_0(r')dr' \Big/ S_{V_0}^{1/2}(\quad) , \tag{2}$$

which can be considered as the transition density of a given ISM giant resonance (ISGMR or the ISGMR2). This transition density, which is energy-dependent, of the corresponding giant resonance, fulfils the condition that the strength function is obtained by

$$S_{V_0}(\quad) = \Big( \qquad _{V_0}(r, \quad)V_0(r)dr \Big)^{2} . \tag{3}$$

In the experimental analysis of inelastic (α,α')-scattering cross sections at small angles the folding model (FM)-DWBA is usually employed. One first determines the optical potential by folding a Fermi distribution for the ground state matter density with a parameterized α-nucleon interaction, determined by a fit to the elastic scattering cross-section. Next, the classical collective ISGMR and ISGMR2 transition densities are folded with the α-nucleon interaction to determine the transition potentials. Then the optical potential and the transition potentials are used as input for the DWBA code. Since only the energy-averaged ISM double transition density can be obtained within the PHDOM, we study the accuracy of this approach by calculating the excitation cross section within the Born approximation. In this approximation, the energy averaged transition strength function is proportional to the strength function $S_{V_{0,q}}$, corresponding to the external field $V_{0,q}(r) = \frac{\sin(qr)}{qr}$. We have considered the energy-averaged strength function $S_{V_0,q}(\quad)$, which determines in the Born approximation the excitation cross-section of the ISGMR and its overtone in $^{208}$Pb by 240 MeV α-particle scattering. In Figs. 1 and 2 we show the strength function evaluated via energy-averaged microscopic double transition density $(r, r', \quad)$ in comparison with the strength functions evaluated with the use of the factorized projected and properly normalized classical transition densities, $_{i}(r, \quad)$ and $_{c,i}(r, \quad)$. As follows from this comparison, the description with the use of the factorized projected transition densities reproduces satisfactorily the "exact" description in a vicinity of the ISGMR (i=1) and ISGMR2 (i=2).

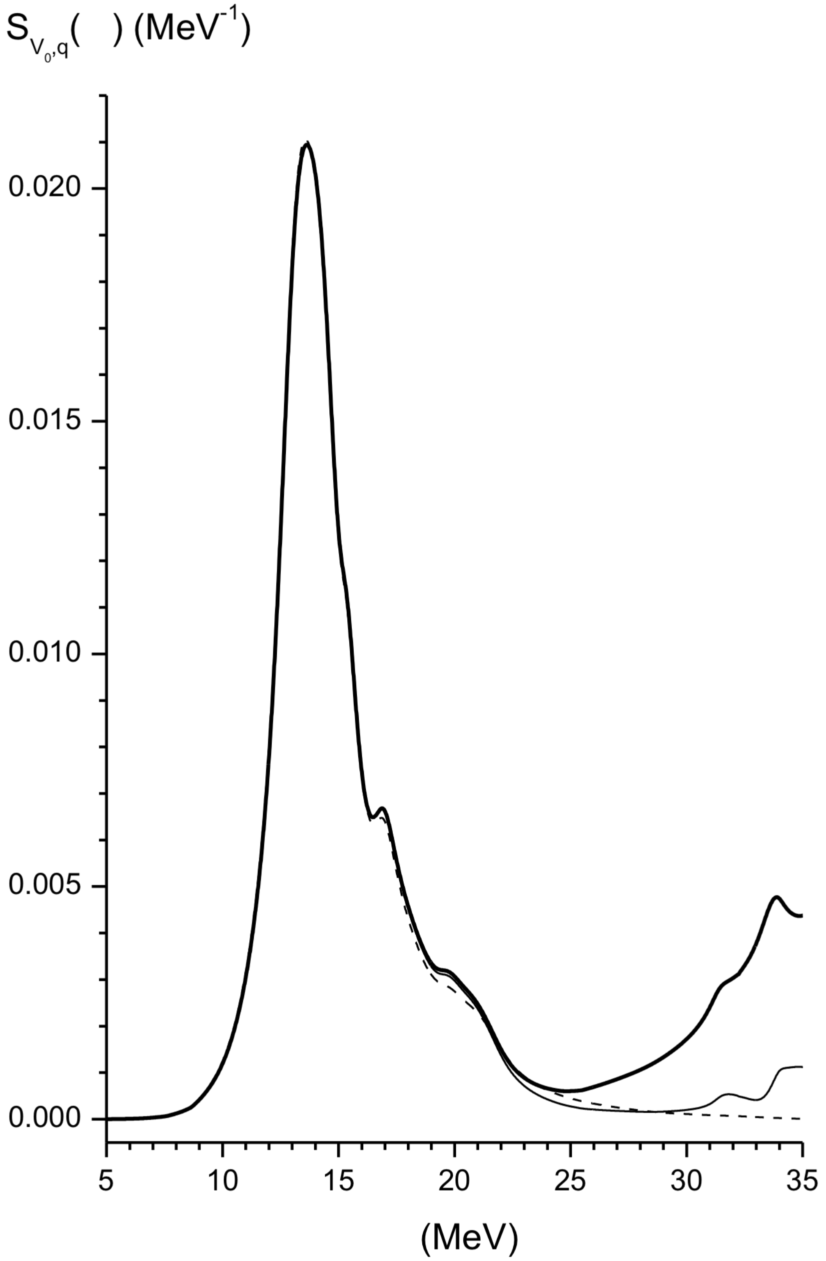

**FIG. 1.** The strength function $S_{V_{0,q}}(\ )$ shown (the solid thick line) in a comparison with the strength function, corresponding to the same external field but calculated with the use of the projected double transition densities $_i(r,r',\ )$ (the solid thin red line) and the properly normalized classical double transition densities $_{c,i}(r,r',\ )$ (the dashed blue line) for the ISGMR (i=1)

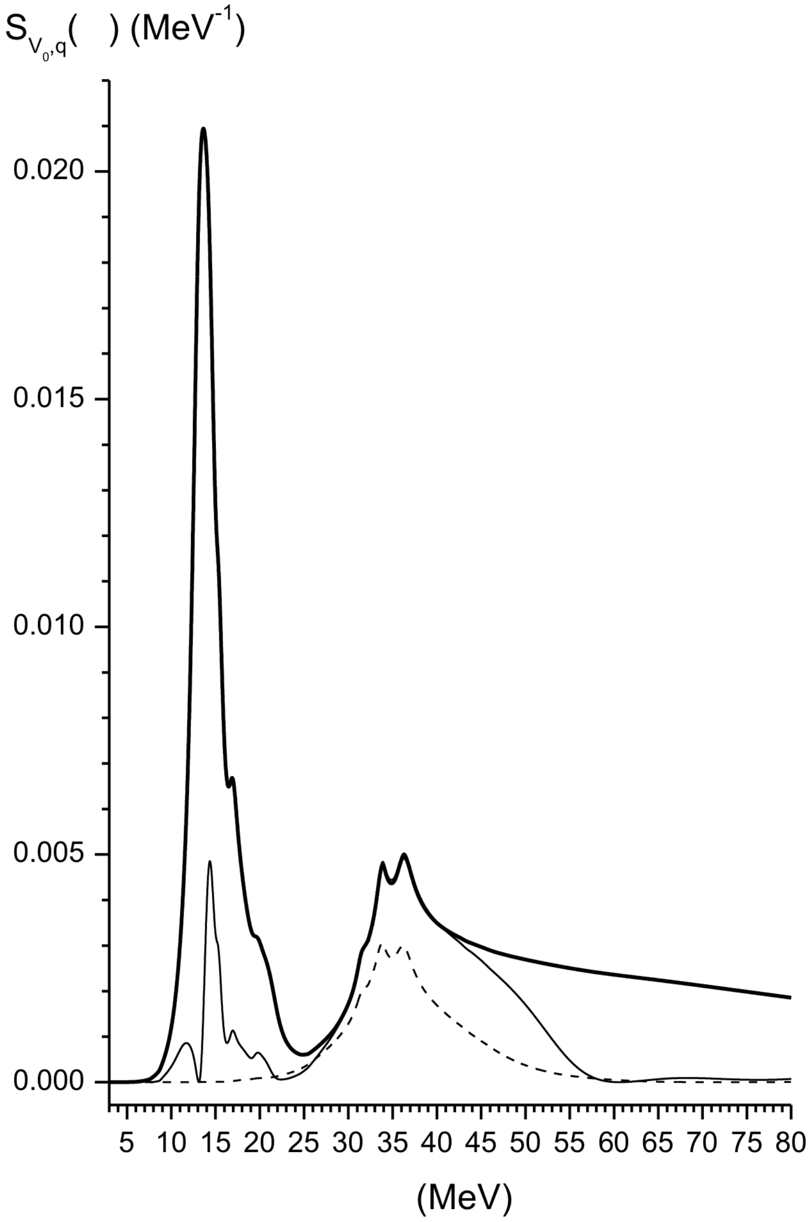

**FIG. 2.** Same as Fig. 1 but for the ISGMR2 (i=2).

[1] M.L. Gorelik, S. Shlomo, B.A. Tulupov, and M.H. Urin, Nucl. Phys. **A** (to be published).

# Isoscalar giant monopole resonances in $^{92,96,98,100}$Mo and $^{90,92,94}$Zr and the incompressibility coefficient of nuclear matter

G. Bonasera, S. Shlomo, D.H. Youngblood, Y.-W. Lui, Krishichayan, and J. Button

The centroid energies of the isoscalar and isovector resonances were calculated for multipoles up to L=3, within a spherical Hartree-Fock based Random Phase Approximation theory (HF-RPA), in $^{92,96,98,100}$Mo and $^{90,92,94}$Zr using 33 commonly employed Skyrme-type effective nucleon-nucleon interactions found in the literature [1].

Here we report on the study of the centroid energy of the Isoscalar Giant Monopole Resonance (ISGMR) as a function of the incompressibility of nuclear matter $K_{NM}$. As can be seen in Fig.1 although

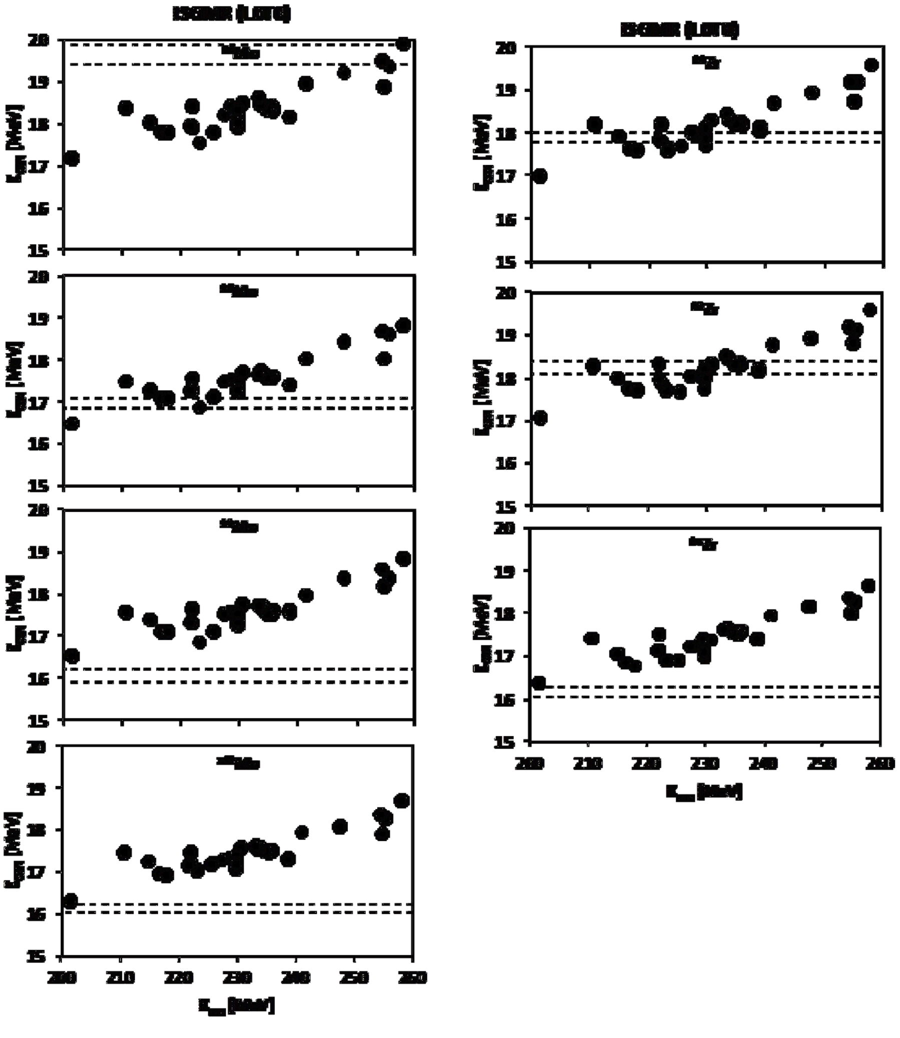

**FIG. 1.** Calculated Centroid Energies in MeV (full circle) of the low energy component of the Isoscalar Giant Monopole Resonance, for the 33 different Skyrme-type interactions, as a function of the incompressibility of nuclear matter $K_{NM}$. Each nucleus has its own panel and the experimental uncertainties are contained by the dotted lines. The Pearson correlation is strong with C~0.87 for all nuclei considered.

we see the usual dependence of the centroid energy on the Incompressibility (Pearson correlation coefficient is C ~ 0.87), we also find for the more neutron rich nuclei, namely $^{98,100}$Mo and $^{94}$Zr, that all the interactions considered here predict the centroid energy above the experimental value. Moreover for the strength distributions themselves, the theory predicts most of the strengths to fall in one symmetric peak, whereas the experimental data show a second peak at higher energy. This effect could be due to the larger deformation of the nucleus as we move farther away from the shell closure. We point out that the experimental analysis of the measured excitation cross sections was carried out using semi-classical transition densities which are independent of the excitation energy. Calculations of the excitation cross-sections with the use of energy-dependent transition densities, obtained from RPA calculations, are required to better understand this issue.

[1] G.Bonasera *et al.*, (to be submitted).

# Isovector giant dipole resonances in $^{40,48}$Ca, $^{68}$Ni, $^{90}$Zr, $^{116}$Sn, $^{144}$Sm, and $^{208}$Pb and the energy weighted sum rule enhancement factor

G. Bonasera, M.R. Anders, and S. Shlomo

We have performed fully self-consistent Hartree-Fock (HF)-based random phase approximation (RPA) calculations of the centroid energies for the isovector resonances up to L=3 multi-polarity for several spherical nuclei over a wide range of mass. The calculations were done using 33 different Skyrme-type effective nucleon-nucleon interaction commonly adopted in the literature.

The Pearson correlation coefficient is calculated for every nuclear matter (NM) property. We then compare our theoretical calculation to the available experimental data and in the cases where we have high correlation we can set limiting values on the NM properties. Here we report on a strong correlation between the Centroid Energies of the Isovector Giant Dipole Resonances and the energy weighted sum rule enhancement factor κ, which is obtained from the $m_1$ energy moment as

$$m_1(L, T = 1) = \frac{NZ}{A^2} m_1(L, T = 0)\left[1 + \kappa - \kappa_{np}\right] \qquad (1)$$

where the isoscalar moment is defined as $m_1(L, T = 0) = \frac{3}{4\pi}\frac{\hbar^2}{2m}A$ , $\kappa_{np}$ is a correction due to the profiles of the neutron and proton density distributions and N, Z, and A are the number of neutrons, protons and nucleons, respectively. In Fig. 1 we show that the centroid energies, of the isovector giant dipole resonance associated with each Skyrme interaction and every resonance, as a function of κ, have a strong Pearson correlation coefficient close to C~0.82 for all nuclei shown. Using the experimental data we can limit the value of κ to be between 0.2 and 0.7. Similar results were found for the isovector resonance with L=2 and 3. Analysis is performed for all the resonances and nuclei [1] and other nuclear matter quantities. These results will be used to determine the next generation nuclear energy density functional with improved predictive power for properties of nuclei and nuclear matter.

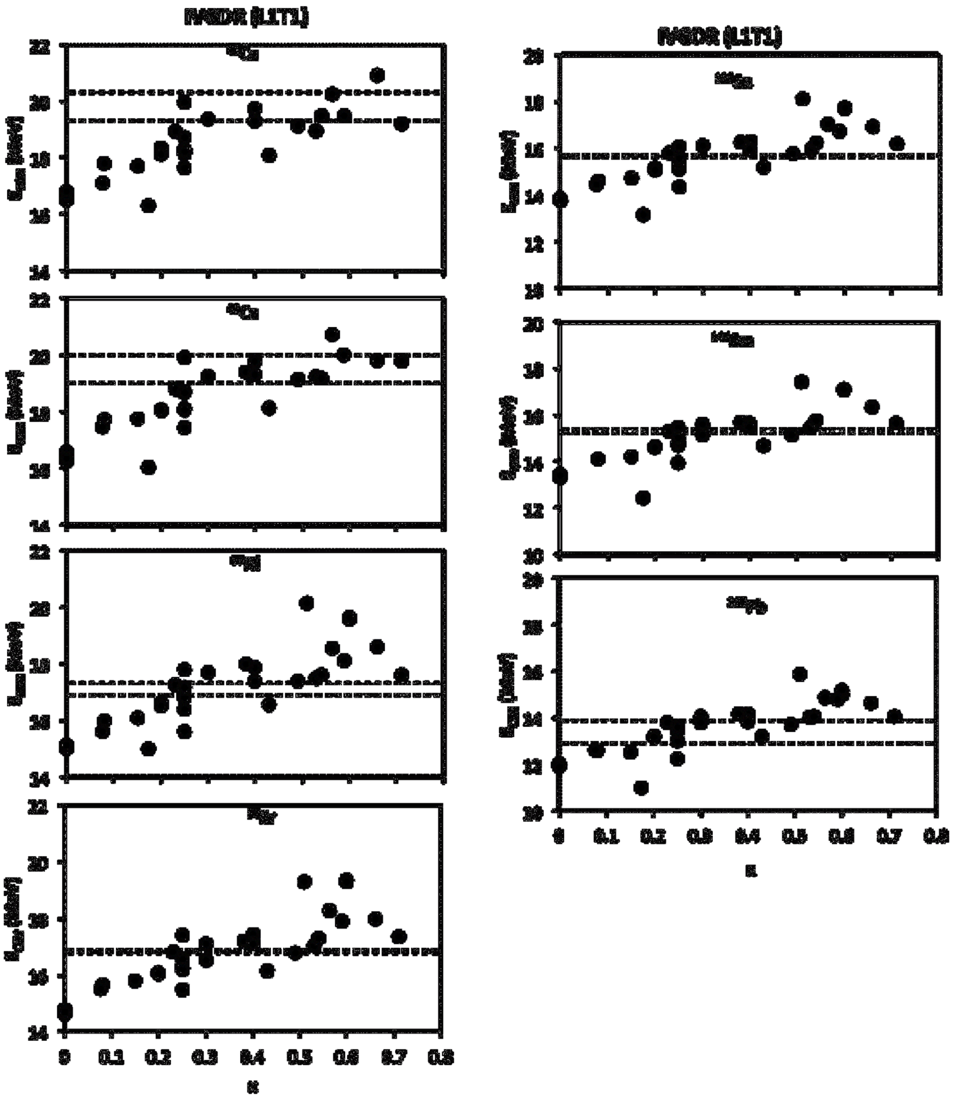

**FIG. 1.** Calculated Centroid Energies in MeV (full circle) of the isovector giant dipole Resonance, for the different interactions, as a function of the energy weighted sum rule enhancement factor κ. Each nucleus has its own panel and the experimental uncertainties are contained by the dotted lines. The Pearson coefficient is C~0.82 for all nuclei shown.

[1] G. Bonasera *et al.*, (to be submitted)..

# The symmetry energy density and isovector giant resonances energies in $^{208}$Pb

M.R. Anders and S. Shlomo

In this work [1], we have carried out fully self-consistent Hartree-Fock (HF)-based random phase approximation (RPA) calculations of the strength functions S(E) and centroid energies $E_{CEN}$ of isovector ($T = 1$) giant resonances of multipolarities $L = 0 - 3$ in $^{208}$Pb using a wide range of 34 commonly employed Skyrme type nucleon-nucleon effective interactions. We determined the sensitivities of $E_{CEN}$ to parameters of the symmetry energy density of nuclear matter (NM), associated with the Skyrme interactions.

The equation of state (EOS) of asymmetric NM, with proton density, $\rho_p$, and neutron density, $\rho_n$, can be approximated by

$$E[\rho_p, \rho_n] = E_0[\rho] + E_{sym}[\rho]\left(\frac{\rho_n - \rho_p}{\rho}\right)^2, \tag{1}$$

where $E_0[\rho]$ is the energy of symmetric NM at matter density, $\rho$, and $E_{sym}[\rho]$ is the symmetry energy, approximated as

$$E_{sym}[\rho] = J + \frac{1}{3}L\left(\frac{\rho - \rho_0}{\rho_0}\right) + \frac{1}{18}K_{sym}\left(\frac{\rho - \rho_0}{\rho_0}\right)^2, \tag{2}$$

where $J = E_{sym}[\rho_0]$ is the symmetry energy at saturation density, $\rho_0$, $L = 3\rho_0 \left.\frac{\partial E_{sym}}{\partial \rho}\right|_{\rho_0}$, and $K_{sym} = 9\rho_0 \left.\frac{\partial^2 E_{sym}}{\partial \rho^2}\right|_{\rho_0}$.

Figs. 1 and 2 show the comparison between the calculated and experimental results for the centroid energies with L and $K_{sym}$, respectively. It is clearly seen that, contrary to statements in the literature, a very weak correlation exist between the centroid energies of the isovector giant resonances and L or $K_{sym}$. Similar results were obtained for J.

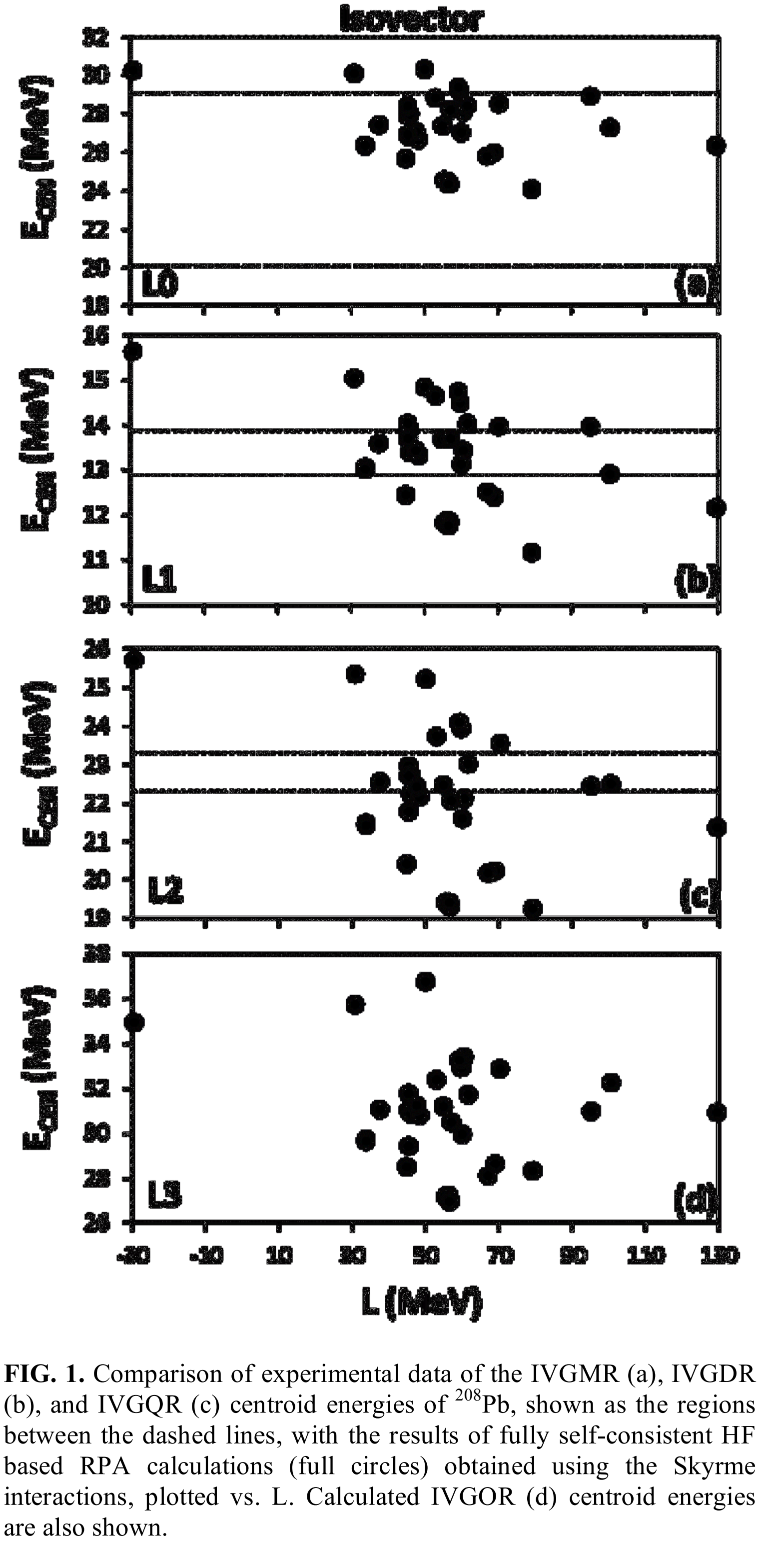

**FIG. 1.** Comparison of experimental data of the IVGMR (a), IVGDR (b), and IVGQR (c) centroid energies of $^{208}$Pb, shown as the regions between the dashed lines, with the results of fully self-consistent HF based RPA calculations (full circles) obtained using the Skyrme interactions, plotted vs. L. Calculated IVGOR (d) centroid energies are also shown.

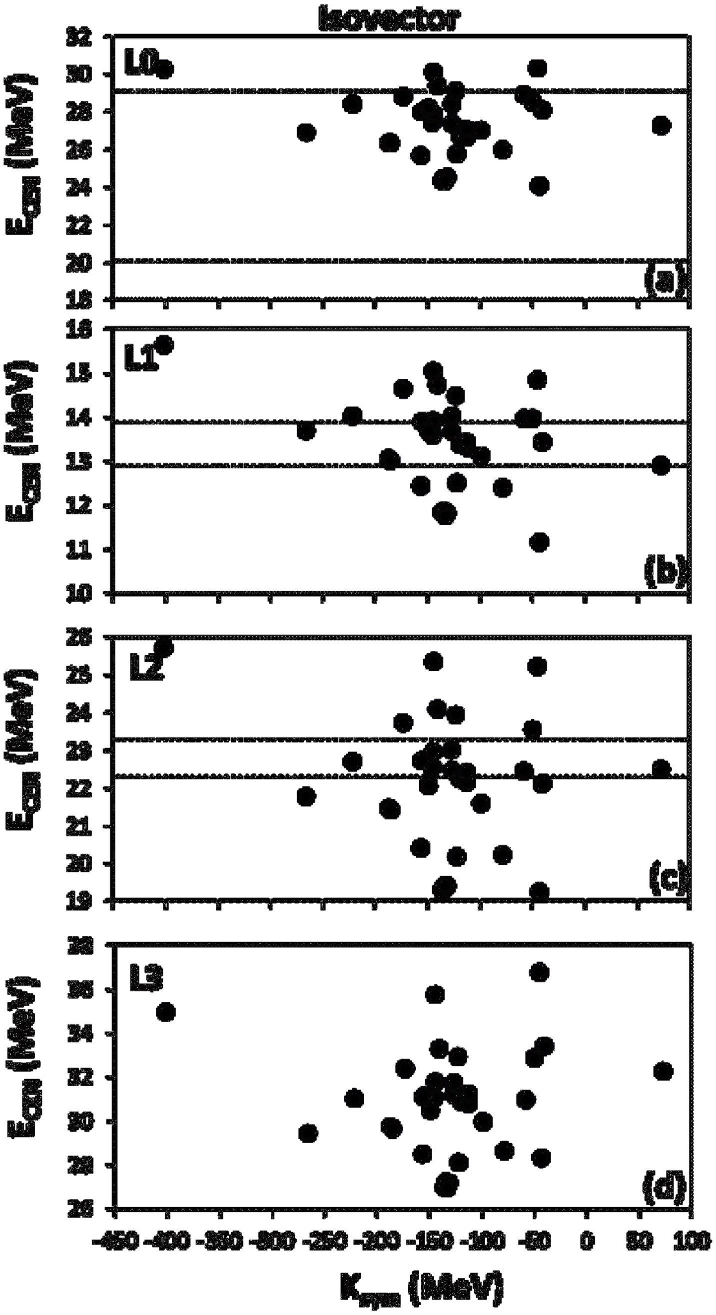

**FIG. 2.** Same as Fig. 1 for $K_{sym}$.

[1] M.R. Anders and S. Shlomo, (to be published).

# Theoretical corrections for the superallowed β decays of the proton-rich nuclei: $^{42}$Ti, $^{46}$Cr, $^{50}$Fe, and $^{54}$Ni

I.S. Towner and J.C. Hardy

In January 2015, Molina et al.[1] reported a measurement of the half-lives and Gamow-Teller branching ratios of the β decays of $^{42}$Ti, $^{46}$Cr, $^{50}$Fe and $^{54}$Ni, convincingly demonstrating that these nuclei are accessible and potentially amenable to more precise measurements. Therefore, it is appropriate that the radiative and isospin-symmetry-breaking corrections be likewise computed so that these transitions can be added to the data base of superallowed Fermi transitions [2] that are used in the determination of weak-interaction parameters, such as the CKM matrix element $V_{ud}$.

A $\beta$ transition is characterized by its *ft* value, where *f* is the statistical rate function and *t* is its partial half-life. To the *ft* value, two theoretical corrections are applied to produce a corrected $\mathcal{F}t$ value, which is defined as

$$\begin{aligned}\mathcal{F}t &= ft\,(1+\delta_R)(1-\delta_C)\\ &= ft\,(1+\delta_R')(1-\delta_C+\delta_{NS}) \qquad (1)\end{aligned}$$

Here $\delta_R$ is the nucleus-dependent part of the radiative correction, and $\delta_C$ is the isospin-symmetry-breaking correction. It is convenient to subdivide $\delta_R$ further as $\delta_R = \delta_R' + \delta_{NS}$ and, since the quantities are small, rearrange the equation to the form displayed in the second line of Eq. (1), which is correct to first order in these corrections. This rearrangement places the nuclear-structure-dependent corrections together in the combination $\delta_C$ - $\delta_{NS}$.

The calculated radiative corrections, $\delta_R'$ and $\delta_{NS}$, for the proton-rich nuclei considered here are given in Table I. The correction $\delta_R'$ comprises the bremsstrahlung and low-energy part of the $\gamma W$ – box graphs and is a standard QED calculation that depends only on the electron's energy and the charge *Z* of the daughter nucleus. The second component $\delta_{NS}$ recognizes that the $\gamma W$ – box graph includes situations in which the γ-nucleon interaction in the nucleus does not involve the same nucleon as that participating in the *W* - nucleon interaction. When this happens, two distinct nucleons are actively involved and a

**Table I.** Calculated radiative corrections $\boldsymbol{\delta_R'}$ and $\boldsymbol{\delta_{NS}}$, and isospin-symmetry-breaking corrections $\delta_{C1}$ and $\delta_{C2}$in percent units. The combination $\delta_C$ - $\delta_{NS}$ brings together all the corrections that are nuclear-structure dependent. From Ref. [3].

| Parent nucleus | $\delta_R'$ | $\delta_{NS}$ | $\delta_{C1}$ | $\delta_{C2}$ | $\delta_C$ - $\delta_{NS}$ |
|---|---|---|---|---|---|
| $^{42}$Ti | 1.427 | -0.235(20) | 0.105(20) | 0.855(60) | 1.195(66) |
| $^{46}$Cr | 1.420 | -0.175(20) | 0.045(20) | 0.715(85) | 0.935(90) |
| $^{50}$Fe | 1.439 | -0.155(20) | 0.025(20) | 0.635(45) | 0.815(53) |
| $^{54}$Ni | 1.430 | -0.165(20) | 0.065(30) | 0.725(60) | 0.955(70) |

detailed shell-model calculation is required to evaluate $\delta_{NS}$. More details on how the calculation is performed is given in Ref. [4].

For calculational convenience, the isospin-symmetry-breaking correction $\delta_C$ is separated into two components

$$\delta_C = \delta_{C1} + \delta_{C2} \tag{2}$$

The idea is that $\delta_{C1}$ follows from a tractable shell-model calculation (usually with a model space of one major oscillator shell) in which specific charge-dependent terms are added to the effective charge-independent interaction. Unfortunately, this procedure does not permit all the ramifications of mixing via the Coulomb force to be included. The correction $\delta_{C2}$ models the impact of Coulomb mixing as a change in the proton radial function. In the β-decay matrix element there is an overlap between the radial functions of the proton and the neutron that participate in the transition, and it is the reduction from unity of the overlap integral that leads to the correction $\delta_{C2}$. Details of how $\delta_{C1}$ and $\delta_{C2}$ are computed are given in Ref. [4] and the results for the proton-rich nuclei of interest here are given in Table I.

With these theoretical corrections now computed, the proton-rich nuclei $^{46}$Cr, $^{50}$Fe and $^{54}$Ni can be added to the data base [2] of superallowed Fermi transitions. Results for $^{42}$Ti were already included in the data base, but have been updated here to incorporate recent results pertaining to its charge radius.

[1] F. Molina *et al.*, Phys. Rev. C **91**, 014301 (2015).
[2] J.C. Hardy and I.S. Towner, Phys. Rev. C **91**, 025501 (2015).
[3] I.S. Towner and J.C. Hardy, Phys. Rev. C **92**, 055505 (2015).
[4] I.S. Towner and J.C. Hardy, Phys. Rev. C **77**, 025501 (2008).

# An in-medium heavy-quark potential from the $Q\bar{Q}$ free energy

Shuai Y.F. Liu and Ralf Rapp

The large suppression and elliptic flow of heavy-flavor spectra in heavy-ion collisions at RHIC and the LHC indicate that heavy quarks couple strongly to the quark gluon plasma (QGP), see Ref. [1] for a recent review. This finding calls for a tractable non-perturbative microscopic model that can bridge first-principles computations in thermal lattice QCD with experimental data. Toward this end we have been developing a many-body T-matrix approach, to evaluate the interactions of heavy quarks in the QGP and connect them to observables [2]. A key input to this approach is the in-medium two-body interaction potential (driving kernel) which must be determined with good accuracy to ensure reliable results. In the present work [3] we investigate the problem of extracting a static potential between a heavy quark and its antiquark in the QGP from lattice-QCD computations of the singlet free energy, $F_{Q\bar{Q}}$.

The original definition of the free energy $F_{Q\bar{Q}}$ [4] implies that it is related to the static $Q\bar{Q}$ 4-point Green function, which can be calculated within the many-body T-matrix formalism. We find that the free energy can be expressed from an underlying potential ansatz resummed in ladder approximation as,

$$F_{Q\bar{Q}}(r) = -T\,ln\left(\int_{-\infty}^{\infty} dE\,\frac{1}{\pi}\frac{(V+\Sigma)_I(E)}{(E-(V+\Sigma)_R(E))^2+(V+\Sigma)_I^2(E)}e^{-\beta E}\right).$$

In the weakly coupled limit, the imaginary part, $(V+\Sigma)_I$, is parametrically small and turns the Lorentzian function in the integrand into a Dirac δ-function, which implies that the real part of "potential", $(V+\Sigma)_R$, equals the free energy, $F_{Q\bar{Q}}(r)$. For a strongly coupled system, however, large imaginary parts of both $Q\bar{Q}$ potential-type and single-quark self-energies are expected from previous results of the T-matrix approach [3]. We find that such large imaginary parts, and in particular their energy dependence which figures in the integrand of the above expression, induce marked deviations of the potential from the resulting free energy. Indeed, when fitting lattice-QCD results [5] of the latter, we obtain a potential as shown in Fig. 1, which is characterized by significant long-range contributions from remnants of the confining force, in stark contrast to the free energy especially at low temperatures close to

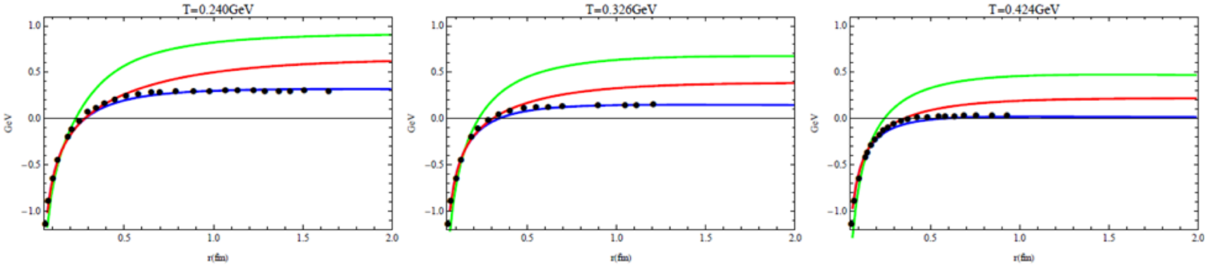
T=0.240GeV

T=0.326GeV

T=0.424GeV

**FIG. 1.** Our fit (blue/lower lines) to the color-singlet $\mathbf{Q\bar{Q}}$ free energy computed in lattice QCD (black dots) [5] at 3 different temperatures, T = 240, 326 and 424 MeV, in the left, middle and right panel, respectively. The red/middle lines are the real parts of the underlying potential, while the green/upper lines represent the corresponding internal energies.

$T_c$. Such a long-range force range will allow heavy quarks to interact with a large number of surrounding medium partons, with important consequences for the properties of heavy quarks and quarkonia in the QGP. For example, preliminary estimates of the pertinent heavy-quark transport coefficient indicate a very small spatial diffusion coefficient and short thermalization time, characteristic for a strongly coupled system.

[1] F. Prino and R. Rapp, arXiv:1603.00529.
[2] F. Riek and R. Rapp. Phys. Rev. C **82**, 035201 (2010); New J. Phys. **13**, 045007 (2011).
[3] S.Y.F Liu and R. Rapp. Nucl. Phys. **A941**, 179 (2015).
[4] L.D. McLerran and B. Svetitsky, Phys. Rev. D **24**, 450 (1981).
[5] O. Kaczmarek, PoS **CPOD07**, 043 (2007).

## Massive Yang-Mills for vector and axialvector spectral functions at finite temperature

Paul M. Hohler and Ralf Rapp

The spontaneous breaking of chiral symmetry (SBCS) in the QCD vacuum is induced by the formation of a (scalar) quark-antiquark condensate, which, however, is not an observable quantity. Rather, SBCS manifests itself in the excitations of the condensate, i.e., the hadron spectrum, where the degeneracy of chiral multiplets (or chiral "partners") becomes broken. Prominent examples are the massive splitting in the scalar-pseudoscalar channel ($\sigma$-$\pi$), the vector-axialvector ($\rho$-$\alpha_1$) and the nucleon and its chiral partner (N-N*(1535)). Of particular interest is the vector channel, as the medium modifications of the $\rho$ meson can be measured in experiment via dilepton invariant-mass spectra [1]. Utilizing QCD and Weinberg sum rules with in-medium order parameters from lattice QCD, it was found in Ref. [2] that the "melting-$\rho$" scenario, which describes available dilepton data, is compatible with chiral symmetry restoration. However, to unravel the mechanism underlying $\rho$-$\alpha_1$ degeneration a microscopic chiral description of both vector (V) and axialvector (AV) spectral functions is needed.

Toward this goal we previously developed a Massive-Yang Mills (MYM) approach (introducing $\rho$ and $\alpha_1$ mesons into the chiral pion lagrangian), which, in particular, enabled the description of the measured vacuum AV spectral function thanks to a resummed $\rho$ propagator in the $\alpha_1$ selfenergy while preserving chiral Ward identities [3]. In the present work [4] we have implemented this approach into a finite-temperature pion gas by evaluating the vacuum loop diagrams using standard thermal-field theory techniques in the Matsubara formalism. Special care has been taken to satisfy the Ward identities for the (partially) conserved (axial-) vector current at finite temperature by systematically evaluating the medium corrections to all vertex correction diagrams.

The resulting spectral functions for MYM in the linear realization of chiral symmetry (linear $\sigma$ model) are shown in Fig. 1. The $\alpha_1$ resonance exhibits a large broadening and significant mass shift toward the $\rho$-meson mass, while the latter is essentially stable. At the same time, the chiral order

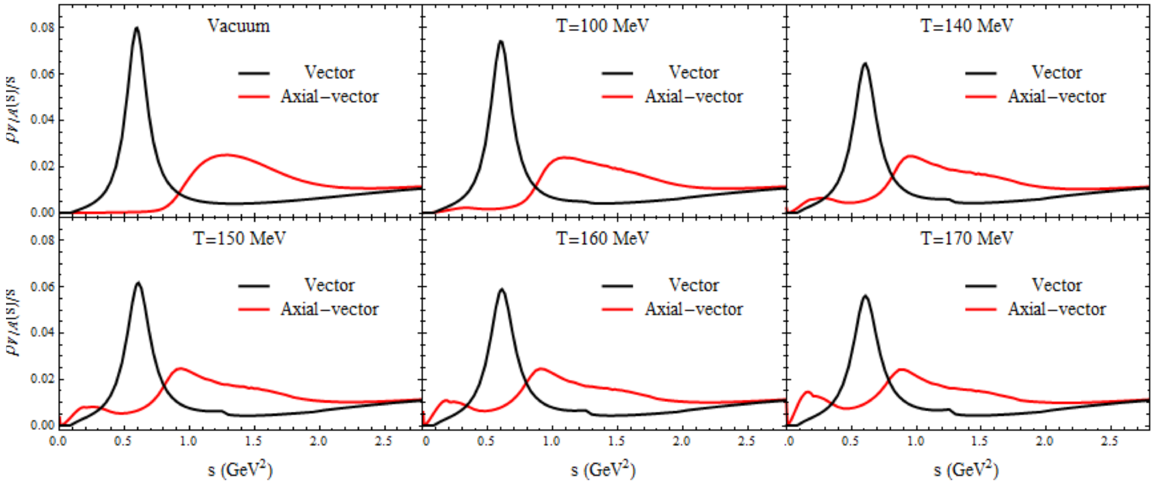

**FIG. 1.** Temperature progression of vector and axialvector spectral functions in a hot pion gas within the linear realization of Massive Yamg-Mills [4].

parameters calculated within the model, i.e., the pion decay constant and the scalar condensate, undergo a noticeable reduction of up to 15-20% at a temperature of T = 160 MeV. Very similar features are found when implementing MYM into the nonlinear pion lagrangian. Our findings can thus be considered robust and suggest that the approach toward chiral restoration (as indicated by the decrease of chiral order parameters) is realized by burning off the chiral mass splitting between ρ and $a_1$ mesons. This mechanism is remarkably similar to what we have found before using QCD and Weinberg sum rule techniques with a realistic in-medium ρ spectral function [2]. Such a mechanism has recently also been found in a lattice QCD computation of finite-temperature correlation functions of the nucleon and its chiral partner, the N*(1535); while the nucleon mass changed little with temperature, the N*(1535) mass drops toward the nucleon one, compatible with degeneration close to $T_c$.

Future work will be aimed at dressing the pion lines in the loop diagrams, and in particular include interactions with baryons into the MYM approach, as they are known to be an essential driver of the low-mass dilepton enhancement observed in heavy-ion experiments.

[1] R. Rapp, H. van Hees, and J. Wambach, Landolt Börnstein **23**, 134 (2010); arXiv:0901.3289[hep-ph].

[2] P.M. Hohler and R. Rapp, Phys. Lett. B **731**, 103 (2014).

[3] P.M. Hohler and R. Rapp, Phys. Rev. D **89**, 125013 (2014).

[4] P.M. Hohler and R. Rapp, Ann. Phys. **368**, 70 (2016).

[5] G. Aarts *et al.*, Phys. Rev. D **92**, 014503 (2016).

# Sequential regeneration of charmonia in heavy-ion collisions

Xiaojian Du and Ralf Rapp

The production systematics of heavy quarkonia, i.e., bound states of a heavy charm or bottom quark and its antiquark, in heavy-ion collisions have long been recognized as a valuable probe of the QCD matter produced in these reactions. Originally, quarkonium suppression was suggested as an indicator of the formation of a deconfined quark-gluon plasma (QGP), but regeneration processes through quark recombination complicate the interpretation of observables considerably, especially for charmonia at collider energies (RHIC and LHC) where charm quarks and antiquarks are produced abundantly. Over the last decade, a kinetic rate equation approach has been developed [1] which allows for a fair description [2], with predictive power [3], of charmonium and bottomonium observables from SPS via RHIC to LHC energies. Rather little attention has been paid to the production of the $\psi$(2S) state to date, primarily due to the difficulty in measuring it. However, recent experiments have shown rather intriguing results, such as a strong suppression in the small d-Au collision system at RHIC [4] versus an enhancement in central Pb-Pb collisions at the LHC [5].

In the present work [6] we have scrutinized $\psi$(2S) production in the rate equation approach. We have first developed a more complete treatment of hadronic dissociation rates by including inelastic reactions with 52 meson species. Assuming the formation of a thermal fireball in d-Au collisions at RHIC, with a significant hadronic phase, the increased absorption in the rate equation can account for the strong suppression of the $\psi$(2S) state observed by PHENIX [4], cf. Fig. 1.

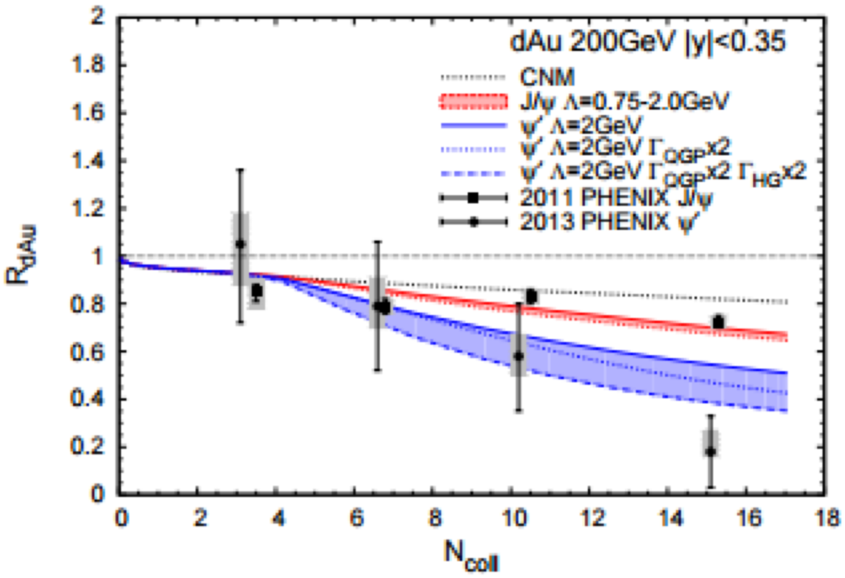

**FIG. 1.** Nuclear modification factor $R_{AA}$ for charmonia with improved treatment of hadronic suppression d-Au(0.2TeV) collisions at RHIC [6], compared to PHENIX data [4].

We have then implemented the updated treatment of the hadronic phase into calculations for Pb-Pb collisions at the LHC. Here, the inelastic hadronic reaction rates induce an appreciable *regeneration* of the $\psi$(2S) state, due to the large abundance of charm and anti-charm quarks. The small binding energy of the $\psi$(2S) compared to the J/$\psi$ state implies that the former is regenerated at lower temperatures, i.e., at later times in the fireball evolution. The stronger radial flow of the $\psi$(2S) at the time of regeneration leads to a $p_T$-dependent $R_{AA}$ which peaks a at higher momenta than for the J/$\psi$ state, cf. Fig. 2 left. This - *sequential regeneration* scenario provides a natural mechanism to explain the puzzling CMS data [5] where the $R_{AA}$ double ratio of $\psi$(2S) over J/$\psi$ exceeds unity for a $p_T > 3$ GeV cut in central Pb-Pb collisions, while showing a suppression for a $p_T > 6.5$ GeV cut, albeit with appreciable uncertainties both theoretically and experimentally, cf. Fig. 2 right.

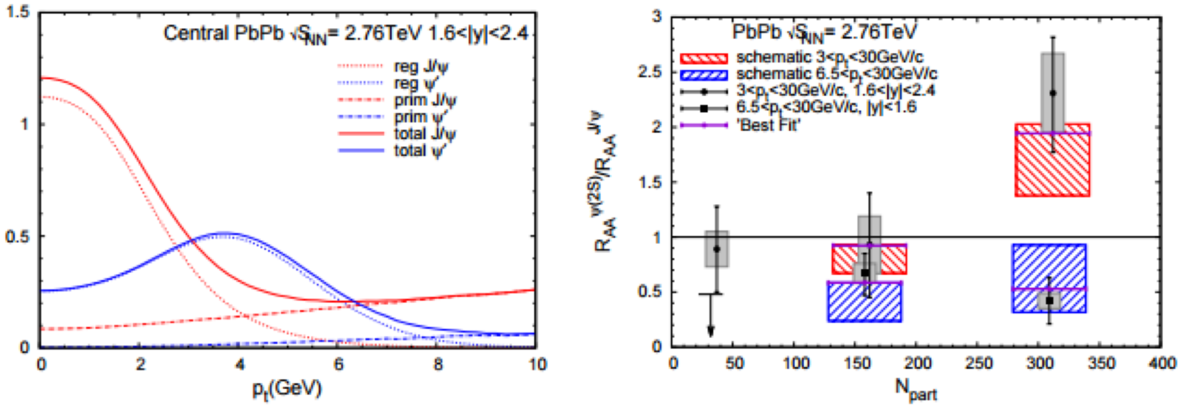

**FIG. 2.** Sequential regeneration mechanism for charmonia in Pb-Pb(2.76TeV) collisions at the LHC [6]. Left panel: Effect of larger flow from later regenerated ψ(2S) relative to J/ψ on their $p_T$-dependent $R_{AA}$ in central Pb-Pb(2.76TeV). Right panel: double ratio of ψ(2S) over J/ψ $R_{AA}$ vs. collision centrality with theoretical uncertainties, compared to CMS data [5].

[1] L. Grandchamp, R. Rapp, G.E. Brown, Phys. Rev. Lett. **92**, 212301 (2003).

[2] X. Zhao, R. Rapp, Phys. Rev. C **82**, 064905 (2010).

[3] X. Zhao and R. Rapp, Nucl. Phys. **A859**, 114 (2011).

[4] A. Adae et al. (PHENIX Collaboration), Phys. Rev. Lett. **111**, 202301 (2013).

[5] V. Khachatryan *et al.* (CMS Collaboration), Phys. Rev. Lett. **113**, 262301 (2014).

[6] X. Du and R. Rapp, Nucl. Phys. **A943**, 147 (2015).

# Thermal dileptons as fireball thermometer and chronometer

Ralf Rapp and Hendrik van Hees

Thermal radiation of dileptons has long been recognized as an excellent messenger of the hot and dense QCD medium formed in high-energy heavy-ion collisions. At low invariant masses, M < 1GeV, the dilepton spectra are dominated by decays of thermally produced ρ(770) mesons, thus directly probing the in-medium modifications of the ρ-meson line shape. At intermediate masses, 1GeV < M < 3GeV, the radiation is continuum-like, and its slope characterizes the (early) temperatures of the fireball medium.

In our recent work [1] we have updated our calculations of thermal dilepton spectra by using a modern lattice-QCD (lQCD) based equation of state for the expanding fireball medium [2]. Thermal emission rates from the quark-gluon plasma (QGP), constrained by lQCD correlation functions [3], are combined with hadronic emission rates based in on an ρ in-medium spectral function calculated from hadronic many-body theory [4]. The predicted broadening and ultimate melting of the ρ-resonance around a pseudo-critical temperature of $T_{pc}$ ~ 170MeV renders a smooth transition from the hadronic to the QGP emission rates. Convoluting these rates over the expanding fireball medium leads to the spectra shown in Fig. 1.

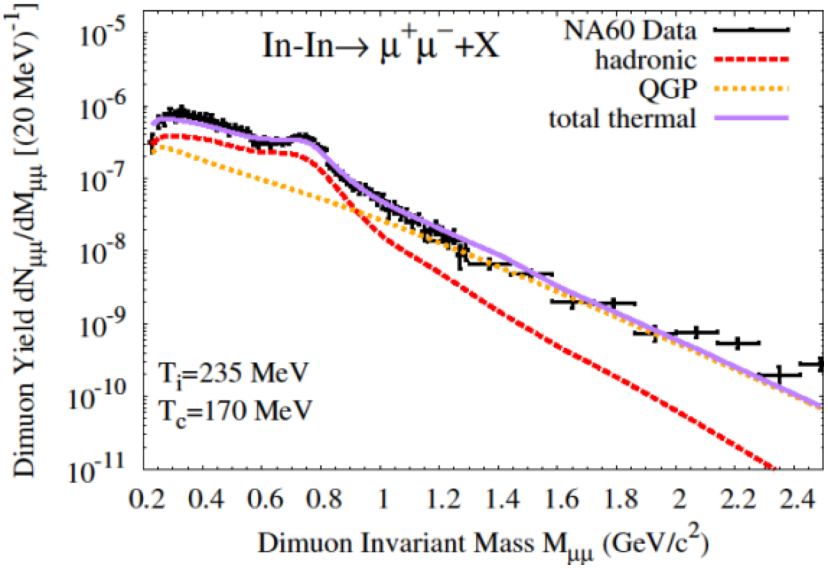

**FIG. 1.** Calculations of thermal dilepton spectra from the QGP (dotted line) and hadronic (dashed line) phases of an expanding fireball [1]. The sum (solid line) is compared to di-muon spectra measured by NA60 in In-In collisions at the SPS [5].

The agreement with the state-of-the-art NA60 dimuon data [5] in √s=17.3 GeV In-In collisions at the SPS allows for the following conclusions: (i) the spectral shape in the low-mass region confirms the melting of the ρ-meson and the total yield quantifies the fireball lifetime to be $\tau_{fb}$=7±1fm/c; (ii) at intermediate masses the spectra are dominated by QGP radiation; its spectral slope (which is blue-shift free) directly yields an average temperature of $T_{avg}$~205±12MeV, corroborating emission from temperatures above $T_{pc}$~170 MeV.

The above framework has been extensively tested in heavy-ion collisions over a large range of energies; it describes all available dilepton data, from HADES at SIS-18 (√s~2.5GeV) [6] via CERES and NA60 at SPS (√s=8.8,17.3GeV) to STAR at RHIC in the beam-energy scan (√s=19.6,27,39,62.4,200GeV) [7], including the recently revised PHENIX data [8]. Based on this robust understanding, we have extracted the excitation function of the low-mass dilepton yields and the spectral slopes of the intermediate-mass dilepton spectra from our calculations [1], cf. Fig. 2.

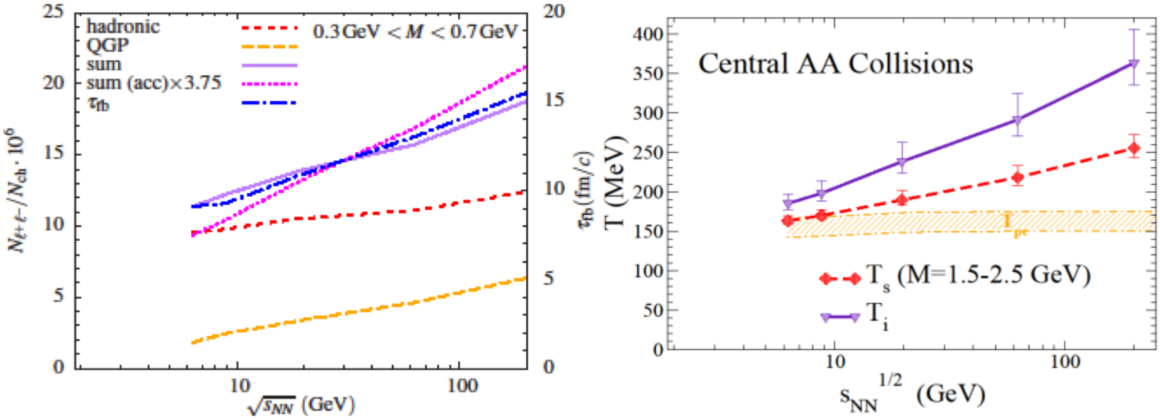

**FIG. 2.** Excitation functions of low-mass dilepton yields and corresponding fireball lifetime (left) and slope parameter, $T_s$, of intermediate-mass spectra compared to initial temperature, $T_i$, and $T_{pc}$ (right).

We have found that the low-mass yields are an excellent measure of the fireball lifetime, while the intermediate-mass slopes reflect an average temperature of the QGP emission source. This temperature closely reflects the transition temperature for collision energies below √s=10GeV, and may thus serve to map out the transition region and a possible onset of a first-order transition via the emergence of a quasi-plateau. At the same time, non-monotonous variations in the fireball lifetime may signal the vicinity to a second-order endpoint.

[1] R. Rapp and H. van Hees, Phys. Lett. B **753**, 586 (2016).
[2] M. He, R.J. Fries, and R. Rapp, Phys. Rev. C **85**, 044911 (2012).
[3] R. Rapp, Adv. High Energy Phys. **2013**, 148253 (2013).
[4] R. Rapp and J. Wambach, Eur. Phys. J. A **6**, 415 (1999).
[5] H.J. Specht *et al.* (NA60 Collaboration) AIP Conf. Proc. **1322**, 1 (2010).
[6] S. Endres, H. van Hees, J. Weil, and M. Bleicher, Phys. Rev. C **92**, 014911 (2015).
[7] P. Huck *et al.* (STAR Collaboration), Nucl. Phys. **A931**, 659 (2014).
[8] A. Adare *et al.* (PHENIX Collaboration), Phys. Rev. C **93**, 014904 (2016).

# Thermal photon emission from the $\pi\rho\omega$ system

Nathan Holt, Paul Hohler, and Ralf Rapp

Ultra-relativistic heavy-ion collisions produce fireballs of strongly-interacting matter at high temperatures and densities. Understanding the phases of this matter is at the forefront of nuclear physics research [1]. Hadronic probes of these fireballs undergo multiple rescatterings, thus losing much of the information from the interior of the fireball. Photons, however, do not interact via the strong nuclear force. Since their electromagnetic mean free paths are much larger than the fireball size, they escape relatively unaltered, carrying valuable information on the properties of the strongly-interacting matter from which they were emitted.

The collision zone in non-central heavy-ion collisions has an initial spatial anisotropy which gets converted into a momentum anisotropy, known as elliptic flow ($v_2$). There currently exists a discrepancy between state-of-the-art calculations and experimental data of direct photon spectra and $v_2$ [2]. In particular the large $v_2$, which takes time to develop, suggests that the expanding fireball contains strong thermal photon sources from the later, hadronic stages of its evolution. In Ref. [3] it was conjectured that there exist additional as-of-yet unidentified sources of thermal photons. In that work it was shown that enhancing the thermal photon emission by hand significantly alleviated the discrepancy between experimental data and calculations of direct photon spectra and $v_2$.

In the present work [4] we have identified a novel source of thermal photons from a system composed of $\pi$, $\rho$, and $\omega$ mesons. We have calculated thermal photon emission rates from scattering processes of $\pi\rho \to \gamma\omega$, $\pi\omega \to \gamma\rho$, and $\rho\omega \to \gamma\pi$ using both thermal field theory (TFT) and relativistic kinetic theory (KT). In our KT calculations for $\pi\omega \to \gamma\rho$ we encountered a singularity in the pion exchange associated with the $\omega \to \pi^0\gamma$ radiative decay, which has already been accounted for in previous works [5]. By using TFT, we both avoided the singularity and identified a criterion to avoid double-counting the $\omega$ radiative decay. In addition, we confirmed the equivalence of the frameworks of TFT and KT in thermal photon rate calculations.

Our resulting total rates from the $\pi\rho\omega$ system are shown in Fig. 1 and compared to existing calculations. We see that our rates are comparable to those from an $\omega$ $t$-channel exchange in $\pi\rho \to \gamma\pi$ scattering, which were earlier found to be significant [5]. Also shown are the rates from $\pi\pi$ scattering Bremsstrahlung [6,7], which are significant for the lower range of photon energies.

This identification of a novel source of thermal photons directly supports the conjecture from Ref. [3] of unaccounted-for hadronic sources of thermal photons which contribute to both photon spectra and $v_2$. Calculations of photon spectra and $v_2$ have been conducted which support our expectation of a significant contribution of our rates [8,9], thus helping to resolve discrepancies with current experimental data.

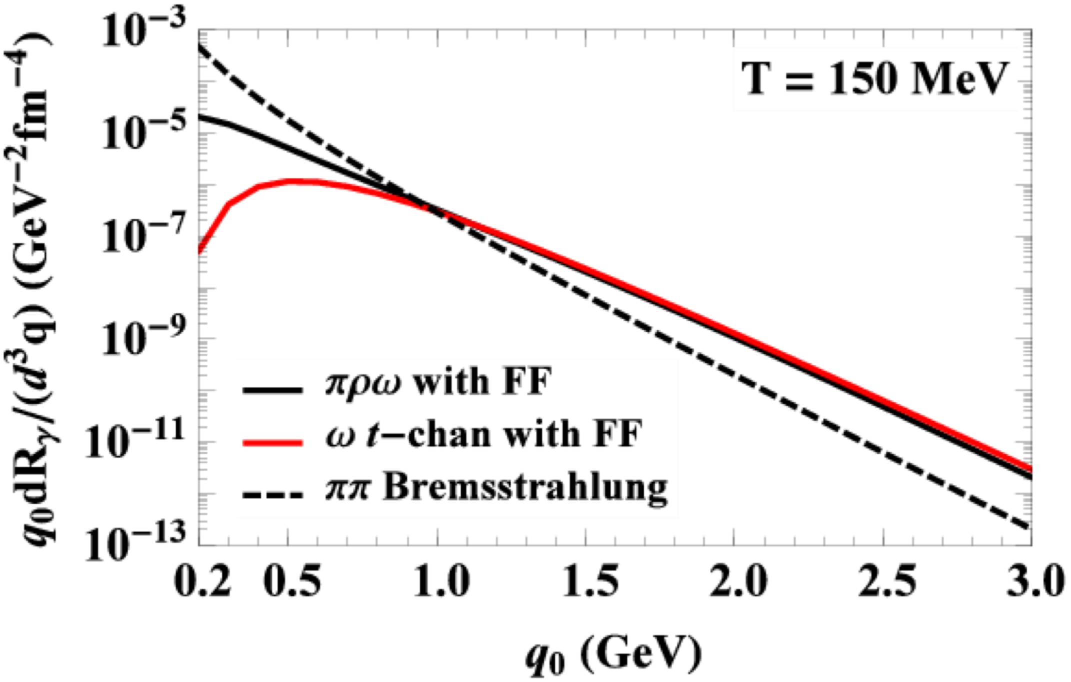

**FIG. 1.** Thermal photon rates at a temperature of T = 150 MeV from the πρω system [4] compared to ω t-channel exchange in πρ → γπ scattering [5] and ππ Bremsstrahlung [6,7].

[1] Y. Akiba *et al.*, arXiv:1502.02730 [nucl-ex].

[2] A. Adare *et al.* (PHENIX Collaboration), arXiv:1509.07758.

[3] H. van Hees, M. He, and R. Rapp, Nucl. Phys. **A933**, 256 (2014).

[4] N.P.M. Holt, P.M. Hohler, and R. Rapp, Nucl. Phys. **A945**, 1 (2015).

[5] S. Turbide, R. Rapp, and C. Gale, Phys. Rev. C **69**, 014903 (2004).

[6] W. Liu and R. Rapp, Nucl. Phys. **A796**, 101 (2007).

[7] M. Heffernan, P. Hohler, and R. Rapp, Phys. Rev. C **91**, 027902 (2015).

[8] J.-F. Paquet *et al.*, Phys. Rev. C **93**, 044906 (2016).

[9] S. Endres, H. van Hees, and M. Bleicher. Phys. Rev. C **93**, 054901 (2016).

# Anomalous transport model study of chiral magnetic effects in heavy ion collisions

Y.F. Sun, C.M. Ko, and Feng Li

Based on the anomalous transport model, which includes the propagation of massless partons according to the chiral kinetic equation [1-4] and allows the change of parton chiralities during their scattering, we have studied the elliptic flow difference between positively and negatively charged partons in non-central relativistic heavy ion collisions [5]. Using initial conditions from a blast wave model and assuming the presence of a strong and long-lived magnetic field, we have obtained an appreciable charge quadrupole moment in the transverse plane of the collision, which then leads to different elliptic flows for particles of positive and negative charges. The elliptic flow difference shows a linear dependence on the total charge asymmetry $A_\pm$ in the collision as show in Fig. 1, where $A_\pm = (N_+ - N_-)/(N_+ + N_-)$ with $N_+$ and $N_-$ being the total number of positively and negatively charged particles. These results are similar to those found from studies based on the anomalous hydrodynamics using similar initial conditions and assuming similar strength and lifetime for the magnetic field [6]. Compared to the experimental data on the elliptic flow difference between positively and negatively charged particles, ours is, however, much smaller. A larger elliptic flow difference could be obtained if we allow the ratio of the charge chemical potential to the temperature in the initial blast wave to be larger in its center and smaller on its surface. Also, the different elliptic flows between charged particles could be partly due to the different mean-field potentials between particles and antiparticles in the partonic [7] and the hadronic [8] matter of finite baryon chemical potential [9]. Nonetheless, our study does indicate that the application of the anomalous transport model based on the chiral kinetic equation to heavy ion collisions can describe the effect of the chiral magnetic wave (CMW) on the elliptic flow of massless fermions of different charges in the

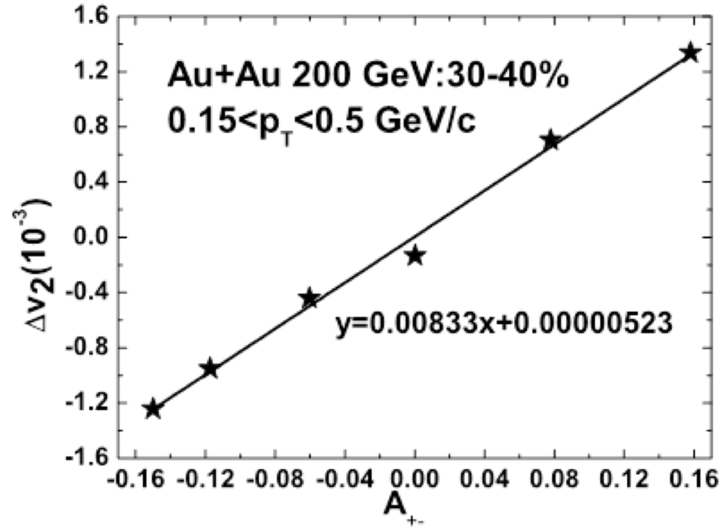

**FIG. 1.** Elliptic flow difference $\Delta v_2$ between negatively and positively charged particles as a function of charge asymmetry $A_\pm$.

presence of a strong magnetic field. However, the justification for the existence of a long-lived magnetic field in relativistic heavy ion collisions remains missing, although its strength is known to be sufficiently strong. More work is needed to understand this very intriguing phenomenon that might be present in relativistic heavy ion collisions.

[1] M.A. Stephanov and Y. Yin, Phys. Rev. Lett. **109**, 162001 (2012).

[2 ] D.T. Son and N. Yamamoto, Phys. Rev. Lett. **109**, 181602 (2012).

[3] J.-W. Chen, S. Pu, Q. Wang, and X.-N. Wang, Phys. Rev. Lett. **110**, 262301 (2013).

[4] C. Manual and J.M. Torres-Rincon, Phys. Rev. D **90**, 076007 (2014).

[5] Y.F. Sun and C.M. Ko, (to be published).

[6] H.-U. Yee and Y. Yin, Phys. Rev. C **89**, 044909 (2014).

[7] C.M. Ko, T. Song, F. Li, V. Greco, and S. Plumari, Nucl. Phys. **A928**, 234 (2014).

[8] J. Xu, L.-W. Chen, C. M. Ko, and Z.-W. Lin, Phys. Rev. C **85**, 041901 (2012).

[9] J. Xu, T. Song, C.M. Ko, and F. Li, Phys. Rev. Lett. **112**, 012301 (2014).

# Heavy quark correlations and the effective volume for quarkonia production in heavy ion collisions

J.P. Liu,[1] C.M. Ko, and F. Li
[1]*Phyiscs Department, Tianjian University, Tianjin, China*

Using the Boltzmann transport approach, we have studied the effect of initial spatial and momentum correlations between a heavy quark pair, such as that produced from a $p + p$ collision, on their collision rate in a partonic medium [1] that is relevant for their thermalization and the production of quarkonium from regeneration [2, 3]. Characterizing this effect by an effective volume given by the inverse of the ratio of their collision rate to the collision rate of a thermally equilibrated and spatially uniformly distributed heavy quark pair in a unit volume, we have found that the effective volume is finite and depends sensitively on the momentum of the heavy quark and the temperature of the medium. Generally, it increases linearly with time $t$ at the very beginning, thus an enhanced collision rate, and the increase then becomes slower due to multiple scattering, and finally it increases as $t^{3/2}$ as shown in Fig.1.

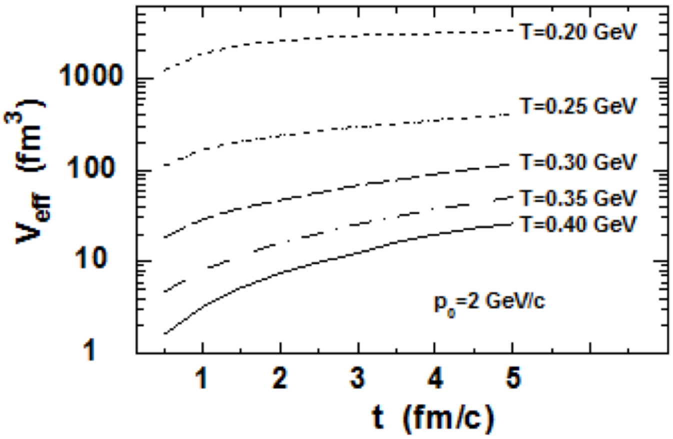

**FIG 1**. Time evolution of the effective volume $V_{eff}$ of heavy quarks with initial charm momentum $p_0 = 2$ GeV/c for different medium temperatures.

Consequently, the chance for a heavy quark pair to collide with each other per unit time decreases monotonically with time. Also, heavy quarks of lower initial momentum in a medium of higher temperature have a larger chance to collide. Furthermore, the distribution of the center of mass energy of the heavy quark air is found to correspond to an effective temperature that is lower than the actual temperature of the medium. All these properties are important for quarkonium regeneration in collisions where heavy quarks are rarely produced.

[1] Y.P. Liu, C.M. Ko, and F. Li, Phys. Rev. C **93**, 034901 (2016).
[2] M.I. Gorenstein, A. Kostyuk, H. Stoecker, and W. Greiner, Phys. Lett. B **509**, 277 (2001).
[3] A. Andronic, P. Braun-Munzinger, K. Redlich, and J. Stachel, Nucl. Phys. **A789**, 334 (2007).

# Jet fragmentation via recombination of parton showers in vacuum

K. Han, R. Fries, and C.M. Ko

We have devised a model to hadronize perturbative parton showers in jets based on quark recombination [1]. This is achieved by turning perturbative parton showers into showers of constituent quarks and antiquarks by gluon decay, and then applying Monte Carlo methods to recombine quarks and antiquarks using probabilities given by the overlap integrals of their Gaussian wave packets with meson and baryon Wigner functions [2]. For remnant quarks and antiquarks that are not used for recombination, they are connected to form short strings and subjected to the usual string fragmentation procedure in PYTHIA [3]. As an example, we have studied hadron production from $e^+$+$e^-$ collisions at center of mass energy of 200 GeV using shower partons generated from PYTHIA. Fig. 1 shows the longitudinal (through the momentum fraction z of the jet) and transverse momentum spectrum $p_T$ of pions, kaons, protons, and Lambdas obtained from recombination, remnant fragmentation, and their sum. For the recombination contribution, we fix the cutoff parameters in meson and baryon Wigner functions by the charge radii of pion, kaon, and proton, and also include decays of excited states from recombination. It is seen that low momentum hadrons are mainly produced from recombination while high momentum ones are dominated by string fragmentation of remnant partons, reflecting the decreasing recombination probability of shower partons with their momentum. The sum of the recombination and short-string fragmentation qualitatively reproduces the results from PYTHIA string fragmentation of original parton showers. Our study differs from early works using quark recombination for hadronization of jets [4] in that parton showers in our study are obtained from the sophisticated parton Monte Carlos available today instead of from fitting to data or from specific models. In addition, earlier works used event-averaged spectra, ignoring fluctuations coming from the small number of partons in each jet. Work is in progress to

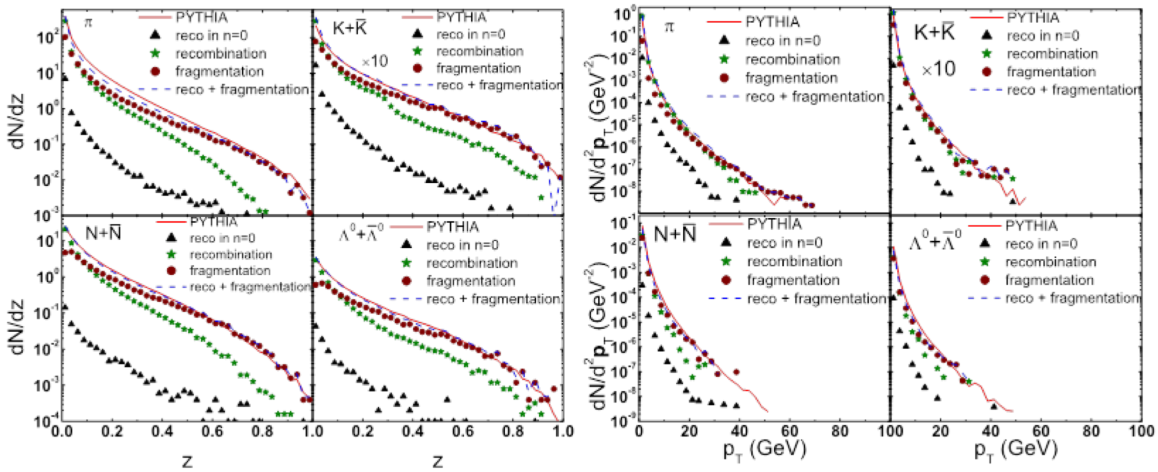

**FIG 1.** Longitudinal momentum fraction dN/dz (left window) and transverse momentum pT spectrum (right window) of pions (upper left panel), kaons (upper right panel), nucleons and antinucleons (lower left panel), and Lambdas and antilambdas (lower right panel) from the recombination of shower partons (stars), fragmentation of remnant partons (circles), and their sum (dashed lines), compared with results from PYTHIA string fragmentation (solid lines) for jets produced in $e^+$+$e^-$ collisions at center of mass energy of 200 GeV.

generalize present approach to include partons from an ambient medium such as the quark-gluon plasma (QGP) produced in relativistic heavy ion collisions by allowing shower partons to recombine with thermal partons at phase transition temperature.

[1] K.C. Han, R. Fries, and C.M. Ko, Phys. Rev. C **93**, 045207 (2016).

[2] V. Greco, C.M. Ko, and P. Levai, Phys. Rev. Lett. **90**, 202302 (2003); Phys. Rev. C **68**, 034904 (2003).

[3] T. Sjostrand, S. Mrenna, and P.Z. Skands, JHEP **0605**, 026 (2006).

[4] R.C. Hwa and C.B. Yang, Phys. Rev. C **70**, 024904 (2004).

# Light (anti-)nuclei production and flow in relativistic heavy-ion collisions

L.L. Zhu,[1] C.M. Ko, and X.J. Yin[1]

[1]*Department of Physics, Sichuan University, Chengdu 610064, China*

We have studied the production of light normal and hyper nuclei and their anti-nuclei in heavy ion collisions at the LHC by using the coalescence model [1]. With the phase-space distributions of protons, neutrons, and Lambdas as well as their antiparticles at freeze out taken from the AMPT model [2] and taking the Wigner functions of these nuclei to be of Gaussian form with their width parameters fitted to the known radii, we have calculated the transverse momentum spectra and elliptic flows of $^2$H-like nuclei that include $^2$H and anti-$^2$H, of $^3$H-like nuclei that include $^3$H, $^3$He, anti-$^3$H, and anti-$^3$He, and of $^3_\Lambda$H-like nuclei that include $^3_\Lambda$H, $^3_\Lambda$He, $^3_\Lambda$n, anti-$^3_\Lambda$H, anti-$^3_\Lambda$He, and anti-$^3_\Lambda$n.

For the transverse momentum spectra, we have found that the default version of the AMPT model gives a better description of the experimental data from the ALICE Collaboration [3,4] for proton and deuteron than the string-melting version of the AMPT model as shown in Fig. 1, and this has been attributed to the baryon problem in the current string-melting version of the AMPT code. From the total yield of these nuclei, we have verified the experimental observation that the yield of light nuclei is reduced by about two orders of magnitude with the addition of a nucleon or Lambda to a nucleus.

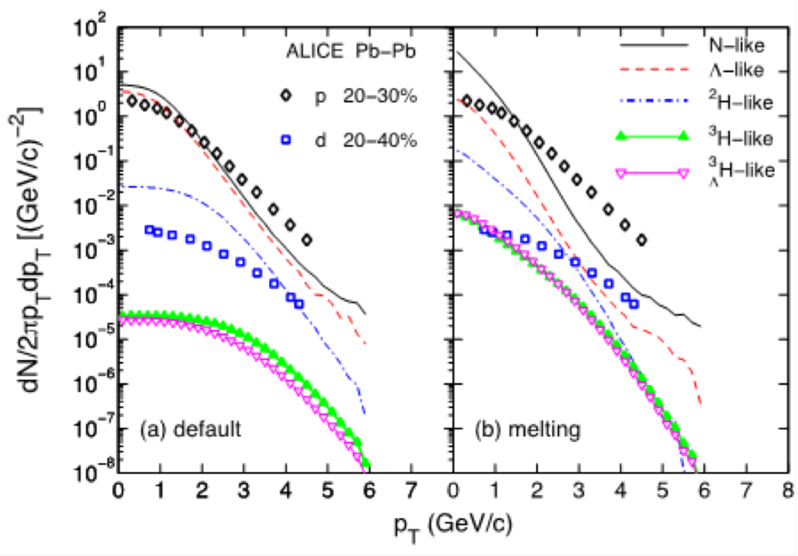

**FIG 1.** Transverse momentum spectra of N-like (solid line), Λ-like (dashed line), and $^2$H-like (dash-dotted line), $^3$H-like (filled triangles), $^3_\Lambda$H-like (open triangles) at midrapidity $|y| \leq 0.5$ from the default (left panel) and the string melting (right panel) AMPT model for Pb+Pb collisions at $\sqrt{s_{NN}} = 2.76$ TeV and impact parameter b = 8 fm. Data for protons (open diamonds) and deuterons (open squares) are from the ALICE Collaboration [3,4].

For the elliptic flows of these nuclei shown in Fig. 2, they are found to show a mass ordering behavior with the heavy nuclei having a smaller elliptic flow, like that in the hydrodynamic description of heavy ion collisions. This behavior is seen in both the default and the string melting AMPT model. We have further found that the elliptic flows of light nuclei display an approximate constituent number scaling in that their elliptic flows at transverse momentum per constituent is the same as a function of the transverse momentum divided by the number of constituents, particularly in the case of the default AMPT model.

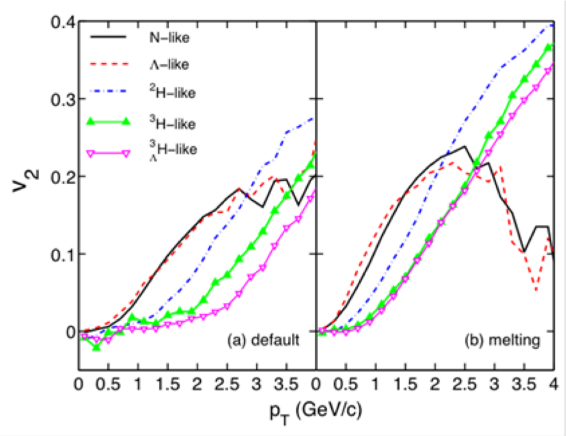

**FIG 2.** Elliptic flows of N-like (solid line), Λ-like (dashed line), and $^2$H-like (dash-dotted line), $^3$H-like (filled triangles), $^3{}_\Lambda$H-like (open triangles) at midrapidity $|y| \leq 0.5$ from the default (left panel) and the string melting (right panel) AMPT model for Pb+Pb collisions at $\sqrt{s_{NN}} = 2.76$ TeV and impact parameter b = 8 fm.

We have further studied the coalescence parameter $B_A$ for light nuclei, which is defined by the ratio of the invariant transverse momentum spectrum of a nucleus to that of its constituents being raised to the power corresponding to the number of constituents in the nucleus. Our results based on both the default and string melting AMPT models indicate that the coalescence parameter increases with increasing transverse momentum of a nucleus, similar to that extracted from the experimental data. Their values are, however, a factor of two larger for $B_2$ and a factor of two smaller for $B_3$ in the case of the default AMPT model. In the string-melting version of the AMPT model, the value of $B_2$ is almost an order of magnitude larger than data at high momentum, but that of $B_3$ agrees with the data.

[1] L.L. Zhu, C.M. Ko, and X.J. Yin, Phys. Rev. C **92**, 064911 (2015).

[2] Z.W. Lin, C.M. Ko, B.A. Li, B. Zhang, and S. Pal, Phys. Rev. C **72**, 064901 (2005).

[3] J. Adam *et al*. (ALICE Collaboration), Phys. Rev. C **93**, 024917 (2016).

[4] J. Adam *et al*. (ALICE Collaboration), Phys. Lett. B **754**, 360 (2016).

# Spinodal instability in baryon-rich quark matter

F. Li and C.M. Ko

The baryon-rich quark matter is expected to undergo a first-order phase transition at finite baryon density. Using the Polyakov Nambu-Jona-Lasinio (PNJL) model [1], which shows both the deconfinement and chiral phase transitions of quark matter at high temperature and density, we have studied the spinodal instability in a baryon-rich quark matter in the linear response theory [2]. Shown in Fig. 1 is the spinodal boundary in the temperature and density plane for different values of the wave number k of the unstable mode in the cases with (right window) and without (left window) a repulsive quark interaction. It is seen that the boundary of the spinodal region shrinks with increasing wave number, and for the same wave number, it is reduced by the repulsive quark vector interaction.

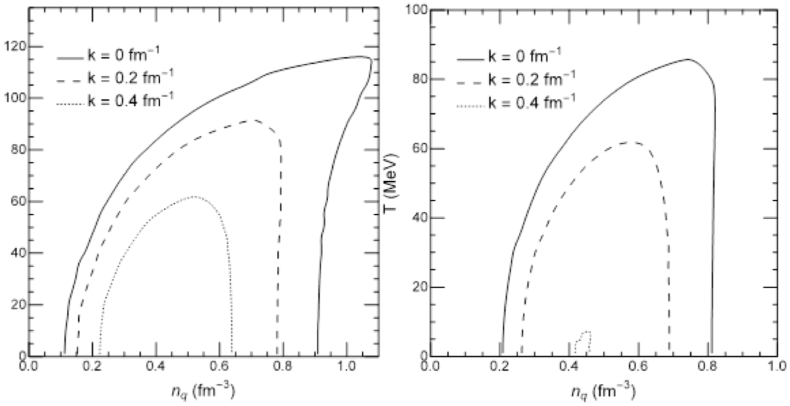

**FIG 1.** Spinodal boundaries in temperature and net quark density plane for different wave numbers with quark vector interaction $G_V = 0$ (left window) and $G_V = 0.2\ G_S$ (right window).

We have also calculated the growth rate of the unstable mode, which is given by the imaginary part of its dispersion relation, as a function of the wave number. For quark matter at temperature T = 70 MeV and net quark density nq = 0.7 fm-3, the growth rate of the unstable model in the absence of vector interaction first increases with the wave number and then decreases with the wave number after reaching a peak value of about 0.01 fm-1 at k ~ 0.15 fm-1. The growth rate is, however, significantly reduced after including the quark vector interaction, resulting in a suppression of the spinodal instability that is greater for unstable modes of shorter wavelength.

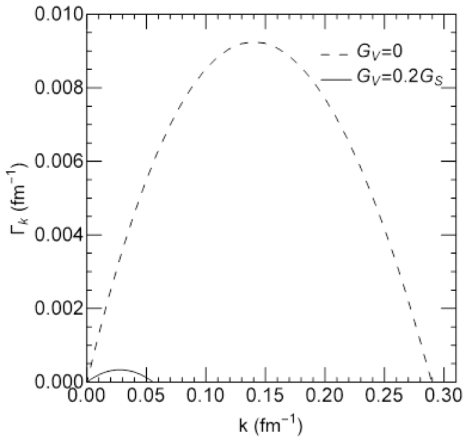

**FIG 2.** Growth rate of unstable modes in a quark matter of net quark density $n_q = 0.7$ fm$^{-3}$ and at temperature T = 70 MeV for quark vector interactions $G_V = 0$ and $G_V = 0.2\ G_S$.

We have further derived a Boltzmann equation based on the Nambu-Jona-Lasinio (NJL) model. It is being solved [3] by the test particle method to study how density fluctuations grow in a baryon-rich quark matter and their effects on physical observables such as the net baryon number [4], rapidity distribution [5] event-by-event fluctuations, the anisotropic flows [6], and the dilepton yield.

[1] K. Fukushima, Phys. Lett. B **591**, 277 (2004).
[2] F. Li and C.M. Ko, Phys. Rev. C **93**, 035205 (2016).
[3] F. Li and C.M. Ko, (to be published).
[4] M.A. Stephanov, Phys. Rev. Lett. **102**, 032301 (2009).
[5] B. Tomasik, M. Schulc, I. Melo, and R. Kopecna, arXiv:1511.00034 [nucl-th].
[6] J. Steinheimer, J. Randrup, and V. Koch, Phys. Rev. C **89**, 034901 (2014).

# The JET collaboration

R.J. Fries and C.M. Ko

The DOE-funded era of the JET Collaboration has successfully come to an end in 2015. The JET collaboration (Topical Collaboration on Jet and Electromagnetic Tomography of Extreme Phases of Matter in Heavy-ion Collisions) was founded in 2009 with initially 16 PIs. 2 PIs were added later, hired in junior faculty positions partially supported by JET. Columbia University, Duke University, Kent State University, Lawrence Berkeley National Laboratory, Lawrence Livermore National Laboratory, Los Alamos National Laboratory, McGill University, Ohio State University, Purdue University, Texas A&M University, University of Colorado, and Wayne State were participating institutions. Che-Ming Ko and Rainer J. Fries at the Texas A&M Cyclotron Institute were among the 16 original PIs of the collaboration.

In 2010 JET was selected as one of 3 topical collaborations in nuclear theory in the first round of solicitations for these new funding instruments. DOE provided funds for postdoc and students, collaboration travel, bridging funds for two junior faculty positions, and support for an annual summer school. At the Cyclotron Institute Kyong Chol Han received his Ph.D. in 2016 on a topic that is directly related to the JET collaboration mission.

Members of the JET collaboration worked on many aspects of hard and electromagnetic probes in high-energy nuclear collisions. A list of publications and other related information can be found on the collaboration wiki page [1]. Particularly noteworthy are three efforts that were milestone achievements of the collaboration.

1. The collaboration published an integrated package (iEBE) for event-by-event viscous hydrodynamic and hadron cascade hybrid model simulations for relativistic heavy-ion collisions. The package is publicly available and allows users to run simulations of the bulk of high energy nuclear collisions.
2. The collaboration extracted the best known value of the jet quenching parameter $\hat{q}$ from leading hadron observables comparing various perturbative calculations of jet quenching with experimental data. The result is $\hat{q} = 1.2 \pm 0.3$ GeV$^2$/fm for 10 GeV quark jets at a temperature around 370 MeV [2].
3. The collaboration constructed all modules needed for a comprehensive in-medium jet shower Monte Carlo (MC). Two parton shower MCs (the Berkeley-Wuhan MC and MATTER++) are now available. The Cyclotron Institute developed a universal hadronization model for jets in vacuum and in medium based on quark recombination and string fragmentation [3].

The DOE-funded era of the JET collaboration and its achievements were celebrated with the entire high energy nuclear physics community at a symposium at McGill University in June 2015, held before the Hard Probes 2015 conference. The JET collaboration will continue its work past its status as a DOE topical collaboration.

[1] http://jetwiki.lbl.gov

[2] Karen M. Burke *et al.*, Phys. Rev. C **90**, 014909 (2014).

[3] Kyong Chol Han, Rainer J. Fries, and Che Ming Ko, Phys. Rev. C **93**, 045207 (2016).

# Early time dynamics of gluon fields in high energy nuclear collisions

G. Chen, R.J. Fries, J.I. Kapusta, and Y. Li

The initial interactions of nuclei colliding at very high energies have been investigated for the last two decades, in order to understand the initial conditions from which quark gluon plasma (QGP) is formed. From experimental data collected at the Relativistic Heavy Ion Collider (RHIC) and the Large Hadron Collider (LHC) we have found that QGP is indeed created and that it is near local kinetic equilibrium very early in the collision (< 1 fm/c). This can be induced from simulations using ideal or viscous relativistic hydrodynamics that are applicable once the system is close to equilibrium. However, the precise initial conditions are still poorly known.

Although direct experimental evidence is still scarce there are very good theoretical arguments that the very first stage of the collision is dominated by a phase of quantum chromodynamics (QCD) called color glass condensate (CGC) in which gluons reach a saturation density ($\sim Q_s^2$) in hadrons or nuclei moving close to the light cone. $Q_s$ is called the saturation scale. Before the collision, and up to a time scale $\sim 1/Q_s$ after the collision color glass should be effectively described by the classical Yang Mills equations coupled to suitably defined color currents on the light cone. After the time $\sim 1/Q_s$ the classical approximation breaks down as fields decohere, and the system is driven towards chemical and kinetic equilibrium. The latter part is still under investigation, but with our work we have effectively solved the first part of the puzzle of the initial phase.

The classical Yang Mills problem immediately after the collision has been solved numerically by several groups in recent years. Our work presents a systematic *analytic* solution based on an expansion of the fields as power series in proper time [1]. A recursion for the coefficients of these series has been found. A resummation into known functions is possible in simple cases, but even in the most general case one can get results for the initial fields and the initial energy momentum tensor order-by-order in time. This method delivers reliable results up to times $\sim 1/Q_s$ at which point the entire classical approximation to CGC loses validity. Results for the initial gluon field strength and the energy momentum tensor are calculated as functions of the color charges in the initial nuclei. For a given collision they are unknown but reasonable models for their statistical distributions exist. We follow the McLerran-Venugopalan model of independent Gaussian fluctuations of charges around a color-neutral mean and calculate expectation values for the components of the energy momentum tensor.

We highlight a few results. It is straight forward in our approach to derive results for the time evolution of initial energy density, transverse pressure and longitudinal pressure in the system after the collision. For example for the ratio of longitudinal to transverse pressure up to second order in time, $\tau$, we find the pocket formula (neglecting some logs),

$$\frac{p_L}{p_T} \approx -\frac{2-3Q_s\tau}{2-2Q_s\tau}.$$

Fig. 1 gives a more detailed account of initial pressures (normalized to energy density) up to fourth order in time. We show a well-established numerical results in comparison [2]. Note that our analytic approach fails around $\tau \sim 1/Q_s$ as expected.

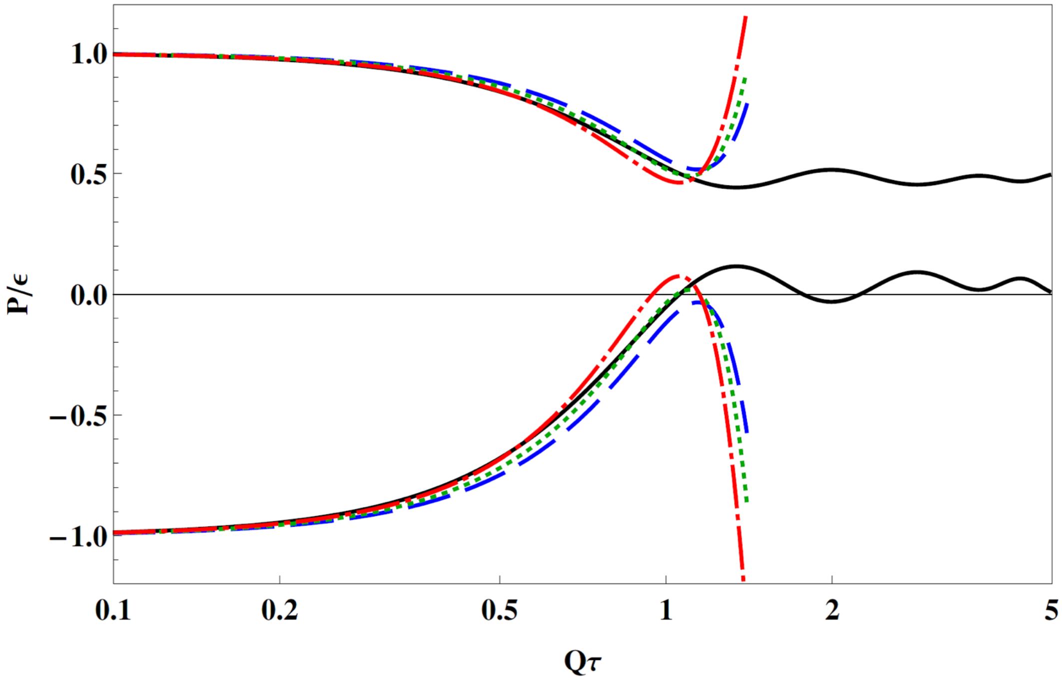

**FIG. 1.** The ratio of transverse pressure to energy density (upper curves) and longitudinal pressure to energy density (lower curves) calculated analytically from our approach for three different numerical treatments of ultraviolet and infrared cutoffs (red dashed-dotted, blue dashed and green dotted lines). For comparison we show the numerical solution of Epelbaum and Gelis [2] (black solid line).

Our approach also yields some interesting insights into early flow phenomena. In particular it established a mechanism how rapidity-odd flow (like directed flow) and angular momentum can be built up in the system. Some of those results have been discussed already in a previous publication [3]. In summary, we found a viable analytic solution to the problem of calculating the very initial time evolution of key quantities in high energy nuclear collisions.

[1] Guangyao Chen, Rainer J. Fries, and Joseph I. Kapusta, Yang, Phys. Rev. C **92**, 064912 (2015).
[2] T. Epelbaum and F. Gelis, Phys. Rev. Lett. **111**, 232301 (2013).
[3] Guangyao Chen and Rainer J. Fries, Phys.Lett. B **723**, 417 (2013).

# Jet fragmentation via recombination of parton showers

K. Han, R.J. Fries, and C.M. Ko

The fragmentation and hadronization process of QCD (quantum chromodynamics) jets has been under investigation for many decades. Partons (quarks or gluons) created by hard (large momentum transfer) processes are not eligible final states since they carry color charges. Rather, such partons have to turn into systems of hardons. They are called jets since they exhibit large boosts in the direction of the original parton, due to the large total momentum carried in the lab frame. Jets have historically been observed in $e^{+}+e^{-}$ collisions, e+p collisions, and p+p collisions. Over the past few years they have been found in A+A (nucleus-nucleus) collisions at the Large Hadron Collider (LHC) and the Relativistic Heavy Ion Collider (RHIC).

The fragmentation of a single parton into a jet of hadrons involves both perturbative and non-perturbative processes. Initially the parton is off-shell and radiates, building up an entire parton shower. This process is modelled based on perturbative principles in many jet shower Monte Carlo generators, like PYTHIA or HERWIG. In A+A collisions the parton shower may be modified due to the presence of quark gluon plasma (QGP), and Monte Carlo simulations describing jet-medium interaction on the parton level are currently being developed. Several models are available to describe the step of hadronizing the parton shower into hadrons. The most successful ones, developed for jets in the vacuum, i.e. not specifically for jets in A+A collisions, are the Lund string model and the cluster hadronization model. None of these are derived from first principles, but they are phenomenologically very successful. In this project [1], carried out as part of our commitment to the JET collaboration, we have developed a new model for hadronization of parton showers, which is based on a hybrid approach including quark recombination and string fragmentation. The advantage of using quark recombination to model hadronization lies in the fact that it is straight forward to generalize to A+A collisions. Recombination of quarks has successfully described many aspects of hadron production in nuclear collisions.

We assume that the Wigner function of the parton shower is provided by a shower Monte Carlo. For our first study [1] we used PYTHIA to estimate the Wigner function of vacuum jets. We used standard PYTHIA to generate showers with a fixed jet energy in momentum space. We introduced the average life-time of intermediate states in their rest frame based on their virtuality. This allowed us to reconstruct expectation values for the space-time positions of the partons in the shower at the end of their perturbative evolution. For each parton we then postulate Gaussian wave packets of a certain width to arrive at a factorized Wigner function for the shower. Gluons are split into quark-antiquark pairs using their remnant virtuality.

We then use the established quark recombination formalism, which allows us to calculate the probability of a quark-anti-quark pair coalescencing into a meson, or a quark triplet coalescencing into a baryon, using the Wigner function of the quarks, and the Wigner function of the bound state. We model hadrons using harmonic oscillator Wigner functions, both for ground and excited states. The parameters of the ground state Wigner functions are fitted to experimentally measured charge radii. We then apply Monte Carlo techniques to decide which partons in a given shower recombine into hadrons. Partons far apart from others in phase-space, e.g. leading partons with large momentum, have small probabilities to recombine. In our model these remnant partons are still connected by strings, and we apply string fragmentation, executed by PYTHIA, to hadronize those remnant partons. Fig. 1 shows results from our model for an ensemble of 100 GeV vacuum showers compared to PYTHIA string fragmentation. We reproduce both the longitudinal and transverse momentum distributions of various hadron species. In the future we will allow recombination of shower partons of jets embedded in QGP with thermal partons. First studies provide promising results.

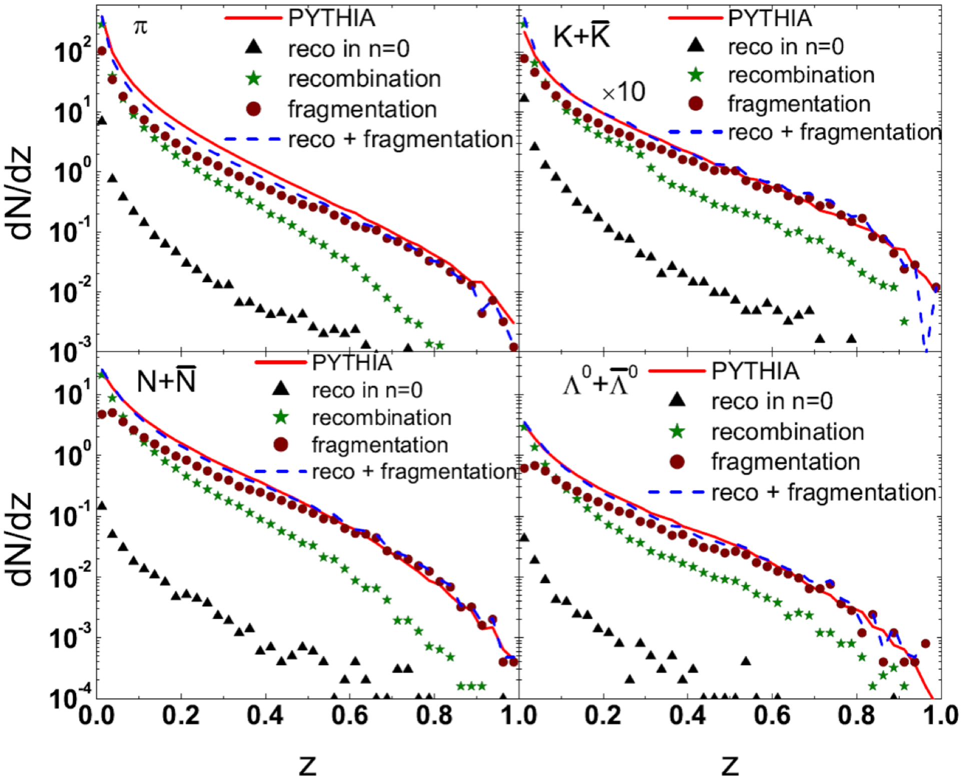

**FIG. 1.** Longitudinal momentum distribution dN/dz in terms of the momentum fraction z of the jet for (clockwise from top left) pion, kaons, Lambdas, and nucleons in 100 GeV quark jets. We show the results from the recombination and string hybrid model discussed here (blue dashed line) compared to pure PYTHIA string fragmentation (red solid line). We also show contributions from remnant strings (brown dots), recombination (green stars), and recombination only into ground state hadrons (black triangles).

[1] Kyong Chol Han, Rainer J. Fries, and C.M. Ko, Phys. Rev. C **93**, 045207 (2016).

# SECTION IV

# SUPERCONDUCTING CYCLOTRON AND INSTRUMENTATION

# K500 operations and development

D.P. May, G.J. Kim, B.T. Roeder, H.L. Clark, and F.P. Abegglen

## Introduction

During the 2015-2016 reporting period a total of 31 different beams, including 15 newly developed beams, were used for experiments, and there were a total of 37 beam tunings for these experiments. The SEE program and the charge-breeding effort are treated separately in this progress report.

## Ion Sources

During the shutdown ECR1 was opened for examination, and it was found that there had been no further deterioration in the damaged spot that had developed over a plasma flute on the aluminum wall..

## Cyclotron Beams

New beams of $^{3}$HD at 24 AMeV, $^{4}$He at 24 AMeV, $^{6}$DHe at 12 AMeV, $^{7}$Li at 24 AMeV,$^{10}$B at 18.2 and 19.2 AMeV, $^{14}$N at 55 AMeV, $^{16}$O at 14 AMeV, $^{28}$Si at 45 AMeV, $^{78}$Kr at 15 and 25 AMeV, $^{84}$Kr at 14 AMeV, $^{86}$Kr at 15 and 25 AMeV were developed for experiments. In addition, a beam of $^{85}$Rb at 14 AMeV was developed using the charge-breeding ECR3 ion source for a light-ion-guide (LIG) test.

## Operations

For the period April 1, 2015 through March 31, 2016, the operational time is summarized in Table I, while Table II lists how the scheduled time was divided.

**Table I.** 2015-2016 operational time.

| Time | Hrs. | %Time |
|---|---|---|
| Beam on target | 6400 | 73 |
| Beam development | 800 | 9 |
| Scheduled maintenance | 1093 | 13 |
| Unscheduled maint | 443 | 5 |
| **Total** | **8736** | **100.0** |

**Table II.** 2015-2016 Scheduled Beam Time.

| **Time** | **Hrs.** | **%Time** |
|---|---|---|
| Nuclear physics | 1190.0 | 16.5 |
| Nuclear chemistry | 1509.5 | 21.0 |
| Outside collaboration | 0.0 | 0.0 |
| Outside users | 3700.5 | 51.4 |
| Beam development | 800.0 | 11.1 |
| **Total** | **7200.0** | **100.0** |

# Texas A&M cyclotron radiation effects facility
## April 1, 2015 – March 31, 2016

H.L. Clark, J. Brinkley, L. Chen, G. Chubarian, S. Gerlt, V. Horvat, B. Hyman,
B. Roeder, and G. Tabacaru

The activity of the Radiation Effects Facility (REF) increased over the previous reporting year. In this reporting period, the facility was used for 3,042 hours, which is a ~1% increase over the 3,024 hours used in the 2014-2015 reporting period and tied highest usage year ever (3,042 in reporting year 2010-2011). Users of the facility (and hours used) over the past year were: Ryoei-Japan (265.5), Sandia National Lab (226), SEAKR (206.5), Honeywell (171), Cobham (168.5), Northrop Grumman (163.5), BAE Systems (151), NASA GSFC (149), Lockheed Martin (148), International Rectifier (141.5), NASA JPL (135.5), Intersil (100.5), NASA LRC (88), Boeing Corporation (81.25), Ball Aerospace (72.75), Thales Alenia-France (71), NAVSEA (56), VPT Inc (56), HIREX-France (54), Texas Instruments (48), L-3 Communications (34), Harris Corporation (33), Defense Threat Reduction Agency (32), Airbus-France (32), KAIST-Korea (32), Johns Hopkins (29.5), Scientic (25.5), General Dynamics (24), JAXA-Japan (24), Microsemi (24), TRAD-France (24), Ensign-Bickford (20), Freebird (16), IRCOS (16), Teledyne DALSA-France (16), ATMEL-France (15), IMT-Italy (14.5), Radiation Group (13), Data Device Corp (12), DSO-Singapore (10.5), Orbital ATK (9.5), Applied Nanotech (8), Custom Test Systems (8), Millennium Space (8), and T2 Research (8). New users included KAIST-Korea, Ensign-Bickford, Freebird, Teledyne DALSA-France, Radiation Group, Applied Nanotech, Custom Test

**Table I.** Radiation Effects Facility usage by commercial and government customers for this and previous reporting years.

| Reporting Year | Total Hours | Commercial Hours (%) | Government Hours (%) |
|---|---|---|---|
| 2015-2016 | 3,042 | 2,326 (76%) | 716 (24%) |
| 2014-2015 | 3,024 | 1,975 (65%) | 1,049 (35%) |
| 2013-2014 | 2,399 | 1,517 (63%) | 882 (37%) |
| 2012-2013 | 2,626 | 1,856 (71%) | 770 (29%) |
| 2011-2012 | 2,673 | 1,630 (61%) | 1,043 (39%) |
| 2010-2011 | 3,042 | 1,922 (63%) | 1,121 (37%) |
| 2009-2010 | 2,551 | 1,692 (66%) | 859 (34%) |
| 2008-2009 | 2,600 | 1,828 (70%) | 772 (30%) |
| 2007-2008 | 2,373 | 1,482 (62%) | 891 (38%) |
| 2006-2007 | 2,498 | 1,608 (64%) | 890 (36%) |
| 2005-2006 | 2,314 | 1,314 (57%) | 1,000 (43%) |
| 2004-2005 | 2,012 | 1,421 (71%) | 591 (29%) |
| 2003-2004 | 1,474 | 785 (53%) | 689 (47%) |
| 2002-2003 | 1,851 | 1,242 (67%) | 609 (33%) |
| 2001-2002 | 1,327 | 757 (57%) | 570 (43%) |
| 2000-2001 | 1,500 | 941 (63%) | 559 (37%) |
| 1999-2000 | 548 | 418 (76%) | 131 (24%) |
| 1998-1999 | 389 | 171 (44%) | 218 (56%) |
| 1997-1998 | 434 | 210 (48%) | 224 (52%) |
| 1996-1997 | 560 | 276 (49%) | 284 (51%) |
| 1995-1996 | 141 | 58 (41%) | 83 (59%) |

Systems, and Millennium Space.

Table I compares the facility usage by commercial and government customers. While commercial hours still dominate, the ratio from this reporting year (76% to 24%) is the lowest in government usage year since the 1999-2000 reporting period (see Fig. 1). Commercial hours increased by 18% and government hours decreased by 32% over hours from 2014-2015. This is largely due to the steady increase in foreign usage of the facility. 15 MeV/u ions were the most utilized and especially 15 MeV/u Au. No new beams were added to SEELine users list. Much of the testing conducted at the facility continues to be for defense systems by both government and commercial agencies. Almost 25% (559 hours) of the commercial hours were for foreign agencies from France, Italy, Korea, and Singapore. It is expected that the facility will continue to be as active in future years.

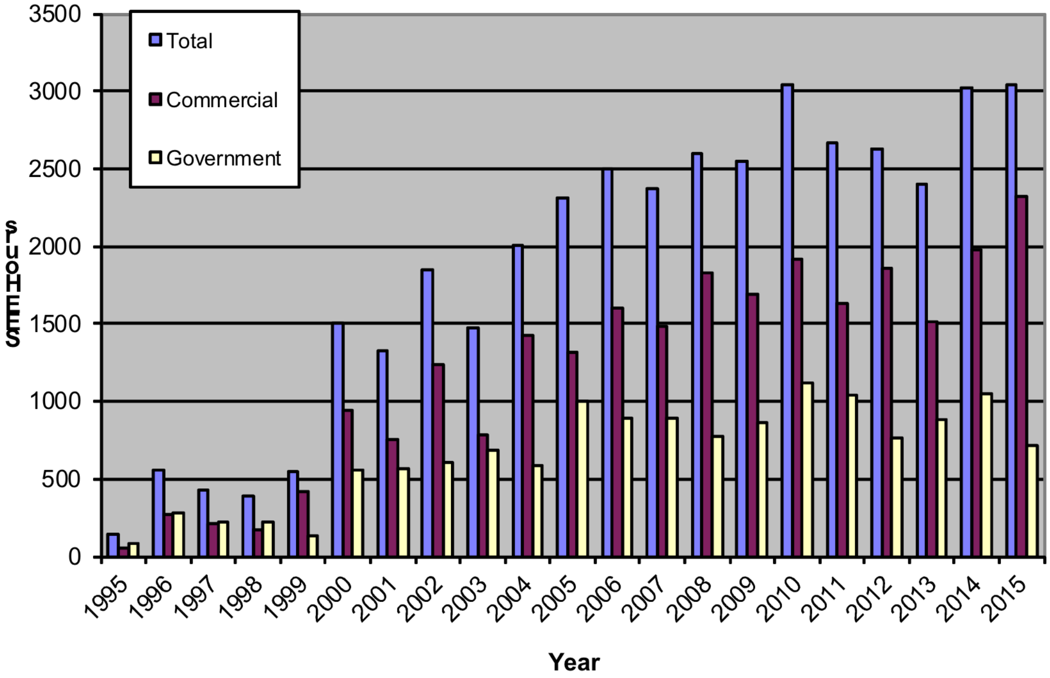

**FIG. 1.** Radiation Effects Facility usage by commercial and government customers for this and previous reporting years. While commercial hours still dominate, the ratio from this reporting year (76% to 24%) is the lowest in government usage year since the 1999-2000 reporting period. Almost 25% (559 hours) of the commercial hours were for foreign agencies from France, Italy, Korea, and Singapore.

# K150 operations and development

G.J. Kim, B.T. Roeder, F. Abegglen, H. Clark, L. Gathings, D.P. May, and H. Peeler

## Introduction

We had a very busy year operating the K150 cyclotron. For the reporting period we logged over 6100 hours of beam-on-target or for beam developments. The 15 MeV proton beam was produced regularly throughout the year for the light ion guide (LIG) project. A few 14 and 15 AMeV heavy ion beams were developed and used in experiments, and several 12 AMeV beams, such as $^{6}\mathrm{Li}^{3+}$, $^{26}\mathrm{Mg}^{10+}$, $^{27}\mathrm{Al}^{10+}$, $^{28}\mathrm{Si}^{10+}$, and $^{32}\mathrm{S}^{11+}$, were extracted and were used by the Tribble and Rogachev groups for experiments in the MDM cave. The Rogachev group also requested a number of 3rd harmonic 1.0 AMeV beams, and fortunately we were able to tune these beams out for them; this is discussed in more detail below. The STAR/LIBERACE group ran four times, using 28 MeV proton and 55 MeV alpha beams; the alpha beam was transported to the neutron ball cave for the first time and the beam optics scheme is discussed below. Also, the K150 beams have been used in two new projects: a feasibility study of the astatine-211 production from irradiation of 29 MeV alpha beam on a bismuth target, and the inauguration of SEE testing using K150 protons beams; the details are discussed below.

## Beam Transport to LIG

We accelerated 15 MeV protons over a dozen separate times for the LIG project. However, the beam transport to the LIG target has been somewhat inconsistent, partly because no viewer or a faraday cup at the target position was available to help guide the beam. The beam current was simply optimized on a faraday cup (FC23) 1.5 m downstream of the LIG target. Later it was realized that getting a small beam spot was important, given that the size of the LIG production target is only 16 mm and that the beam must pass through a 16 mm aperture just a few centimeters upstream of the target. We undertook a beam transport study to improve the beam transmission to the LIG gas cell. With a viewer mounted at the target position, without the gas cell or the restrictive aperture in place, we first verified that the all beamline quadrupoles were aligned correctly. Next we had to reposition the gas cell by about 13 mm transverse to the beam, and then we were able to get a beam spot under 13 mm on the center of the viewer. Also, in order to minimize the neutron radiation in the cave, we replaced the window over the upstream 16 mm aperture with a thinner (from 5 μm to 2.5 μm) Havar foil and also we enlarged the downstream beam aperture from 16 mm to 32 mm. The beam transport improved to almost 100% transmission from FC02 to FC22 (FC22 is located 0.5 m upstream of the LIG gas cell) and then to about 75% to FC23. Given its location and its size, FC23 very likely does not catch all of the protons which go through the gas cell. The neutron radiation level in the LIG cave was also reduced after the changes.

## Third Harmonic Beams

We described the new beam tuning method using the valley coil 4 (VC04) in the last year's progress report. This VC04 technique was extended to third harmonic beams and we successfully extracted a few 3rd harmonic beams. Unlike our previous 3rd harmonic beams, these were stable enough that they were transported and were used in experiments. 1.0 AMeV $^{16}O^{2+}$, 1.0 AMeV $^{22}Ne^{3+}$, and 1.4 AMeV $^{32}S^{5+}$ beams were developed for G. Rogachev's group and were used in astrophysical measurements in the MDM cave. We, however, have not quite solved the 3rd harmonic tuning problems as we were unable to extract a 4 AMeV deuteron beam. These 1 AMeV beams had less than 1% throughput (ILC02 to FC02 beam current ratio), which is less than 3% throughput observed for a little higher energy, 4-5 AMeV, 3rd harmonic beams, due in large part to very poor 5”-to-35” internal beam transmission of only 15 to 25%; a better vacuum in the cyclotron could have helped to improve the beam transmission. Another problem we have had with these low energy beams was that the beam transport to the MDM target was very poor, about 5 to 10 times worse than any first harmonic beams (6 AMeV and higher) we had transported to MDM. Up to the FC05 faraday cup (located just upstream of the BM04 dipole magnet, or at about halfway from FC02 to the MDM target) all beams showed similar transport efficiency, about 30 to 50% of the FC02 current. With beam losses occurring somewhere downstream of the FC05 for these low energy beams, one obvious reason for the beam losses is the poor vacuum and we will seek to improve the beam transport by improving the vacuum through the beamline in the MDM cave.

## Expansion of K150 Usage

We have three new uses for the K150 beams. One is the SEE testing with the installation of a new SEE testing station, the second is the beam irradiation using a small beam box located behind the analyzing magnet, and the third is the initiation of the neutron ball experiments with K150 beams.

With the SEE community's interest in our proton beams, a portable SEE testing station has been installed on a K150 beam line, presently at the end of the Heavy Ion Guide (HIG) line. The testing station is similar to the K500 SEE station, which includes shutters, beam dosimetry counters to monitor the beam flux, and in-air target positioning system. To get ready for the users, we needed to show that the beams could be spread out uniformly as needed by the testers. Spreading the beam uniformly over 3”x3” square was a challenge, especially since the target location is only 3.7 meters from the last quadrupole doublet, whereas for the K500 it is over 10 meters. After demonstrating that we can obtain uniformly spread out beams, four different groups have come to use our 30 to 49 MeV proton beams.

G. Akabani's group was very interested in a high intensity irradiation using a 29 MeV alpha beam on a $^{209}Bi$ target to produce $^{211}At$, and the back of the Analyzing Magnet was identified as a possible site for this irradiation work. One advantage of this plan was that it will keep expected high radiation from the intense alpha beam inside the K150 vault. One concern was that the beam spot might be too large given that the last focusing quadrupole doublet is located about 5 m from the target. A small beam box was mounted behind the Analyzing Magnet along the straight line from the exit of the K150, and an initial beam optics test showed that a 0.6” to 0.75” diameter spot was possible. Then in July 2015 a thin, slanted bismuth target was irradiated for one hour with a 100 nA of 29 MeV alpha beam. Subsequent analysis of the target showed that indeed $^{211}$At was produced and that the unwanted $^{210}$At was much suppressed compared with $^{211}$At. Another irradiation run is being planned to more precisely determine the production rates of $^{211}$At and the $^{210}$At.

The STAR/LIBERACE group has been working to expand their work with gamma detection with their HYPERION system to neutron detection with our Neutron Ball detector. A 55 MeV alpha beam has

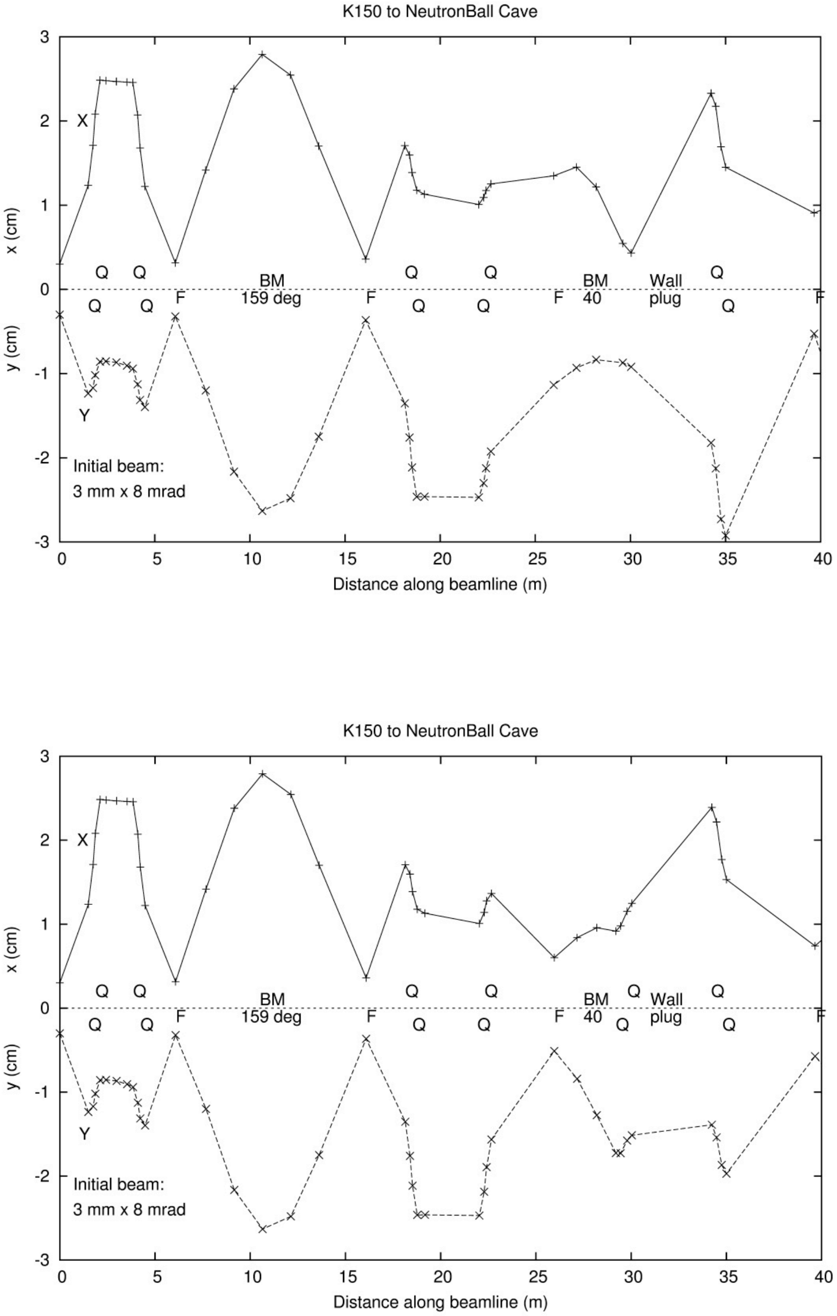

**FIG. 1.** X and Y beam profiles for the transport to the Neutron Ball Cave, (a) with a new quadrupole doublet installed after the BM04, (b) without the quadrupole doublet.

been transported to the Neutron Ball target; this marked the first time a K150 beam was transported to this cave. The beam optics scheme should be very similar to the MDM beam transport, especially if a quadrupole doublet could be installed just downstream of the BM04 dipole, see Fig. 1. However, currently no doublet has been installed, and due to the limited space between BM04 and the wall, and also because this line is in middle of two other beamlines, it would seem to be very difficult to install a new quadrupole doublet to this line. Between having the doublet (Fig. 1a) and no doublet (Fig. 1b), there is a small difference in the final magnification, especially for the x direction, but the main difference is the size of the beam in the y direction around the last quadrupole before the target. The large size of the beam through the last quadrupoles may lead to a larger growth than what is shown in this first order calculation. We have transported the alpha beam twice to the Neutron Ball and both times a nice small beam spot was achieved. The beamline collimators had to be rather tight to get the beam spot at the expense of the beam intensity, but less than one nanoampere of beam was needed for the experiment.

# Texas A&M Cyclotron K150 radiation effects facility
## April 1, 2015 – March 31, 2016

B. Hyman, H.L. Clark, S. Gerlt, V. Horvat, G.J. Kim, B. Roeder, and S. Russell

Several improvements have been made to the Radiation Effects Facility K150 beam line. Improvements include the installation of a backscatter measurement system to conduct high-flux dosimetry and the installation of a beam energy degrader system.

The backscatter measurement system consist of a set of four tantalum foils and four detectors aligned to measure backscattered protons from the foils. The foils are placed perpendicular to the beam path at 90° intervals radially about the beam line center. The detectors, consisting of plastic scintillators coupled to photomultiplier tubes, are angled to face the foils and are located out of the beam path. Beam uniformity is first adjusted at a lower beam flux (< 1E7 part/cm$^2$/s) and then a calibration measurement is taken, measuring the ratio of backscattered counts to counts from the forward facing central detector. High-flux live dosimetry is conducted using this calibration measurement and live counts from the backscatter detectors.

A rotatable degrader wheel has been installed after the exit window of the beam line (see Fig. 1).

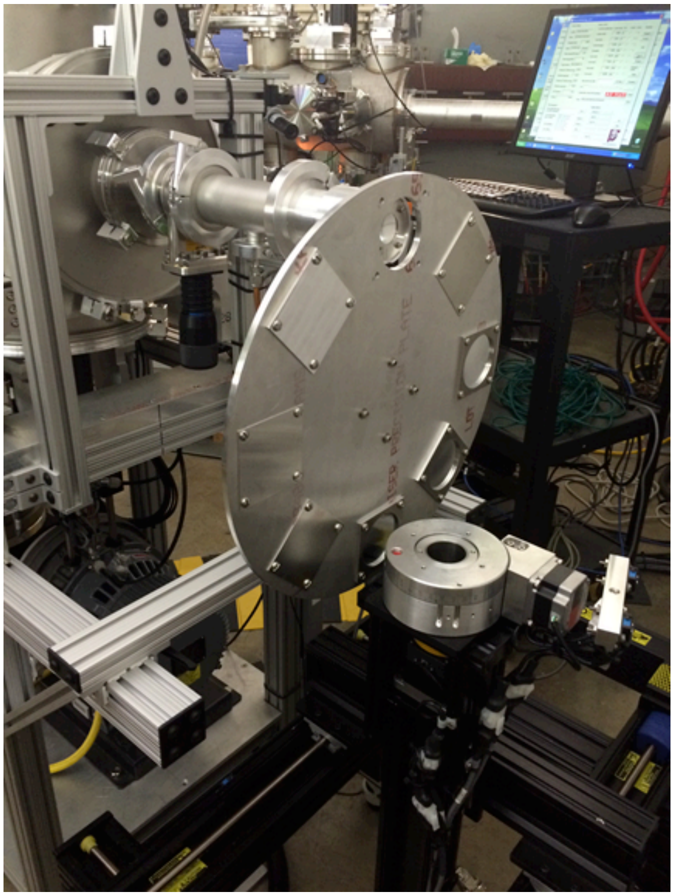

**FIG. 1.** Rotatable degrader wheel for K150 Radiation Effects Facility beam line.

The degraders, made of aluminum foils and sheets, allow beam energy changes without cyclotron re-tuning. The wheel accommodates up to seven degraders of varying thickness and one opening for an un-degraded beam and is remotely controlled through custom software. Degraders can be swapped out as needed. A standard set of degraders has been developed and tested.

The primary use for the beam line continues to be for space electronics and materials testing with proton beams. Our first external customer use of the beam line occurred in June of 2015. Four additional external customers have conducted proton testing during this reporting period and an increase in external customer use of the beam line in the near future is anticipated.

# Status of ECR2: Development of aluminum beam using the ECR2 high-temperature oven and reduction of the reflected microwave power with a new copper back plate

H. Peeler, F.P Abegglen, B.T. Roeder, and D.P. May

The ECR2 development work this year was mainly concerned with the production of a high-intensity aluminum beam for use in experiments at the Cyclotron Institute, and also the development of a new copper microwave plate to reduce the reflected power measured from the 14.5 GHz klystron.

The development of the high-temperature oven for axial mounting on ECR2 described in the last two progress reports continued [1,2]. Last year, it was found that liquid aluminum was migrating from the tantalum crucible onto the oven heat shields and onto the wall of the plasma chamber. This was happening because aluminum, unlike titanium and other metals, has a lower melting temperature (660° C) than its temperature (820° C) for a sufficient vapor pressure for the ion source. Several ideas were tried to prevent the heated, liquid aluminum from leaking out of the crucible. These ideas included covering the aluminum source material with a tungsten mesh, different tantalum crucible designs, and the use of different ECR source support gases such as "air" instead of the usual pure oxygen. The most effective of these ideas was to seal the ends of the tantalum crucible as tightly as possible. This prevented the aluminum liquid from leaking out of the ends of the crucible when it was heated, although, some liquid still escaped through the exit hole. With this improvement, it was possible to extract observable amounts of aluminum from ECR2 with high temp oven powers as low as 83.3 W (0.920 V, 90.6 A on power supply), whereas previously more than 100 W was needed.

During typical operation, the aluminum load lasted about four days. An ECR source scan showing the aluminum-charge states just after an increase in the oven power is shown in Fig. 1. Typical

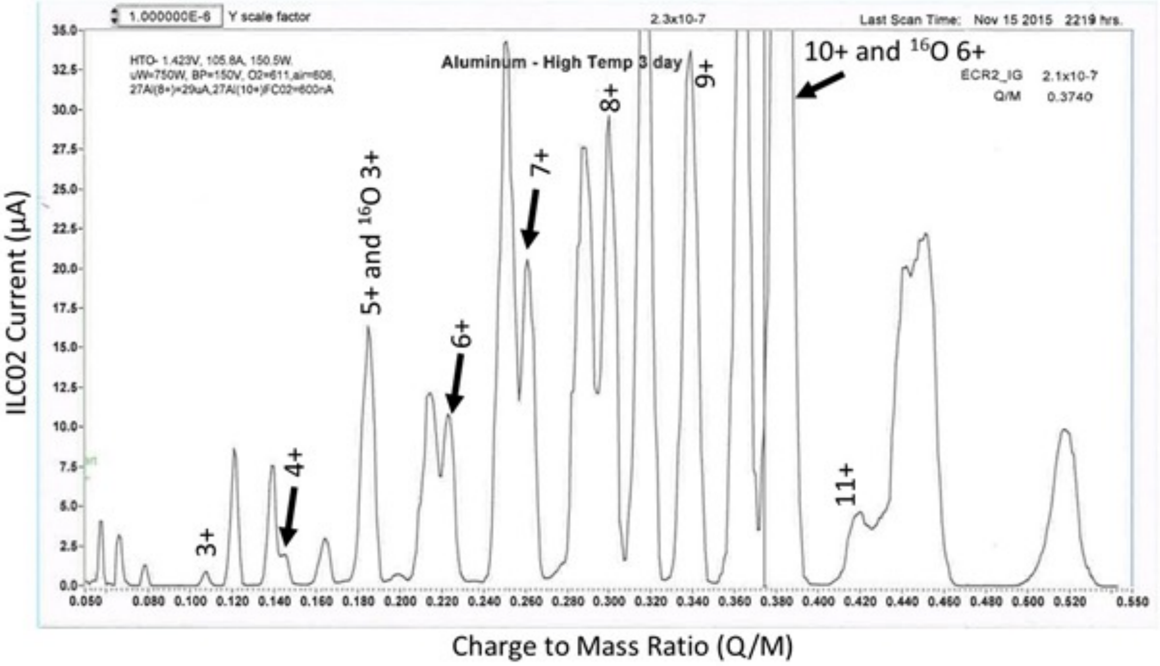

**FIG. 1.** Scan showing the Aluminum spectrum obtained from the High Temperature oven with ECR2. Aluminum charge states are labeled. This scan was taken when the 10+ charge state was optimized.

source outputs from ECR2 were 20 μA for $^{27}Al^{7+}$ and 29 μA for $^{27}Al^{8+}$. To maintain the beam output, the power on the heater of the high temp oven needed to be increased 10 W - 20 W every 12 hours. Leaking some "air" into the source in addition to pure oxygen as the support gas helped to stabilize the beam output, although, over time, only a power increase on the oven would restore the beam. It was possible to restore the aluminum beam output with an oven power increase up to 170 W. Above that amount of power, it was observed that the aluminum source material had been depleted.

Also this year, it was observed that there was a large amount of reflected power from the 14.5 GHz Klystron when the dual-frequency back plate, made of stainless steel, is mounted to the back of ECR2. More than 20% reflected microwave power was measured. This large amount of reflected power contributed to the instability of the ion source output and limited the amount of forward microwave power that could be used to produce high-charged ion beams. However, it was noticed that while the high temp oven back plate, made of copper, was mounted, the reflected power was much reduced. In light of this observation, a new dual-frequency back plate made of copper has been constructed. Initial testing has shown that the reflected power from the 14.5 GHz klystron has been reduced to about 6% of the total forward microwave power. This allows the klystron to operate with forward microwave power up to 1.5 kW while maintaining the ion source stability.

A comparison of the reflected microwave power measured from the 14.5 GHz klystron between the stainless steel dual-frequency back plate, the copper high-temp oven back plate, and the new copper dual-frequency back plate is shown in Fig. 2.

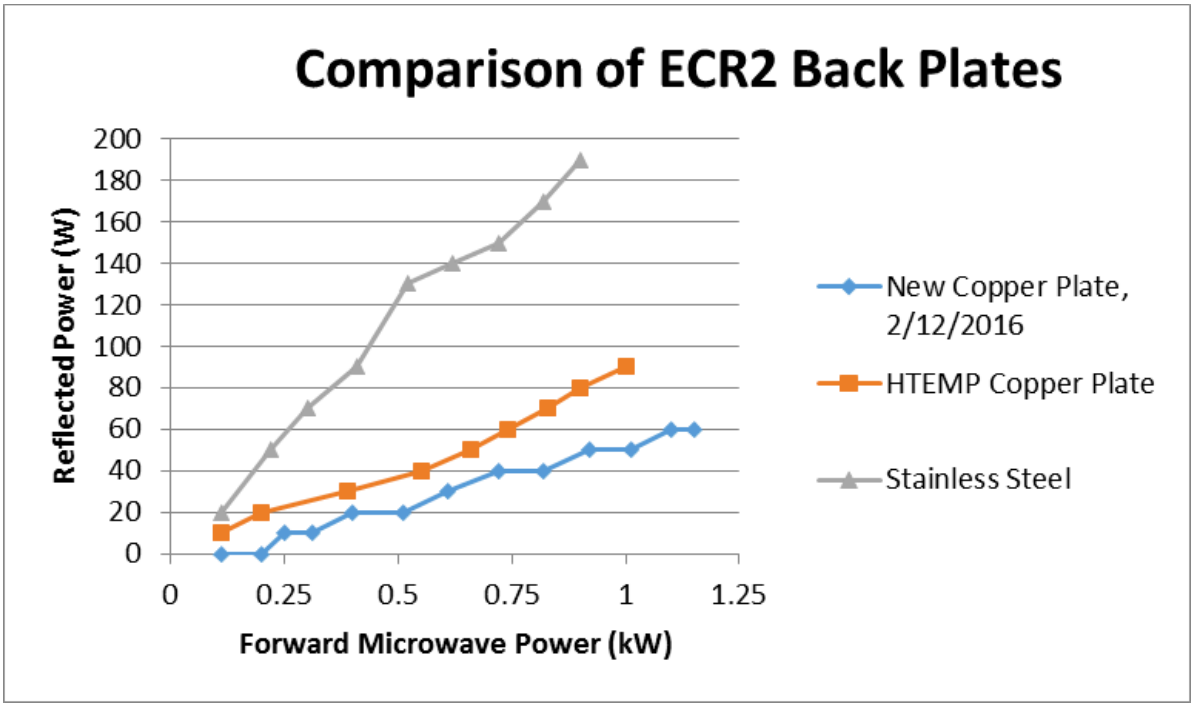

**FIG. 2.** Plot showing the increase in reflected microwave power for the 14.5 GHz Klystron for different back plates. The reflected power was much lower for when the new copper back plate was used.

[1] H. Peeler *et al.*, *Progress in Research*, Cyclotron Institute, Texas A&M University (2014-2015), p. IV-7; http://cyclotron.tamu.edu/2015 Progress Report/index.html.

[2] F.P. Abegglen *et al.*, *Progress in Research*, Cyclotron Institute, Texas A&M University (2013-2014), IV-3; http://cyclotron.tamu.edu/2014 Progress Report/index.html.

## Heavy-ion guide RFQ System

G. Chubarian

To capture radioactive species after the heavy-ion guide gas catcher and direct them to the different devices, a complex RFQ system has been designed. The RFQ system consists of

- A 30 cm long DC-drag cooling RFQ (Fig. 1) located immediately after the gas catcher's exit hole at a relatively high gas pressure zone caused by the flow of helium gas from the gas catcher.

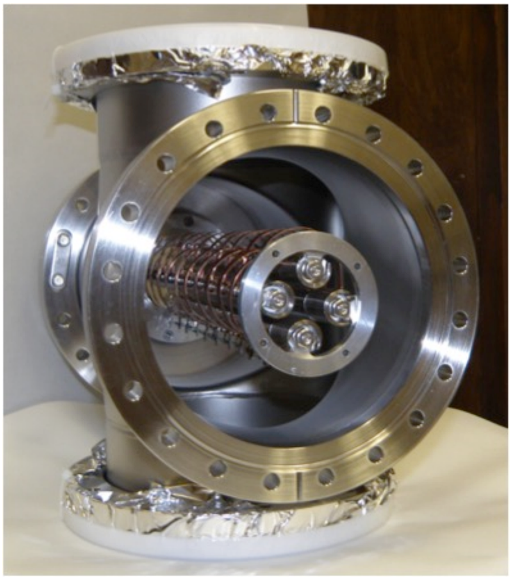

**FIG. 1.** The 30 cm long DC-drag cooling RFQ assembly**.**

- At the end of the DC-drag cooling RFQ, a micro-RFQ is mounted (Fig. 2). The micro-RFQ is 2 cm long and has a 4.5 mm exit hole, which is necessary to ensure efficient differential pumping

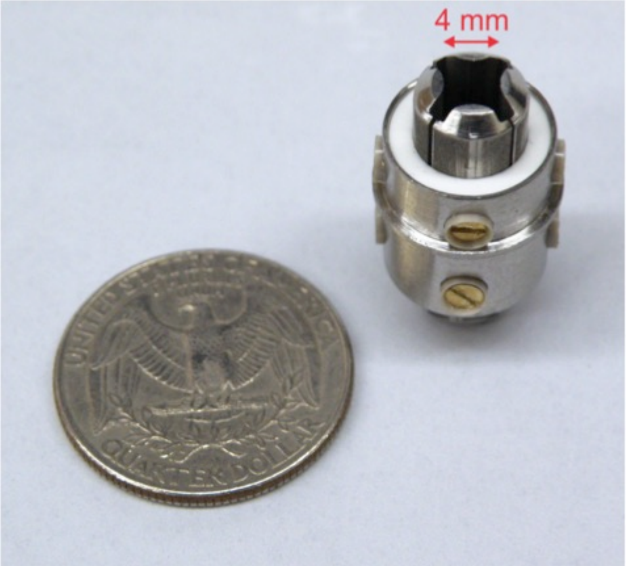

**FIG. 2.** The micro-RFQ after the DC-drag cooling RFQ.

The Micro-RFQ can be coupled individually with three other DC-drag RFQs (branching system Fig. 3), which are mounted inside the large vacuum chamber on a remotely controlled position system. Two curved RFQs deliver radioactive ions to either the CB-ECR ion source injection line (in the horizontal plane) or vertically to the TAMU Trap's beam line. Additionally, there is a third straight section RFQ that leads to the Ortho-TOF mass spectrometer and a fourth 90 degree port that points directly to the CB-ECR ion source for tuning the injection line with 1+ alkali ion sources. The four branching RFQ sections have different lengths ranging from 45 cm to 63 cm.

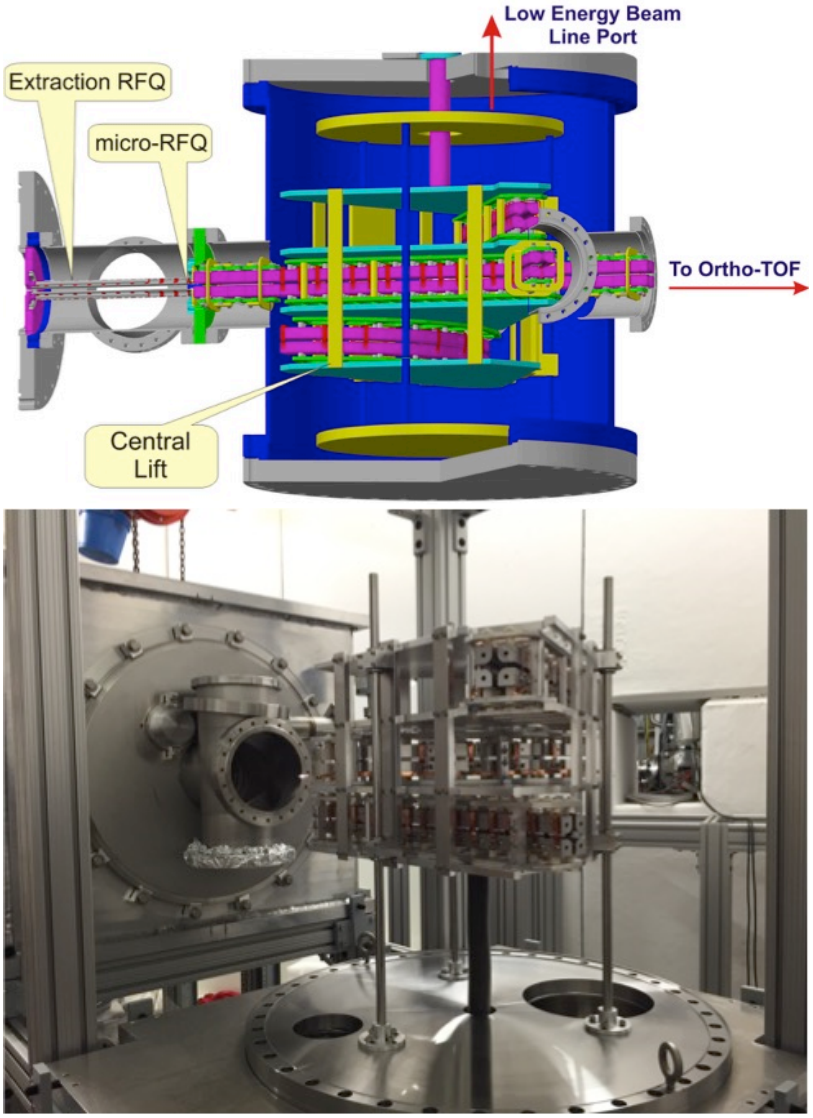

**FIG. 3.** The Branching-RFQ system.

Depending on the mass of the ion, RFQs can operate in a range of frequencies from 600 to 1500 kHz. They were individually tested and based on preliminary results transport efficiency is in the range of high 90 percentile.

# Acceleration and identification of charge-bred $^{85}$Rb ions

B.T. Roeder, J. Arje, G.J. Kim, A. Saastamoinen, and G. Tabacaru

The re-acceleration of charge bred, radioactive isotope beams from the TAMU light-ion guide and charge breeding electron-cyclotron resonance ion source (CB-ECR) for the T-REX project [1] presents several challenges. When beams of stable isotopes are accelerated though the K500 cyclotron, typically their intensities are of the order of $10^7$ particles/sec (about 10 pA) or greater. Thus, the stable beams can be measured with a beam probe in the cyclotron and Faraday cups outside the cyclotron for tuning purposes. However, the charge bred, radioactive isotope beams are expected to have much weaker intensities than the stable beams. Even in the best cases when $10^6$ particles/sec could be available for re-acceleration, these intensities are too low to be observed in the same way as the stable beams. Also, due to the high electric and magnetic fields present inside the K500 cyclotron, it is difficult to mount a particle detector, such as a photomultiplier tube and plastic scintillator (PMT-Scint), inside the cyclotron to tune the radioactive beams.

Fortunately, one of the advantages of charge breeding the radioactive ions in the CB-ECR is that several different charge states will be produced for re-acceleration through the K500. At the same time, since the plasma of the CB-ECR is supported by gases of stable isotopes such as oxygen, nitrogen or carbon, the CB-ECR also simultaneously produces stable beams at much higher intensities. By selecting charge states of the radioactive ions that have similar charge-to-mass (Q/M) ratios to the Q/M ratios of the stable beams, the more intense stable beam can be used as a “pilot beam” to guide the tune of the radioactive beam through the K500 cyclotron and ultimately to an experimental setup. After the pilot beam is tuned, if the difference in Q/M ratio between the pilot beam and the radioactive beam of interest is large enough, a slight change in the K500 radio-frequency on the order of 10-100 kHz is all is needed to accelerate and select the radioactive ions instead of the pilot beam. Ideally, once this single parameter is changed, the radioactive beam is tuned and ready to be further optimized with particle detectors in the beamline outside of the K500 cyclotron and finally transported to the experiments.

To practice this pilot beam tuning technique, a test experiment was conducted in February 2016 to accelerate $^{85}$Rb$^{16+}$ ions produced from a 1$^+$ ion gun and charge-bred by the CB-ECR. Although $^{85}$Rb$^{15+}$ and $^{85}$Rb$^{17+}$ ions from the CB-ECR were accelerated through the K500 in 2013 [2], the $^{85}$Rb ions in that case were not measured after the cyclotron with particle detectors to verify their identity. Further, the $^{85}$Rb$^{16+}$ ions have a similar Q/M ratio to $^{16}$O$^{3+}$ ( Q/M $^{16}$O$^{3+}$ = 0.1876 versus Q/M $^{85}$Rb$^{16+}$ = 0.1885 ). While the $^{16}$O$^{3+}$ beam is indistinguishable from the $^{85}$Rb$^{16+}$ ions produced in the CB-ECR before acceleration, they are easily separated during acceleration by the K500 cyclotron. Due to their difference in Q/M ratio, it was calculated that a change of 56 kHz in the K500 radio-frequency for 14 MeV/u would change the accelerated beam from the $^{16}$O$^{3+}$ to the $^{85}$Rb$^{16+}$ without changing any other parameters. Once the 56 kHz radio-frequency change was made, the change from $^{16}$O$^{3+}$ to $^{85}$Rb$^{16+}$ could be verified by measurements after the K500 cyclotron with the MARS spectrometer [3] and silicon detectors.

The experiment was conducted as follows. A stable beam of $^{84}$Kr$^{16+}$ at 14 MeV/u was produced by the ECR1 ion source and tuned through the K500 cyclotron to the MARS spectrometer. The $^{84}$Kr$^{16+}$ beam impinged on a thin, 6.4 μm aluminum foil to strip off the electrons and produce $^{84}$Kr ions in several different charge-states ranging from fully-stripped 36+ ions down to 29+ ions. The $^{84}$Kr could be identified by the different magnetic rigidities of its charge-states as predicted by the LISE++ program model of the MARS spectrometer [4, 5] and by its energy deposit in a silicon detector telescope mounted at the focal plane of MARS. In this way, the $^{84}$Kr beam was used to calibrate the silicon detector telescope and verify the predictions of the LISE++ spectrometer model. The measurement of the $^{84}$Kr$^{31+}$ charge state in the silicon detector telescope is shown in Fig. 1. By comparing the energy deposited in the telescope for $^{84}$Kr charge states 31+ through 36+, the energy of the $^{84}$Kr was measured to be 1110 ± 5 MeV, slightly lower than 14 MeV/u because of the energy loss of the beam in the aluminum stripper foil, but in agreement with the predictions of the LISE++ model.

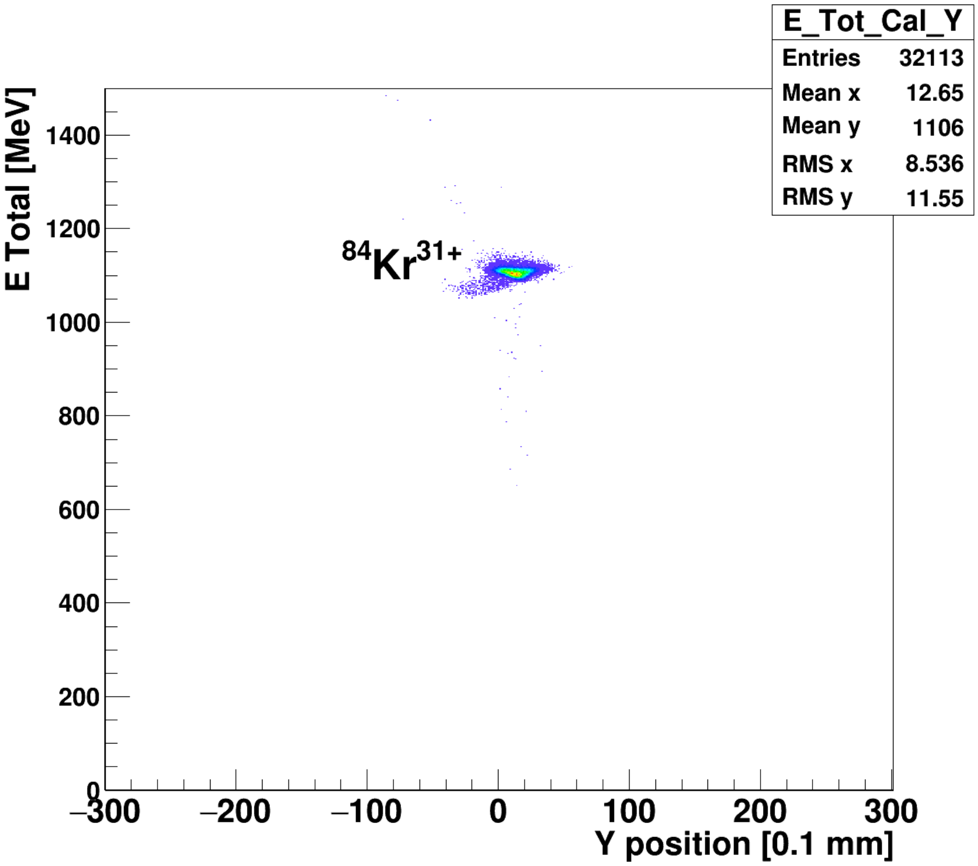

**FIG. 1.** $^{84}$Kr$^{31+}$ ion measured at the MARS focal plane with the silicon detector telescope for detector calibration.

Once the MARS silicon detector telescope was calibrated, the $^{85}$Rb$^{16+}$ was tuned as follows. First, $^{16}$O$^{3+}$ at 14 MeV/u produced by ECR1 was tuned through the K500 cyclotron to a beam viewer slightly upstream of the aluminum stripper foil at the entrance of the MARS spectrometer. Then the cyclotron injection line was changed to accept the $^{16}$O$^{3+}$ beam instead from the CB-ECR and $^{16}$O$^{3+}$ was still measured on the Faraday cup after the K500 cyclotron and observed on the beam viewer at the entrance of MARS. After turning on the Rb 1+ ion gun, the K500 cyclotron radio-frequency was increased by 56 kHz. Immediately, a weak beam spot of $^{85}$Rb$^{16+}$ was observed in almost the same position on the beam viewer at the entrance of MARS that the $^{16}$O$^{3+}$ had been seen previously. After some slight optimization of the cyclotron tune, about 50 pA of $^{85}$Rb$^{16+}$ were obtained.

Next, the beam viewer was removed and the $^{85}$Rb$^{16+}$ was impinged on the aluminum stripper foil at the entrance of MARS, as was done previously with the $^{84}$Kr beam. By changing the magnetic rigidity of MARS, charge states 37+ through 33+ were observed using the silicon detector telescope. The measurement of the $^{85}$Rb$^{33+}$ charge state in the silicon detector telescope is shown in Fig. 2. The energy of the $^{85}$Rb was measured to be 1127 ± 5 MeV, again in agreement with the prediction of LISE++ taking into account the energy losses in the aluminum stripper foil and the slight change in the initial $^{85}$Rb$^{16+}$ energy because of the cyclotron radio-frequency increase.

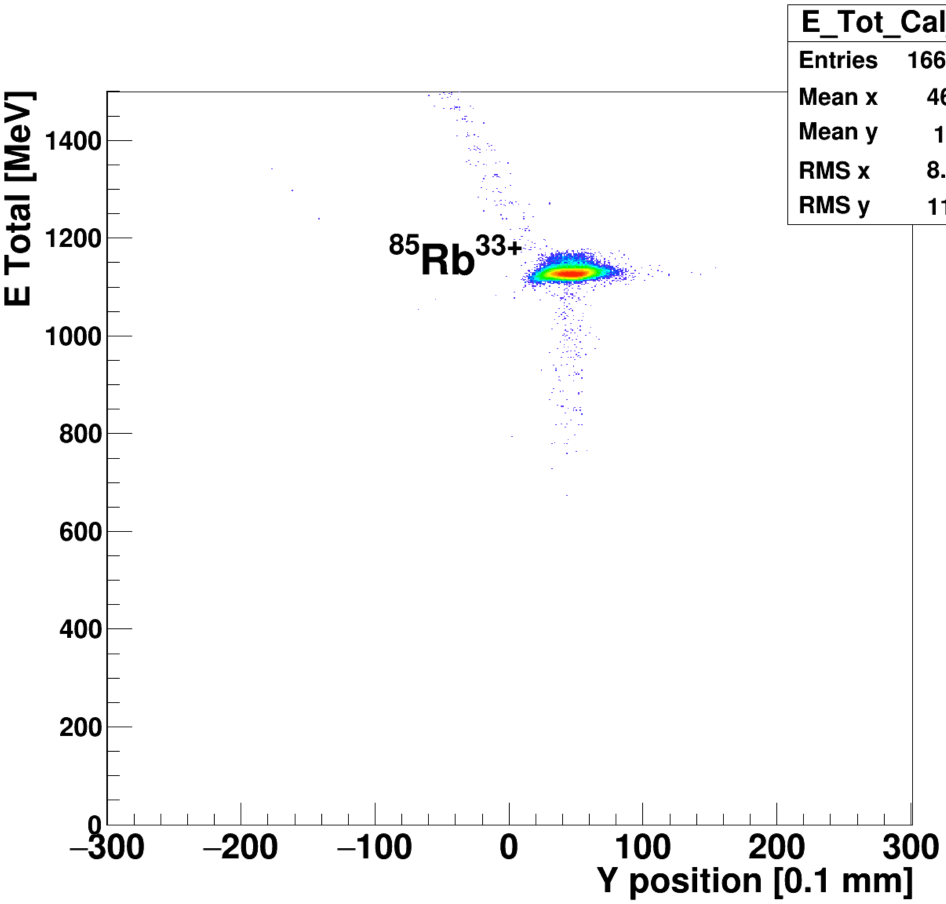

**FIG. 2.** $^{85}$Rb$^{33+}$ ions measured at the MARS focal plane with the silicon detector telescope.

As a final test of the pilot beam technique, a test was done to observe the “width” of the $^{16}$O$^{3+}$ beam at 14 MeV/u with respect to the cyclotron radio-frequency. While observing the $^{16}$O$^{3+}$ beam, stripped to $^{16}$O$^{8+}$, with a PMT-Scint detector at the MARS focal plane, the cyclotron frequency was varied in steps of 1 kHz to see when the $^{16}$O beam completely disappeared on the detectors. This test was important because if the radioactive beam Q/M ratio was too close to the pilot beam, perhaps the cyclotron would not be able to completely separate the two beams. To completely remove the $^{16}$O beam from the detector at the MARS focal plane, a radio-frequency shift greater than 12 kHz was needed. Since the frequency shift for $^{85}$Rb$^{16+}$ at 14 MeV/u was 56 kHz, the $^{85}$Rb$^{16+}$ was indeed fully separated from the $^{16}$O$^{3+}$ during acceleration by the K500 cyclotron. However, it appeared that ions with Q/M ratio differences of less than about 0.0002, corresponding to a frequency shift of about 12 kHz for 14 MeV/u, cannot be separated by the K500 cyclotron. This result is in agreement with previous observations with other stable beams, such as $^{20}$Ne$^{4+}$ and $^{40}$Ar$^{8+}$, which have nearly equal Q/M ratios and can not be cleanly separated when both are injected into the cyclotron. In the cases where this occurs, other methods such as a stripper foil after the cyclotron can be used to remove the pilot beam and select the radioactive ions

In summary, charge-bred $^{85}$Rb$^{16+}$ ions from 1+ ion gun source and the CB-ECR have been tuned through the K500 cyclotron by first tuning an $^{16}$O$^{3+}$ pilot beam at 14 MeV/u and then increasing the radio-frequency of the cyclotron 56 kHz to select instead the $^{85}$Rb$^{16+}$ ions at 14 MeV/u. The $^{85}$Rb$^{16+}$ ions were cleanly separated from the $^{16}$O$^{3+}$ beam. The $^{85}$Rb$^{16+}$ was transported to the MARS spectrometer and stripped by a thin aluminum stripper foil. Five separate charge states were measured and their predicted energy was verified by a silicon detector telescope.

In the coming year, it is expected that charge-bred, radioactive $^{64}$Ga ions produced by the $^{64}$Zn(p,n) reaction and transported by the light-ion guide will be available for re-acceleration by the K500 cyclotron. Since the $^{64}$Ga$^{12+}$ Q/M ratio is 0.18771, nearly the same Q/M ratio as $^{16}$O$^{3+}$, a similar technique as was used for the $^{85}$Rb$^{16+}$ could be employed to tune a $^{64}$Ga$^{12+}$ radioactive ion beam and identify it at the MARS spectrometer. It is also expected that elastically scattered $^{64}$Zn$^{12+}$ ions, Q/M ratio = 0.18773, from the production target will also be present.

[1] R.E. Tribble *et al.*, Eur. Phys. J. Spec. Top. **150**, 225 (2007).

[2] H.L. Clark *et al.*, *Progress in Research*, Cyclotron Institute, Texas A&M University (2012-2013), p. IV-8; http://cyclotron.tamu.edu/2013 Progress Report/index.html.

[3] R.E. Tribble, R.H. Burch, and C.A. Gagliardi, Nucl. Instrum. Methods Phys. Res. **A285**, 441 (1989).

[4] O.B. Tarasov and D. Bazin, Nucl. Instrum. Methods Phys. Res. **B266**, 4657 (2008).

[5] B.T. Roeder and O.B. Tarasov, *Progress in Research*, Cyclotron Institute, Texas A&M University (2013-2014), p. IV-40; http://cyclotron.tamu.edu/2014 Progress Report/index.html.

# Cyclotron computing

R. Burch, K. Hagel, and S. Wuenschel

The enhancement of computing resources at the Cyclotron Institute in the past year was concentrated on extending disk storage capabilities, network capabilities, and further development of waveform digitizer capabilities.

The appetite for data storage continues to increase with time. Experiments continue to become more sophisticated acquiring more and more parameters. In addition, there is a move toward using waveform digitizers to consolidate functionality in triggering, timing, pulse height, and/or charge integration. Some experiments also need to leverage information contained in the waveform itself. Such requirements drive this need for increased storage. To that end, we rolled out two new file servers that are currently provisioned with 4 6Tb disk drives in RAID for 12 Tb of usable space. They have the capacity of 8 more 6Tb drives for a total usable capacity of 60Tb. The extra drives will be added as necessary in order to take advantage of price decreases that occur with time.

We made an incremental network upgrade in order to keep up with the data demands by implementing new switches with 10Gb backbones. In addition, we outfitted the file servers with 10Gb cards in order to enhance the speed with which we can access the data on these servers.

Over the past few years, we have moved various administration computers not having significant requirements of CPU, memory, or disk resources to small off the shelf commodity computers that can be purchased for less than $100. Most of the computers of this nature are Rasberry pi computers. In the past year, we have taken advantage of the low price of outfitting these computers to increase the redundancy of our authentication systems.

The migration of our email to the Texas A & M University Exchange Server is complete. The Institute mail server was turned off when the last user was migrated and the MX record was changed to point to the Exchange Server.

New experiments are showing increasing demand for waveform digitizers. We purchased two model 3316 digitizers from Struck Innovative Systems in the past year to add to the several that were purchased earlier. We have used them successfully in several experiments and the combined functionality that they provide is significant. Many software enhancements have been made to more completely leverage the significant capabilities that these modules possess. In addition, the company has made enhancements to the firmware in order to provide additional capabilities.

# MARS status report for 2015-2016: Development of rare isotope beams of $^{25}$Si, $^{6}$He, $^{9}$Li, $^{23}$Si, and $^{22}$Ss

B.T. Roeder, A. Saastamoinen, and M.R.D. Rodrigues[1]
[1]*Instituto de Física, Universidade de São Paulo, São Paulo-SP, Brasi*

This year we developed five new rare isotope beams for the physics program at the Cyclotron Institute at Texas A&M University with the Momentum Achromat Recoil Separator (MARS) [1]. The $^{25}$Si beam was employed to commission the AstroBox2 detector. The $^{6}$He and $^{9}$Li beams were developed for future experiments to be conducted near the neutron dripline. The $^{23}$Si and $^{22}$Si beams were developed to study exotic decay schemes such as multiple proton decay near the proton dripline. The $^{23}$Si and $^{22}$Si beams are also of note because they are five and six particles away, respectively, from the nearest stable silicon isotope. This makes these two beams among the most exotic rare isotope beams ever produced with the MARS spectrometer.

## $^{25}$Si beam production for the AstroBox2 commissioning run

The $^{25}$Si rare isotope beam was originally produced in October 2010 during the search for a method of producing $^{27}$P [2]. In October 2010, a $^{28}$Si primary beam at 40 MeV/u was fragmented on several different targets including $^{9}$Be, $^{27}$Al, and Havar. While $^{25}$Si was produced with all the targets, the best production was found when an aluminum target was used. Since the beta-delayed proton decay of $^{25}$Si is relatively well known [3], and its proton decay branching ratios are relatively high, $^{25}$Si decay was determined to be a good case for the commissioning of the AstroBox2 detector [4] in April 2015. To produce $^{25}$Si, $^{28}$Si at an energy of 40 MeV/u from the K500 cyclotron was used to bombard a 254 μm thick aluminum target. The resulting reaction products were separated and transported through MARS. The magnetic rigidity of MARS was set assuming that the best reaction mechanism to produce $^{25}$Si was the fragmentation reaction. As a result of this reaction, $^{25}$Si was produced at a rate of 5.3 eV/nC with the MARS momentum slits at ± 0.5 cm, which corresponds to a momentum spread of the secondary beam of $\Delta P/P \approx 0.6\%$. The magnetic rigidity was 1.5153 T·m. This production rate gave about 100-200 $^{25}$Si particles/sec at the MARS focal plane. This amount of $^{25}$Si was ideal for the calibration of the AstroBox2 and will used again in the future runs.

## $^{6}$He rare isotope beam production

In May 2015, we produced and separated $^{6}$He with MARS for an experiment for the group of G. Rogachev. Details of the measurement are given in a separate report. The $^{6}$He beam was developed previously in 2009 [5], but it was never used. For this measurement, the $^{6}$He was made in inverse kinematics with the d($^{7}$Li,$^{6}$He)$^{3}$He transfer reaction in inverse kinematics with $^{7}$Li primary beam at 7.0 MeV/u from the K150 cyclotron. Deuterium gas at a pressure of 2 atm and at a temperature of 77K was used in the MARS gas cell target. With the MARS momentum slits at ± 1.5 cm, which corresponds to a momentum spread of the secondary beam of $\Delta P/P \approx 1.8\%$, a production rate of 397 eV/nC was obtained.

The total energy of the $^{6}$He beam was 35.4 MeV. Tritium ($^{3}$H) contamination was also present in the secondary beam and came at about the same rate as the $^{6}$He. The maximum production of the $^{6}$He was found within a very narrow range of magnetic rigidity, which is a result consistent with the direct transfer reaction mechanism. The final tune of the $^{6}$He secondary beam as measured by the MARS target detector is shown in Fig. 1.

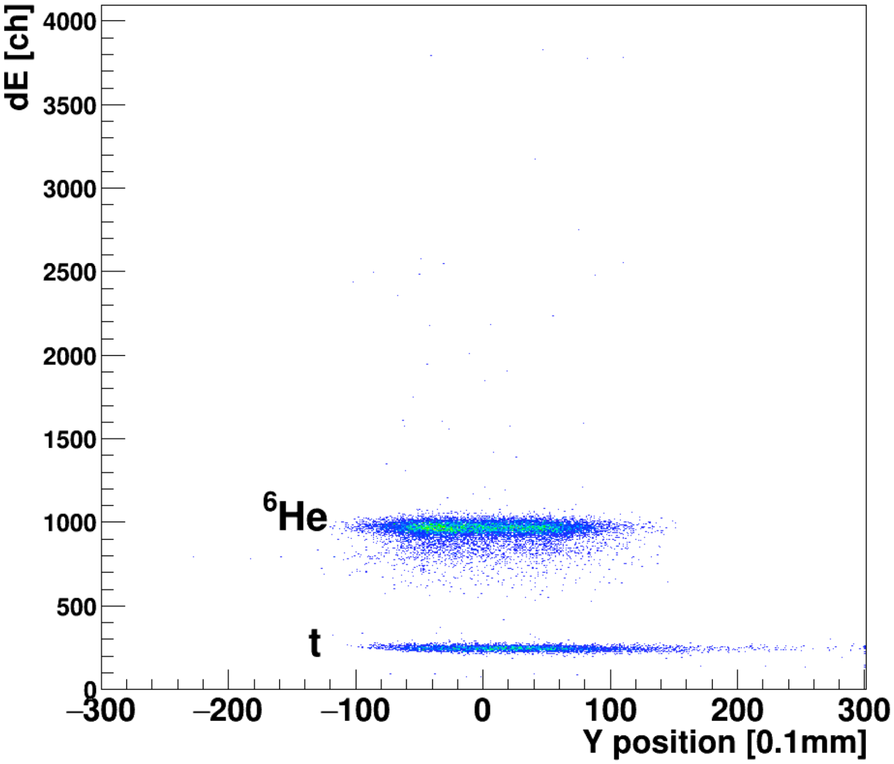

**FIG. 1.** Result of the $^{6}$He MARS tuning for the May 2015 experiment. Note the tritium ($^{3}$H) contamination at the same focal plane position as the $^{6}$He.

### $^{9}$Li rare isotope beam production

In November 2015, we produced and separated $^{9}$Li for the first time with MARS for another upcoming experiment for the group of G. Rogachev. The $^{9}$Li was made in inverse kinematics with the $^{11}$B+$^{9}$Be two-proton removal reaction in inverse kinematics with $^{11}$B primary beam at 23 MeV/u from the K500 cyclotron. A solid $^{9}$Be target 456 μm thick was employed as the production target. 23 MeV/u was chosen as the initial energy because it provided the maximum energy available while still allowing the $^{9}$Li recoil particles to be transported through MARS highly rigid. With the MARS momentum slits at ± 1.5 cm, which corresponds to a momentum spread of the secondary beam of $\Delta P/P \approx 1.8\%$, a production rate of 55 eV/nC was obtained for $^{9}$Li. The total energy of the $^{9}$Li beam was 174 MeV. $^{6}$He at a rate of 46 eV/nC and tritium ($^{3}$H) at a rate of 190 eV/nC were also present as contamination in the secondary beam.

While the tritium rate is about 3.5 times higher than the $^{9}$Li, this amount of contamination is acceptable for the upcoming experiment. The maximum production of the $^{9}$Li was found with the magnetic rigidity setting predicted by LISE++ [6] for the "fragmentation" reaction mechanism, although the reaction mechanism at this beam energy is more likely a deep inelastic transfer reaction. The final tune of the $^{9}$Li secondary beam as measured by the MARS target detector is shown in Fig. 2.

### Production of $^{23}$Si and $^{22}$Si rare isotope beams

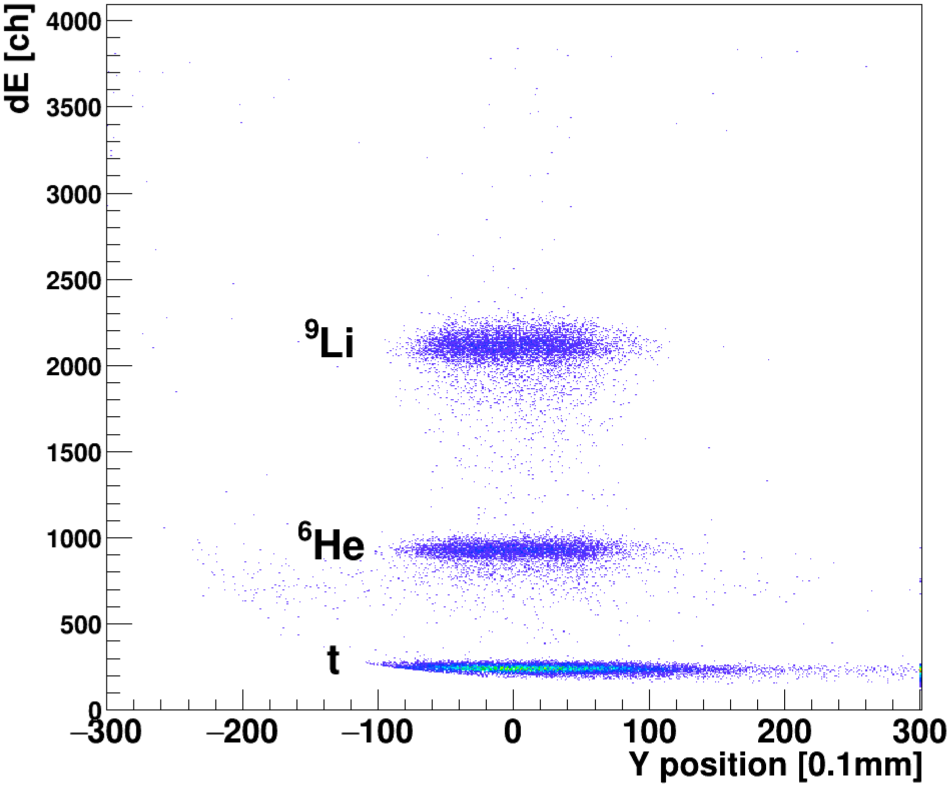

**FIG. 2.** Result of the $^{9}$Li production test with MARS. The main contaminants of the secondary beam are from $^{6}$He and $^{3}$H which come at the same position in the MARS focal plane.

In March 2016, $^{23}$Si and $^{22}$Si were produced for the first time with MARS for an upcoming experiment in collaboration with a group from Warsaw University in Poland. $^{23}$Si and $^{22}$Si were made in inverse kinematics with the fragmentation reaction in inverse kinematics with $^{28}$Si primary beam at 45 MeV/u from the K500 cyclotron. A solid natural nickel target 150 μm thick was employed as the production target. Nickel was chosen as the production target because it provided the lowest threshold energy for the reactions needed to produce the $^{23}$Si and $^{22}$Si. Also, in some previous MARS production tests with nickel and Havar targets, there have been some indications of five and six particle removal from the primary beam. With the MARS momentum slits at ± 1.5 cm, which corresponds to a momentum spread of the secondary beam of $\Delta P/P \approx 1.8\%$, a maximum production rate of 13 eV/μC was obtained for

$^{23}$Si at a magnetic rigidity of 1.398 T·m, close to the prediction of the LISE++ program [6]. With the primary beam intensity available, this gives about 1 particle of $^{23}$Si per 5 seconds, which is enough for the planned experiment. By tuning MARS toward lower magnetic rigidities, some $^{22}$Si events were also observed. When MARS was set for a magnetic rigidity of 1.344 T·m, both $^{23}$Si and $^{22}$Si were obtained simultaneously at the MARS focal plane at different positions on the silicon detector. The $^{23}$Si at this rigidity had a production rate of 6.5 eV/μC, or about 1 particle per 15 seconds, and the $^{22}$Si had a production rate of 0.5 eV/μC, or about 1 particle per 5 minutes. The particle identification plot where both $^{23}$Si and $^{22}$Si were present is shown in Fig. 3. Despite these small production rates, the collaborators from Warsaw University are planning experiments with both of these rare isotope beams in the coming year.

Following the success of producing rare isotopes five and six particles from stability in the cases of $^{23}$Si and $^{22}$Si, it is also planned in the near future to attempt to produce other rare isotopes near the proton dripline using fragmentation on a nickel target.

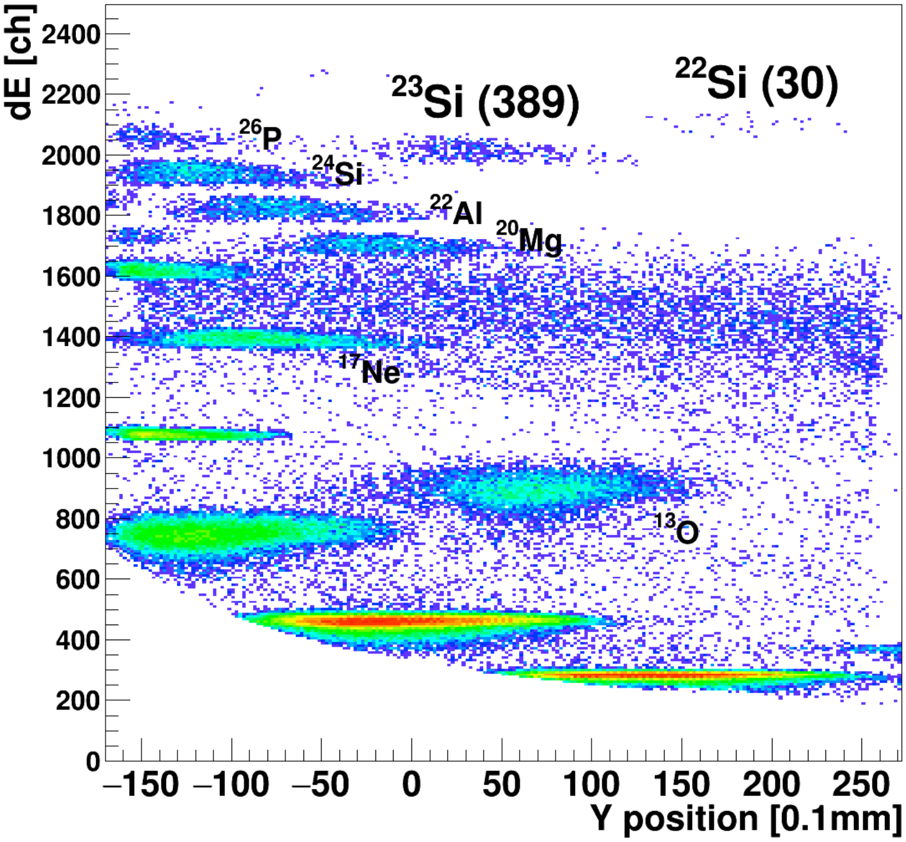

**FIG. 3.** Result of the two hour measurement at the MARS magnetic rigidity setting where both $^{23}$Si and $^{22}$Si were present. The number in parentheses shows the number of $^{23}$Si and $^{22}$Si events that were obtained during the measurement. Other rare isotopes produced are also labeled.

[1] R.E. Tribble, R.H. Burch, and C.A. Gagliardi, Nucl. Instrum. Methods Phys. Res. **A285**, 441 (1989).

[2] E. Simmons *et al.*, *Progress in Research*, Cyclotron Institute, Texas A&M University (2010-2011), p. I-49, http://cyclotron.tamu.edu/2011 Progress Report/index.html.

[3] J.C. Thomas *et al.*, Eur. Phys. J. **A 21**, 419 (2004).

[4] A. Saastamoinen *et al.*, *Progress in Research*, Cyclotron Institute, Texas A&M University (2014-2015), p. IV-33, http://cyclotron.tamu.edu/2015 Progress Report/index.html.

[5] L. Trache *et al.*, *Progress in Research*, Cyclotron Institute, Texas A&M University (2008-2009), p. *Production of new radioactive beams $^{46}V$, $^{6}He$, $^{20}Mg$, and $^{13}O$ with MARS*, http://cyclotron.tamu.edu/2009 Progress Report/index.html.

[6] O.B. Tarasov and D. Bazin, Nucl. Instrum. Methods Phys. Res. **B266**, 4657 (2008).

# Preparation of a $^{124}$Te target for neutron irradiation

T.A. Werke and C.M. Folden III

The fabrication of suitable targets for nuclear reaction studies is an important experimental method in the field of Nuclear Chemistry and Physics. In the past, our research group has used the molecular plating [1, 2] technique to fabricate targets of enriched isotopes of Gd for fusion-evaporation reactions with $^{48}$Ca, $^{44}$Ca, and $^{45}$Sc projectiles [3-5]. The molecular plating technique has the advantages of high efficiency and robustness and a wide range of targets can be made with this technique. In addition to the enriched Gd targets, we have made a target of $^{110}$Cd [6] which was used in a neutron irradiation to test internal conversion theory [7]. A $^{124}$Te has now been fabricated for a similar purpose.

To prepare a target of $^{124}$Te, a small (1-2 mg) amount of $^{124}$Te metal powder was dissolved in ~200 $\mu$L of 2 $\underline{\mathrm{M}}$ HNO$_3$. The sample was evaporated to dryness under Ar gas, and was then reconstituted with 7 $\mu$L of 0.1 $\underline{\mathrm{M}}$ HNO$_3$ and ~ 12 mL of pure, anhydrous isopropanol. This solution was then added to the electrodeposition cell (see [8] for details on the cell) and the $^{124}$Te was deposited onto a 10 $\mu$m thick Al backing at 700 V for 1 hour. The resulting target was then baked at 200°C for 30 minutes to convert the tellurium nitrate to tellurium oxide. Example targets using $^{\mathrm{nat}}$Te were prepared and analyzed using energy-dispersive X-ray spectroscopy (EDS). The EDS technique identifies chemical elements using their characteristic X-ray energies, and an EDS spectrum from a $^{\mathrm{nat}}$Te target is presented in Fig. 1. EDS is a destructive technique, and the $^{\mathrm{nat}}$Te targets were fabricated and analyzed so as not to waste the enriched $^{124}$Te. The results from the neutron irradiation of the $^{124}$Te will be discussed in separate contributions by N. Nica.

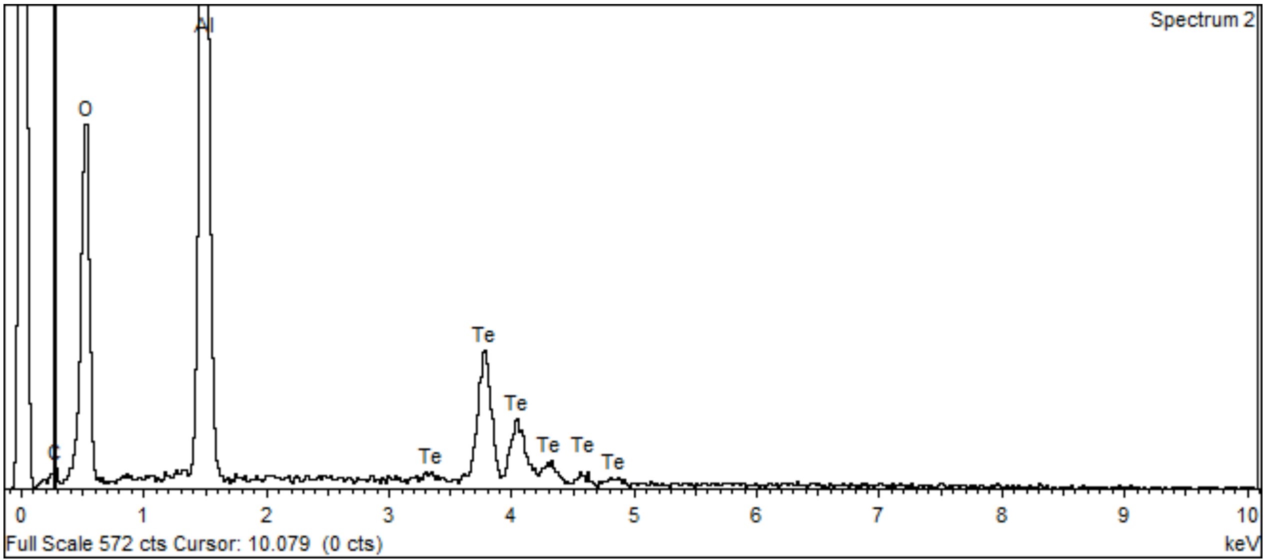

**FIG. 1.** EDS spectrum of the $^{\mathrm{nat}}$Te target. The Te peaks were unambiguously identified. The O peak comes from the chemical form of the target (tellurium oxide), the Al peak comes from the Al backing material and the sample holder, and the C peak comes from the carbon tape which was used to adhere the sample to the sample holder. The peak near 0 keV is background.

[1] W. Parker and R. Falk, Nucl. Instrum. Methods **16**, 355 (1962).

[2] W. Parker, H. Bildstein, N. Getoff, H. Fischer-Colbrie, and H. Regal, Nucl. Instrum. Methods **26**, 61 (1964).

[3] D.A. Mayorov, T.A. Werke, M.C. Alfonso, M.E. Bennett, and C.M. Folden III, Phys. Rev. C **90**, 024602 (2014).

[4] T.A. Werke, D.A. Mayorov, M.C. Alfonso, M.E. Bennett, M.J. DeVanzo, M.M. Frey, E.E. Tereshatov, and C.M. Folden III, Phys. Rev. C **92**, 034613 (2015).

[5] T.A. Werke, D.A. Mayorov, M.C. Alfonso, E.E. Tereshatov, and C.M. Folden III, Phys. Rev. C **92**, 054617 (2015).

[6] T.A. Werke, D.A. Mayorov, M.M. Frey, and C.M. Folden III, *Progress in Research*, Cyclotron Institute, Texas A&M University (2013-2014), p. IV-48.

[7] N. Nica, J.C. Hardy, V.E. Iacob, T.A. Werke, C.M. Folden III, L. Pineda, and M.B. Trzhaskovskaya, Phys. Rev. C **93**, 034305 (2016).

[8] D.A. Mayorov, T.A. Werke, M.E. Bennett, and C.M. Folden III, *Progress in Research*, Texas A&M University (2012-2013), p. II-7.

# GEANT4 simulation of a high-efficiency neutron camera

G. Christian and S. Ota

Neutron spectroscopy is a valuable experimental tool for studies pertinent to both nuclear structure and nuclear astrophysics. In the coming years, we will be beginning a program of neutron spectroscopy experiments using re-accelerated radioactive beams from the Texas A&M University Cyclotron Institute. Broadly defined, we are planning two types of experiment employing neutron spectroscopy: measurement of neutron-emitting transfer reactions, such as *(d, n)*; and invariant-mass spectroscopy of neutron-unbound states. The former are valuable tools for extracting proton single-particle spectroscopic information, in particular for astrophysical proton capture reactions involving radioactive species and for proton-rich systems near the $Z = 8$ shell closure. The latter provide valuable information on very neutron-rich systems, probing changes in the effective nuclear interaction at extreme neutron-to-proton ratios. For both types of experiment, we are planning to couple the TexAT active target (currently being commissioned by G. Rogachev's group) with a high-efficiency neutron detector. These studies will utilize inverse kinematics (i.e. heavy beam impinging on a light target), with beam energies ranging from roughly 10 – 20 AMeV. This requires detection of neutrons with energies ranging from around 1 – 30 MeV, depending on the laboratory angle. This method provides a number of advantages over passive-target experiments, in particular when working with low-intensity radioactive beams. Because the reaction position within the TexAT extended gas target can be reconstructed with high precision, a thick target (density up to ~$10^{22}$ atoms/cm$^2$) can be used without degrading energy resolution. Additionally, tracking of the incoming beam and all outgoing reaction products in TexAT provides a kinematically-complete measurement of the reaction.

Historically, neutron spectroscopy has been challenging since the neutrons can only be detected indirectly, by means of secondary charged particles created in nuclear reactions. For neutrons with energies greater than ~1 MeV, the overwhelming majority of experiments utilize liquid or solid plastic scintillators. These rely on *n-p* elastic scattering to generate energetic protons which then deposit energy into the detector. A number of large, high-efficiency scintillator arrays are presently being used for neutron detection at a variety of facilities worldwide. Some examples include VANDLE [1] and MoNA [2] solid plastic scintillator arrays, and the DEMON [3] and DESCANT [4] liquid scintillator arrays. Although valuable tools for neutron spectroscopy, these detectors suffer from relatively poor position resolution, which in all cases is on the order of 3 – 10 cm. The limited position resolution decreases angular and energy resolution for spectroscopic measurements, decreasing measurement quality. To improve this situation, we are investigating applying the Anger Camera technique [5] to a large-area, high-efficiency neutron detector. The envisioned detector is a large volume of either solid or liquid scintillator, coupled to a grid of photomultiplier tubes on the downstream face. Using this design, the interaction position of neutrons can be deduced from the relative signal sizes recorded in the various photomultipliers, with significant higher granularity than the photomultiplier spacing. The proposed detector would consist of four 1 m × 1 m detectors of varying thickness. The modularization allows for multiple configurations to be employed, increasing the overall range of experiments which can be performed with the device.

In the present work, we report on GEANT4 simulations of a single Anger Camera neutron detector module. The module consists of a volume of BC-519 liquid scintillator contained within a rectangular Aluminum container. The container front face dimensions are 1 m × 1 m, and the thickness was varied in the simulations to probe its influence on position resolution and detection efficiency. The downstream face of the detector contains a 4 × 4 grid of photomultiplier tubes for light collection. Each phototube is coupled to a light guide whose broad end has dimensions of 25 cm × 25 cm, such that the light collection is evenly and completely distributed between the phototubes. The simulations utilize the MENATE_R [6] package, which includes realistic, data-driven modelling of both neutron-proton and neutron-carbon interactions. The simulation also includes realistic generation, transport, and detection of optical photons, as well as realistic statistical fluctuations in the number of photons recorded in each phototube. From the simulated distributions of photon intensity vs. phototube position, we have extracted $x$, $y$, and $z$ positions by fitting the simulated distributions with the following response function,

$$f = \oint \frac{I}{4\pi r^2}\, \hat{\boldsymbol{n}}\, \mathrm{d}\boldsymbol{A},$$

where $I$ is a normalization constant related to the total photon intensity; $\hat{\boldsymbol{n}}$ is the unit vector from the interaction point to the light guide; and the integral is evaluated over the area covered by the light guide. This integral evaluated analytically in Cartesian coordinates to

$$\frac{I}{4\pi}\tan^{-1}\left(\frac{x'y'}{z'\sqrt{x'^2 + y'^2 + z'^2}}\right).$$

The fit was performed by minimizing the negative log-likelihood, which was shown to produce better results than the more conventional $\chi^2$ technique. Some sample results for 15 MeV neutrons impinging on a 1 m × 1 m × 30 cm detector volume are shown in Fig. 1. Shown in the figure are the difference between the extracted neutron hit position from the fitting procedure and the actual hit position, for 10,000 incoming neutron events with randomized hit positions. These distributions have a FWHM of around 1 cm in the $x$ direction and 1.5 cm in the $z$ direction. The resulting position resolution is better than even the highest-resolution detectors presently available, and it comes without the decrease in efficiency suffered from using a thin detector. Future work will focus on further optimizing the detector design for maximum efficiency and resolution, followed by construction and offline testing of the first detector module.

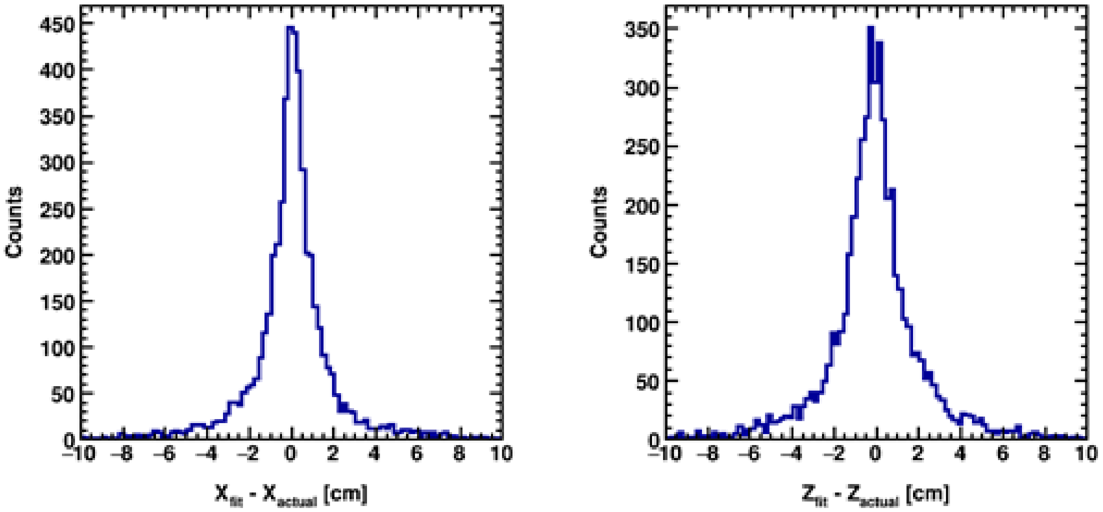

**FIG. 1.** Simulated error in the horizontal (left panel) and longitudinal (right panel) directions, using the Anger Camera technique. Results for the vertical axis are statistically identical to the horizontal axis.

[1] C. Matei *et al.*, Proceedings of the Ninth International Symposium on Nuclei in the Cosmos, vol. **138**, Proceedings of Science, 2008, pp. 1–5.

[2] B. Luther *et al.*, Nucl. Instrum. Methods Phys. Res. **A505**, 33 (2005).

[3] I. Tilquin *et al.*, Nucl. Instrum. Methods Phys. Res. **A365**, 446 (1995).

[4] P.E. Garrett, Hyperfine Interact. **225**, 137 (2014).

[5] H.O. Anger, J. Nucl. Med. **5**, 515 (1964).

[6] B. Roeder, *Development and Validation of Neutron Detection Simulations for EURISOL*, EURISOL Design Study, Report, pp 31-44 (2008).

# Final results of the first upgrade of the Oxford detector

A. Spiridon, R. Chyzh, M. Dag, E. McCleskey, M. McCleskey, B.T. Roeder, A. Saastamoinen, R.E. Tribble, L. Trache,[1] E. Pollacco,[2] and G. Pascovici[1]
[1]*IFIN, Bucharest-Magurele, Germany*
[2]*IRFU, CEA Saclay, Gif-sur-Yvette, France*

The Oxford detector [1] is one of the two focal plane detectors of the Multipole-Dipole-Spectrometer (MDM). It's a gridded ionization chamber with 4 avalanche counters and a scintillator. Particle identification is done using the energy loss in the gas, dE, and the stopping energy left in the scintillator, E. This detector was used successfully for nuclear astrophysics studies involving nuclei with $A \leq 26$. However at higher masses than that, it was found that the limited resolution of both dE (10-13%) and E (16-20%) signals was causing significant difficulties in particle identification. The upgrade of the Oxford detector was focused on improving the resolution of both of these signals. For details on the project see ref [2], [3], and [4]. The first step in this upgrade was to improve the dE signal by introducing Micromegas [5], a new technology shown to provide gains of ~ $10^4$, as well as very good energy resolution.

The physical modifications required for this were completed in November 2014 and can be seen in Fig. 1. The original aluminum anode plate was replaced with a Micromegas one containing 28 individual detection pads. The signals were read using 2 D-SUB 25 connectors and processed through 2 Mesytec MPR-16 preamplifiers, 2 Mesytec MSCF-16 shapers and one Mesytec ADC.

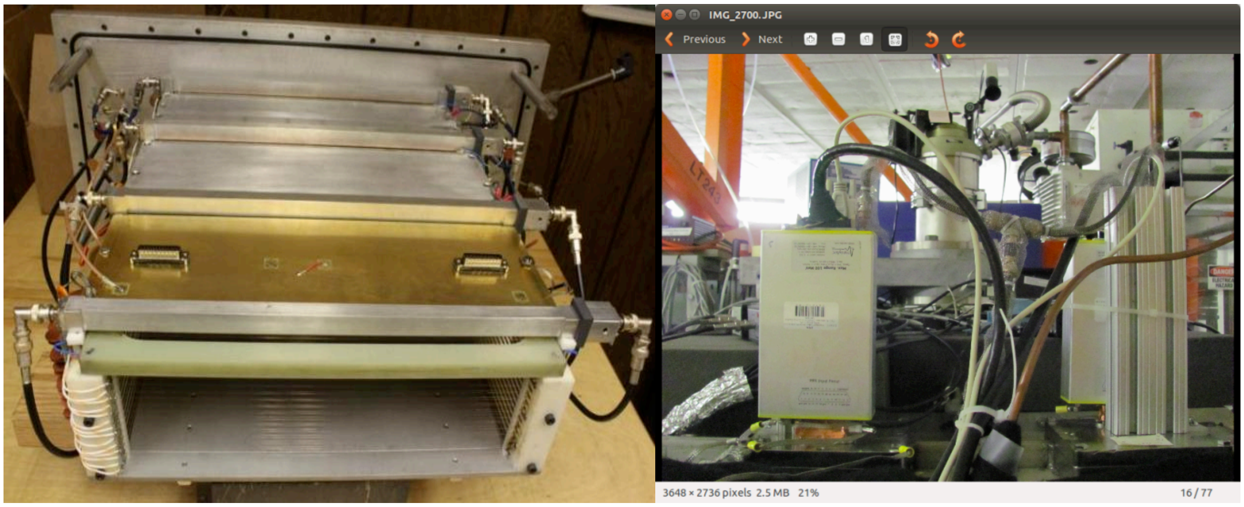

**FIG. 1.** (left) Photograph showing the detector components inside the chamber. (right) Photograph showing the outside of the detector chamber, including the new flanges and the MPR-16 modules.

Tests were done over a 14 month period with a variety of beams. Fig. 2 shows an example of the individual pad response as well as the full anode response for a tightly collimated $^{16}$O beam. The

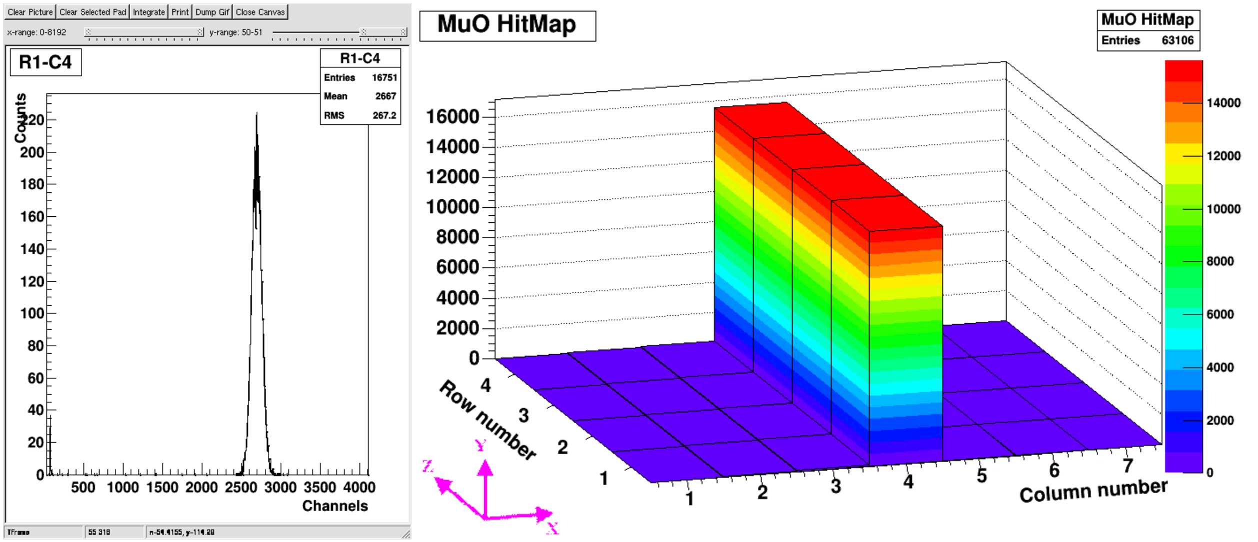

**FIG. 2.** (left) Hisogram showing the response of pad in row 1 column 4. (right) 3-D map of the column 4 pads 'hit' as a $^{16}$O beam passes through the gas.

Micromegas behavior was observed for different gas (isobutane) pressures, different bias voltages, as well as different ionizing particles. Fig. 3 summarizes the determined micromegas gain behavior under these different conditions.

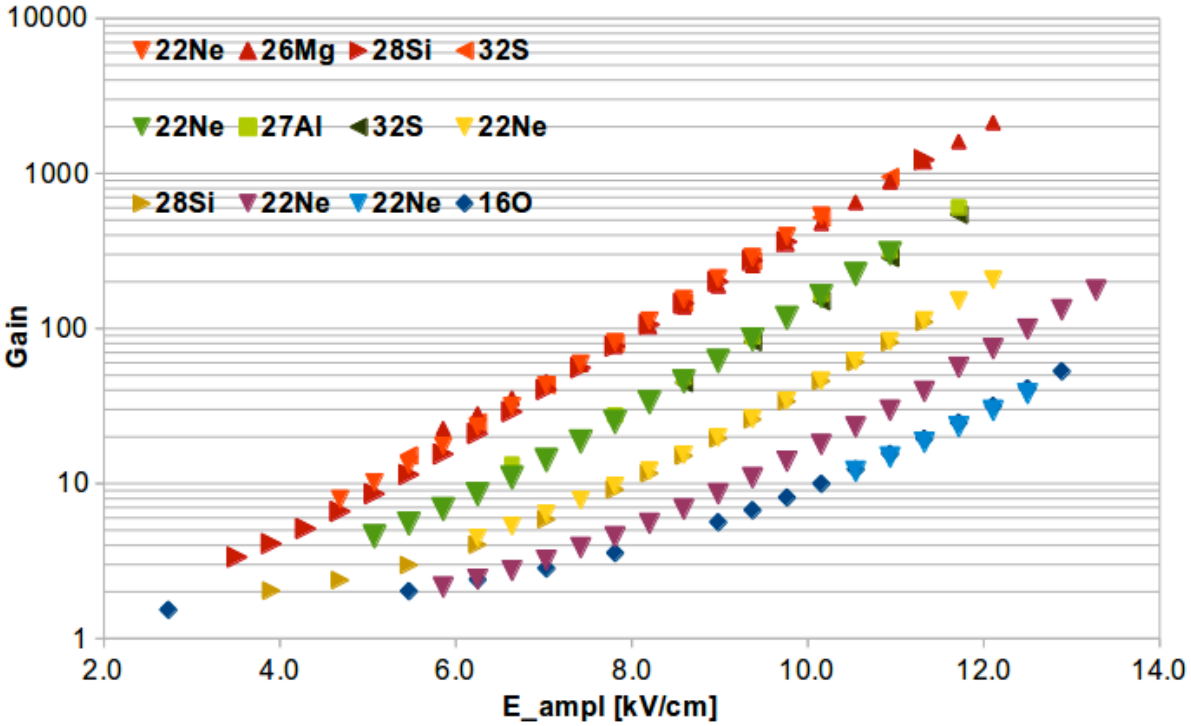

**FIG. 3.** Micromegas gain curves for all the ionizing particles used in the testing. The different gas pressures are color coded (Torr): red=30, green=50, yellow=70, purple=85, and blue=100.

Individual pad resolution varied with the gas pressure from ~5.5% (at 100 Torr) to ~10-11% (at 30 Torr). Averaging the energy over the 28 pads, the resolution improved by almost a factor of 2, as can be seen in Fig. 4.

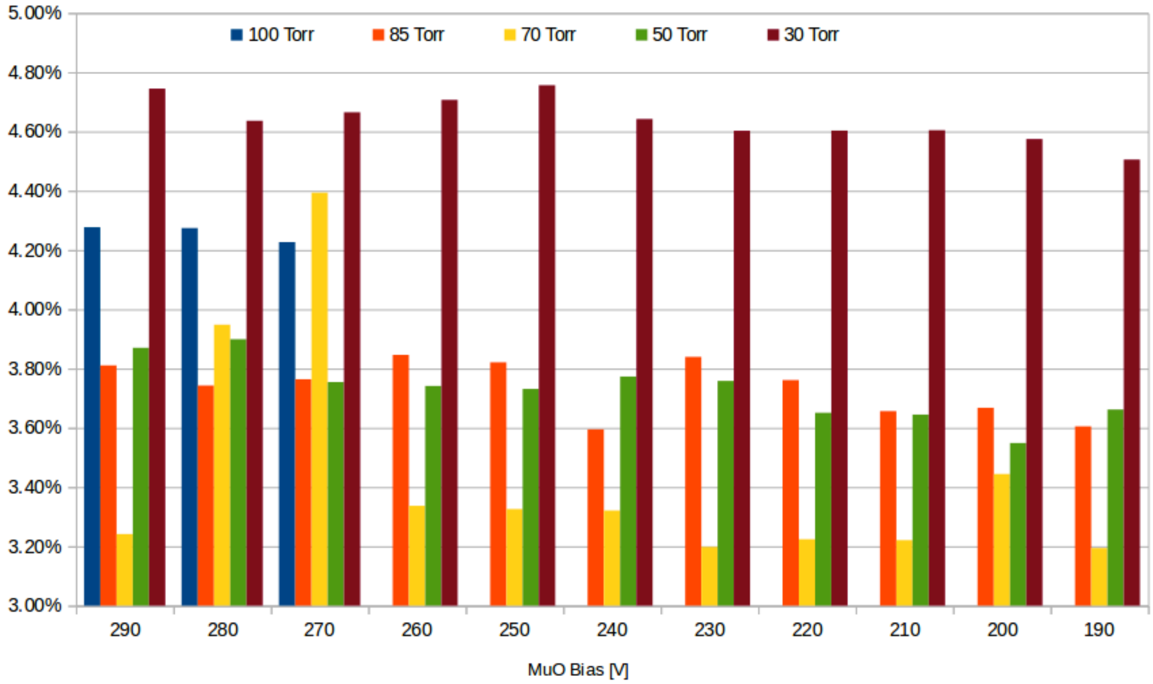

**FIG. 4.** Plot showing the energy loss resolution for the Micromegas anode (averaged over the 28 pads) for different bias voltages of the Micromegas and different gas pressures.

At similar pressures, the Micromegas detect the energy lost in the gas with a resolution a factor of 3 better than the ionization chamber. In conclusion, the upgrade was considered successful and has already been in use for nuclear astrophysics studies focused on nuclei with A>26 (like, $^{28}$Si and $^{32}$S).

The second step of the upgrade will involve replacing another aluminum anode with a Micromegas plate. The 2-Micromegas anodes configuration is intended for use an independent dE-E telescope, where one anode will detect the energy loss signal, dE, and the second one will detect the stopping energy, E. This setup will allow the use of higher gas pressures (for better resolution), as well as studies at higher angles and/or at particle lower energies.

[1] D.H. Youngblood *et al.*, Nucl. Instrum. Methods Phys. Res. **A361**, 359 (1995); M. McCleskey, Ph.D Thesis, Texas A&M University, 2011.

[2] A. Spiridon *et al.*, in *Progress in Research*, Cyclotron Institute, Texas A&M University (2012- 2013), p. IV-50

[3] A. Spiridon *et al.*, in *Progress in Research*, Cyclotron Institute, Texas A&M University (2013- 2014), p.IV-45

[4] A. Spiridon *et al.*, in *Progress in Research*, Cyclotron Institute, Texas A&M University (2014- 2015), p.IV-29.

[5] Y. Giomataris *et al.*, Nucl. Instrum. Methods Phys. Res. **A376**, 29 (1996).

# Offline tests of the AstroBoxII with 128 μm and 64 μm Micromegas

R. Chyzh, A. Saastamoinen, B. Roeder, A. Spiridon, M. Dag, R.E. Tribble,
M.R.D. Rodrigues,[1] E. Pollacco,[2] and L. Trache[3]
[1]*Instituto de Fisica, Universidade de Sao Paulo, Caixa Postal 66318, Sau Paulo, SP, Brazil*
[2]*IRFU, CEA Saclay, Gif-sur-Yvette, France*
[3]*National Institute for Physics and Nuclear Engineering Horia Hulubei, Bucharest, Romania*

Proton capture reactions X(p, γ)Y play an important role in stellar environments like X-ray bursts or novae [1-3]. Reactions like $^{22}$Na(p, γ)$^{23}$Mg, $^{12}$C(p,γ)$^{13}$N(β$^{+}$)$^{13}$C, $^{16}$O(p, γ)$^{17}$F(β$^{+}$)$^{17}$O are particularly important in the novae explosions [1-3]. These reactions are characterized by the location and the strength of the resonances. Many of the important resonances lie just above proton separation threshold $S_p$ these resonances can be studied by indirect methods such as β-decay. In this case, we populate the important states by means of β-decay. This will necessarily bring up the problem of dealing with β-background. The AstroBoxII was specially designed for this purpose and it allows a dramatic reduction of the β-background and opens up an opportunity to measure proton energies of just few keV [4] [6]. It is a newly build detector that is an improvement over the original AstroBox[5]. One of the key elements of the AstroBoxII is a Micromegas anode plate that has 29 pads located symmetrically along the beam direction. Above the Micromegas plate there is a set of wires, the gating grid (GG), that allows control of the transparency of the gas gap between the GG and the Micromegas. The wires themselves are split into two sets that can be biased independently. This gives a greater flexibility when controlling transparency of the GG. Also a big part of the upgrade of the detecting system was acquiring special switch that could be programmed to control gating grid (GG) voltage automatically. That would allow us to remotely control transparency of GG in certain intervals of time.

We have received two Micromegas detectors with β-mesh for testing purposes. First, we have installed a Micromegas with 128 μm amplification gap. Fig. 1 shows the results of one of our test which

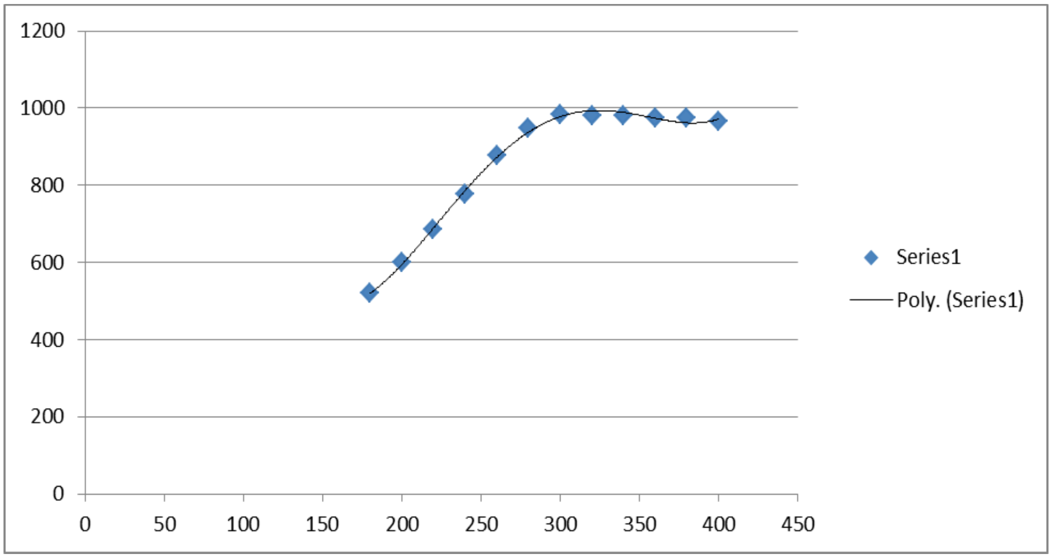

**FIG. 1.** This figure presents the position of the main peak (y-axis) vs the voltage on the GG (Gating Grid) in volts (x-axis). Experimental points (blue dots) approximated by polynomial fit.

we used for the optimization of the GG voltage. Also, we scanned all the pads to see the energy resolution which was in the order of 17-20% for different pads. For testing purposes, we placed the source of Fe-55 right below the C3 pad which corresponds to the center of the Micromegas where we normally want particles to be stopped. Energy spectrum in the C3 pad from a Fe-55 source can be seen in Fig. 2. This pad had a resolution 20%.

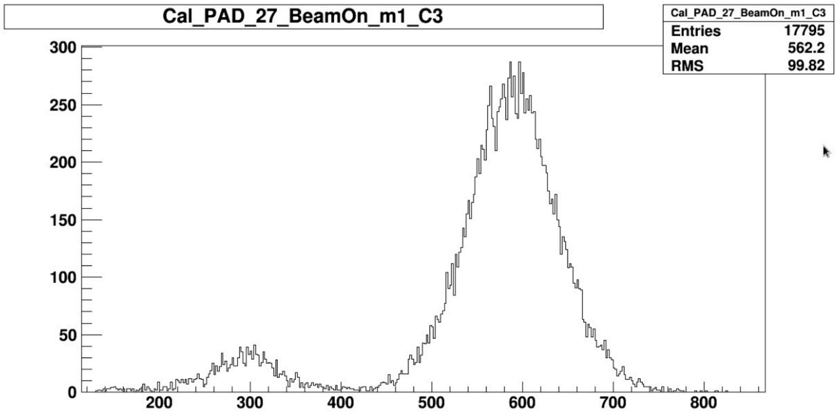

**FIG. 2.** Calibrated energy spectrum from the C3 pad of a Micromegas with 128 μm amplification gap. Calibrated energy on the x-axis (should be multiplied by factor of 10 to get "eV" units) vs number of counts on the y-axis. The peak from Fe-55 X-ray source (5899 keV) can be seen in the spectrum.

After that we ran a series of similar tests with a 64 μm Micromegas. It proved to be a little worse in terms of resolution. Fig. 3. shows the energy spectrum of the Fe-55 source recorded in the C3 central

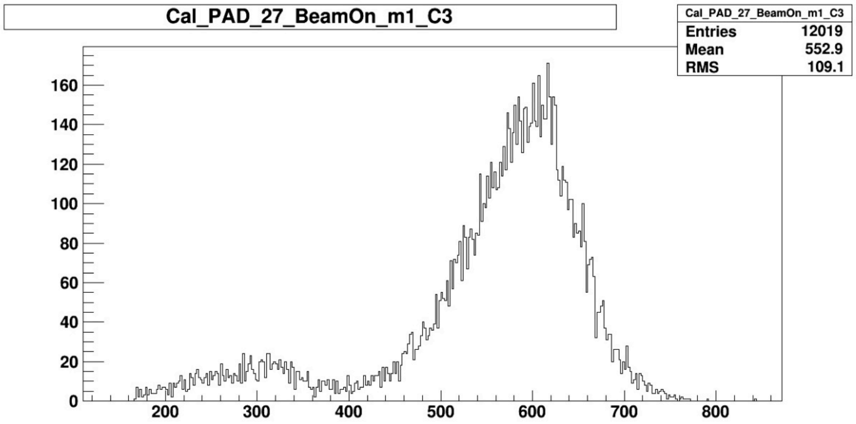

**FIG. 3.** Calibrated energy spectrum from the C3 pad of a Micromegas with 64 μm amplification gap. The same X-ray source Fe-55 was used. The shape of the main peak (5899 eV) is significantly deviated from a normal Gaussian distribution.

pad for the 64 μm Micromegas. This particular pad had a resolution roughly 23%. The shape of the main peak (5899 eV) is slightly deviated from a normal Gaussian.

[1] J. Jose and C. Iliadis, Rep. Prog. **74**, 096901 (2011).
[2] J. Jose and M. Hernanz, Eur. Phys. J. A **27**, Supplement 1, 107 (2006).
[3] J. Jose, M. Hernanz, and C. Iliadis, Nucl. Phys. **A777**, 550 (2006).
[4] A. Saastamoinen *et al.*, Nucl. Instrum. Methods. Phys. Res. **A376**, 357 (2016).
[5] E. Pollacco *et al.*, Nucl. Instrum. Methods Phys. Res. **A723**, 102 (2013).
[6] A. Saastamoinen *et al.*, Progress in Research, Cyclotron Institute, Texas A&M University (2014-2015), p. IV-33.

# An electron gun system for alignment of the Penning trap magnetic field

E. Bennett, B. Fenker, M. Mehlman, D. Melconian, J. Patti, and P.D. Shidling

One important aspect regarding the design of the TAMUTRAP experiment is beam alignment with the magnetic field and with the Penning trap itself. The 7 T field generated by the generally cylindrical superconducting magnet is – understandably – not perfect. There is both deviation within the field itself and alignment of the field lines with the entry and exit ports on either side of the cylindrical magnet. Additionally, it is important to align the small entry and exit ports of the Penning trap along the field lines and place the center of the Penning trap as close to the center of the cylindrical magnet as possible; otherwise, ions from the beam line feeding the trap will not be captured and reduce the efficiency of the system. Thus, to trap ions, it is necessary for there to be a high degree of accuracy in end-to-end alignment – on the order of about 0.2 mm.

To achieve this degree of accuracy, an alignment tool is required: an electron gun. A drawing of the electron gun designed specifically for the TAMUTRAP is shown in Fig. 1. The system spans the length of the beampipe resting within the 7 T cylindrical magnet so as to place an electron-generating tungsten filament at the center of the bore of the magnet. The beampipe itself can then be manipulated to place the electron-generating filament at or near the center of the magnet. Internal Faraday cups and collimators are provided both near the center and near the ends to assist in alignment (manipulation) of the beampipe with the field.

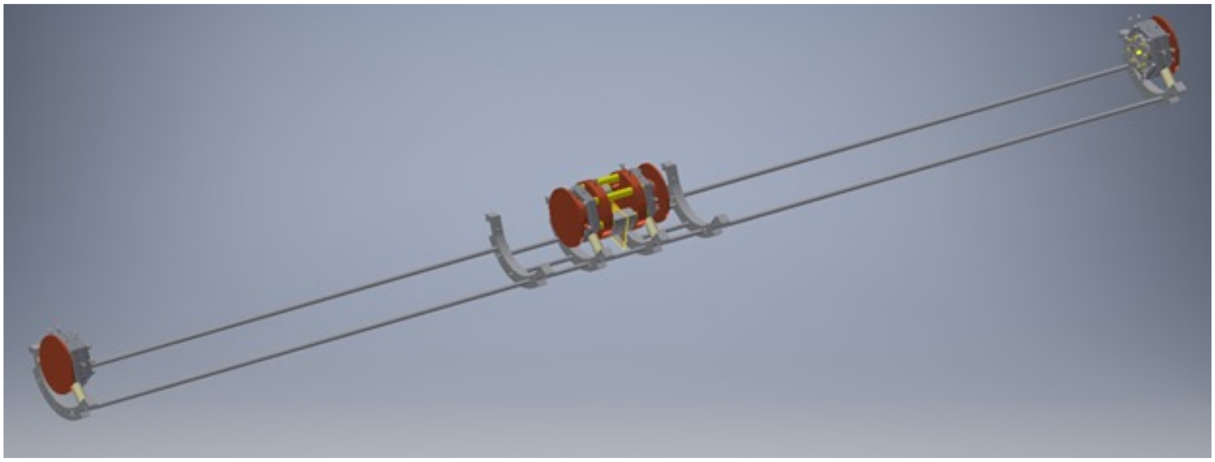

**FIG. 1.** AutoCAD drawing of the electron gun used to align the magnetic field of the Penning trap magnet with the beamline.

The collimators are paired with each of the Faraday cups and are identical to one another. The purpose is to generate a fine pencil beam of electrons across the entire length of the beampipe. These collimators are aligned using an optical transit outside of the vacuum to ensure a direct line of sight between each end and the filament. The collimators are also held in place by a hexagonal upper support having three alignment bolts – which adjust the center position of the ports in the collimators.

The electron gun has been built and we expect to have the field aligned with the beampipe in the summer of 2016.  Once commissioned, a patent application will be forthcoming based on this design.

## Status of TAMUTRAP facility

E. Bennett, B. Fenker, M. Mehlman, D. Melconian, J. Patti, and P.D. Shidling

We began the year by continuing the systematic studies of radio frequency quadrupole (RFQ) trap (Section 1 in Fig.1), which included the testing and optimization of the RFQ in bunched mode, injection optics and the extraction optics. For these studies, we used microchannel plate (MCPs) for single ion counting and beam optics optimization in bunched and pulsed operation modes (Diagnostic 3 station in Fig. 1). The diagnostic stations along the beam-line are combinations of MCPs and Faraday cups (FC).

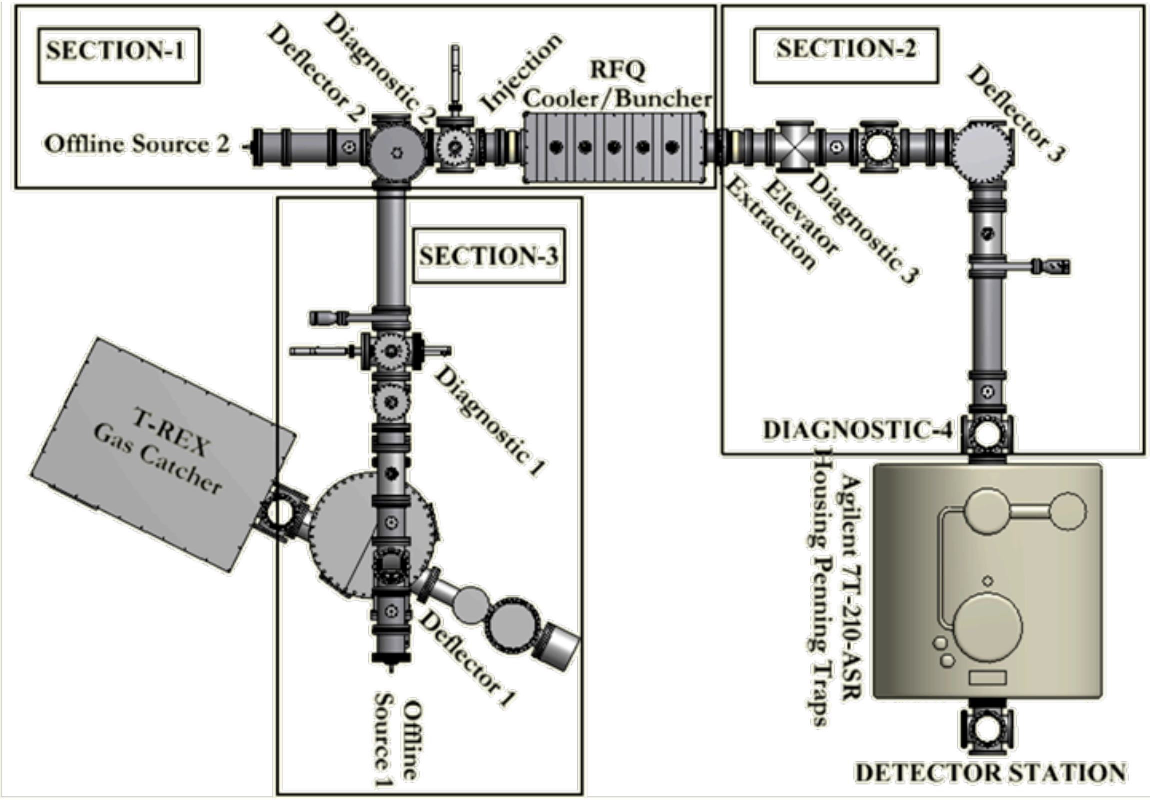

**FIG. 1.** Commissioned TAMUTRAP beamline, which includes the RFQ, pulsing cavity, diagnostic station, cylindrical and spherical deflectors, and two ion guns.

The time spectrums were recorded for different gas pressure in RFQ, different ejection time, and different cooling time. In addition to these studies, three different modes of extraction of the bunched beam from the RFQ trap were studied. In the first mode, only the potential on the last electrode (#30) was lowered and the ions drifted out of the trap. In the second mode, the potential on the last electrode (#30) was lowered at the same time as the potential on the third from the last electrode (#28) was raised, thus kicking the ions out of the trap. In the third mode, we coupled the last two electrodes (#29 and #30) and the trap was formed using the third electrode (#28) from the last. These systematic studies helped us to confirm further that the multi peak observed in the timing spectrum for some settings of ejection time was not because of the multi traps being formed in the RFQ, but because of more than one mass being released from the ion source. The FWHM of the bunch's time spread is around 1.1 μs with energy of the extracted bunch's being 10 keV (See Fig. 2).

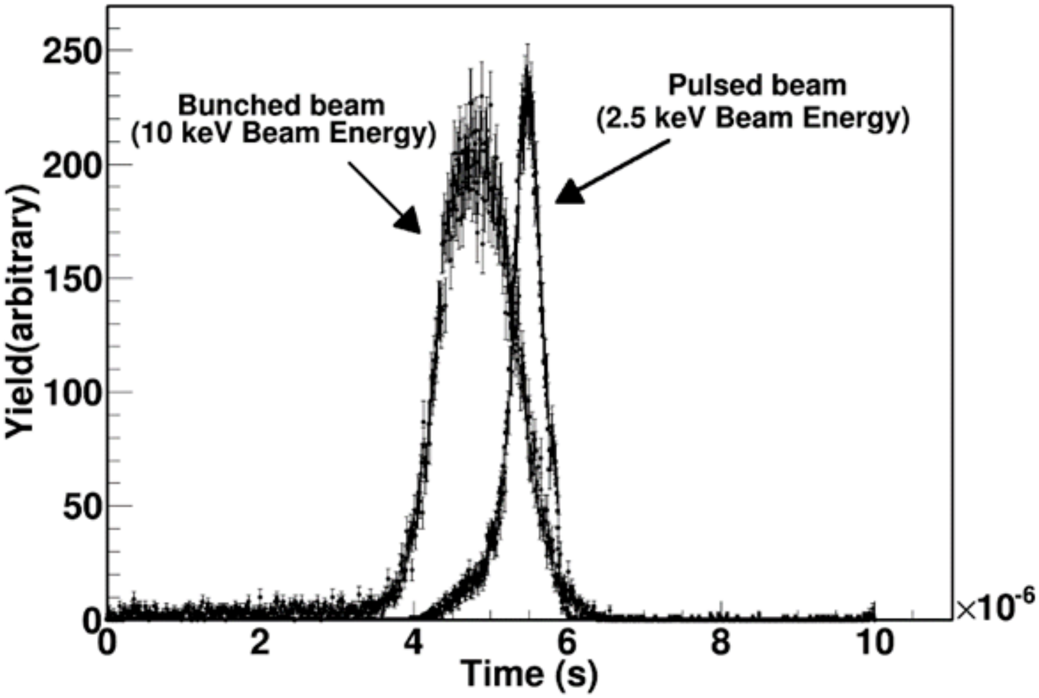

**FIG. 2.** Time spectrum of bunched and pulsed ions.

After the systematic studies with RFQ, a pulsing drift tube (elevator in Section 2 of Fig.1) was coupled to the extraction optics to redefine the energy of the extracted bunch. The pulsing drift tube employs a 400 mm long drift tube and has been designed as a floating element able to sit within the beam line. The support structure consists of three semi-circular legs that can be placed arbitrarily along the length of the electrode, and are held in place via set screws. In pulsed mode the energy of the extracted bunch is the potential difference between the floating voltage of RFQ platform and drift tube. The principle is illustrated as follows: the ion pulse is accelerated towards a pulsing drift tube and the kinetic energy gained by the ion pulse is the potential difference between the RFQ high voltage platform and drift tube. Once the ions are inside the drift tube, its potential is switched to ground potential using a behlke high-voltage switch. Thus, the ions leave the drift tube at a ground potential with a kinetic energy equal to the potential difference between the RFQ and drift tube. The kinetic energy of the ion pulse after the pulsing drift tube is around 2.5 keV. Following the pulsing drift tube, the pulsed beam is guided using a combination of einzel lens and x-y steerer and, further bent by 90 degree using cylindrical deflector. Additional einzel lens, x-y steerer and a beam diagnostic station (Diagnostic 4) is coupled after the final bend (Section -2 of Fig.1).

Alignment of section-1 collinear to section-2 was performed by setting up two optical transits, one along the axis of RFQ and one along the axis of superconducting magnet. After aligning the electrostatic components of both the sections, offline tests were performed using offline ion source 2 (see

Fig.1). Beam was successfully loaded into the RFQ, bunched and cooled in RFQ, pulsed using pulsing drift tube, and bent by 90 degree using cylindrical deflector (deflector 3 in Fig.1). The time spectrum was recorded using MCP detector at diagnostic station-4 for different settings of RFQ, and for different combination of cylindrical deflector plate voltages. The settings of other electrostatic components (Einzel lens, steerer, injection optics, and extraction optics) were also optimized to maximize the transport efficiency. The timing spectrum of bunched and pulsed ions is compared in Figure 2. The FWHM of pulsed ions is narrower than the bunched ions. One of the main reasons for this is the existence of more than one mass in the bunched spectrum, which gets separated by time of flight in pulsed mode. The FWHM of pulsed ions is less than 1μs.

Section-3 (Fig. 1) was further coupled to the spherical deflector (Deflector 2 in Fig.1). This includes three einzel lenses, 2 x-y steerer, beam emittance and diagnostic station, cylindrical deflector, and offline ion source (Offline Source 1 in Fig.1). To achieve the required vacuum, turbo pump with pumping speed 450 L/s and backed by dry scroll pump is placed before beam diagnostic station. Alignment of section-3 collinear to section-1 and section-2 was performed by setting two optical transits, one along the axis of section-3 and one along the axis of RFQ. Detail procedure of alignment is explained in last year's annual report [1].

An in-house-designed ion gun employing a sodium ion source (offline source 1 in Fig.1) was developed and mounted before the first cylindrical deflector for testing lenses, steerer, and spherical deflector of Section-1. The beam was transported with high efficiency from offline source 1 and further bent by $90^0$ using spherical deflector. The settings of spherical deflector plate voltages were optimized by measuring current in the Faraday cups located at diagnostic stations 1 and 2. The functioning of lenses, x-y steerer, and spherical deflector guided the ions into the RFQ from offline source-1. The ions were cooled/bunched, pulsed and bent by 90 degree using cylindrical deflector (Deflector-3). The time spectrum observed at diagnostic station 4 was similar to that shown in Fig.2.

The immediate outlooks for the TAMUTRAP facility involves the coupling of Penning trap system to the TAMUTRAP beam line and trap the ions from the stable ion source. The large bore magnet (Magnex Scientific) for the Penning trap has been energized to the full 7T field with <2 ppm inhomogeneities at the centre. We are in the process of installing the assembled prototype trap system after the completion of scheduled maintenance. More details about the Penning trap system are provided in another report.

[1] E. Bennett *et al.*, *Progress in Research*, Cyclotron Institute, Texas A&M University (2014-2015), p. IV-36.

# Laser-based calibration of source-detector geometry for precision γ-ray measurements

V.E. Iacob and J.C. Hardy

A critical ingredient in our measurements of precise branching ratios is the photopeak efficiency of our HPGe detector: The absolute efficiency is known to better than 0.2% over the energy range 50-1400 keV [1] but this high precision cannot be obtained in any on-line measurement in the absence of a strictly controlled source-to-detector distance. All the calibration measurements reported in Ref. [1] have been made at a distance of 151 mm, measured from the source to the edge of the lip on the front-face of the Al container surrounding the Ge crystal (see Fig. 1). Thus, any experiment that needs this precise absolute efficiency must be performed at the same distance.

In the past we determined this distance with a Mitutoyo mechanical inside micrometer set. We placed a flat Al plate over the front of the detector and pressed it against the lip of the detector container; then we adjusted the distance between the plate and the source to the appropriate value set on the micrometer, the source being coaxial with the HPGe crystal and the container.

However, during the past decade, the HPGe detector experienced several loss-of-vacuum incidents affecting the chamber containing the HPGe crystal. The cause was identified to be related to cracks in the glue bonding the thin Be window to the Al container (see Fig. 1). We fixed this by patching the front edge of the HPGe container with Armstrong A-12 Epoxy Adhesive Resin. As an undesired side-effect, this converted the flat lip of the Al container into a hilly surface. The "small" peaks (up to ~0.3 mm), not necessarily located at diametrically opposed locations, made it extremely difficult to define a reference position on the front of the cup containing the HPGe. To overcome this problem, we have moved from the micrometer-based distance calibration towards a system using a laser-sensor, the AR700-8 (by Acuity).

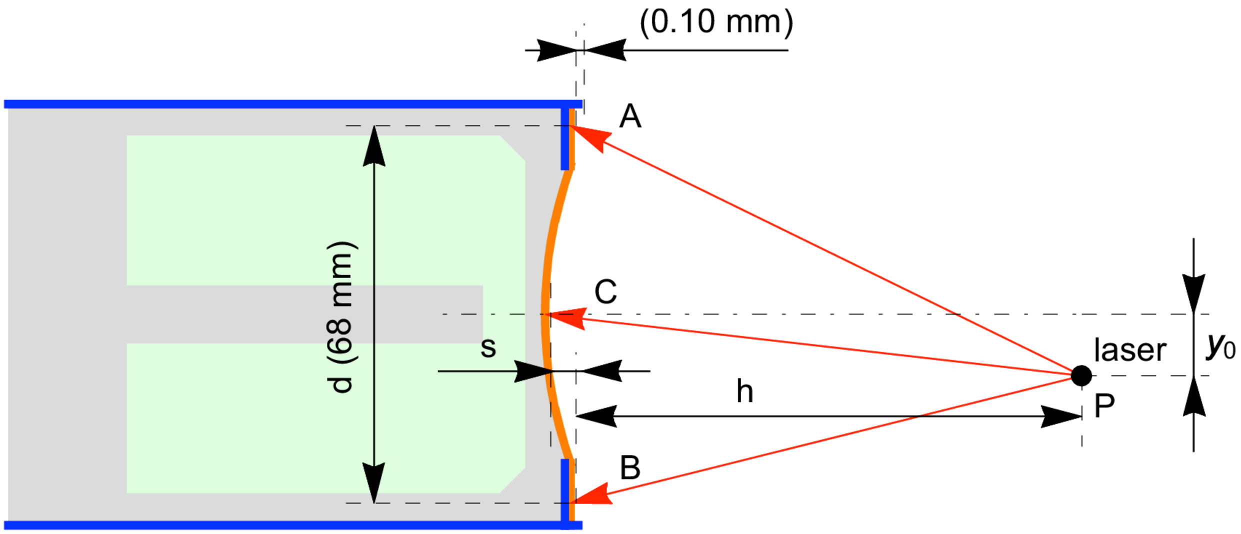

**FIG. 1.** Top view of the HPGe-Laser assembly. The laser sensor can pivot about the vertical axis P and aim towards points A, B, and C and determine corresponding distances (in red). These along with the distance between points A and B (d = 68 mm) allow for the calculation of the sag "s" of the Be window (orange) and the distance "h" from point P to the plane tangent to the Be window. The geometry of the Al container (blue) includes at its edge the δ = 0.10 mm lip that extends beyond the Be window.

The new laser sensor is mounted on a holder that puts the laser beam in a horizontal plane containing the HPGe axis; the holder can pivot about a vertical axis (point P in Fig. 1), thus allowing for reading distances to the maximum-sag position (in the Be window) and to points on the window that are mechanically supported by the Al seat: These are the distances P-C, P-A, and P-B, respectively, marked in red in Fig. 1. Any unbalance between the P-A and P-B distances makes for an easy test of any off-axis placement ($y_0$ in Fig. 1) of the pivoting point P. As the distance between the points A and B is known ($d_{\text{A-B}}$ = 68 mm) the distance $h$ between the pivot and the plane tangent to the front-face of the Be window is easily calculable. That distance, along with a reading of the distance P-C, yields a measurement of the sag of the Be window. We found that sag to be $s$ = 1.02(5) mm. This establishes the distance along the axis between the center of the Be window and a plane touching the lip of the Al container to be 1.12(5) mm.

In setting up our counting geometry, we place the laser at approximately 500 mm from the detector window and as close to the central axis as possible (*i.e.* $y_0$ is close to zero). We then place the source in its fixed holder approximately 151 mm from the detector and between the detector and the laser. We then measure the distance from the laser to the source. Next the source is removed and the distance from the laser to the center of the Be window is measured. Finally, the detector is adjusted on its supporting rails until the difference between the two measurements (source distance and window distance) is exactly 152.12 mm. Under this condition, the distance from the source to the plane of the lip of the Al detector-container is exactly 151.0 mm, the precise calibration distance. The active range of the AR700-8 laser-sensor requires that the two distances be between 331 mm and 533 mm.

We note an additional benefit to our using the laser sensor for setting the source-detector distance. Any mechanical micrometer needs to make physical contact at its end-points. In our case this means the micrometer must be in contact with the source and the plate resting on the HPGe container lip. This necessarily adds some small elastic deformations in both source and plate, potentially leading to our determining slightly shorter distances than the true value. Obviously, the laser-based distance reading is free from this source of error.

[1] J.C. Hardy *et al.*, Appl. Radiat. Isot. **56**, 65 (2002); R.G. Helmer *et al.*, Nucl. Instrum. Methods Phys. Res. **A511**, 360 (2003); R.G. Helmer *et al.*, Appl. Radiat. Isot. **60**, 173 (2004).

# Restoration of Poissonian events that were missed due to extending dead time

V. Horvat and J.C. Hardy

If a known extending dead time is imposed to a Poissonian sequence of events, some of the events will be lost. We are trying to develop a method of replacing those lost events by *simulated* events in a way that guarantees (within precision of the best available measurements) that the resulting event sequence is purely Poissonian and statistically indistinguishable from the original sequence of events. This problem proved not to be as trivial as it may seem, even in the simplest case (considered here), in which the ideal rate of the original Poissonian events is constant and known.

In this report we describe a solution to this problem, along with some potentially interesting properties of the event distributions that were discovered along the way. The method of event restoration shown here is found to be effective and appropriate, and it can be set to work within any desired level of accuracy. For brevity, we will use the term *event restoration* instead of the more meaningful term *replacement of events (lost due to dead time) by a statistically equivalent set of simulated events*.

The method of event restoration proposed here is explained based on an example of a data set with approximately 60 million events simulated assuming constant ideal event rate $\rho = 10\ \mathrm{s}^{-1}$, and partitioned into one thousand samples, each having 100 channels spanning the duration of 100 s. An extendable dead time per event, $\tau_{e,}$ is then imposed to this event sequence. Several values of $\tau_e$ up to as high as 120 ms, were used in order to prove the applicability of the method even in the extreme situations. Specifically, at $\tau_e$ = 120 ms, the expected fraction of surviving events [given by $\exp(-\rho\tau_e)$] is only about 30%.

Given that the sequence of known live times associated with the surviving events is Poissonian, it may seem appropriate to map all consecutive dead-time intervals into a single continuous time interval, fill that single interval with simulated events at the nominal ideal event rate, and then map each dead-time interval together with its events back into the interval's original place in the time sequence. Even though this process produces a statistically correct number of restored events, the resulting time sequence is non-Poissonian and can be identified as such by looking at the distribution of its time intervals or by looking at the variance of the resulting number of events per channel of a chosen size as a function of time. Furthermore, reapplying the dead time to this sequence of events yields a secondary event set significantly different from that obtained originally. Nevertheless, a method similar in concept to this one, referred to as the "shadow method", has been used in the analysis of muon-decay spectra [1].

In order to restore the lost events so that the resulting event time sequence is Poissonian, it is necessary to observe and respect the following four properties of the secondary-event sequence:

(*i*) a dead-time interval cannot be shorter than $\tau_e$,

(*ii*) if a dead-time interval length is $\tau_e$, then no events have been lost,

(*iii*) if a dead-time interval is longer than $\tau_e$, then one lost event has originally occurred at time $\tau_e$ before the end of the dead-time interval, and eventually, (*iv*) any number of events may have occurred before that, provided that the differences between arrival times of the consecutive lost events are less than $\tau_e$.

While incorporating properties (*i*) through (*iii*) is trivial, simulating the events that may have occurred before the last lost event in a dead-time interval longer than $\tau_e$ proved to be challenging. Specifically, if one event is generated at a time, then the arrival time of the last lost event (that is known to have happened) relative to the previous event (obtained in a simulation) will not be properly distributed. In fact, longer intervals will occur more often than shorter intervals, which is opposite to what Poissonian distribution requires.

Furthermore, simulating a series of events restricted to time intervals shorter than $\tau_e$ results in a wrong time-interval distribution and a significantly overestimated number of restored events. Although the cumulative probability of a truncated probability density scales with that of an unrestricted probability density for a single time interval, the two do not scale when a sequence involving more than one time interval is involved. Specifically, density of the probability of having exactly one lost event in a dead-time interval, $t_d$ (which occurs at $t_d$ - $\tau_e$), is given as a function of $t_d$ by

$$dP_{1L}/dt_d = \left| \begin{array}{ll} 0 & 0 < t_d \le \tau_e \\ \rho \exp[-\rho(t_d-\tau_e)] \,/\, [1-\exp(-\rho\tau_e)] & \tau_e < t_d \le 2\tau_e \\ 0 & t_d > 2\tau_e \end{array} \right. \qquad (1)$$

which scales with $\rho \exp[-\rho(t_d-\tau_e)]$. However, the density of the probability of having exactly two lost events in a dead-time interval, $t_d$ (one of which occurs at $t_d$ - $\tau_e$), is given by

$$dP_{2L}/dt_d = \left| \begin{array}{ll} 0 & 0 < t_d \le \tau_e \\ \rho^2(t_d-\tau_e) \exp[-\rho(t_d-\tau_e)] \,/\, [1-\exp(-\rho\tau_e)]^2 & \tau_e < t_d \le 2\tau_e \\ & \\ \rho^2(3\tau_e-t_d) \exp[-\rho(t_d-\tau_e)] \,/\, [1-\exp(-\rho\tau_e)]^2 & 2\tau_e < t_d \le 3\tau_e \\ 0 & t_d > 3\tau_e\ , \end{array} \right. \qquad (2)$$

which does scale with $\rho^2(t_d-\tau_e) \exp[-\rho(t_d-\tau_e)]$ for $\tau_e \le t_d \le 2\tau_e$ because in this case the first event can occur anywhere in the range between 0 and the second event (which occurs at $t_d$ - $\tau_e$), but this scaling does not extend to $2\tau_e \le t_d \le 3\tau_e$ because in this case the occurrence of the first event is restricted to $(t_d-2\tau_e, \tau_e)$ as a consequence of the fact that time intervals between consecutive events larger than $\tau_e$ are ruled out. Similar formulas for multiple event loss could be derived and used, but this approach was found to be impractical because the formulas become more complex as the number of events lost increases, and because there is no limit to the number of events that could have been lost.

To solve this problem, an appropriate and effective approach is suggested here, in which the entire sequences of unrestricted events are simulated repeatedly for each dead-time interval longer than $\tau_e$, until a sequence is found that has all arrival-time differences between consecutive events less than $\tau_e$ and also features an event occurring, within the selected tolerance, at time $\tau_e$ before the end of the dead-time interval. This method was found capable of producing an event set statistically indistinguishable from the original event set and therefore, in the resulting histogram of the number of events per channel of a chosen size as a function of time, the best estimate of the variance of the number of events in each channel equals the number of events in that channel. This was verified to be true. It was also verified that the distribution of time intervals between consecutive events is exponential and corresponding to the nominal ideal rate, as expected.

However, there are several caveats associated with the way the tolerance is defined in this method. Although a tighter tolerance will lead to a more accurate result, it will also increase the computation time. Also, a tolerance imposed in a biased way produces a biased result and requires tighter restrictions (leading to more computation time) in order to yield a result with the desired accuracy. Therefore, the goal is to define tolerance in an unbiased way, in order to obtain the desired accuracy faster, *i.e.*, by imposing restrictions that are less tight. To do that properly, one must be aware of the discontinuities in the distribution functions for the dead-time interval durations and the associated numbers of events, as well as the fact that the latter are combinations of compactly supported functions

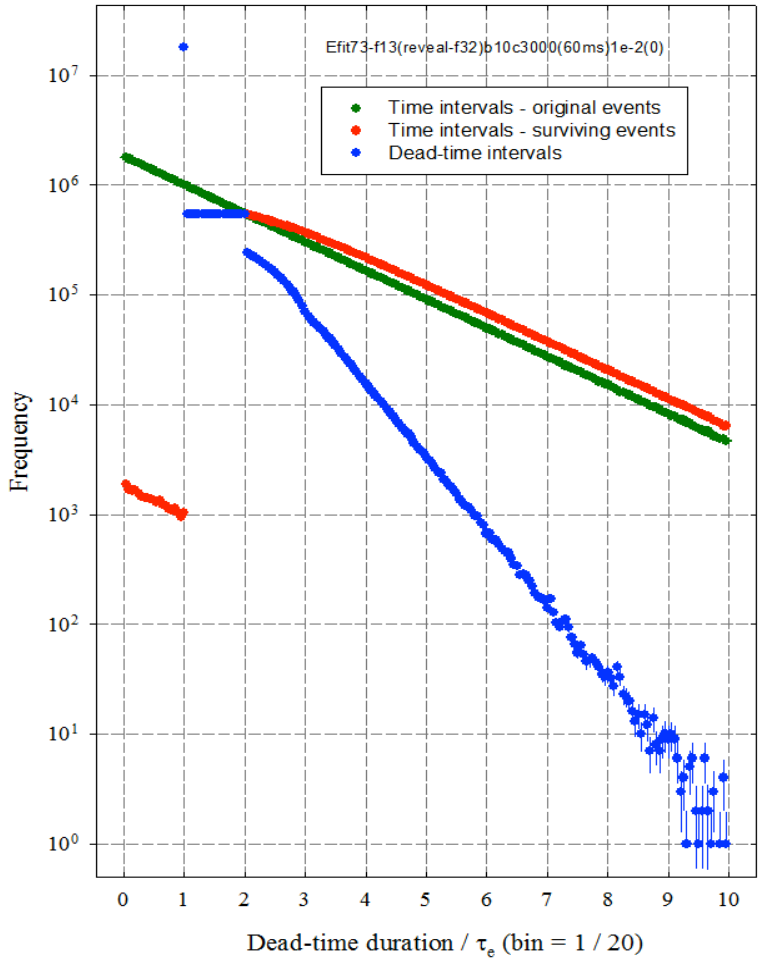

**FIG. 1.** Distribution of dead-time interval durations in units of $\tau_e$, shown with a bin size of 1/20 (blue circles), and compared with the corresponding distribution of arrival-time-differences between consecutive events that survived the imposition of extendable dead time (red circles) and those that were present before the imposition of dead time (green circles). In this example

that are non-zero only over a domain extending between two characteristic integer multiples of $\tau_e$ and that their derivatives have discontinuities at the integer multiples of $\tau_e$ within their domain. [Examples are the distributions defined by Eqs.(1-2)].

The graphs in Figs. 1-2 are given in order to illustrate these facts. Fig. 1 shows the distribution of dead-time interval durations in units of $\tau_e$, with a bin size of 1/20. It demonstrates that the distribution of dead-time intervals (shown in blue) is flat for $\tau_e < t_d \le 2\tau_e$. For $0 < t_d \le \tau_e$, the distribution is a delta function, $\delta(t_d\text{-}\tau_e)$, since, by definition, there can be no dead-time intervals shorter than $\tau_e$. For $t_d > 2\tau_e$ the distribution seems continuous, but it obviously changes its dependence on $t_d / \tau_e$ at $t_d = 3\tau_e$. The same is expected to occur at $t_d / \tau_e = 4, 5, 6, \ldots$ , but it is less obvious. The remaining two distributions shown in Fig. 1 are well known and understood [2], noting that the red circles between 0 and 1 correspond to the first events in the samples, which are not affected by the dead time, and therefore reflect the distribution shown with the green circles. Also note that the blue circles in the flat part of the distribution overshadow

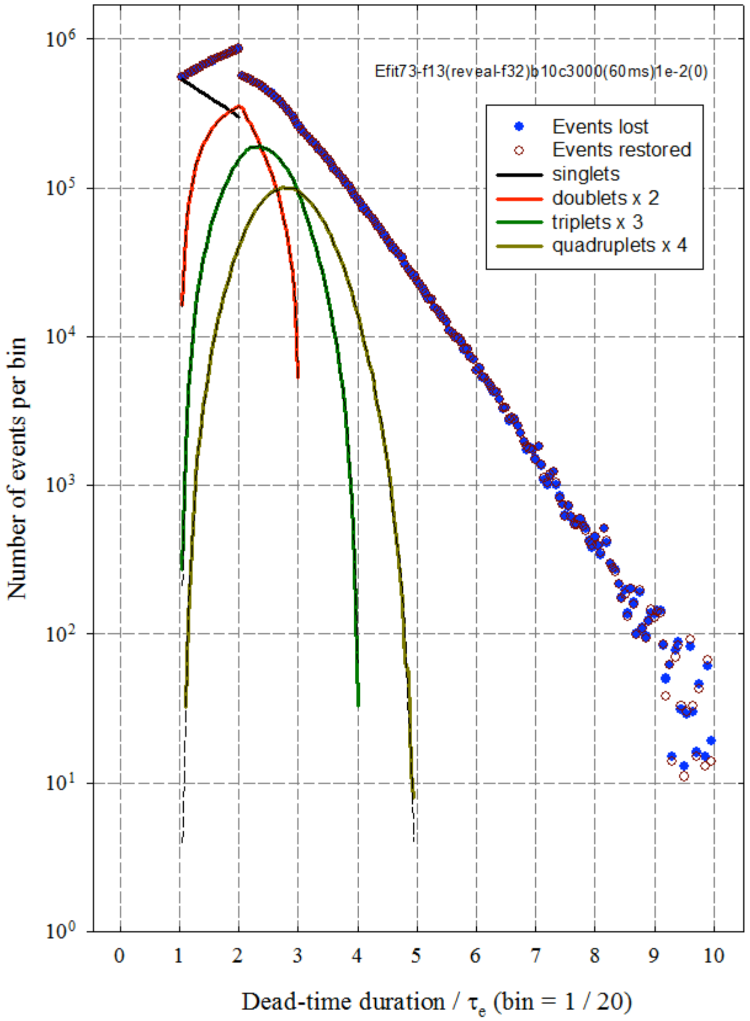

**FIG. 2.** Distribution of the number of events lost (or restored using the method proposed here) as a function of dead-time-interval duration in units of $\tau_e$, shown with a bin size of 1/20. The solid blue circles and hollow brown circles show the total number of events lost and restored, respectively, while the lines show the contributions based on the number of events lost or restored in the dead-time interval.

the red circles. The overlap is expected to be exact in the central limit, but otherwise, the events contributing to them are not necessarily the same.

Fig. 2 shows the distribution of the number of events lost as a function of dead-time-interval duration in units of $\tau_e$, with a bin size of 1/20. In addition, it shows the breakdown of contributions based on the number of events per dead-time interval for up to and including four events per interval. The sum of all these contributing distributions without their multipliers results in the distribution shown in Figure 1 with the blue solid circles, except, of course, the point at $t_d = \tau_e$, since in that case the dead time interval is present, but no events are lost. The distributions corresponding to the events restored using the method proposed here are the same as those corresponding to the lost events, although the numbers of lost and restored events in a given dead-time interval are not necessarily the same.

It should be pointed out that, while testing this method using a simulated set of events, one must make sure that the program used for the event simulation and the program used for the analysis of the secondary set of events employ different sequences of random numbers (generated using different seeds).

[1] Kevin R. Lynch, Nucl. Phys. B - Proceedings Supplements, **189**, 15 (2009).
[2] J.W. Mueller, Nucl. Instrum. Methods Phys. Res. **A301**, 543 (1991).

# Auxiliary detectors for TexAT detector

S. Bedoor, G. Chubarian, E. Koshchiy, and G.V. Rogachev

The active target detector system TexAT (Texas Active Target) is being constructed at the Cyclotron Institute to study nuclear reactions with radioactive beams (see the 2015 Cyclotron Annual Report for general outline of the detector). One of the important applications of the TexAT detector is to study the transfer reactions, such as (*d,p*) and (d,$^3$He), in inverse kinematics using radioactive ion beams (RIBs). That requires auxiliary detector systems to be implemented for TexAT. The sketch of the complete system is shown in Fig. 1.

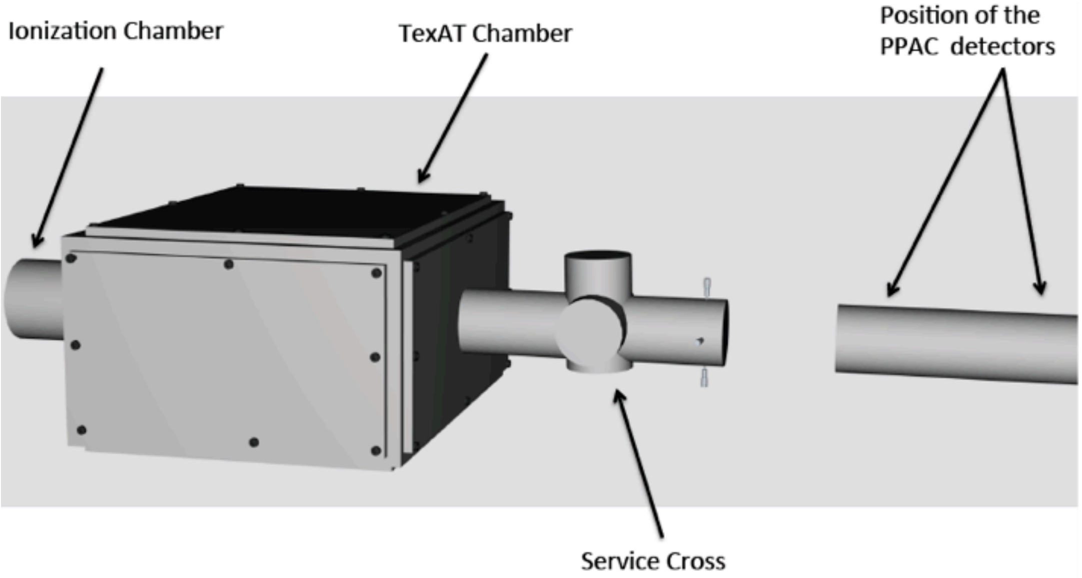

**FIG. 1**. General sketch of the custom vacuum and target gas chamber of the Texas Active Target (TexAT) Detector.

First, a beam monitor detector system should be added to the TexAT detector to facilitate rare isotope beams development and diagnostics and to provide additional beam tracking capabilities during the experiment. Two PPAC detectors [1-2] will be installed to measure the profile of the radioactive ion beam and track the incoming beam ions. Both PPAC detectors are 2D position-sensitive. The PPAC detectors will consist of two orthogonal planes of wires (X and Y directions), which serve as anodes. The active area of the PPAC detector is 1024 mm$^2$ (32x32 mm). PPAC detector board circuits are shown in Fig. 2. The wire planes (X and Y) are separated by 10 mm. They consist of 32 wires of ~0.02 mm gold-plated tungsten, equally separated by 1 mm and soldered on a printed circuit. The signal of each wire will be read separately and will be sent to the GET readout electronics system through a protection board. The whole detector is operated inside a container closed by two 1.5 μm self-supporting Mylar windows. These windows will be strongly stretched and glued on a metallic frame. The windows have to be as thin as possible to minimize the energy loss of the beam, which makes the PPAC detector quite suitable for use as a transparent detector. The PPAC is operated under a pressure between 10 and 30 Torr. Using two

PPAC detectors separated by approximately sufficient distance will provide a measurement of the particle's position.

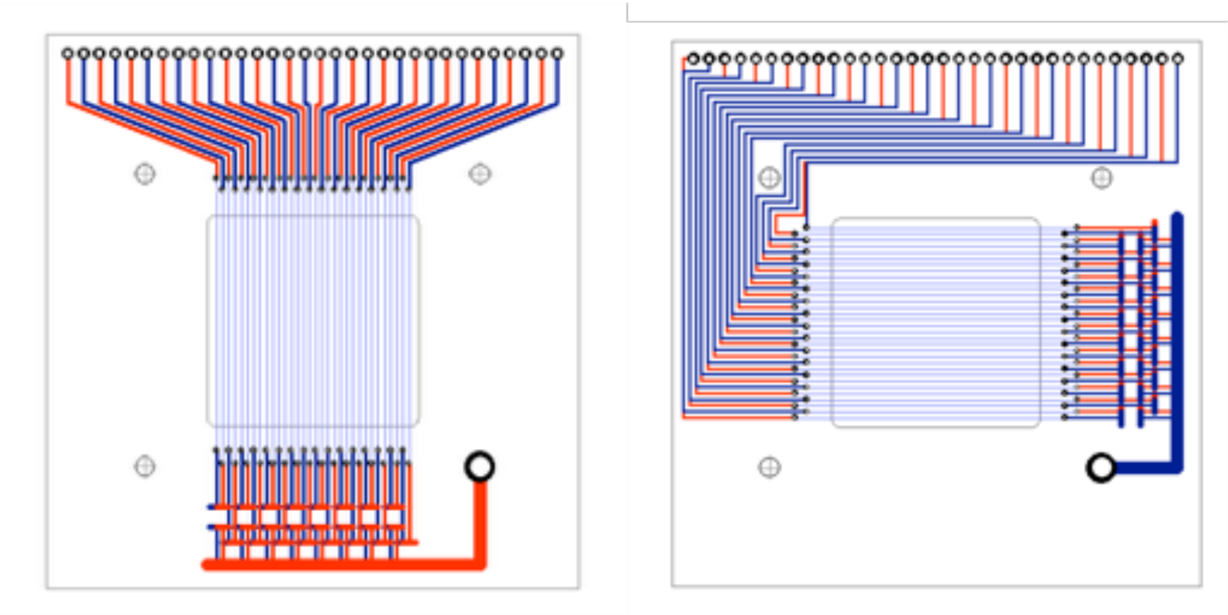

**FIG. 2.** PPAC detector board circuits. X-Grid (Left) and Y-Grid(right). A total of 32 gold plated tungsten wires are equally soldered over each frame.

A monitor detector will be needed to measure the spot size of the beam. For this purpose we will use a position-sensitive double striped silicon detector from Micron Semiconductor Ltd. It will be used offline to measure the beam spot size. The mechanical system will be designed and developed to install the monitor detector and to be pulled in and out of the beam-line without breaking vacuum.

To extend the capabilities of the TexAT detector, it is necessary to efficiently and accurately detect beam and beam-like ions downstream at forward angles in coincidence with the light particles detected in the TexAT detector. A new ionization chamber (4,5) that can detect particles at rates above 100 kcps with efficiency close to 100% and with a Z resolution of Z/Z better than 2% is under development at the Cyclotron Institute. One of the main targets to design this Ionization Chamber detector is to have the power to differentiate between the different contaminations usually excited in the radioactive ion beams from different elements having the same energy and masses. The anode and cathode electrodes will be made of copper frames. Gold-coated tungsten wires will be soldered to the frames with 2 mm spacing. The electrode grids will be supported by four steel rods that are shielded by thin electric insulation. The design of the wired grid will allow for most low energy particles to travel through without any energy loss. However, there is a small probability that incoming particles will be totally screened by the wires and be completely stopped, resulting in a loss of efficiency. For grids with 2 mm spaced wires, this loss of efficiency is less than 1% per grid. The chamber is filled with an inert gas such as Tetrafluoromethane ($CF_4$) that is ionized as the heavy recoils move through it. The entrance window will be made of a thin Mylar film (~5 um thick). The alternating arrangement of anode and cathode planes close together (~ 0.5 Inch) will achieve a short drift time for released negative and positive ions, allows fast counting rates. The signals from the first several anodes are combined together to give an energy loss (ΔE) signal for the incident particle, and the remaining anodes are used for the residual energy (E) signal. Using the Ionization Chamber detector will allow us to track the path of ions as they move through the chamber at fast counting rates.

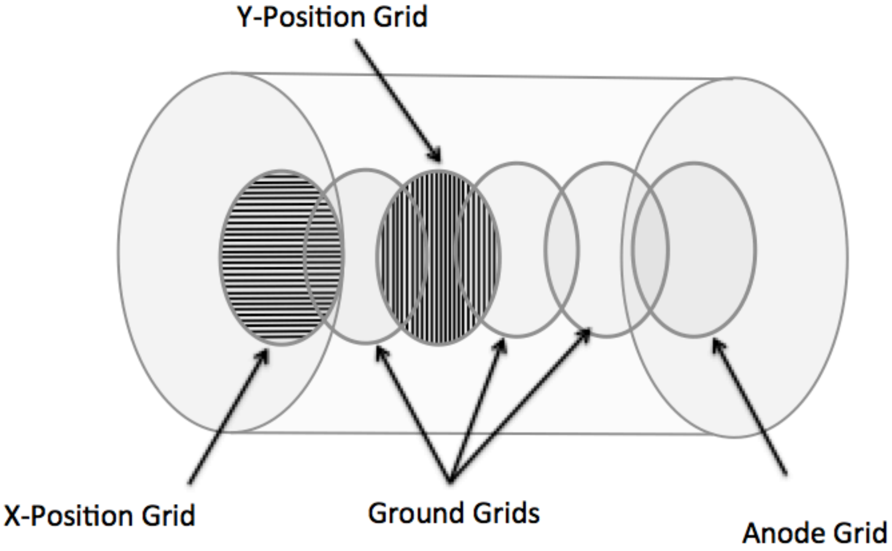

**FIG. 3.** Configuration of the position-sensitive ionization detector.

[1] R.C. Jared *et al.*, Nucl. Instrum. Methods **150**, 597 (1978).
[2] H. Kumagai *et al.*, Nucl. Instrum. Methods Phys. Res. **B317**, 717 (2013).
[3] K.Y. Chae *et al.*, Nucl. Instrum. Methods Phys. Res. **A751**, 6 (2014).
[4] J.C. Blackmon, private communication.

# CsI(Tl) array for Oxford detector at MDM spectrometer

E. Koshchiy, G.V. Rogachev, S. Bedoor, J. Hooker, H. Jayatissa, and S. Upadhyayula

A new upgrade of a focal plane Oxford [1] detector of the MDM-2 [2] spectrometer has been made. A residual energy detector, which completely stops the particles and allows to measure total energy, was modified. In existing setup this detector is a plastic scintillator, read out by two photomultipliers from the sides. The energy resolution of this detector is good enough for high energy particles, but inadequate for the low energy particles. Moreover, the 50 mm thick Kapton exit window that is installed in front of the scintillator makes low energy ions invisible in the current setup. All of the above makes it impossible to use this setup for low energy experiments that are of interest for astrophysics.

We improved the existing detector by replacing the plastic scintillator with CsI(Tl) detectors, which were initially designed for TexAT project. This is a low cost upgrade, that turned out to be very effective.

Photodiode detector V50 PM 40/ 18-E2-Cs from SCIONIX [3] is CsI(Tl) 50 x 50 x 40 mm$^3$. It is readout by Si PIN photodiode S3204-08 (Hamamatsu). The crystal is wrapped in a reflective material and covered with a aluminized mylar film for protection. The thickness of the aluminized mylar on the entrance side is 2 mm, allowing to minimize energy losses of detected products. The SCIONIX supplies detectors with the custom low noise Charge Sensitive Preamplifiers (gain is about 4 V/pC). To reduce the noise level the preamplifiers are mounted directly on the photodetector body via silicon cooky.

The detectors were tested with standard radiation sources. The typical energy resolution of 13 - 15% is achieved for 661 keV g-rays from $^{137}$Cs (Fig.1), and about 5% from mixed ($^{148}$Gd, $^{239}$Pu, $^{241}$Am, and $^{244}$Cm) α - source (Fig.2).

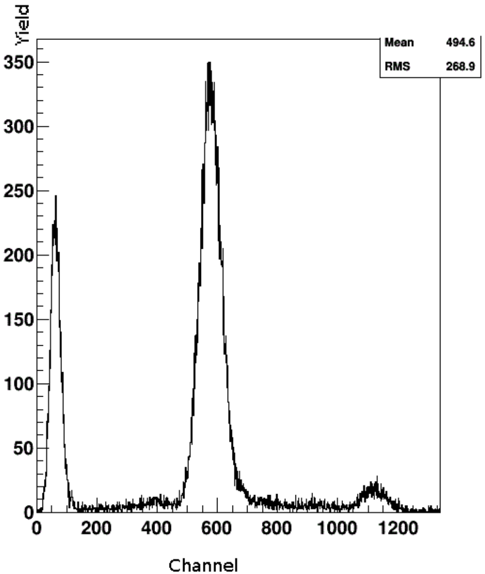

**FIG. 1.** A $\gamma$-ray energy spectrum from $^{137}$Cs ($E_\gamma$=661 keV), measured by CsI(Tl) scintillator detector.

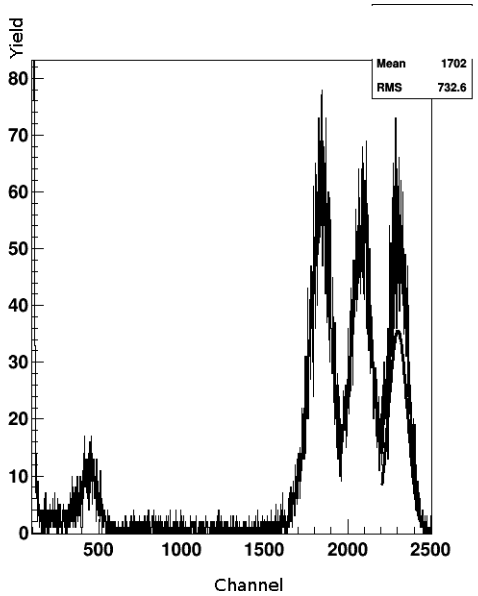

**FIG. 2.** Energy spectrum from a mixed *a*-source in CsI(Tl)- detector. $E_a$ =3.178 MeV; 5.143 MeV; 5.474 MeV; 5.788 MeV.

A set of 7 CsI(Tl) scintillation detectors has been arranged in a line and mounted onto the modified back flange of the Oxford detector at MDM, as shown at Fig.3. Signals from the preamplifiers goes to the Mesytec shaper through the vacuum feedthrough. The preamplifier power (+12V, 50 mW/ channel) was taken from NIM bin, and the PIN detector bias (30V – 70V) was supplied by MPOD system from "W-IE-NE-R, Plein & Baus, Corp." [5].

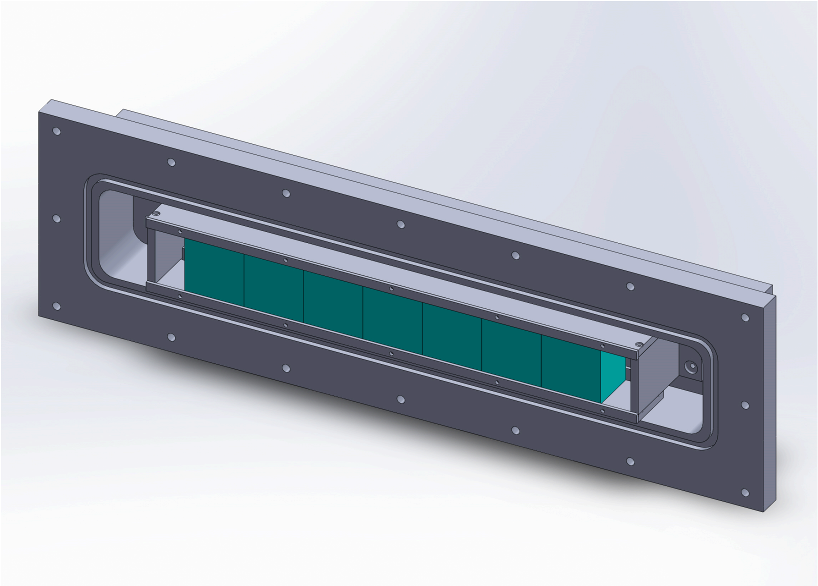

**FIG. 3.** A general view of the CsI(Tl) array, installed on the back flange of the Oxford detector.

The array was beam tested in April, 2016. A spectrum of deuterons, scattered on the Gold target at 5 degrees at the deuteron beam energy of 8 MeV, is shown in Fig.4. The energy resolution for the

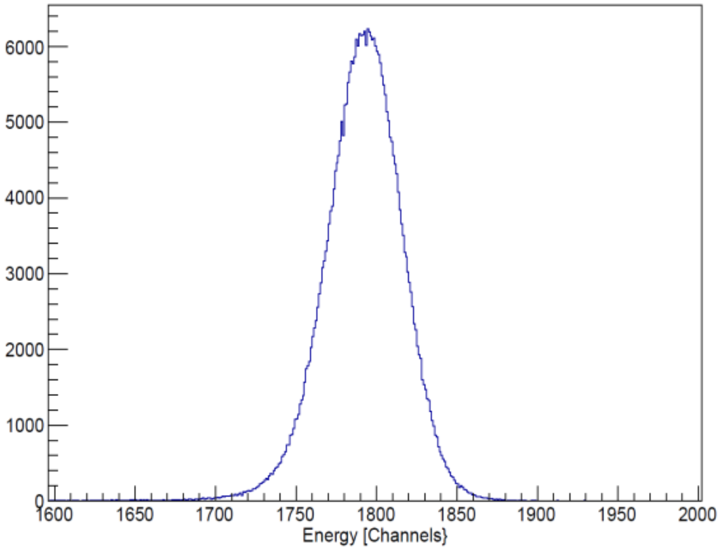

**FIG. 4.** Energy spectrum of deuterons ($E$=8 MeV), scattered from a Gold target (MDM spectrometer, $q = 5^{o}$), as measured by CsI(Tl) scintillator detectors.

deuterons, stopped in the central CsI(Tl) detector of the array proved to be surprisingly good: at the level of 3%. The CsI(Tl) array has already been used in recent low energy a-transfer experiment experiment $^{6}$Li($^{22}$Ne,d)$^{26}$Mg, performed at 1 MeV/u of $^{22}$Ne beam [4].

The latest upgrades of the Oxford detector with the CsI(Tl) array and the MicroMegas detector [6] substantially improve the performance of the detector and most importantly allow for low energy measurements to be performed.

[1] J.S. Winfield *et al.*, Nucl. Instrum. Methods Phys. Res. **A251**, 297 (1986).

[2] D.M. Pringle, W.N. Catford *et al.*, Nucl. Instrum. Methods Phys. Res. **A245**, 230 (1986).

[3] http://www.scionix.nl

[4] H. Jayatissa, G.V. Rogachev, V.Z.Goldberg *et al. Progress in Research*, Cyclotron Institute, Texas A&M University (2015-2016) p. I-49.

[5] http://www.wiener-d.com/sc/power-supplies/mpod--lvhv/mpod-crate.html

[6] A. Spiridon, R. Chyzh, M. Dag *et al. Progress in Research*, Cyclotron Institute, Texas A&M University (2014-2015), p. IV-29.

# Simulation of (d,p) reactions in inverse kinematics in Texas Active Target (TexAT) detector

C. Magana, S. Bedoor, and G.V. Rogachev

Direct nucleon transfer reactions have been used extensively in the past with stable beams to study structure of atomic nuclei. The angular distribution of the outgoing particles reflects the transferred angular momentum. In addition, since the cross-section is a measure of the overlap between the initial and final states, (d,p) transfer reactions are ideal for studies of nuclear structure and the main tool to probe single-particle structure in nuclei. These reactions are also important for the nuclear stewardship applications, where they can be used as surrogate reactions to constrain neutron capture (n,γ) reaction cross sections on neutron rich radioactive isotopes that are products of nuclear fission. The focus of this study is the implementation of the (d,p) reactions using the new active-target time projection chamber TexAT (Texas Active Target) [1] with the reaccelerated radioactive beams. The obvious advantage of the active target is that it provides a very thick target without loss of energy resolution, therefore opening up the possibility to study (d,p) reactions with the beam intensities as low as 1,000 pps.

The main goal of this study is to investigate the performance of the TexAT detector for the (d,p) reactions in inverse kinematics. We used the GEANT4 [2] based Monte Carlo simulations package developed for the TexAT detector and already tested for the elastic scattering reactions. The test reaction being studied here is $^{20}$O(d,p) populating the ground state of $^{21}$O. The beam energy was set to 8 MeV/u. The gas used inside the TPC is $D_2$ and $CO_2$ with 95/5 ratio respectively. The gas pressure was set to 350 Torr and the electric field setting in the drift region of TexAT was 150 V/cm to drift electrons towards the MicroMegas board.

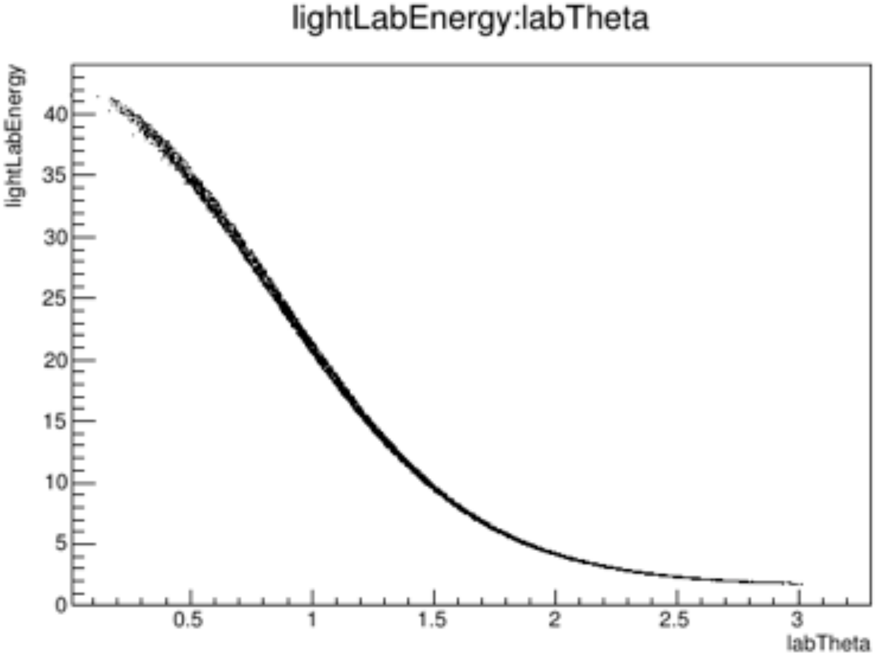

**FIG. 1.** Kinematics for the $^{20}$O(d,p) reaction. Energy of protons (in MeV) is shown as a function of scattering angle (in rad.).

The track reconstruction algorithms for TexAT are generally based on time matching of the hits in the MicroMegas board. The MicroMegas board, located in the tracking volume, has three separate regions. The left and right regions consist of strips and chains, times for which are matched to determine the x-y coordinates of the discrete track point. The central region, located below the beam, determines the coordinates of the track by recording the electron count for each rectangular pad of a certain width. Fig. 1 shows the kinematics of the test transfer reaction. Fig. 2 shows the tracks generated for a (d,p) transfer reaction event. Fig. 3 demonstrates a reconstructed (d,p) event in TexAT detector.

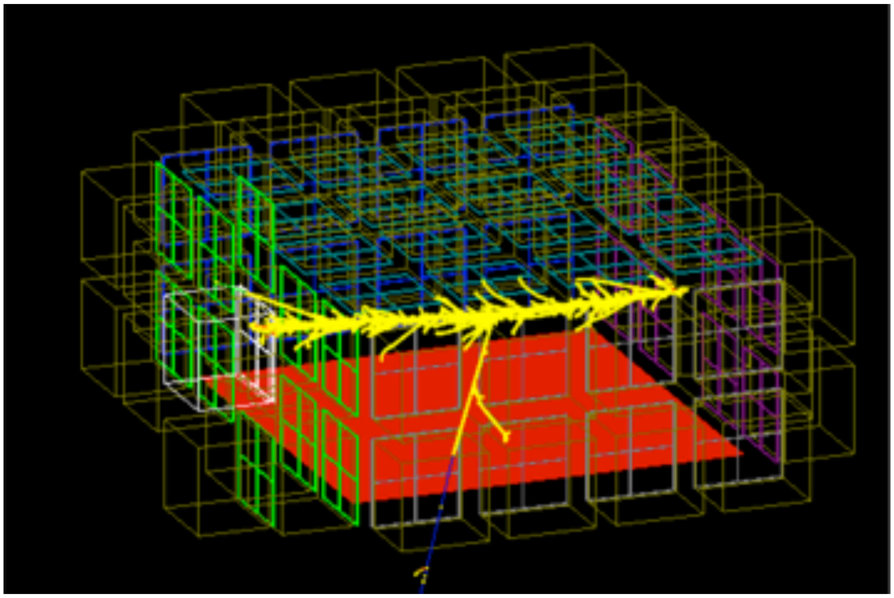

**FIG. 2. GEANT4 s**imulation of the 20O(d,p) reaction in the TexAT detector. The beam comes in from the right. The proton hits the CsI-backed silicon detector on the left (with respect to the beam) plate. The heavy recoil continues through the front plate. The white colored detectors indicate that they have been removed.

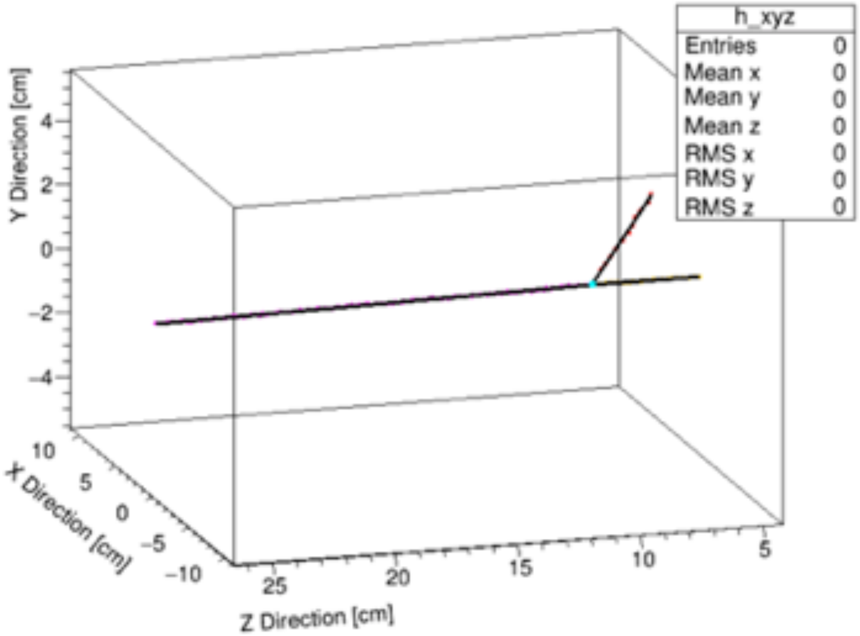

**FIG. 3.** Reconstructed (d,p) reaction event.

Testing of the track reconstruction is underway. Fig. 4 shows a comparison of the generated light product angle (blue) and the reconstruction of that angle (red). If the reconstruction fails, the value is set to zero. The dip in the middle of the red plot corresponds to a lab angle of 90 degrees. Reconstruction at this angle fails due to improper matching of times between the strips and chains in the MicroMegas detector. Algorithm that allows to mitigate that problem is being developed. The energy and angular resolution will be determined after this problem is resolved.

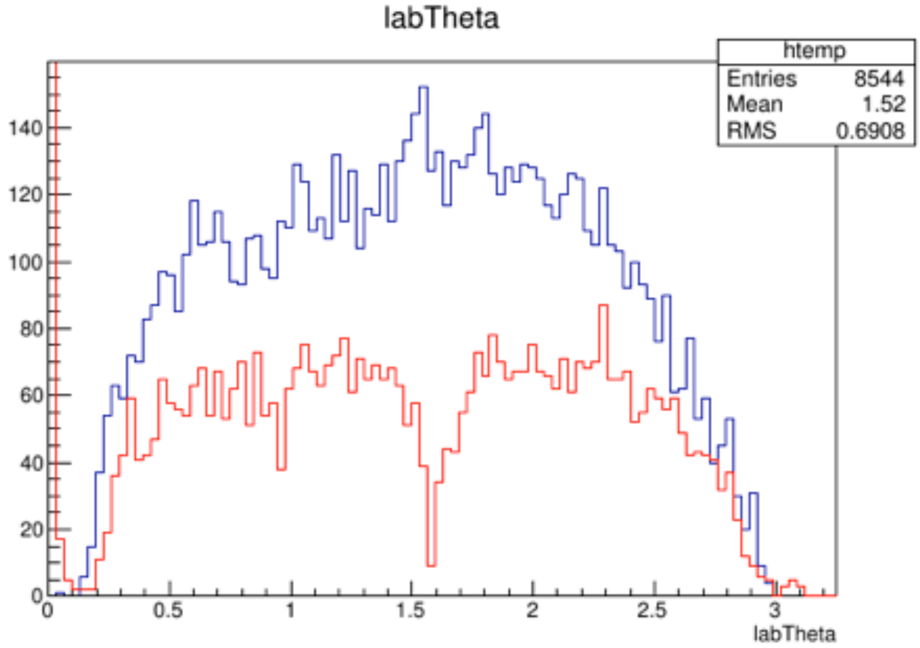

**FIG. 4.** Plot of the simulated light product lab angle (blue) versus the reconstructed light product lab angle (red).

In summary, Monte Carlo simulations of the TexAT detector are currently being developed to incorporate (d,p) reactions. The track reconstruction for the (d,p) events work well for most angles, except for angular region around $90^{o}$ in the Lab. frame.

[1] E. Koshchiy *et al.*, *Progress in Research*, Cyclotron Institute, Texas A&M University (2014-2015), p. IV-42; E. Uberseder *et al.*, *Progress in Research*, Cyclotron Institute, Texas A&M University (2014-2015), p. IV-47; E. Uberseder *et al.*, *Progress in Research*, Cyclotron Institute, Texas A&M University (2014-2015), p. IV-51.

[2] S. Agostinelli *et al.*, Nucl. Instrum. Methods Phys. Res. **A506**, 250 (2003).

# ZAP board development for TexAT

E. Uberseder, E. Koshchiy, G.V. Rogachev, and E. Pollacco[1]
[1] *IRFU, CEA Saclay,Gif-Sur-Ivette, France*

The Texas Active Target (TexAT) detector for nuclear reaction studies with rare isotope beams at low energies is currently under development at the Cyclotron Institute [1]. It combines a highly segmented Time Projection Chamber (TPC) surrounded by two layer of solid state detectors – Si semiconductor and CsI(Tl) scintillation detectors, a total of about 1300 channels. Readout electronics for all these detectors is based on GET ASICs chips of 64 channels each, loaded into single AsAd card. To attach detectors to the AsAd cards, a special "ZAP"/Adapter boards have been designed. ZAP- board allows to read-out signals from detectors, to bias them (individual or group), and to protect AsAd cards from the electrical breakdown.

The board-to-board concept was used to reduce noise and to avoid eventual connection problems with high density cables between electronic components. The same basic schematic diagram [2] is utilized for all detectors of TexAT, but specific components are different for different detectors. The electronic schematic of ZAP- board for Si- detectors is shown in Fig.1. Every Si detector (16 per AGET chip) is biased from MPOD Power supply unit separately (group of 4 quadrance) through the serial circuit of 1M - 10M resistors. Signals from detectors go through SAMTEC connector to the internal AGET preamplfier. The protection circuitry, based on diode bridge is also implemented on ZAP board.

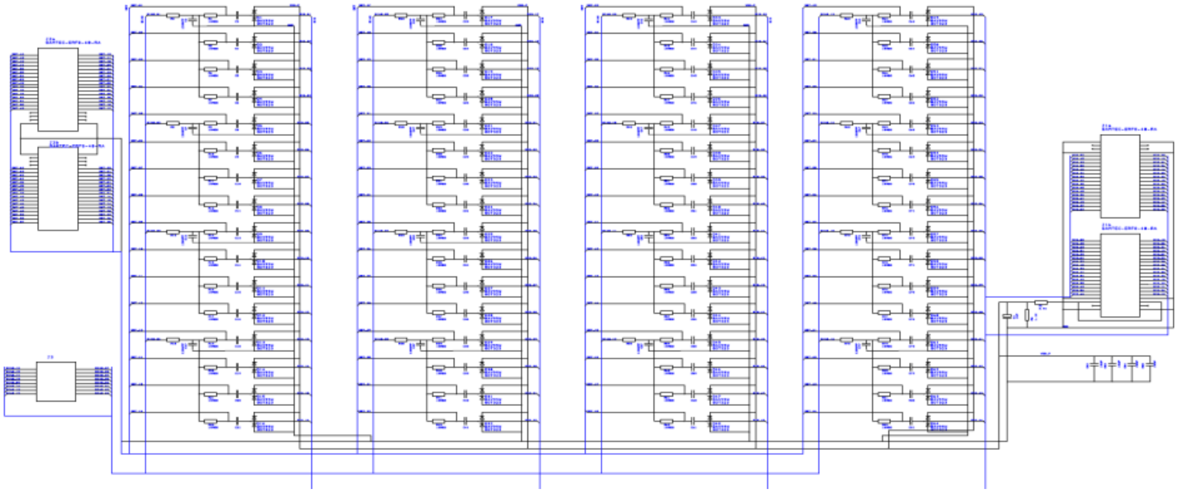

**FIG. 1.** Schematic diagram of Si-detectors ZAP-board for TexAT.

The PCB design was made using electronics rapid prototyping software Design Spark PCB 7.1 [3]. The board has 4 layers and all elements are surface mounted. Two factors were taken into account in the design: a) it was decided to place all electronic components outside of TexAT scattering chamber to simplify the replacement in case of electronic failures; b) Instead of making one common ZAP- board for AsAd-card (256 channels/64 detectors), we use separate ZAP- board for each of four AGET- chips (64 channels/16 detectors). The form-factor of AsAd card limits the maximal width of ZAP board to the 1.8in, which is practically the width of SAMTEC ERF-8-40 connectors. It appears to be difficult to place all electronic components at the board so an additional "Offset" board (9.2in x 1.6in) was designed to match ZAP board to AsAd. It expands spacing for single ZAP- board to the acceptable level. The final dimensions of Si ZAP- board is 2.2in x 4.0in.

An additional Si- "Transition" (2.2 in x 8.0 in) board was also designed to provide all signals inside the scattering chamber. The board does not have any electronic components, only the connectors. "Transition"- board is epoxi-sealed to the custom vacuum flange, making a signal feed-through to the TexAT scattering chamber. The general view of Si- boards assembly is shown at Fig.2. Each board serves one AGET2 chip (64 channels).

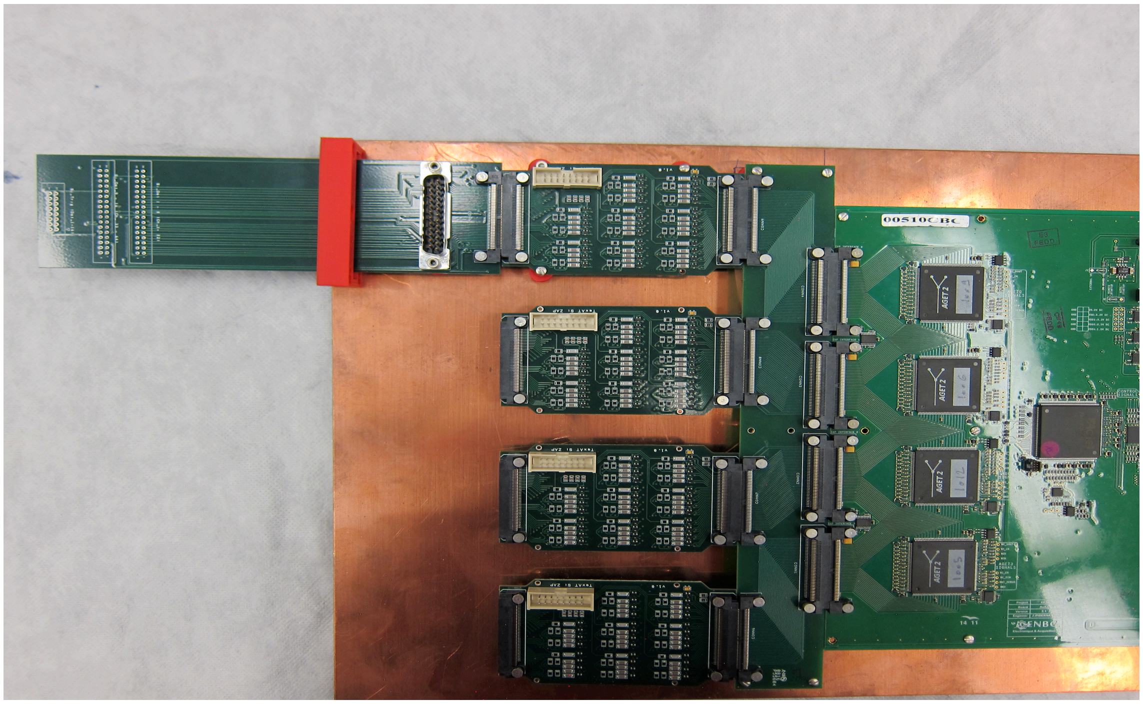

**FIG. 2**. Image of the Board-to-Board Front End connections of Si-detectors for TexAT. From right to left: AsAd card; "Offset"- board; "ZAP"- board; "Transition"- board**.**

All PC boards were fabricated and assembled by Advanced Circuit Co. They were tested and now they are ready for use now. The final design of Micromegas ZAP-board will be made after getting of Micromegas PCB board (expected at the end of June, 2016). The design of ZAP- board for scintillator detectors is now under development.

[1] E. Koshchiy *et al.*, *Progress in Research*, Cyclotron Institute, Texas A&M University (2014-2015), p. IV-42; E. Uberseder et al., *Progress in Research*, Cyclotron Institute, Texas A&M University (2014-2015), p. IV-47; E. Uberseder et al., *Progress in Research*, Cyclotron Institute, Texas A&M University (2014-2015), p. IV-51.

[2] E.Pollacco *et al*. Phys. Procedia **37**, 1799 (2012).

[3] http://www.designspark.com/pcb

# Calibrations of LCP data from recent FAUST campaign - 2015 annual report

L. Heilborn, K. Hagel, M. Huang, A. Jedele, L.W. May, E. McCleskey, A.B. McIntosh, M. Youngs, A. Zarrella, and S.J. Yennello

Data has been recorded for Light Charged Particles (LCP) from reactions of 40A MeV $^{40}$Ar+$^{58}$Fe,$^{70}$Zn, and $^{40}$Ca+$^{58}$Ni at the Texas A&M Cyclotron Institute, with the upgraded Forward Array Using Silicon Technology (FAUST) detectors and electronics.

FAUST is comprised of sixty-eight ΔE-E telescopes arranged to provide coverage of particles emitted from quasiprojectiles (QP, the excited source resulting from heavy ion reactions) [1]. Each telescope consists of a 2x2 cm 300 μm thick position-sensitive Dual-Axis Dual-Lateral (DADL) silicon diode backed by a CsI(Tl)-photodiode detector [2]. The status of current calibrations of data from the successful campaign with this position-sensitive upgrade is described here. These calibrations include energy calibrations for the Si and CsI. These CsI calibrations are themselves dependent upon successful particle identification (PID) calibration.

In energy calibrations of the silicon detectors in FAUST with a $^{228}$Th source, the five dominant alpha energies of $^{228}$Th and its daughters result in the raw summed Front spectrum shown in Fig. 1a. The width of these Gaussian peaks at each energy is increased by some position-dependence with location of the α, due to incomplete charge collection. In order to investigate the position dependence, the sum vs. the difference of the two either front or back signals is a raw way of plotting the energy of the alpha particle against the one-dimensional (1D) position of the hit on the detector. These plots should be linear and horizontal, as the energies deposited by the single energy alpha particles should not be dependent upon the position of the incident radiation. The resultant two-dimensional (2D) histogram from the Front signals is shown in Fig. 1b. This histogram is clearly curved, rather than flat as would be expected from a purely uniform detector, indicating that the response of the DADL detectors is not completely linear as a function of position on the detector face.

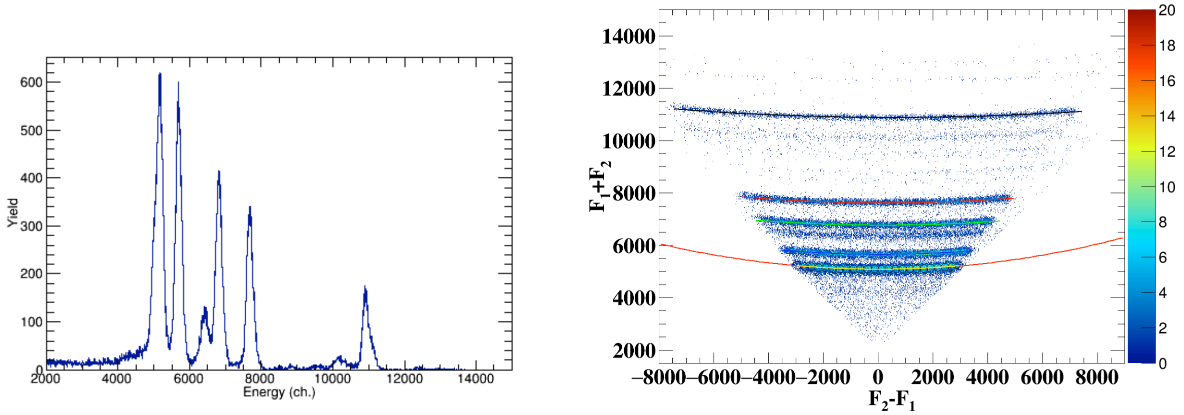

**FIG. 1.** (a) Energy spectrum of the alpha particles emitted by the $^{228}$Th on detector 11. The raw Full-Width at Half Maximum (FWHM) is 300 keV for the highest energy α. (b) Sum vs. difference for $^{228}$Th source on detector 11. These lines are somewhat parabolic in shape, and asymmetric about zero. Each line is fit quadratically.

A position-dependent correction improves the resolution of the raw energies before they can be fully calibrated. The correction necessary can be ascertained by a quadratic fit of the signals from alpha particles of different energies. Each of the lines corresponding to an energy of alpha particles from the $^{228}$Th source were fit quadratically. So “a” represents the curvature of the line, “b” corresponds to the linear component, and “c” tells the y-intercept. Where x=0, the alpha particle hit the middle of the detector, and the measured values at x=0 are used as a reference to which the values at other locations are mapped. The results of this fit are also depicted in Fig. 1b.

Our aim here is to remove any position dependence of the energy. The curvature and linearity of the fits vary with the energy of the α particles. In this case, the “c” parameter of the fit is where the single-energy alpha line crosses the center of the detector, so it is some measure of the energy of the alpha particle. The non-linear components of this fit can be subtracted from the overall energy, to give a corrected spectrum and improve the energy resolution.

Because curvature and linearity are dependent upon the sum, or the c value, a and b can be replaced with linear functions that describe this relationship. Once these substitutions are made, the resultant equation for the corrected energy of any two Front or Back signals looks like this:

$$\mathrm{Sum}_{\mathrm{corr}} = \mathrm{sum} - a(\mathrm{sum})\mathrm{diff}^2 - b(\mathrm{sum})\mathrm{diff}.$$

The 2D histogram with the straightened, horizontal lines after the correction is made is shown in Figure 2b. Once the position-dependence is accounted for, the peaks from the different energy alpha particles have much better resolution. The resulting position-corrected spectrum is shown in Figure 2a. Even a merely cursory comparison between Figures 1a and 2a, the spectrum before and after, shows that the resolution of the detector is much improved by these fits and the resultant correction. This process has been implemented on all detectors for a single source run. The measured known peaks of the alphas in the thorium source spectrum have been used to convert the position-corrected raw values into MeV.

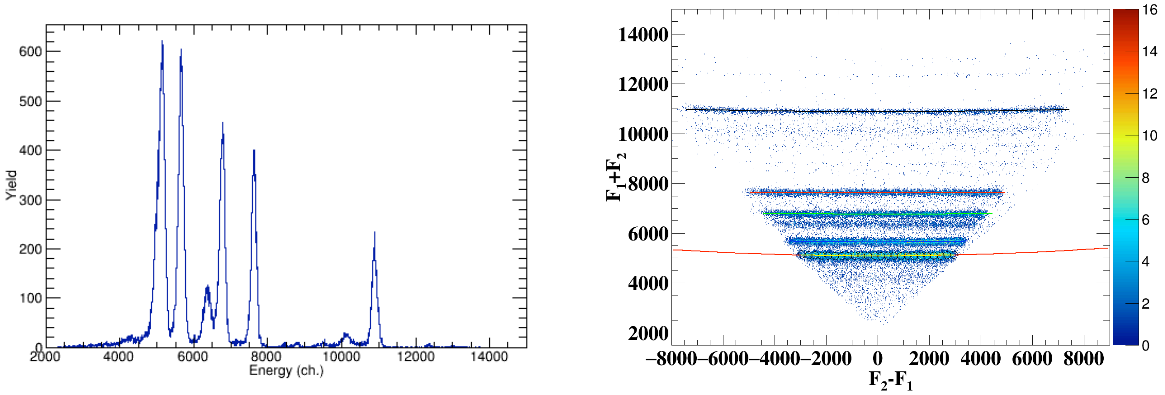

**FIG. 2.** (a) Corrected energy spectrum of the alpha particles emitted by the $^{228}$Th source on detector 11. The FWHM is now 180 keV for the highest energy α, a significant improvement. (b) The sum vs. difference plot fit again after correction for position-dependence of energy. The highest energy alpha fit is black, followed, in order of decreasing energy, by red, green, blue, and yellow lines of fit.

The CsI energy calibration is dependent upon the PID. The ΔE-E plot, derived from Si and CsI(Tl) signals, demonstrating the excellent p-d-t differentiation for raw signals, is shown in Fig. 3a.

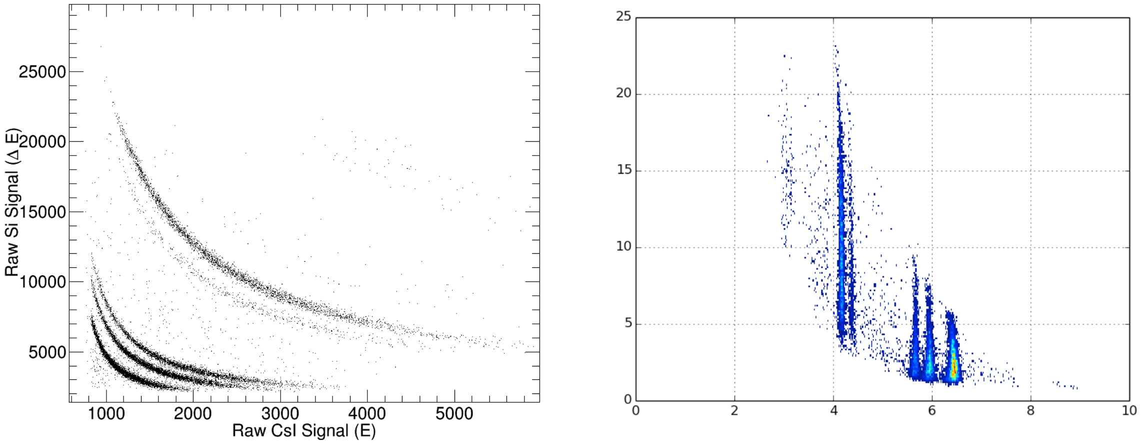

**FIG. 3.** (a) Representative ΔE-E plot, detector 60 for the reaction of 40A MeV $^{40}$Ar + $^{58}$Fe. (b) Back ΔE vs. PID value, demonstrating the linearization achievable via PID equation in text.

The PID values can be extracted using the following equation:

$$PID = b * \ln(p_0) - \ln(b * \Delta E) - (b-1)\ln(E+p_1+\Delta E)$$

where b is defined as:

$$b = p_2 - (p_3\Delta E/p_4)$$

and slopes and intercepts for the energy calibration of Si (ΔE) and CsI (E) are allowed to be free parameters. All the parameters ($p_0$, $p_1$, $p_2$, $p_3$, $p_4$, b and the slopes and intercepts of the Si and CsI calibrations) are varied by hand while viewing PID vs Si or PID vs CsI as shown in Fig. 3b. The parameters result in the distribution of the PID vs Si or PID vs CsI being vertical bands when the free parameters are finalized. These free parameters are each unique to a detector, but are not observed to vary within a single system.

The subsequent linearity, demonstrated in Fig. 3b, is then good for determining the identity of particles before calibrating the CsI energy. Based on previous successful test runs and preliminary analysis, excellent PID and energy resolution are expected to be achieved in the final calibration.

Energy and position calibrations of this data set are ongoing, from which proton-proton correlation functions will be extracted. The data will then be compared to simulation results for the purpose of investigating the impact of the asymmetry energy term of the equation of state on the shape and magnitude of the correlation function, which is predicted to be significant [3].

[1] F. Gimeno-Nogues, *et al.* Nucl. Instrum. Methods Phys. Res. **A399**, 94 (1997).

[2] S.N. Soisson, *et al.*, Nucl. Instrum. Methods Phys. Res. **A613**, 240 (2010).

[3] L.W. Chen, V. Greco, C.M. Ko, and B.A. Li, Phys. Rev. Lett. **90**, 162701 (2003).

# New prospects for automated particle identification

A.B. McIntosh, S. Wuenschel, K. Hagel, S.J. Yennello, S. He,[1] and J. Huang[1]
[1]*Department of Statistics, Texas A&M University, College Station, Texas*

A new method for analysis of raw experimental data to obtain PID (particle identification) in an automated way is being explored. This report contains a brief description of the goals of PID and the drawbacks of current methods. This report focuses on the description of the new method in development, and the successes and current status of the new method. A much more detailed description will be submitted to a statistics journal in the coming months.

Particle identification in nuclear physics experiments has become incredibly sophisticated over the last few decades. Detector arrays have become larger and have achieved new records in particle isotopic resolution. This allows new physical phenomena to be explored, but comes at a price: the particle identification is incredibly labor intensive. For example, in the NIMROD array, nearly 200 detector telescopes employ the ΔE-E technique for charged particle identification for Z>2 and pulse shape discrimination for lighter ions. Each 2D spectrum contains a series of visually discernible bands (see Fig. 1), which correspond to unique particle types. The goal of the PID process is to develop an algorithm that

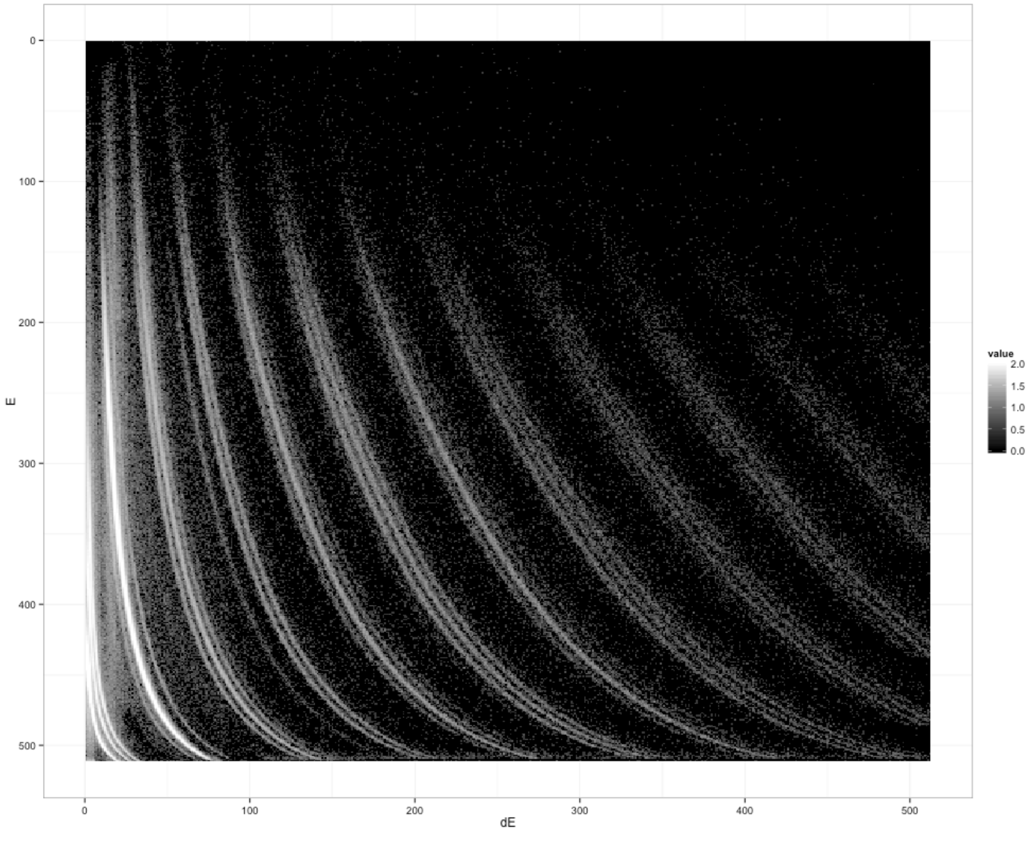

**FIG. 1.** Raw E vs ΔE histogram for a detector of the NIMROD array showing isotopic resolution. The reaction producing the charged particles is Kr+Ni@35AMeV.

can sift through the hundreds of millions of events and automatically determine what type of particle each datum corresponds to. To date, this process relies on humans to generate a large series of curves along the bands of data by manually defining points through which they desire the curve to pass. This labor-intensive step is measurable in man-years. The goal of the present investigations is automation through statistical methods.

The new method shows much promise already at automatically finding curves to describe the ridges in the data. The first step in the process is to bin the data appropriately and apply a smoothing function to minimize the effects of statistical fluctuations. Fig. 2 shows a smoothed version of the data in Fig. 1. The isotopic resolution is still clearly discernible. The smoothing uses a wavelet method. Briefly, this takes the two-dimensional surface and applies a local transformation akin to a Fourier transform to filter out undesirable frequency components.

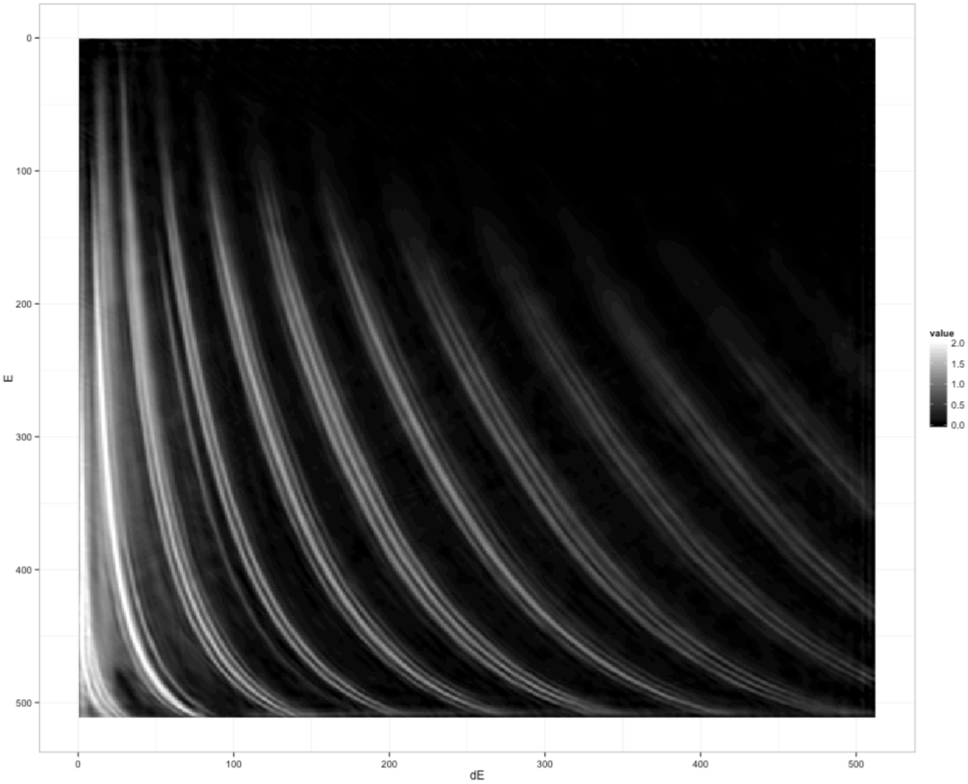

**FIG. 2.** A smoothed version of the data in figure 1. See text for explanation.

The new method then examines slices of this smoothed two-dimensional surface to find local maxima. The results of this are shown in Fig. 3. The gray data points show the same raw data represented in Figs 1 and 2. The red points are the automatically obtained local maxima. The local maxima describe an impressive range of isotopic loci from Z=1 to Z=11. A nearest neighbor algorithm is then able to group these maxima together to allow each series of point to be fit with a spline that follows the ridge in the original data.

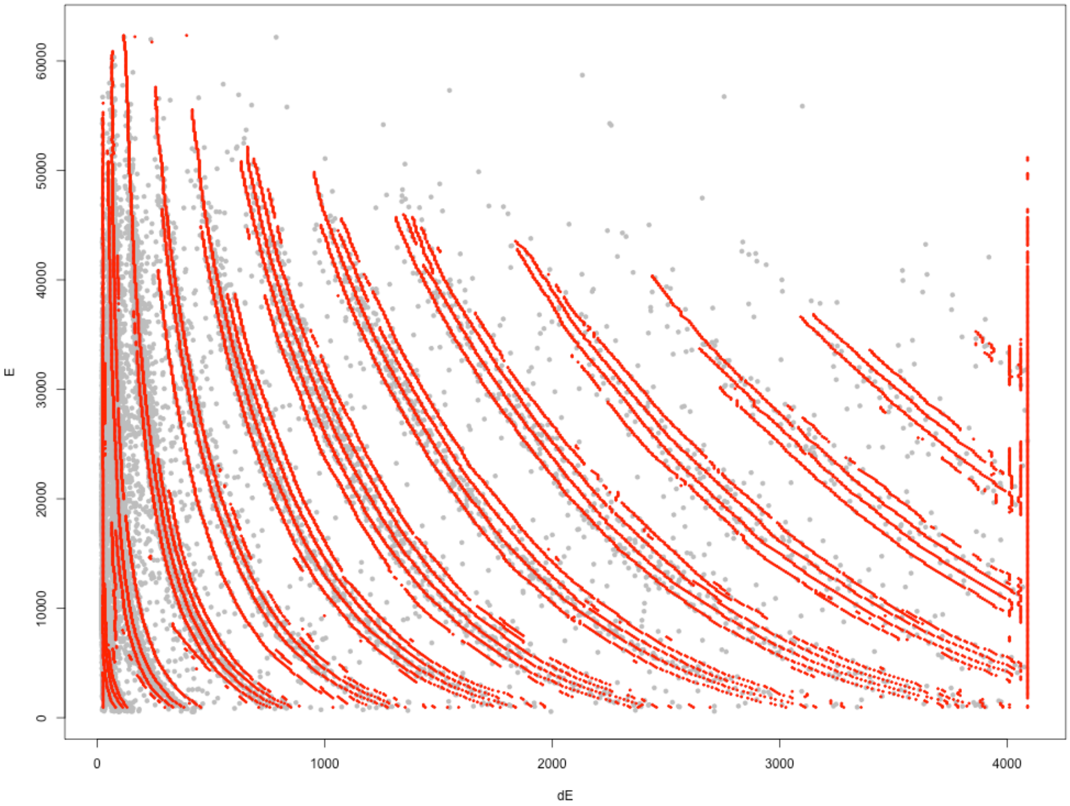

**FIG. 3.** Same raw data (gray) as for Figs 1 and 2. The red points are obtained automatically by finding the local maxima in Fig. 2.

The algorithm is being testing on a broader range of detectors to test is robustness. The ease with which these local maxima are obtained already suggests that this algorithm and derivatives of it may find widespread use in particle identification and similar problems in nuclear science.

This work is part of a broad initiative to advance scientific output in “Big Data” experiments through collaboration between scientists and statisticians. This work is supported by the Department of Energy (DE-FG02-93ER40773, Cyclotron Inst.), the Welch Foundation (A-1266, Chemistry Dept.), and the National Science Foundation (DMS-1208952, Statistics Dept.).

# The ParTI array for studying pionic fusion

A. Zarrella, A. Bonasera, L. Heilborn, A. Jedele, A.B. McIntosh, and S.J. Yennello

Pionic fusion is the process by which two nuclei fuse during a collision and then deexcite by the exclusive emission of a pion. The resulting compound nucleus is left in or near its ground state [1]. The process requires that nearly all of the available kinetic and potential energy in the colliding system be concentrated into two degrees of freedom - the rest mass and kinetic energy of the emitted pion. Thus, the energy of the emitted pion is limited by the number of available final states of the fusion residue [2]. The combination of limited available energy and the extreme coherence required in the process ensures that the pionic fusion channel is greatly suppressed. Indeed, the measured pionic fusion cross sections range from hundreds of nanobarns for the lightest systems (He + He) to hundreds of picobarns as one moves to larger systems ($A_{tot}$ = 6 - 24) [2-12].

During this past year we have continued making progress towards measuring pionic fusion cross sections using the Momentum Achromat Recoil Spectrometer (MARS) [13] and the newly constructed Partial Truncated Icosahedron (ParTI) phoswich array. In July of 2015, we ran an experiment in which we calibrated a representative phoswich detector using secondary beams at the back of MARS and developed a method for calibrating the ParTI array based on the results of this representative unit. In December of 2015, we performed the first test of a significantly populated (12 of the 15 total phoswich units) ParTI array in beam in order to develop a procedure for aligning the array and to see particle identification lines in all detectors. The most recent test run took place in February of 2016 and sought to test various aspects of the Pionic Fusion experiment and to attempt to identify pions using 4 ParTI phoswich detectors.

During the phoswich calibration test experiment in July of 2015, we were able to measure the phoswich detector response for Z = 1, 2, and 3 charged particles at known energies using secondary beams created by the reaction of $^{14}$N + $^{9}$Be at 40 MeV/u and the MARS. This information was used to correct the resulting ΔE-E particle identification plots and produce energy-calibrated data. Fig. 1a shows some raw ΔE-E data from that run which shows particle identification lines for charged particles through 6Li. The y-axis is the integration of the phoswich response inside of a “fast” gate encompassing the first approximately 50 ns of the signal. The x-axis is the integration of the phoswich response inside of a “slow” gate encompassing approximately 400 ns of the phoswich response separated from the end of the fast gate by 200 ns. Fig. 1b shows the corrected, energy-calibrated data from Fig. 1a. Now, the y-axis corresponds to the energy deposited in the fast plastic component of the phoswich and the x-axis corresponds to the energy deposited in the CsI component of the phoswich. Using Fig. 1b we have developed a method for energy calibrating the ParTI array using a similar technique as that reported in [14].

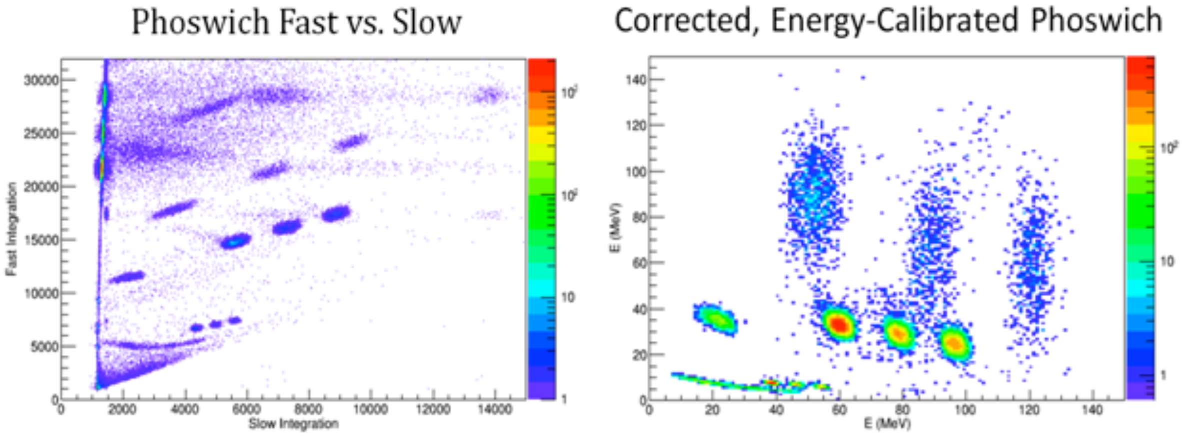
Phoswich Fast vs. Slow

Corrected, Energy-Calibrated Phoswich

**FIG. 1**. a) Fast Integration vs. Slow Integration results for a representative phoswich using secondary beams produced by MARS. Moving from bottom to top, we can identify the particle lines: the positively sloped line at the bottom is the neutron/gamma line, above that is the proton line (4 poorly resolved proton energies) followed by 3 energies of deuterium, 1 energy of $^{3}$He, 3 energies of alpha, 3 energies of $^{6}$Li and, finally, a single energy of 10B. b) A ΔE-E plot representing data for Z = 1, 2, and 3 from a) after being corrected and energy calibrated.

In the test run performed in December of 2015, we confirmed that we were able to install and successfully align the populated ParTI array inside the MARS production chamber. A beam of 16O at 60 MeV/u was collided with a gold target and fragments were measured in the backward direction. Two representative fast vs. slow plots are shown in Fig. 2. As in Fig. 1a, the y-axis is the integration of the phoswich signal inside the fast gate and the x-axis is the integration of the signal inside the slow gate. The obtained particle identification was quite poor in this test experiment. The cause of this poor resolution was determined to be because of the construction of the PMT bias cables powering the detector array. The old ribbon cable design has since been replaced with an all coaxial cable design. This test run also alerted us to the need for further shielding of the ParTI array from beam halo and unwanted contamination accompanying the beam down the line and entering the phoswiches from the back. In response to this, we have added a tungsten alloy radiation shield behind the detector array.

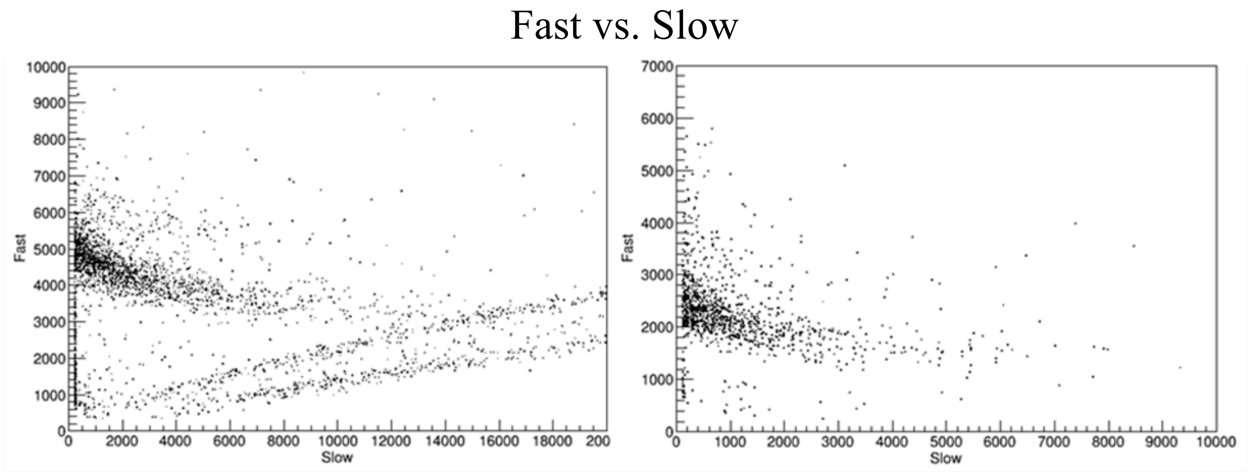
Fast vs. Slow

**FIG. 2.** Two fast vs. slow particle identification plots from two representative detectors from the test experiment in December of 2015. In both cases, we can see a prominent band representing Z = 1 particles with some counts above in each case which could potentially be the beginnings of a Z = 2 band. However, we have clearly lost resolution compared to Figure 1 as isotopic lines are not distinguishable in either case.

During the beam experiment in February of 2016 we used a beam of alpha particles at 55 MeV/u to diagnose quite a few aspects of our experimental plan. Firstly, an aluminum beam degrader was inserted into the line inside the K500 vault which slowed the beam down to approximately 46.5 MeV/u. This degraded beam was then able to be focused onto our target position with an intensity loss of approximately a factor of 10, an acceptable loss for performing the pionic fusion background measurement. Next, we were able to show that a newly inserted Faraday cup located inside the MARS D1 magnet was capable of registering a beam current for both the 55 MeV/u and degraded alpha beams. This cup will provide a continuous proportional measure of beam intensity during the pionic fusion production run. Lastly, 4 phoswich detectors were arranged inside the production chamber. In order to test the resolution of the phoswiches using the new coaxial cables and to measure traditionally produced pions, a gold target was inserted into the 55 MeV/u alpha beam and reaction products were measured. Figure 3 shows data from one of the detectors in this experiment. The fast vs. slow plot is similar to those in Figures 1a and 2. It is clear that we are getting much better energy resolution and, consequently, much clearer particle identification lines for Z = 1 particles. While this data has helped develop algorithms for identifying pions using their characteristic decay response inside the detectors, we were unable to definitively identify any pions in our data.

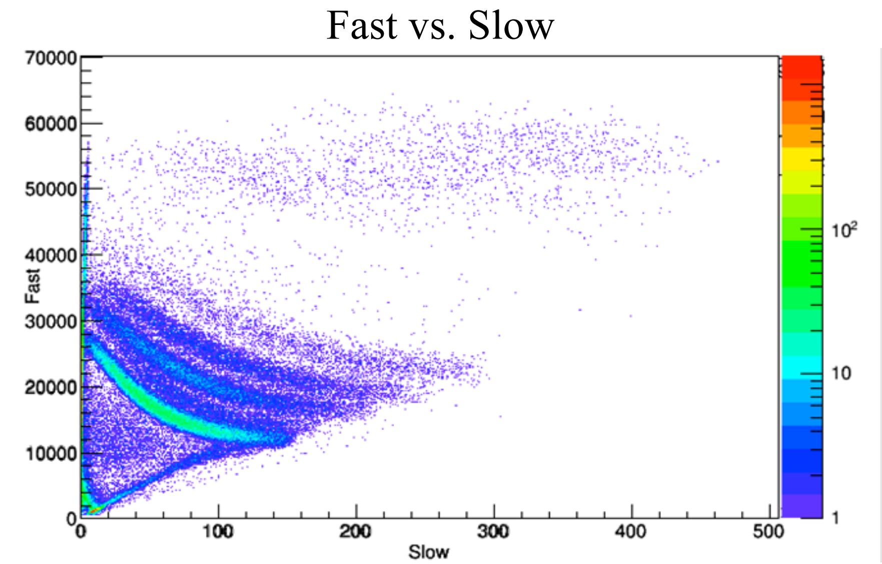

**FIG. 3**. A fast vs. slow particle identification plot produced by one of the detectors during the February 2016 test experiment. It is clear to see the better resolution as compared to the plots from figure 2. Here we see well separated particle identification for (moving up the plot) the neutron/gamma line, protons, deuterons, tritons and, at the very top, a band of Z = 2 particles. There is a somewhat weaker line located above the triton line and arriving at the y-axis at approximately 42,000, which corresponds to proton double hits.

In the summer of 2016, we plan to remeasure the transmission efficiency for our residues of interest through MARS and to run a second phoswich calibration experiment similar to the one from July of 2015. This second calibration experiment will reflect new electronics and measurement techniques that we have implemented over the last year. A pionic fusion production run is scheduled for next year.

[1] P. Braun-Munzinger and J. Stachel. Ann. Rev. Nucl. Part. Sci. **37**, 97 (1987).

[2] D. Horn, *et al*. Phys. Rev. Lett. **77**, 2408 (1996).
[3] Y. Le Bornec, *et al*. Phys. Rev. Lett. **47**, 1870 (1981).
[4] L. Joulaeizadeh, *et al.* Phys. Lett. B **694**, 310. (2011).
[5] W. Schott, *et al*. Phys. Rev. C **34**, 1406 (1986).
[6] M. Andersson, *et al.* Nucl. Phys. A **779**, 47 (2006).
[7] M. Andersson, *et al.* Phys. Lett. B **481**, 165 (2000).
[8] M. Andersson, *etal.* Phys. Scr. **T104**, 96 (2003).
[9] L. Bimbot, *et al.* Phys. Rev. C **30**, 739 (1984).
[10] L. Bimbot, *et al.* Phys. Lett. B **114**, 311 (1982).
[11] J. Homolka, *et al.* Phys. Rev. C **38**, 2686 (1988).
[12] N. Willis, *et al.* Phys. Lett. B **136**, 334 (1984).
[13] R.E. Tribble, *et al*. Nucl. Instrum. Methods Phys. Res. **A285**, 441 (1989).
[14] D.A. Cebra, *et al.* Nucl. Instrum. Methods Phys. Res. **A313**, 367 (1992).

# Implementation of flash digitizers in the ParTI phoswich array for identification of charged pions

A. Zarrella, L. Heilborn, A. Jedele, A.B. McIntosh, and S.J. Yennello

The Partial Truncated Icosahedron (ParTI) phoswich array has been designed and constructed for the purpose of detecting charged pions emitted through the pionic fusion process. This process is quite rare with measured cross sections ranging from hundreds of nanobarns to hundreds of picobarns depending upon the size of the reacting system [1-12]. The experimental plan is to mount the ParTI array inside the target chamber in the Momentum Achromat Recoil Spectrometer (MARS) beam line where it will detect charged pions created at the target position from pionic fusion reactions while the pionic fusion residues will be collected at the back of the MARS. The low reaction cross section, broad angular distribution, and the resulting high beam intensity necessary to measure these reactions have necessitated the development of advanced triggering and data acquisition techniques, which have been made possible through the use of fast-sampling ADC digitizers.

The ParTI array is made up of 15 phoswich detector units oriented such that they cover approximately the hemisphere backward of the target (with respect to the beam). Each phoswich is made up of 4 parts: a 3 mm thick EJ-212 fast-scintillating plastic, a 1.5 cm thick CsI(Tl) scintillator, a 1 inch thick Lucite light guide, and a R-1924A Hamamatsu photomultiplier tube. All faces of the detectors are wrapped in white Teflon tape except the front face which is covered with a sheet of aluminized mylar. The phoswiches come in three different shapes - hexagons, pentagons, and partial hexagons - corresponding to the faces of the truncated icosahedrons. Fragments from the nuclear reactions on the target enter the front face of the detectors and deposit energy in the two scintillating components differentially with respect to the energy and species of the fragment. Using the different scintillating characteristics of these detectors, it is possible to achieve elemental separation through at least $Z = 5$ and isotopic resolution up to at least $Z = 2$ using fast and slow gating pulse shape discrimination (PSD) techniques. Please refer to the annual report entitled “The ParTI Array for Studying Pionic Fusion” for examples of the particle identification capabilities of these detectors.

The charged particle identification capabilities for phoswich detectors are fairly well established and can be accomplished with analog electronics [12-17]. The ParTI array, though, will be tasked with identifying charged pions resulting from the very rare pionic fusion process from a background of gamma rays, neutrons and charged particles that will be 6-7 orders of magnitude higher intensity. A GEANT4 simulation of the phoswich detectors was produced which showed that charged pions could be identified in the traditional manner of fast and slow pulse shape discrimination as a charged particle band below the protons and similar to the charged baryon lines. Fig. 1 is a fast vs. slow particle identification plot which shows charged baryons in black, pions in red, neutrons in blue, and gammas in green. This result was expected and encouraging. However, the simulation also predicted the pion line to extend through regions of the particle ID space populated by neutrons, gamma rays, and incomplete light collection in other charged baryon events. This has since been confirmed in several test beam experiments and, in practice, these background processes will completely swamp the few pionic fusion pions that we expect in any given detector. Pions interacting with the detectors will also have characteristic decays (first, the pion-to-muon decay with average lifetime of around 30 ns followed by the muon-to-electron decay with average lifetime around 2.2 μs) which will deposit energy in the scintillators at varying times with respect to the PSD gates. As a result, many pions do not lie on the particle ID line and have values on the slow axis beyond the neutron/gamma line.

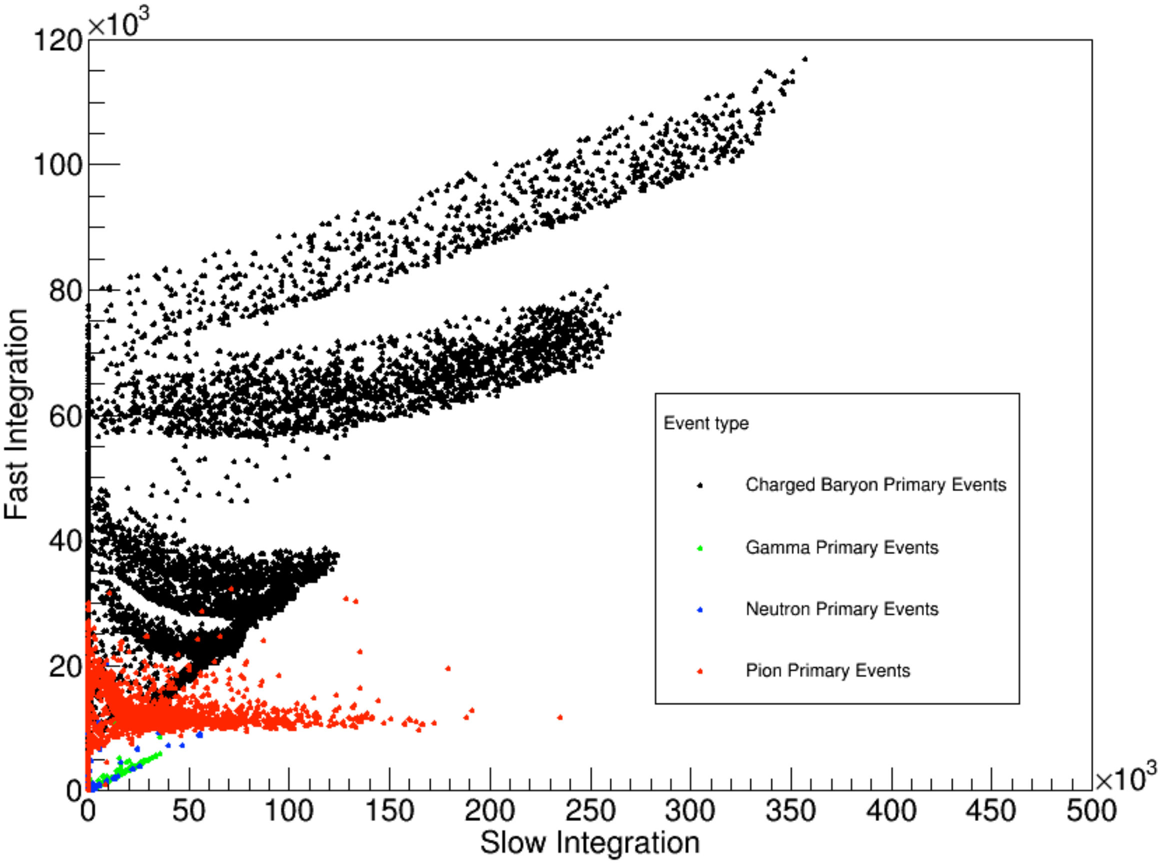

**FIG. 1.** A fast vs. slow (ΔE-E) particle identification plot produced by the GEANT phoswich simulation. The x-axis is the integrated phoswich signal inside of the slow gate which is 400 ns wide and starts 1 μs from the beginning of the signal. The y-axis is the integrated phoswich signal inside the fast gate which is 15 ns wide and begins at the start of the signal. Moving up from the bottom of the figure, neutron and gamma events (blue and green points, respectively) populate the neutron/gamma line. Above that is the pion band shown in red followed by particle bands for the light charged baryons. There is good isotopic resolution of p, d, and t followed by a Z = 2 band populated by $^3$He and $^4$He and finally a band for $^6$Li.

Ultimately, it has become clear that relying on a pronounced fast vs. slow particle ID line for pions is not an option given the very low stats, high background in the region, and uncertainty of the position of individual pions. However, the GEANT simulation was also able to predict the full waveform response of the phoswiches. Figure 2 shows representative GEANT-simulated phoswich responses for charged baryons, neutron/gammas, and pions (panels a, b, and c, respectively). The characteristic decay of the muon associated with pion implantations that was contributing to the difficulty of identifying pions using fast vs. slow integrations could be used to identify pions using the total waveforms. In order to accomplish this, one needs to digitize the phoswich signals, parse the waveforms (either in the hardware FPGA mounted on the digitizer or in the software backend) for the presence of a second pulse, and then cross check both pulses using the fast vs. slow PSD technique to eliminate background events. Using this technique in a beam test performed in February of 2016 with the phoswich detectors, we have been able to efficiently classify pion candidate events. When this technique is combined with the coincident measurement of the complementary fusion residue in MARS, we will be able to identify pionic fusion events with extremely high accuracy.

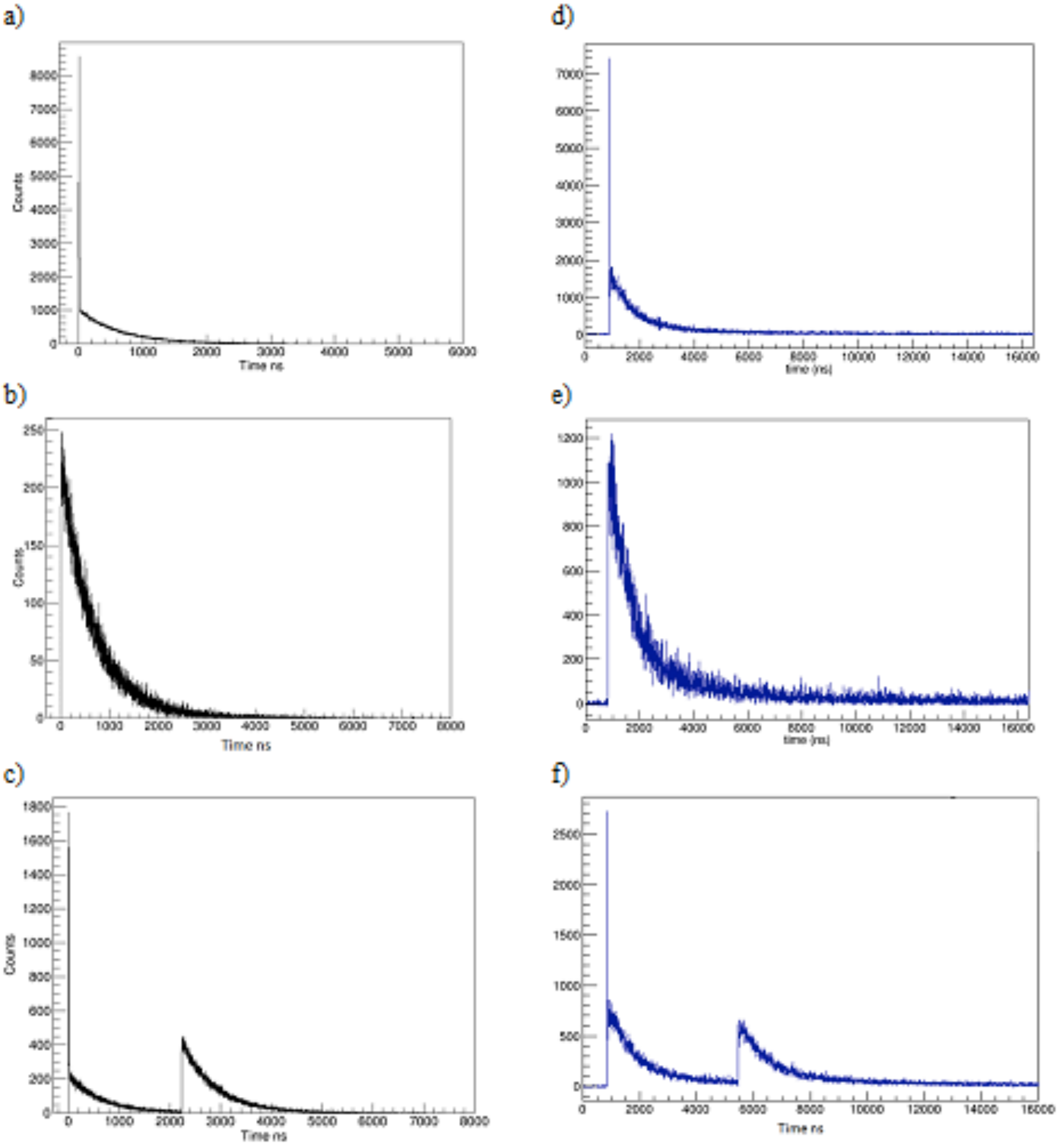

**FIG. 2.** Predicted phoswich responses produced by the GEANT4 simulation for representative events of a light charged baryon, neutron/gamma, and pion (panels a, b, and c, respectively) with comparable representative digitized experimental events from the February 2016 beam experiment in panels d, e, and f. The muon decay, with mean lifetime of 2.2 μs accompanying pion implantations,provides a very clear pion event signature.

For the fast-sampling digitizer we have chosen to use the SIS3316 unit produced by Struck Innovative Systeme. This is a 16-channel, 14 bit resolution VME unit with a 250 MSsamples/s sampling rate. In beam tests, we have shown that we can perform the fast vs. slow PSD technique by integrating over sampled bins (see annual report for the ParTI array noted previously). In panels d, e, and f of Figure 2 are shown three digitized phoswich waveforms from the test run in February of 2016 which correspond very closely to their respective response types predicted by the GEANT4 simulation. The waveform in Figure 2f is a very strong pion candidate possessing the characteristic decay pulse with a reasonable decay time, a primary peak with a fast vs. slow particle identification located between the proton and neutron/gamma line, and a secondary peak with a fast vs. slow particle identification located in the expected area for the decay electrons.

While the complete waveforms digitized by the SIS3316 have allowed for the more accurate identification of pions, their necessity has also increased the data overhead of the acquisition by approximately 4000x (>8000 digitized bins per channel vs. one fast and one slow integration per channel from the QDCs). The consequence of collecting this much more data per event is that it greatly reduces the event rate that can be written to disk while maintaining and acceptable dead time for the low cross section reactions of interest. In order to circumvent this new issue, we will utilize an advanced triggering mechanism implemented in the on-board FPGA of the digitizer that was developed by Struck Innovative Systeme and Dr. Sara Wuenschel. This "pileup" trigger parses the signals coming into the module in real time in order to identify secondary peaks. Upon finding a second peak in a given time window, a trigger will be produced and the event of interest is written to disk. In practice, this advanced triggering mechanism will suppress the number of triggers resulting from non-pion events and allow for much higher beam rates as a result. The pileup trigger has been tested in the laboratory and beam tests.

The ParTI array and digitizer-based pion identification technique described above will be used in the pionic fusion experiment scheduled for 2016 and the following data analysis. There will also be a detector test at the pion/muon beam facility at the Paul Scherrer Institute in Switzerland. In this test run, a beam of pions/muons will be scattered into representative phoswich modules in order to better constrain the detector's response to charged pions and the corresponding muon decays.

[1] D. Horn *et al.*, Phys. Rev. Lett. **77**, 2408 (1996).
[2] Y. Le Bornec *et al.*, Phys. Rev. Lett. **47**, 1870 (1981).
[3] L. Joulaeizadeh *et al.*, Phys. Lett. B **694**, 310 (2011).
[4] W. Schott *et al.*, Phys. Rev. C **34**, 1406 (1986).
[5] M. Andersson *et al.*, Nucl. Phys. **A779**, 47 (2006).
[6] M. Andersson *et al.*, Phys. Lett. B **481**, 165 (2000).
[7] M. Andersson *et al.*, Phys. Scr. **T104**, 96 (2003).
[8] L. Bimbot *et al.*, Phys. Rev. C **30**, 739 (1984).
[9] L. Bimbot *et al.*, Phys. Lett. B **114**, 311 (1982).
[10] J. Homolka *et al.*, Phys. Rev. C **38**, 2686 (1988).
[11] N. Willis *et al.*, Phys. Lett. B **136**, 334 (1984).
[12] D. Fox *et al.*, Nucl. Instrum. Methods Phys. Res. **A374**, 63 (1996).
[13] W. Gawlikowicz *et al.*, Nucl. Instrum. Methods Phys. Res. **A491**, 181 (2002).
[14] H.K.W. Leegte *et al.*, Nucl. Instrum. Methods Phys. Res. A**313** 26 (1992).
[15] Fredrik Liden *et al.*, Nucl. Instrum. Methods Phys. Res. **A253**, 305 (1987).
[16] J. Pouliot *et al.*, Nucl. Instrum. Methods Phys. Res. **A270**, 69 (1988).

[17] H.R. Schmidt *et al.*, Nucl. Instrum. Methods Phys. Res. **A242**, 111 (1985).

# Online commissioning of the AstroBox2 detector

A. Saastamoinen, B.T. Roeder, A. Spiridon, R. Chycz, M. Dag, R.E. Tribble, E. Pollaco,[1]
L. Trache,[2] G. Pascovici,[2] and M.R.D. Rodrigues[3]
[1] *IRFU, CEA Saclay, Gif-sur-Yvette, France*
[2] *National Institute of Physics and Nuclear Engineering, Bucharest-Magurele, Romania*
[3] *Instituto de Física, Universidade de São Paulo, São Paulo, Brazil*

In past years we have done several studies of beta-delayed proton emitters of astrophysical interest by implantation technique [1-5]. It was realized rather soon that shrinking the physical detection volume of elements in Si detector did not reduce the beta-background enough to create background free spectrum in the typical energy range of astrophysically interesting decays ($E_p$ ~ few hundred keV). To further reduce the beta-background a novel detector, AstroBox, based on Micro Pattern Gas Amplifier Detector (MPGAD) was developed [6]. Recently we have built an upgraded version of the detector, called AstroBox2 [7]. The construction of the detector and the offline commissioning of the first Micromegas detector element is described in the previous annual reports [8,9].

We have tested the first AstroBox2 Micromegas detector with 128 μm amplification gap in online conditions with beta-decays of and $^{25}$Si, $^{20}$Na, and $^{23}$Al. The beams were produced through deep-inelastic fragmentation ($^{25}$Si), or fusion evaporation ($^{20}$Na, $^{23}$Al) reactions, in inverse-kinematics at energies of 40-45 MeV/u and separated with Momentum Achromat Recoil Separator (MARS) before being implanted into the gas volume of the detector.

Good overall production rate of $^{25}$Si (~5 ions/nC), in combination with the high branching ratio for low energy beta-delayed proton emission (4.75(32)% absolute intensity for 401 keV proton [10)], makes it an ideal case to test and optimize various parameters of the setup. A sample spectrum from decay of $^{25}$Si, with a comparison to GEANT4 simulation, is shown in Fig. 1. We have optimized our

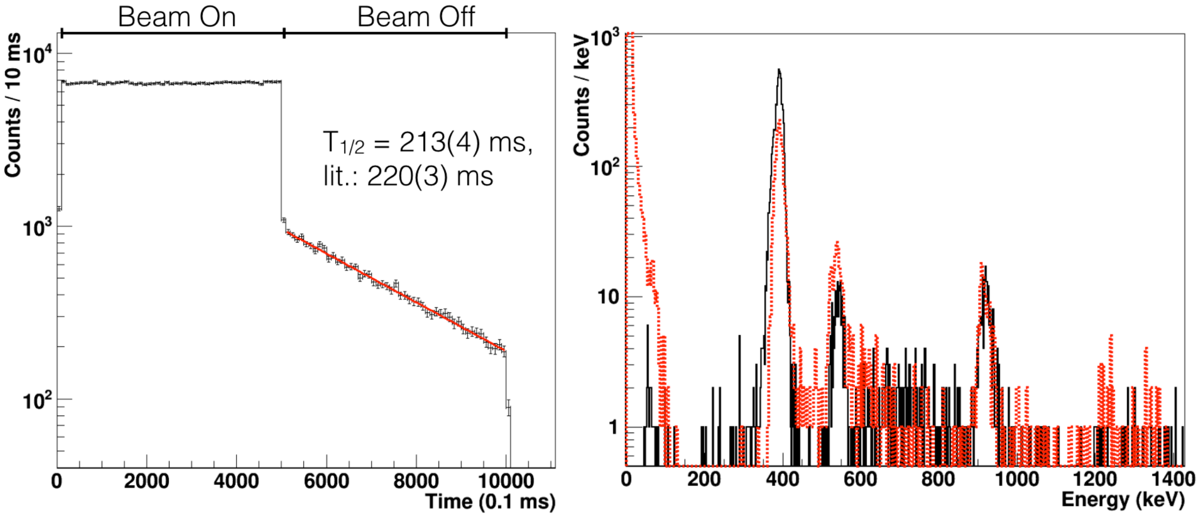

**FIG. 1.** Left: Decay time spectrum of $^{25}$Si gated by the decay energies of the 401, 555, and 943 keV proton peaks. Right: Measured beta-delayed proton spectrum of $^{25}$Si (black, solid) compared to a GEANT4 simulation (red, dashed) when decays are confined into one pad active volume. Resolution of the 401 keV proton group is ~4%. The data was collected during beam off period of a pulsed beam with a cycle of 500 ms on and 500 ms off.

implantation efficiency by reducing the distance from the beam energy degrader to the window separating the gas volume from the beam line vacuum. At the moment more than 50% of the activity produced, as measured with MARS target detector, is implanted inside AstroBox2 and contained over the centermost readout pads. The remaining losses are most likely due to MARS target detector ladder and the zero length reduced coupling the setup to the MARS target detector chamber. This implantation activity rate of $^{25}$Si allows thorough calibration of the detector in about one shift, making the detector in its present stage fully functional for decay studies. However, we are studying possible optimizations in form of new mesh technologies, better gas mixtures, and improved gating grid structures that should improve and push the performance beyond the present capabilities.

[1] A. Saastamoinen *et al.*, Phys. Rev. C **83**, 044808 (2011).
[2] L. Trache *et al.* PoS (NIC X), 163 (2008).
[3] A. Saastamoinen *et al.*, AIP Conf. Proc. **1409**, 71 (2011).
[4] J. Wallace *et al.*, Phys. Lett. B **712**, 59 (2012).
[5] M. McCleskey *et al.*, Nucl. Instrum. Methods Phys. Res. **A700**, 124 (2013).
[6] E. Pollaco *et al.*, Nucl. Instrum. Methods Phys. Res. **A723**, 102 (2013).
[7] A. Saastamoinen *et al.*, Nucl. Instrum. Methods Phys. Res. **B376**, 357 (2016).
[8] A. Saastamoinen *et al.*, *Progress in Research*, Cyclotron Institute, Texas A&M University (2013-2014), p. IV-55.
[9] A. Saastamoinen *et al.*, *Progress in Research*, Cyclotron Institute, Texas A&M University (2014-2015), p.IV-33.
[10] J.-C. Thomas *et al.*, Eur. Phys. J. A **21**, 419 (2004).

# SECTION V

# PUBLICATIONS

# PAPERS PUBLISHED
## April 1, 2015 – March 31, 2016

**Isoscalar E0, E1, E2 and E3 strength in $^{92,96.98.100}$Mo**, D.H. Youngblood, Y.–W. Lui, Krishichayan, J. Button, G. Bonasera, and S. Shlomo, Phys. Rev. C **92**, 014318 (2015).

**Isoscalar giant resonances in $^{90,92.94}$Zr**, Krishichayan, Y.–W. Lui, J. Button, D.H. Youngblood, G. Bonasera, and S. Shlomo, Phys. Rev. C **92**, 044323 (2015).

**The β decay of $^{38}$Ca: sensitive test of isospin symmetry-breaking corrections from mirror superallowed $0^+\rightarrow 0^+$ transitions**, H.I. Park, J.C. Hardy, V.E. Iacob, M. Bencomo, L. Chen, V. Horvat, N. Nica, B.T. Roeder, E. Simmons, R.E. Tribble, and I.S. Towner, *Proc. Conf. Advances in Radioactive Isotope Science (ARIS2014)*, JPS Conf. Proc. **6**, 020033 (2015).

**Nuclear structure beyond the neutron drip line: The lowest energy states of $^{9}$He via their T=5/2 isobaric analogs in $^{9}$Li**, E. Uberseder, G.V. Rogachev, V.Z. Goldberg, E. Koschiy, B.T. Roeder, M. Alcorta, G. Chubarian, B. Davids, C. Fu, J. Hooker, H. Jayatissa, D. Melconian, and R.E. Tribble, Phys. Lett. B **754**, 323 (2016).

**Precise measurement of branching ratios in the β decay of $^{38}$Ca**, H.I. Park, J.C. Hardy, V.E. Iacob, M. Bencomo, L. Chen, V. Horvat, N. Nica, B.T. Roeder, E. McCleskey, R.E. Tribble, and I.S. Towner, Phys. Rev. C **92**, 015502 (2015).

**Theoretical corrections and world data for the superallowed *ft* values in the β decays of $^{42}$Ti, $^{46}$Cr, $^{50}$Fe and $^{54}$Ni**, I.S. Towner and J.C. Hardy**,** Phys. Rev. C **92**, 055505 (2015).

**Precise measurement of $a_K$ and $a_T$ for the 150.8-keV *E*3 transition in $^{111}$Cd: Test of internal-conversion theory**, N. Nica, J.C. Hardy, V.E. Iacob, T.A. Werke, C.M. Folden III, L. Pineda, and M.B. Trzhaskovskaya**,** Phys. Rev. C **93**, 034305 (2016).

**The current evaluation of $V_{ud}$**, J.C. Hardy and I.S. Towner**,** In *Proceedings of the 12th International Conference on the Intersections of Particle and Nuclear Physics*, CIPANP2015, eConf C15-05-19, **60** (2015);arXiv:1509.04743.

**Nuclear data sheets for A = 157**, N. Nica, Nucl.Data Sheets **132**, 1 (2016).

**Revalidation of the isobaric multiplet mass equation for the A = 20 quintet**, B.E. Glassman, P.D. Shidling *et al.,* Phys. Rev. C **92**, 042501(R) (2015).

**Status of the TAMUTRAP facility and initial characterization of the RFQ cooler/buncher**, M. Mehlman, P.D. Shidling, R. Burch, E. Bennett, B. Fenker, and D. Melconian, *Proceedings of the 6th International Conference on Trapped Charged Particles and Fundamental Physics (TCP 2014)*, Hyperfine Interact. **235**, 77 (2015).

**New measurement of the alpha asymptotic normalization coefficient of the 1/2(+) state in O-17 at 6.356 MeV that dominates the C-13(alpha, n)O-16 reaction rate at temperatures relevant for the s process**, M.L. Avila, G.V. Rogachev, E. Koshchiy, L.T. Baby, J. Belarge, K.W. Kemper, A.N. Kuchera, D. Santiago-Gonzalez, Phys. Rev. C **91**, 048801 (2015).

**Reaction rate of the C-13(alpha, n)O-16 neutron source using the ANC of the-3 keV resonance measured with the THM**, M. La Cognata, C. Spitaleri, O. Trippella, G.G. Kiss, G.V. Rogachev, A.M. Mukhamedzhanov, M. Avila, G.L. Guardo, E. Koshchiy, A. Kuchera, L. Lamia, S.M.R. Puglia, S. Romano, D. Santiago, R. Sparta, Nucl. Phys. Astrophys. Vi (Npa6) **665**, 012013 (2016).

**Quasimolecular states in a reaction with carbon isotopes**, S.Yu. Torilov, N.A. Maltsev, V.Z. Goldberg, K.A. Gridnev, V.I. Zherebchevsky, T. Lonnroth, B.G. Novatskii, J.M.K. Slotte, Yu.G. Sobolev, W.H. Trzaska, G.P. Tyurin, and S.V. Khlebnikov, JETP Lett. **102**, 69 (2015).

**Direct measurement of the astrophysical $^{38}$K(p, $\gamma$)$^{39}$Ca reaction and its influence on the production of nuclides toward the end point of nova nucleosynthesis**, G. Lotay, G. Christian, C. Ruiz, C. Akers, D. S. Burke, W.N. Catford, A.A. Chen, D. Connolly, B. Davids, J. Fallis, U. Hager, D. A. Hutcheon, A. Mahl, A. Rojas, and X. Sun, Phys. Rev. Lett. **116**, 132701 (2016).

**Investigation of the role of $^{10}$Li resonances in the halo structure of $^{11}$Li through the $^{11}$Li(p,d)$^{10}$Li transfer reaction**, A. Sanetullaev, R. Kanungo, J. Tanaka, M. Alcorta, C. Andreoiu, P. Bender, A. Chen, G. Christian, B. Davids, J. Fallis, J. Fortin, N. Galinski, A. Gallant, P. Garrett, G. Hackman, B. Hadinia, S. Ishimoto, M. Keefe, R. Krücken, J. Lighthall, E. McNeice, D. Miller, J. Purcell, J. Randhawa, T. Roger, A. Rojas, H. Savajols, A. Shotter, I. Tanihata, I. Thompson, C. Unsworth, P. Voss, and Z. Wang, Phys. Lett. B **755**, 481 (2016).

**Observation of a crossover of $S_{2n}$ in the island of inversion from precision mass spectrometry**, A.A. Kwiatkowski, C. Andreoiu, J.C. Bale, A. Chaudhuri, U. Chowdhury, A.T. Gallant, A. Grossheim, A. Lennarz, D. Lunney, T.D. Macdonald, M.R. Pearson, B.E. Schultz, T. Rauch, S. Seeragi, M.C. Simon, V.V. Simon, J. Dilling, Phys. Rev. C **92**, 061301 (2015).

**Extraction chromatography of the Rf homologs Zr and Hf using the TEVA and UTEVA resins from HCl, $HNO_3$, and $H_2SO_4$**, M.C. Alfonso, M.E. Bennett, and C.M. Folden III, J. Radioanal. Nucl. Chem. **307**, 1529 (2016).

**Thallium extraction from hydrochloric acid media into pure ionic liquids**, E.E. Tereshatov, M.Yu. Boltoeva, V. Mazan, M.F. Volia, and C.M. Folden III, J. Phys. Chem. B **120**, 2311 (2016).

**Hot fusion-evaporation cross sections of $^{44}$Ca-induced reactions with lanthanide targets**, T.A. Werke, D.A. Mayorov, M.C. Alfonso, E.E. Tereshatov, and C.M. Folden III, Phys. Rev. C **92**, 054617 (2015).

**Evaporation residue excitation function measurements in $^{50}$Ti- and $^{54}$Cr-induced reactions with lanthanide targets**, D.A. Mayorov, T.A. Werke, M.C. Alfonso, E.E. Tereshatov, M.E. Bennett, M.M. Frey, and C.M. Folden III, Phys. Rev. C **92**, 054601 (2015).

**Hot fusion-evaporation cross sections of $^{45}$Sc-induced reactions with lanthanide targets**, T.A. Werke, D.A. Mayorov, M.C. Alfonso, M.E. Bennett, M.J. DeVanzo, M.M. Frey, E.E. Tereshatov, and C.M. Folden III, Phys. Rev. C **92**, 034613 (2015).

**Resin ion exchange and liquid-liquid extraction of indium and thallium from chloride media**, E.E. Tereshatov, M.Yu. Boltoeva, and C.M. Folden III, Solvent Extr. Ion Exc. **33**(6), 607-624 (2015).

**New recoil transfer chamber for thermalization of heavy ions produced in fusion-evaporation reactions**, M.C. Alfonso, E.E. Tereshatov, M.J. DeVanzo, J.A. Sefcik, M.E. Bennett, D.A. Mayorov, T. A. Werke, and C.M. Folden III, Nucl. Instrum. Methods Phys. Res. **A798**, 52 (2015).

**Constraining supernova equations of state with equilibrium constants from heavy-ion collisions**, M. Hempel, K. Hagel, J.B. Natowitz, G. Röpke, and S. Typel, Phys. Rev. C **91**, 045805 (2015).

**SπRIT: A time-projection chamber for symmetry-energy studies,** R. Shane, A. McIntosh, T. Isobe, W. Lynch, H. Baba, J. Barney, Z. Chajecki, M. Chartier, J. Estee, M. Famiano, B. Hong, G. Jhang, R. Lemmon, F. Lu, T. Murakami, N. Nakatsuka, M. Nishimura, R. Olsen, W. Powell, H. Sakurai, A. Taketani, S. Tangwancharoen, M. Tsang, R. Wang, S.J. Yennello, and J. Yurkon, Nucl. Instrum. Methods Phys. Res. **A784**, 513 (2015).

**Studying heavy-ion collisions with coverage near zero degrees with FAUST-QTS**, P. Cammarata, M. Chapman, A. McIntosh, G. Souliotis, L. Bakhtiari, S. Behling, G. Bonasera, L. Heilborn, J. Mabiala, L. May, A. Raphelt, M. Youngs, A. Zarrella, and S.J. Yennello, Nucl. Instrum. Methods Phys. Res. **A792**, 61 (2015).

**Novel technique to extract experimental symmetry free energy information for nuclear matter**, J. Mabiala, H. Zheng, A. Bonasera, P. Cammarata, K. Hagel, L. Heilborn, Z. Kohley, L. May, A. McIntosh, M. Youngs, A. Zarrella, and S.J. Yennello, Phys. Rev. C **92**, 024605 (2015).

**Effects of repulsive three-body force in 12C +12C scattering at 100*A*MeV**, W.W. Qua, G.L. Zhang, S. Terashima, T. Furumoto, Y. Ayyad, Z.Q. Chen, C.L. Guoa, A. Inoue, X.Y. Le, H.J. Ong, D.Y. Pang, H. Sakaguchi, Y. Sakuragi, B.H. Sun, A. Tamii, I. Tanihataa, T.F. Wang, R. Wada, Y. Yamamoto, Phys. Lett. B **751**, 1 (2015).

**Freezeout concept and dynamical transport model in intermediate-energy heavy-ion reactions**, X. Liu, W. Lin, M. Huang, R. Wada, J. Wang, Z. Chen, Q. Wang, P. Ren, Y. Yang, S. Jin, P. Ma, J. Ma, Z. Bai, and Q. Hu, Phys. Rev. C **92**, 014623 (2015).

**Trojan Horse measurement of the $^{18}$F(p,α)$^{15}$O astrophysical S(e) factor**, R.G. Pizzone, B.T. Roeder, M. McCleskey, L. Trache, R.E. Tribble, C. Spitaleri, C.A. Bertulani, S. Cherubini, M. Gulino, I. Indelicato, M. La Cognata, L. Lamia, G.G. Rapisarda, R. Sparta, Eur. Phys. J. A **52**, 24 (2016).

**Asymptotic normalization coefficients and radiative widths**, A.M. Mukhamedzhanov and D.Y. Pang, Phys. Rev. C **92**, 014625 (2015).

**Improvement of the high-accuracy $^{17}$O(p,alpha)$^{14}$N reaction-rate measurement via the Trojan Horse method for application to $^{17}$O nucleosynthesis**, M.L. Sergi, C. Spitaleri, M. La Cognata, L. Lamia, R.G. Pizzone, G.G. Rapisarda, X.D. Tang, B. Bucher, M. Couder, P. Davies, R. DeBoer, X. Fang, L. Lamm, C. Ma, M. Notani, S. O'Brien, D. Roberson, W. Tan, M. Wiescher, B. Irgaziev, A.M. Mukhamedzhanov, J. Mrazek, and V. Kroha, Phys. Rev. C **91**, 065803 (2015).

**New approach to folding with the Coulomb wave function**, L.D. Blokhintsev, A.S. Kadyrov, A.M. Mukhamedzhanov, and D.A.Savin, J. Math. Phys. **56**, 052102 (2015).

**Updated THM astrophysical factor of the $^{19}$F(p, α)$^{16}$O reaction and influence of new direct data at astrophysical energies,** M. La Cognata, S. Palmerini, C. Spitaleri, I. Indelicato, A.M. Mukhamedzhanov, I. Lombardo, and O. Trippella, Astrophys. J. **805**, 128 (2015).

**THM determination of the 65 keV resonance strength intervening in the $^{17}$O( p ,α) $^{14}$N reaction rate,** M.L. Sergi, C. Spitaleri, S.V. Burjan, S. Cherubini, A. Coc, M. Gulino, F. Hammache, Z. Hons, B. Irgaziev, G.G. Kiss, V. Kroha, M. La Cognata, L. Lamia, A.M. Mukhamedzhanov, R.G. Pizzone, S.M. R. Puglia, G.G. Rapisarda, S. Romano, N. de Séréville, E. Somorjai, and A. Tumino, AIP Conference Proceedings **1645**, 392 (2015).

**Properties of high-energy isoscalar monopole excitations in medium-heavy mass spherical nuclei**, M.L. Gorelik, S. Shlomo, B.A. Tulupov, and M.H. Urin, Phys. of Atom. Nucl. **78**, 551 (2015).

**Short range correlations and the 3$s_{1/2}$ wave function in $^{206}$Pb**, M.R. Anders, S. Shlomo, and I. Talmi, Phys. Rev. C **92**, 034318 (2015).

**A novel method for determining the mean-feld directly from the single particle matter density**, S. Shlomo, J. of Phys. Conference Series **633**, 012028 (2015).

**Neutron stars and supernova explosions in the framework of Landau's theory**, Hua Zheng, Jaime Sahagun, and Aldo Bonasera, Int. J. Mod. Phys. E **24**, 1550059 (2015).

**Systematic analysis of hadron spectra in p+p collisions using Tsallis distributions,** H. Zheng, Lilin Zhu, and A. Bonasera, Phys. Rev. D, **92**, 074009 (2015).

**Microscopic dynamical description of proton-induced fission with the constrained molecular dynamics model,** N. Vonta, G.A. Souliotis, M. Veselsky, and A. Bonasera, Phys. Rev. C, **92**, 024616 (2015).

**Novel technique to extract experimental symmetry free energy information for nuclear matter,** J. Mabiala, H. Zheng, A. Bonasera, P. Cammarata, K. Hagel, L. Heilborn, Z. Kohley, L.W. May, A.B. McIntosh, M.D. Youngs, A. Zarrella, and S.J. Yennello, Phys. Rev. C, **92**, 024605 (2015).

**Triple α resonances in the $^6$Li + $^6$Li → 3α reaction at low energy,** A. Tumino, A. Bonasera, G. Giuliani, M. Lattuada, M. Milin, R.G. Pizzone, C. Spitaleri, S. Tudisco, Phys. Lett. B, **750**, 59 (2015).

**Signals of Bose Einstein condensation and Fermi quenching in the decay of hot nuclear systems,** P. Marini, H. Zheng, M. Boisjoli, G. Verde, A. Chbihi, P. Napolitani, G. Ademard, L. Augey, C. Bhattacharya, B. Borderie, R. Bougault, J.D. Frankland, Q. Fable, E. Galichet, D. Gruyer, S. Kundu, M. La Commara, I. Lombardo, O. Lopez, G. Mukherjee, M. Parlog, M.F. Rivet, E. Rosato, R. Roy, G. Spadaccini, M. Vigilante, P.C. Wigg, A. Bonasera (INDRA Collaboration), Phys. Lett. B, **756**, 194 (2016).

**Introduction to low-momentum effective interactions with Brown-Rho scaling and three-nucleon forces**, T.T.S. Kuo, J.W. Holt, and E. Osnes, Phys. Scr**.** **91**, 033009 (2016).

**Chiral symmetry and effective field theories for hadronic, nuclear and stellar matter**, J.W. Holt, M. Rho, and W. Weise, Phys. Rep. **621**, 2 (2016).

**An in-medium heavy-quark potential from the Q-Qbar free energy**, S.Y.F. Liu and R. Rapp, Nucl. Phys. **A941**, 179 (2015).

**Sequential regeneration of charmonia in heavy-ion collisions**, X. Du and R. Rapp, Nucl. Phys. **A943**, 147 (2015).

**Thermal dileptons as fireball thermometer and chronometer**, R. Rapp and H. van Hees, Phys. Lett. B **753**, 586 (2016).

**Heavy-flavour and quarkonium production in the LHC era: From proton-proton to heavy-ion collisions**, A. Andronic *et al.*, Eur. Phys. J. C **76**, 107 (2016).

**Thermal photon emission from the πρω system**, N.P.M. Holt, P.M. Hohler, and R. Rapp, Nucl. Phys. **A945**, 1 (2016).

**Massive Yang-Mills for vector and axial-vector spectral functions at finite temperature**, P.M. Hohler and R. Rapp, Annals Phys. **368**, 70 (2016).

**Physics perspective of heavy-ion collisions at very high energy**, N. Chang *et al.*, Sci. China Phys. Mech. Astronom. **59**, 621001 (2016).

**Mean-field effects on particle and antiparticle elliptic flows in the beam-energy scan program at RHIC**, J. Xu, C.M. Ko, F. Li, T. Song, and H. Liu, Nucl. Phys. Rev. **32**, 146 (2015).

**Light (anti-)nuclei production and flow in relativistic heavy ion collisions**, L.L. Zhu, C.M. Ko, and X. J. Yin, Phys. Rev. C **92**, 064911 (2015).

**Heavy quark correlations and the effective volume for quarkonia production**, Y.P. Liu, C.M. Ko, and F. Li, Phys. Rev. C **93**, 034901 (2016).

**Spinodal instability of baryon-rich quark-gluon plasma in the Polyakov-Nambu-Jona-Lasinio model**, F. Li and C.M. Ko, Phys. Rev. C **93**, 035205 (2016).

**Understanding transport simulations of heavy-ion collisions at 100A and 400A MeV: Comparison of heavy-ion transport codes under controlled conditions**, J. Xu, C.M. Ko *et al.*, Phys. Rev. C **93**, 044609 (2016).

**Jet fragmentation via recombination of parton showers**, K.C. Han, R. Fries, and C.M. Ko, Phys. Rev. C **93**, 045207 (2016).

**(Anti-)strangeness production in heavy ion collisions**, P. Moreau, F. Li, C.M. Ko, W. Cassing, and E. Bratkovskaya, J. Phys. Conf. Ser. **668**, 012072 (2016).

**Modifications of heavy-flavor spectra in $\sqrt{s_{NN}}$ = 62.4 GeV Au-Au collisions**, Min He, Rainer J. Fries, and Ralf Rapp, Phys. Rev. C **91**, 024904 (2015).

**QCD back-scattering photons in relativistic heavy ion collisions**, Somnath De, Rainer J. Fries, and Dinesh K. Srivastava, Proc. Indian Natl. Sci. Acad. **81**, 217 (2015).

**Early time dynamics of gluon fields in high energy nuclear collisions**, Guangyao Chen, Rainer J. Fries, Joseph I. Kapusta, and Yang Li, Phys. Rev. C **92**, 064912 (2015).

**Probing parton dynamics of QCD matter with Ω and φ production**, L. Adamczyk *et al.* (STAR Collaboration), Phys. Rev. C **93**, 021903 (2016).

**Centrality dependence of identified particle elliptic flow in relativistic heavy ion collsions at $\sqrt{s_{NN}}$ = 7.7-62.4 GeV**, L. Adamczyk *et al.* (STAR Collaboration), Phys. Rev. C **93**, 014907 (2016).

**Observation of transverse spin-dependent azimuthal correlations of charged pion pairs in $\vec{p}p$at $\sqrt{s_{NN}}$ = 200 GeV**, L. Adamczyk *et al.* (STAR Collaboration), Phys. Rev. Lett. **115**, 252302 (2015).

**Azimuthal anisotropy in U+U and Au+Au collisions at RHIC**, L. Adamczyk *et al.* (STAR Collaboration), Phys. Rev. Lett. **115**, 222301 (2015)

**Measurement of interaction between antiprotons**, L. Adamczyk *et al.* (STAR Collaboration), Nature **527**, 345 (2015).

**Energy dependence of acceptance-corrected dielectron excess mass spectrum at mid-rapidity in Au+Au collisions at $\sqrt{s_{NN}}$ = 19.6 and 200 GeV**, L. Adamczyk *et al.* (STAR Collaboration), Phys. Lett. B **750**, 64 (2015).

**Measurements of dielectron production in Au+Au collisions at $\sqrt{s_{NN}}$ = 200 GeV from the STAR experiment**, L. Adamczyk *et al.* (STAR Collaboration), Phys. Rev. C **92**, 024912 (2015).

**Energy dependence of $K\pi$, $p\pi$, and $Kp$ fluctuations in Au+Au collisions from $\sqrt{s_{NN}}$ = 7.7 to 200 GeV**, L. Adamczyk *et al.* (STAR Collaboration), Phys. Rev. C **92**, 021901(R) (2015).

**Precision measurement of the longitudinal double-spin asymmetry for inclusive jet production in polarized proton collisions at $\sqrt{s_{NN}}$ = 200 GeV**, L. Adamczyk *et al.* (STAR Collaboration), Phys. Rev. Lett. **115**, 092002 (2015).

**Long-range psuedorapidity dihaderon correlations in *d*+Au collisions at $\sqrt{s_{NN}}$ = 200 GeV collisions**, N.M. Abdelwahab *et al.* (STAR Collaboration), Phys. Lett. B **747**, 265 (2015).

**Beam-energy-dependent two-pion interferometry and the freeze-out eccentricity of pions measured in heavy ion collisions at the STAR detector**, L. Adamczyk *et al.* (STAR Collaboration), Phys. Rev. C **92**, 014904 (2015).

**Di-hadron correlations with identified leading hadrons in 200 GeV Au+Au and d+Au collisions at STAR**, L. Adamczyk *et al.* (STAR Collaboration), Phys. Lett. B **751**, 233 (2015).

**Observation of charge asymmetry dependence of pion elliptic flow and the possible chiral magnetic wave in heavy-ion collisions**, L. Adamczyk *et al.* (STAR Collaboration), Phys. Rev. Lett. **114**, 252302 (2015).

**Isolation of flow and nonflow correlations by two- and four-particle cumulant measurements of azimuthal harmonics in $\sqrt{s_{NN}}$ = 200 GeV collisions**, N.M. Abdelwahab *et al.* (STAR Collaboration), Phys. Lett. B **745**, 40 (2015).

**Charged-to-neutral correlation at forward rapidity in Au+Au collisions at $\sqrt{s_{NN}}$ = 200 GeV**, L. Adamczyk *et al.* (STAR Collaboration), Phys. Rev. C **91**, 034905 (2015).

**Beam energy dependence of the third harmonic of azimuthal correlations in Au+Au collisions at RHIC**, L. Adamczyk *et al.* (STAR Collaboration), Phys. Rev. Lett. **116**, 112302 (2016).

**Scaling properties of fractional momentum loss of high-$p_T$ hadrons in nucleus-nucleus collisions at $\sqrt{(s_{NN})}$ from 62.4 GeV to 2.76 TeV**, A. Adare *et al.* (PHENIX Collaboration), Phys. Rev. C **93**, 024911 (2016).

**Transverse energy production and charged-particle multiplicity at midrapidity in various systems from $\sqrt{(s_{NN})}$=7.7 to 200 GeV**, A. Adare *et al.* (PHENIX Collaboration), Phys. Rev. C **93**, 024901 (2016).

**Centrality and transverse momentum dependence of elliptic flow of multistrange hadrons and $\phi$ meson in Au+Au collisions at $\sqrt{(s_{NN})}$ = 200 GeV**, L. Adamczyk *et al.* (STAR Collaboration), Phys. Rev. Lett. **116**, 062301 (2016).

**Measurements of elliptic and triangular flow in high-multiplicity $^3$He+Au collisions at $\sqrt{(s_{NN})}$=200 GeV**, A. Adare *et al.* (PHENIX Collaboration), Phys. Rev. Lett. **115**, 142301 (2015).

**Energy dependence of acceptance-corrected dielectron excess mass spectrum at mid-rapidity in Au+Au collisions at $\sqrt{(s_{NN})}$ = 19.6 and 200 GeV**, L. Adamczyk *et al.* (STAR Collaboration), Phys. Lett. B **750**, 64 (2015).

**Effect of event selection on jetlike correlation measurement in d+Au collisions at $\sqrt{(s_{NN})}$=200 GeV**, L. Adamczyk *et al.* (STAR Collaboration), Phys. Lett. B **743**, 333 (2015).

**Systematic study of azimuthal anisotropy in Cu+Cu and Au+Au collisions at $\sqrt{(s_{NN})}$ = 62.4 and 200 GeV**, A. Adare *et al.* (PHENIX Collaboration), Phys. Rev. C **92**, 034913 (2015).

**The quest to understand QCD matter using heavy nuclei in collisions**, S. Mioduszewski, Phys. Scripta **90**, 108014 (2015).

**Azimuthal elliptic anisotropy $v_2$ of high-$p_T$ direct gamma in Au+Au collisions at $\sqrt{(s_{NN})}$ = 200 GeV**, Ahmed M. Hamed (for the STAR Collaboration), J. Phys. Conf. Ser. **589**, 012009 (2015).

**First observation of low-energy gamma-ray enhancement in the rare-earth region**, A. Simon, M. Guttormsen, A.C. Larsen, C.W. Beausang, P. Humby, J.T. Burke, R.J. Casperson, R.O. Hughes, T.J. Ross, J.M. Allmond, R. Chyzh, M. Dag, J. Koglin, E. McCleskey, M. McCleskey, S. Ota, A. Saastamoinen, Phys. Rev. C **93**, 034303 (2016).

**Investigation of Y-88 via (p,d gamma) reactions**, R.O. Hughes, J.T. Burke, R.J. Casperson, J.E. Escher, S. Ota, J.J. Ressler, N.D. Scielzo, R.A.E. Austin, B. Abromeit, N.J. Foley, E. McCleskey, M. McCleskey, H.I. Park, T.J. Ross, A. Saastamoinen, Phys. Rev. C **93**, 024315 (2016).

**Gamma-ray decay from neutron-bound and unbound states in Mo-95 and a novel technique for spin determination**, M. Wiedeking, M. Krticka, L.A. Bernstein, J.M. Allmond, M.S. Basunia, D.L. Bleuel, J.T. Burke, B.H. Daub, P. Fallon, R.B. Firestone, B.L. Goldblum, R. Hatarik, P.T. Lake, A.C. Larsen, I.Y. Lee, S.R. Lesher, S. Paschalis, M. Petri, L. Phair, N.D. Scielzo, A. Volya, Phys. Rev. C **93**, 024303 (2016).

**Spin differences in the Zr-90 compound nucleus induced by (p, p'), (p, d), and (p, t) surrogate reactions**, S. Ota, J.T. Burke, R.J. Casperson, J.E. Escher, R.O. Hughes, J.J. Ressler, N.D. Scielzo, I.J. Thompson, R.A.E. Austin, B. Abromeit, N.J. Foley, E. McCleskey, M. McCleskey, H.I. Park, A. Saastamoinen, T.J. Ross, Phys. Rev. C **92**, 054603 (2015).

**Improved measurement of the half-life of the J(pi)=8(-) nuclear isomer Eu-152m2**, P. Humby, A. Simon, C.W. Beausang, T.J. Ross, R.O. Hughes, J.T. Burke, R.J. Casperson, J. Koglin, S. Ota, J.M. Allmond, E. McCleskey, M. McCleskey, A. Saastamoinen, R. Chyzh, M. Dag, K. Gell, T. Tarlow, G. Vyas, Phys. Rev. C **91**, 024322 (2015).

**Measurement of the gamma emission probability of Yb-173 using surrogate reactions**, O. Delaune, A. Blanc, J.T. Burke, R. Casperson, P. Chau Huu-Tai, E. McCleskey, M. McCleskey, V. Meot, O. Roig, A. Saastamoinen, EPJ Web of Conferences **93**, 02010 (2015). DOI: 10.1051/epjconf/20159302010.

**Y-87(n,gamma) and (89'9)0Zr(n,gamma) cross sections from a surrogate reaction approach**, S. Ota, J.T. Burke, R.J. Casperson, J.E. Escher, R.O. Hughes, J.J. Ressler, N.D. Scielzo, I. Thompson, R.A.E. Austin, E. McCleskey, M. McCleskey, A. Saastamoinen, T. Ross, EPJ Web of Conferences **93**, 02001 (2015), DOI: 10.1051/epjconf/20159302001.

**Validating (d,p gamma) as a surrogate for neutron capture**, A. Ratkiewicz, J.A. Cizewski, S.D. Pain, A.S. Adekola, J.T. Burke, R.J. Casperson, N. Fotiades, M. McCleskey, S. Burcher, C.M. Shand, R.A.E. Austin, T. Baugher, M.P. Carpenter, M. Devlin, J.E. Escher, S. Hardy, R. Hatarik, M.E. Howard, R.O. Hughes, K.L. Jones, R.L. Kozub, C.J. Lister, B. Manning, J.M.O. Donnell, W.A. Peters, T.J. Ross, N.D.

Scielzo, D. Seweryniak, S. Zhu, EPJ Web of Conferences **93**, 02012 (2015), DOI: 10.1051/epjconf/20159302012.

**Investigating the photon strength function to discrete levels**, M. Wiedeking, L.A. Bernstein, D.L. Bleuel, J.T. Burke, R. Hatarik, S.R. Lesher, N.D. Scielzo, M. Krticka, J.M. Allmond, M.S. Basunia, P. Fallon, R.B. Firestone, B.L. Goldblum, P.T. Lake, I.-Y. Lee, S. Paschalis, M. Petri, and L. Phair, 1st International African Symposium on Exotic Nuclei Proceedings (2015), p.375, DOI: 10.1142/9789814632041_0040.

# SECTION VI

# APPENDIX

# TALKS PRESENTED
## April 1, 2015 – March 31, 2016

*The current evaluation of $V_{ud}$,* **J.C. Hardy**, **Invited talk,** 12th International Conference on the Intersections of Particle and Nuclear Physics, CIPANP 2015, Vail, Colorado (May 2015).

*Testing CVC and CKM unitarity via superallowed nuclear beta decay,* **J.C. Hardy**, **Invited talk,** 5th International Conference on Proton-emitting Nuclei, Lanzhou, China (July 2015).

*Nuclear tests of the standard model: Vector current conservation and CKM unitarity,* **J.C. Hardy**, **Colloquium,** Physics Department, Notre Dame University, South Bend, Indiana (November 2015).

*Update of internal conversion coefficient measurement: 150.8-keV, E3 transition in $^{111m}$Cd,* **N. Nica**, **Invited talk,** 21st Technical Meeting of the Nuclear Structure and Decay Data Network, IAEA, Vienna, Austria (April 2015).

*Production of isomerically clean xenon samples for CTBTO,* **T. Eronen**, International Noble Gas Experiment (INGE2015) Workshop, Austin, Texas (December 2015).

*RHIC cold QCD plan: p+A collisions*, **C.A. Gagliardi**, **Invited Talk**, Emerging Spin and Transverse Momentum Effects in pp and p+A Collisions, Brookhaven, New York (February 2016).

*TMDs and GPDs (and closely related measurements) at RHIC*, **C.A. Gagliardi**, **Invited Talk**, From 1D Fragmentation Towards 3D Correlated Fragmentation, Trento, Italy (October 2015).

*Gluon polarization in longitudinally polarized pp collisions at STAR*, **Z. Chang** (for the STAR Collaboration), **Invited Talk**, 2105 RHIC/AGS Ann. Users' Meet., Brookhaven, New York (June, 2015).

*Recent transverse spin results from the STAR experiment at RHIC*, **M.M. Mondal** (for the STAR Collaboration), **Invited Talk**, 2105 RHIC/AGS Ann. Users' Meet., Brookhaven, New York (June, 2015).

*Measurement of the transverse single spin asymmetries for $\pi^0$ and electromagnetic jets at forward rapidities at STAR*, **M.M. Mondal** (for the STAR Collaboration), 2015 APS April Meet., Baltimore, Maryland (April 2015).

*Energy calibration of the NewSUBARU storage ring by laser Compton-scattering gamma rays and its applications*, **Y.-W. Lui**, **Invited Talk**, 3rd International Symposium on Energy Challenges and Mechanics - Towards a Big Picture, Aberdeen, Scotland, United kingdom (July 2015).

*Recent giant resonances measurements and its future*, **Y.-W. Lui**, **Invited Talk**, Lanzhou, China (September 2015).

*What do we learn from the giant monopole resonance measurement at Texas A&M University*? **Y.-W. Lui**, **Invited Talk**, Clustering effects of nucleon in nuclei and quarks in multi-quark states, Kavli Institute for Theoretical Physics China at the Chinese Academy of Sciences, Beijing, China (March 2016).

*The TITAN facility at TRIUMF: Precision experiments with ion traps*, **A.A. Kwiathowski**, ISOLDE PG Seminar, ISOLDE-CERN, Geneva, Switzerland (October 2015).

*The TITAN facility at TRIUMF: Precision experiments with ion traps*, **A.A. Kwiathowski**, Max-Plank-Institut für Kernphysik, Heidelberg, Germany (October 2015).

*Highly charged ions for mass measurements and in-trap decay spectroscopy*, **A.A. Kwiathowski**, **Invited Talk**, Colloque GANIL 2015, Anglet, France (October 2015).

*Mystery of* $^{9}$*He and structure of the neutron rich nuclei,* $^{8}$*He,* $^{10}$*He,* $^{7}$*H*, **V.Z. Goldberg**, **Invited Talk**, X Int. Conf. Nuclear Structure and Dynamics 2015, Portoroz, Slovenia (June 2015).

*Study of very neutron rich nuclei through their isobar analogs*, **V.Z. Goldberg**, **Invited Talk**, LXV Int. Conf. on Nucleus 2015 - New Horizons in Nuclear Physics, Nuclear Engineering, Femto- and Nanotechnologies, Saint-Petersburg, Russia (June 2015).

*Program in the low energy resonance reaction studies*, **V.Z. Goldberg**, **Invited Seminar**, Nazarbayev University, Astana, Kazakhstan (August 2015).

*New physics in resonance scattering induced by R/A beams*, **V.Z. Goldberg**, **Invited Talk**, International Workshop on Rare Isotope Science, Seoul, South Korea (December 2015).

*Upgrade of the TAMU MDM-focal plane detector with MicroMegas technology*, **A. Spiridon**, Workshop on Active Targets and TPC for Nuclear Physics Experiments, Michigan State University, East Lansing, Michigan (May 2015).

*Development of the TexAT detector at Texas A&M University*, **E. Uberseder**, Workshop on Active Targets and TPC for Nuclear Physics Experiments, Michigan State University, East Lansing, Michigan (May 2015).

*Clustering in* $^{10}$*Be and astrophysical aspects of clusters in oxygen isotopes*, **G. Rogachev**, **Invited Talk**, Gordon Research Conference on Nuclear Chemistry, New London, New Hampshire (May 2015).

*Structure of* $^{9}$*He studied in* $^{8}$*He+p resonance scattering*, **E. Uberseder**, Gordon Graduate Students and PostDocs meeting, New London, New Hampshire (May 2015).

*Light exotic nuclei studied via resonance scattering*, **G. Rogachev**, **Invited Talk**, Canadian Association of Physicists, Edmonton, Canada (June 2015).

*Probing the structure of the unbound nuclei* $^{9}$*He and* $^{10}$*N through proton elastic scattering*, **E. Uberseder**, The 12th International Conference on Nucleus Nucleus Collisions, Catania, Italy (June 2015).

*Constraining the key alpha-capture astrophysical reaction rates using the sub-Coulomb alpha-transfer reactions*, **G. Rogachev**, **Invited Talk**, The 12th International Conference on Nucleus Nucleus Collisions, Catania, Italy (June 2015).

*Unbound states of light nuclei and nuclear clustering*, **G.V. Rogachev**, 2015 Low Energy Community Meeting, ReAX Workshop, Michigan State University, East Lansing, Michigan (August 2015).

*Structure of* $^{10}$*N via* $^{9}$*C+p resonance scattering*, **J. Hooker**, 2015 APS Division of Nuclear Physics meeting, Santa Fe, New Mexico (October 2015).

*Measurement of the nuclear polarization in optically-pumped* $^{37}$*K: Progress towards a measurement of the* $\beta$*-asymmetry parameter,* **B. Fenker**, 6th International Symposium Symmetries in Subatomic Physics

(SSP 2015), Victoria, British Colombia, Canada (June 2015).

*Nuclear physics with trapped atoms and ions,* **D. Melconian**, "Pizza and Profs" presentation for the Texas A&M University Honors Program, Texas A&M University, College Station, Texas (April 2015).

*Exploring clustering in near Fermi energy collisions*, **J.B. Natowitz**, **Invited Talk**, Custipen Workshop, Shanghai, China (December 2015).

*Giuseppe Viesti - An appreciation*, **J.B. Natowitz**, **Invited Talk**, 11th Latin American Symposium, Medellin, Colombia (December 2015).

*Chemical equilibrium in low density nuclear matter*, **J.B. Natowitz**, **Invited Talk**, NUSYM15, Krakow, Poland (June 2015).

*Exploring clustering in alpha conjugate nuclei using the thick target inverse kinematic technique for multiple alpha emission,* **M. Barbui**, 2015 APS Division of Nuclear Physics Meeting, Santa Fe, New Mexico (October 2015).

*Study of $^{12}C$ excited states decaying into three alpha particles using the thick target inverse kinematic technique*, **M. Barbui**, International Conference on Nucleus-Nucleus Collisions (NN2015), Catania, Italy (June 2015).

*Studying nuclear reactions in plasma conditions,* **M. Barbui**, 8th European Summer School on Experimental Nuclear Astrophysics, Santa Tecla, CT, Italy (September 2015).

*Single event effect microchip testing at the Texas A&M University Cyclotron Institute*, **S.J. Yennello**, **Invited Talk**, 2015 APS Division of Nuclear Physics meeting, Santa Fe, New Mexico (October 2015).

*Nuclear reactions*, **S.J. Yennello**, **Invited Talk**, Exotic Beam Summer School, Florida State University, Tallahassee, Florida (August 2015).

*Stable & Rare Beams at the Texas A&M University Cyclotron Institute*, **S.J. Yennello**, **Invited Talk**, SHE Conf. Symposium on SUPER HEAVY NUCLEI, Texas A&M University, College Station, Texas (March 2015).

*Constraints on the asymmetric equation-of-state from heavy-ion collisions*, **S.J. Yennello**, **Invited Talk**, 12th International Conference on Nucleus-Nucleus Collisions (NN2015), Catania, Italy (June 2015).

*Isospin equilibration in heavy-ion collisions*, **S.J. Yennello**, **Invited Talk**, 5th International Symposium on Nuclear Symmetry Energy NuSYM15, Kraków, Poland (June 2016).

*From 'fixing women' to 'institutional transformation': An ADVANCE case study*, **S.J.Yennello**, **Invited Talk**, Meeting of American Association of Physics Teachers (AAPT), Baltimore, Maryland (July 2015).

*Stable and radioactive ion beams at the Texas A&M University Cyclotron Institute*, **S.J. Yennello**, **Invited Talk**, LECM, East Lansing, Michigan (September 2015).

*Using heavy-ion collisions to elucidate the asymmetric equation-of-state*, **S.J. Yennello**, **Invited Talk**, XXI International School on Nuclear Physics and Applications & International Symposium on Exotic Nuclei (2015), Varna, Bulgaria (September 2015).

*There's data...and then there's data: Telling your institution's story*, **S.J.Yennello**, **Invited Talk**, ADVANCE/GSE Program Workshop, Baltimore, Maryland (June 2015).

*Connections between nuclear reactions and astrophysics*, **S.J. Yennello**, **Invited Talk**, Exotic Beam Summer School, Florida State University, Tallahassee, Florida (August 2015).

*Producing exotic nuclei*, **S.J. Yennello**, **Invited Talk**, Meeting of American Association of Physics Teachers (AAPT), New Orleans, Louisiana (January 2016).

*How to observe equilibration in a femto-scale system on a zepto-second timescale*, **A.B. McIntosh**. Pacifichem: International Chemical Congress of Pacific Basin Societies, Honolulu, Hawaii (December 2015).

*New prospects for characterizing the asymmetry dependence of the nuclear caloric curve*, **A.B. McIntosh**, 2015 APS Division of Nuclear Physics Meeting, Santa Fe, New Mexico (October 2015).

*Measurements of proton-proton correlations with the upgraded FAUST array (FAUSTUPS)*, **L. Heilborn**, 2015 APS Division of Nuclear Physics Meeting, Santa Fe, New Mexico (October 2015).

*Using particle ratios to explore the limits of the thermodynamic model of heavy ion collisions*, **M. Youngs**, 2015 APS Division of Nuclear Physics Meeting, Santa Fe, New Mexico (October 2015).

*Rate of N-Z equilibration in a deformed nuclear system*, **A. Jedele**, 2015 APS Division of Nuclear Physics Meeting, Santa Fe, New Mexico (October 2015).

*How much cooler would it be with some more neutrons?* **A.B. McIntosh**, Nucleus-Nucleus 2015, Catania, Sicily, Italy (June 2015).

*Heavy ion collisions and tests of the supernova equation of state*, **K. Hagel**, 2015 APS Division of Nuclear Physics Meeting, Santa Fe, New Mexico (October 2015).

*From femtonova to supernova: Heavy ion collisions and the supernova equation of state*, **K. Hagel**, 12th International Conference on Nucleus-Nucleus Collisions (NN2015), Catania, Italy (June 2015).

*Search for high energy alpha particles in the reactions of 7.5 AMeV $^{197}$Au with $^{232}$Th,* **S. Wuenschel**, J.B. Natowitz, K. Hagel, M. Barbui, J. Gauthier, X. Cao, C. Ma, R. Wada, S. Kowalski, K. Schmidt, Z. Majka, Z. Sosin, and A. Wieloch, 2015 APS Division of Nuclear Physics Meeting, Santa Fe, New Mexico (October 2015).

*Heavy element research at Texas A&M University*, **C.M. Folden III**, **Invited Talk**, Symposium on “The Expanding Periodic Table: New Discoveries and Chemistry of the Heaviest Elements” at the 2015 International Chemical Congress of Pacific Basin Societies (Pacifichem 2015), Waikiki, Hawaii, (December 2015).

*Chemistry and nuclear reactions at the bottom of the periodic table*, **C.M. Folden III**, **Invited Talk**, Texas A&M University Cyclotron Institute Colloquium, College Station, Texas (September 2015).

*Opportunities for heavy element science with ReA,* **C.M. Folden III**, **Invited Talk**, ReA3-12 Upgrade Workshop, East Lansing, Michigan (August 2015).

*Production of heavy and superheavy elements using projectiles with Z ≥ 20*, **C.M. Folden III**, 250th American Chemical Society National Meeting, Boston, Massachusetts (August 2015).

*Study of chemical behaviour of Tl and In as light homologues of element 113*, **E.E. Tereshatov**, 250th American Chemical Society National Meeting, Boston, Massachusetts (August 2015).

*The interplay of chemistry and physics at the bottom of the periodic table*, **C.M. Folden III**, **Invited Talk**, Lawrence Berkeley National Laboratory Nuclear Physics Forum, Berkeley, California (July 2015).

*Nuclear forensics analysis of separated plutonium of foreign fuel cycles (NFASP) project: Assessment of unique trace elements and isotope ratios in separated plutonium from low burnup nuclear fuel* **C.M. Folden III**, (with Sunil S. Chirayath), DNDO ARI Grantees Program Review Conference, Dallas, Texas (July 2015).

*Heavy element research at Texas A&M University*, **C.M. Folden III**, 5th International Conference on the Chemistry and Physics of the Transactinide Elements (TAN 15), Urabandai, Fukushima, Japan (May 2015).

*Prospects for the discovery of the next new element and new methods for liquid-phase chemistry of heavy and superheavy elements*, **C.M. Folden III**, **Invited Talk**, University of Kentucky Department of Chemistry Colloquium, Lexington, Kentucky (April 2015).

*Production of near-spherical nuclei in hot fusion reactions*, **C.M. Folden III**, **Invited Talk**, Super Heavy Nuclei Symposium 2015, College Station, Texas (April 2015).

*Direct measurements of radiative capture reactions with DRAGON*, **G. Christian**, **Invited Talk**, 2015 APS Division of Nuclear Physics Meeting, Santa Fe, New Mexico (October 2015).

*A novel method for determining the mean-field directly from the single particle matter density*, **S. Shlomo**, **Invited Talk**, 4th International Conference on Mathematical Modeling in Physical Science (IC-Msquare4), Mykonos Island, Greece (June 2015).

*A novel method for determining the mean-field directly from the single particle matter density: Application to the measured charge density difference between the isotones* $^{206}Pb$ *–* $^{205}Tl$, **S. Shlomo**, **Invited Talk**, LXV International Conference on Nuclear Physics "NUCLEUS- 2015" New Horizens in Nuclear Physics, Nuclear Engineering, Femto-and Nanotechnologies, Saint Petersburg, Russia (June 2015).

*Determining a modern energy density functional for nuclei and the status of the equation of state of nuclear matter*, **S. Shlomo**, **Invited Talk**, Aristotle University of Thessaloniki, Thessaloniki, Greece (May 2015).

*Determining a modern energy density functional for nuclei and the status of the equation of state of nuclear matter*, **S. Shlomo**, **Invited Talk**, National and Kapodistrian University of Athens, Athens Greece (June 2015).

*Unitarity of the particle-hole dispersive optical model*, **M.L. Gorelik**, S. Shlomo, B.A. Tulupov, and M. H. Urin, LXV International Conference on Nuclear Physics "NUCLEUS-2015" New Horizens in Nuclear Physics, Nuclear Engineering, Femto- and Nanotechnologies, Saint Petersburg, Russia (June 2015).

*The $^{132}$Sn giant dipole resonance as a constraint on properties of nuclear matter*, **B. Roach**, G. Bonasera and S. Shlomo, 2015 Fall Meeting of the APS Division of Nuclear Physics, Santa Fe, New Mexico (October 2015).

*Primordial astrophysical reaction $^4$He(d,gamma)$^6$Li and the $^6$Li isotope puzzle*, **A.M. Mukhamedzhanov**, **Invited Talk**, ATOMKI, Debrecen, Hungary (April 2015).

*Indirect methods in nuclear atrophysics*, **A.M. Mukhamedzhanov**, **Invited Talk**, International Conference Nucleus-Nucleus Collisions, Catania, Italy (June 2015).

*Equation of state and pairing properties of neutron matter from chiral EFT*, **J. Holt**, **Invited Talk**, Pairing Phenomena from Neutron Stars to Cold Gases, Physics by the Falls 2016, University of Buffalo, Buffalo, New York (March 2016).

*Using lasers for nuclear physics: Measuring cross-sections in (non) equilibrium plasmas*, **A. Bonasera**, **Invited Talk**, Padova, Italy (May 2015).

*Bose Einsten condensation, fermionic quenching and Efimov states from HIC*, **A. Bonasera**, **Invited Talk**, Rostock, Germany (August 2015).

*Using lasers for nuclear physics: Measuring cross-sections in (non) equilibrium plasmas*, **A. Bonasera**, **Invited Talk**, Shanghai Institute of Applied Physics (SINAP) and Shanghai Institute of Optics and Fine Mechanics (SIOM), Shanghai, China (January 2016).

*Bose Einsten condensation, fermionic quenching and Efimov states from HIC*, **A. Bonasera**, **Invited Talk**, Shanghai Institute of Applied Physics (SINAP), Shanghai, China (January 2016).

*Heavy-flavor interactions in medium*, **R. Rapp**, **Invited Talk**, 6th Workshop of the APS Topical Group on Hadronic Physics, Baltimore, Maryland (April 2015).

*Interactions of heavy flavor in medium*, **R. Rapp, Invited Talk,** the Kavli Institute for Theoretical Physics China (KITPC) Program on "sQGP and Extreme QCD", Chinese Academy of Science, Beijing, China (May 2015).

*Thermal EM radiation in heavy-ion collisions*, **R. Rapp, Invited Talk,** Symposium on "Jet and Electromagnetic Tomography of Dense Matter", McGill University, Montreal, Canada (June 2015).

*Dileptons and chiral symmetry restoration*, **R. Rapp**, 7th International Conference on Hard and Electromagnetic Probes of High-Energy Nuclear Collisions ("Hard Probes 215"), McGill University, Montreal, Canada (June 2015).

*Recent developments for heavy flavor in medium*, **R. Rapp**, **Invited Opening Talk**, Workshop on "Selected Topics in Heavy-Flavor Production in High-Energy Collisions", Tsinghua University, Beijing, China (September 2015).

*QCD matter in heavy-ion collisions*, **R. Rapp**, **Invited Inaugural Talk**, Center for Nuclear Theory QGP-Meet 2015 Workshop, Variable Energy Cyclotron Centre, Kolkata, India (November, 2015).

*Selected discussion points and opportunities from CNT QGP-meet 2015*, **R. Rapp**, **Invited Summary Talk**, Center for Nuclear Theory QGP-Meet 2015 Workshop, Variable Energy Cyclotron Centre, Kolkata, India (November 2015).

*Heavy flavor in medium*, **R. Rapp, Invited Talk,** Int. Workshop XLIV on Gross Properties of Nuclei and Nuclear Excitations on “WCD Matter: Dense and Hot”, Hirschegg, Austria (January 2016).

*From dileptons in heavy-ion collisions to chiral restoration at high temperature*, **R. Rapp**, **Invited Nuclear/Particle Physics Seminar**, Tsinghua University, Beijing, China (May 2015).

*Spectral analysis of primordial QCD matter*, **R. Rapp**, Tsinghua University, Beijing, China (May 2015).

*Search for chiral symmetry restoration in QCD matter*, **R. Rapp**, **Invited Nuclear/Particle Physics Seminar**, Nanjing University, Nanjing, China (September 2015).

*Phenomena of the strong nuclear force, or: Why the vacuum is not empty*, **R. Rapp**, **Physics Colloquium**, Nanjing University of Science and Technology, Nanjing, China (September 2015).

*Search for chiral symmetry restoration in QCD matter*, **R. Rapp**, Institute for Theoretical Physics, Frankfurt University, Germany (October 2015).

*Spectral analysis of primordial QCD matter*, **R. Rapp**, Physics colloquium, Technical University, Darmstadt, Germany (October 2015).

*Sequential regeneration of charmonia in heavy-ion collisions*, **X. Du**, Nuclear/Particle Physics Seminar, Tsinghua University, Beijing, China (January 2016).

*Direct photon + hadron correlations to study parton energy loss with the STAR experiment*, **Nihar R. Sahoo** (for the STAR Collaboration), Quark Matter 2015 (XXV International Conference on Ultrarelativistic Nucleus-Nucleus Collisions), Kobe, Japan (September 2015).

*Quarkonium formation time in heavy ion collisions*, **C.M. Ko**, **Invited Talk**, Jet Symposium, Montreal, Canada (June 2015).

*(Anti)nulcei production and flow in ultra-relativistic heavy-ion collisions*, **C.M. Ko**, **Invited Talk**, EMMI Workshop on Anti-Matter, Hyper-Matter and Exotic Production at the LHC, CERN, Geneva, Switzerland (July 2015).

*Light nuclei production and flow in relativistic heavy ion collisions*, **C.M. Ko**, **Invited Talk**, Heavy Ion Conference, Shanghai, China (August 2015).

*Jet fragmentation in a hot medium*, **C.M. Ko**, **Invited Talk**, 11th International Workshop on QCD Phase Transition and Relativistic Heavy Ion Physics, Harbin, China (August 2015).

*Quarkonium formation time in heavy ion collisions*, **C.M. Ko**, **Invited Talk**, 2nd International Workshop on Heavy Flavor Productions in High Energy Collisions, Beijing, China (September 2015).

*Overview on coalescence model: Theoretical developments and applications*, **C.M. Ko**, **Invited Talk,** International Workshop on Exotic Hadrons from High Energy Collisions", Kyoto, Japan (March 2016).

*Charmonia production in heavy ion collisions*, **C.M. Ko**, **Invited Seminar**, Physics Department, Yonsei University, Seoul, Korea (August 20, 2015).

*Jet fragmentation via shower parton recombination in vacuum and in medium*, **C.M. Ko**, **Invited Seminar**, Physics Department, Yonsei University, Seoul, Korea (August 2015).

*The Quark recombination model and applications to high energy collisions*, **R.J. Fries**, **Invited Seminar**, Rice University, Houston, Texas (April 2015).

*Quark recombination and jet shower hadronization*, **R.J. Fries**, **Invited Talk**, Symposium on Jet and Electromagnetic Tomography of Dense Matter (JET Symposium), McGill University, Montreal, Quebec, Canada (June 2015).

*Jet hadronization in vacuum and in the medium*, **R.J. Fries**, 7th International Conference on Hard and Electromagnetic Probes of High-Energy Nuclear Collisions (Hard Probes 2015), McGill University, Montreal, Quebec, Canada (June 2015).

*Jet hadronization in vacuum and in the medium*, **R.J. Fries**, XXVth International Conference on Ultrarelativistic Nucleus-Nucleus Collisions (Quark Matter 2015), Kobe, Japan (September 2015).

*The (3+1)-D structure of nuclear collisions*, **R.J. Fries**, RBRC Workshop on Longitudinal Dynamics, Brookhaven National Laboratory, Upton, New York (January 2016).

## RESEARCH PERSONNEL AND ENGINEERING STAFF

### April 1, 2015 - March 31, 2016

### Faculty and Research Group Leaders

Aldo Bonasera, Senior Scientist
Charles M. Folden III, Assist. Prof. of Nuclear Chemistry
Gregory Christian, Assist. Prof. of Physics – From 9/1/15
Rainer Fries, Assoc. Professor of Physics
Carl A. Gagliardi, Professor of Physics
John C. Hardy, Professor of Physics, Ralph and Marsha Schilling Chair in Physics
Jeremy Holt, Assist. Professor of Physics – From 1/18/16
Che Ming Ko, Professor of Physics
Dan Melconian, Assoc. Professor of Physics
Ania Kwiatkowski, Assist. Professor of Physics – From 9/1/15
Saskia Mioduszewski, Assoc. Prof. of Physics
J. B. Natowitz, Professor of Chemistry (25%)
Ralf Rapp, Professor of Physics
Grigory Rogachev, Professor of Physics
Shalom Shlomo, Senior Scientist
Robert E. Tribble, Professor of Physics (20%)
Sherry J. Yennello, Professor of Chemistry, Bright Chair, Director
Dave H. Youngblood, Professor of Physics
Akram M. Zhanov, Senior Scientist

### Research Staff

Juha Arje – From 12/10/15
Marina Barbui, Assist. Research Scientist
Henry Clark, Accelerator Physicist (50%)
Grigor Chubaryan, Research Scientist
Vladilen Goldberg, Research Scientist
John C. Hagel, Research Scientist (50%)
Vladimir Horvat, Research Scientist (50%)
Victor Iacob, Research Scientist
Yevgen Koshchiy, Assist. Research Scientist
Yiu-Wing Lui, Research Scientist
Ninel Nica, Associate Research Scientist
Alan McIntosh, Assist. Res. Scientist
Antti Saastamoinen – From 2/1/16
Praveen Shidling – From 7/1/15
Sara Wuenschel – From 7/1/15
Roichi Wada – From 6/1/15

### Visiting Scientists

Yuri Oganessian – From 1/16/15 To 8/31/15
Tommi Eronen – From 10/1/15
Guoqiang Zhang – From 3/20/16

### Accelerator Physics and Radiation Line Staff

Joseph Brinkley, Research Associate
Lixin Chen, Research Associate
Henry Clark, Accelerator Physicist (50%)
Vladimir Horvat, Research Scientist (50%)
Bruce Hyman, Research Associate
George Kim, Accelerator Physicist
Don May, Accelerator Physicist
Brian Roeder, Accelerator Physicist
Gabriel Tabacaru, Accelerator Physicist

### Computer Systems Staff

Robert Burch, Jr., Lead Microcomputer/LAN Administrator
John C. Hagel, Research Scientist (50%)

### Engineering Staff

Robert Olsen, Senior Mechanical Engineer

**Postdoctoral Research Associates**

Taun K. Bhardwaj – To 6/30/15
Shadi Bedoor – From 10/26/15
Xiguang Cao
Jerome Gauthier
Paul Hohler – To 12/1/15
Meirong Huang – From To 3/31/16
Dario Lattuada – To 11/30/15
Ellen McCleskey – To 12/31/15
Mirganka Mondal – To 1/31/16
Shuya Ota – From 3/1/16
Hyo-In Park
Antti Saastamoinen – To 1/31/ 16
Nihar Sahoo
Praveen Shidling – To 6/30/15
Renee Steinbruegge – From 2/15/16
Sara Wuenschel – To 6/30/15
Evgeny Tereshatov
Ethan Uberseder – To 1/26/16
Michael Youngs – To 1/11/16
Zhen Zhang – From 2/1/16

# STUDENTS

## April 1, 2015 - March 31, 2016

### Graduate Students

Mason Anders – To 12/31/15
Marisa Alfonso – To 5/31/15
Joseph Atchison
Matteo Barbarino – To 12/19/15
Eames Bennett – From 1/15/15
Miguel Bencomo
Giacomo Bonasera
Jonathan Button
Zilong Chang
Roman Chyzh
Murat Dag
Xiaojian Du
Benjamin Fenker
Alex Fleming – From 1/12/16
Kevin Glennon – From 2/1/16
Kyong Choi Han
Lauren Heilborn
Laurence Henderson
Nathan Holt
Josh Hooker
Curtis Hunt
Heshani Jayatissa
Andrea Jedele
Feng Li
Shuai Liu
Yanfang Liu
Cordero Magana – From 9/1/14
Larry May – To 8/17/15
Demitri Mayorov – To 7/20/15
Michael Mehlman – To 5/31/15
Matthew Morrison – From 1/15/16
John Patti – From 8/20/15
Steven Rose
Issac Sarver
Alexandra Spiridon
Sidharth Somanathan
Sriteja Upadhyayula – From 1/15/15
Merinda Volia – From 1/16/15
Tyler Werke
David Wright – From 3/21/16
Zhaojie Xu – From 12/17/15
Andrew Zarrella

### Undergraduates and Student Technicians

Raymond Barringer – From 6/9/14
Lindsay Bryce
Matthew Chapman
Stephen Gerlt
Srivivas P. Harshal – From 1/12/15
Jesse Lopez – From 1/15/15
Christine Lawrence – From 9/1/15
Magaret Moetteli
David Rosenbaum – From 1/15/15

# ORGANIZATIONAL CHART - CYCLOTRON INSTITUTE

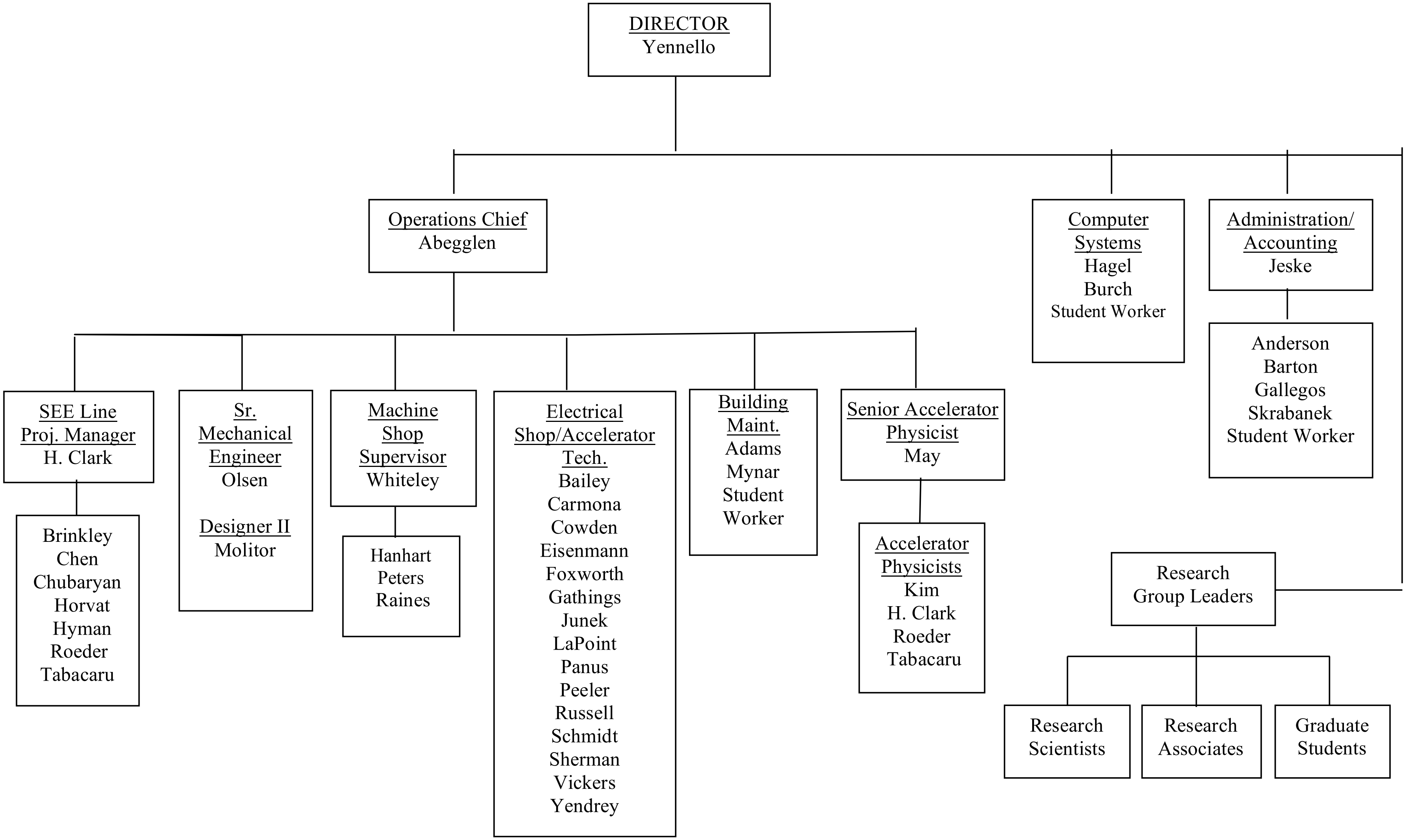

# STUDENTS WHO RECEIVED GRADUATE DEGREES FROM THESIS WORK CONDUCTED AT THE CYCLOTRON INSTITUTE

## April 1, 2015 – March 31, 2016

| Name | Year | Thesis Title | Advisor | Present Position |
|---|---|---|---|---|
| Paul Cammarata | 2015 | *Ternary breaking of the reaction systems in heavy-ion collisions below the Fermi energy* | S.J. Yennello | Senior Analyzer Sytem Engineer, Dow Chemical, Houston Texas |
| Michael Simon Mehlman | 2015 | *Development of TAMUTRAP beam line, RFQ, and ion traps for precision β-decay studies* | D. Melconian | Scientist, Exponent Scientific and Engineering Consulting, Menlo Park, California |
| Dmitriy Mayorov | 2015 | *Synthesis of shell-stabilized nuclides in fusion-evaporation reactions induced by* $^{48}$*CA,* $^{50}$*Ti, or* $^{54}$*Cr projectiles* | C.M. Folden III | Post Doc. Los Alamos National Lab., Los Alamos, New Mexico |
| Spencer Behling | 2015 | *Measurement of the beta asymmetry paramenter,* $A_\beta$*, in* $^{37}$*K* | D. Melconian | Post. Doc. Pacific Northwest National Laboratory, Richland, Washington |
| Larry Wayne May jr. | 2015 | *Isospin equilibration in Fermi-energy heavy-ion nuclear collisions* | S.J. Yennello | Faculty at San Jacinto Community College in Houston, Texas |
| Mason Robert Anders | 2015 | *Determination of constraints on the Skyrme energy density functional and the mean field via the* $3S_{1/2}$ *state in* $^{206}$*Pb* | S. Shlomo | Post-Doctoral Fellow at the University of Texas Southwestern Hospital, Dallas, Texas |

# INSTITUTE COLLOQUIA AND SEMINARS
## April 1, 2015 - March 31, 2016

**2015**

| | | |
|---|---|---|
| April 7 | Prof. G.A. Souliotis, Laboratory of Physical Chemistry, Department of Chemistry, National and Kapodistrian University of Athens, Athens, Greece | *Microscopic Calculations of Low and Intermediate Energy Fission with the Constrained Molecular Dynamics (CoMD) Model* |
| April 13 | Academician Prof. Yuri Ogsnessian, JJINR, Dubna, Russia/Cyclotron Institute, Texas A&M University, College Station, Texas | *Distinguished Lecture Series No. 3 on Super Heavy Elements* |
| April 20 | Academician Prof. Yuri Ogsnessian, JJINR, Dubna, Russia/Cyclotron Institute, Texas A&M University, College Station, Texas | *Distinguished Lecture Series No. 4 on Super Heavy Elements* |
| April 21 | Dr. Livius Trache, "Horia Hulubei" National Institute for Physics and Nuclear Engineering (IFIN-HH), Bucharest, Romania | *Nuclear Methods and Results in the Study and Preservation of Cultural Heritage at IFIN-HH Bucharest* |
| April 27 | Academician Prof. Yuri Ogsnessian, JJINR, Dubna, Russia/Cyclotron Institute, Texas A&M University, College Station, Texas | *Distinguished Lecture Series No. 5 on Super Heavy Elements* |
| April 28 | Dr. Aliya Nurmukhanbetova, Nazarbayev University, Astana, Kazakhstan | *Progress in Nuclear Astrophysics at Astana, Kazakhstan* |
| July 21 | Prof. J.N. De, Saha Institute of Nuclear Physics, Kolkata, India | *Exploring the Equation of State of Nuclear Matter from Empirical Constraints* |
| July 28 | Dr. Gorelik Mikhail, National Research Nuclear University "MEPhI", Moscow, Russia | *On the Properties of High-Energy Isoscalar Monopole (P-H)- Type Excitations in Medium-Heavy Mass Spherical Nuclei* |
| August 11 | Prof. Sait Umar, Department of Physics & Astronomy, Vanderbilt University, Nashville, Tennessee | *Nuclear Dynamics from Neutron Stars to Superheavy Elements* |
| August 25 | Prof. LarryZamick, Deapartment of Physics and Astronomy at Rutgers, the State University of New Jersey, New Jersey | *Back to the Future: J=0 Pairing and Maximum J Pairing in Nuclei* |

| | | |
|---|---|---|
| September 1 | Prof. C. Dorso, Departamento de Física, FCEN, Universidad de Buenos Aires, Buenos Aires, Argentina | *Italian Delicacies Served in Neutron Stars Crust* |
| September 8 | Dr. Danyang Pang, Baihang University, Beijing, China | *Status of Deuteron Stripping Reaction Theories* |
| September 29 | Dr. Charles M. Folden III, Cyclotron Institute, Texas A&M University, College Station, Texas | *Chemistry and Nuclear Reactions at the Bottom of the Periodic Table* |
| November 3 | Dr. P.M. Moller, Theoretical Division, LANL, Los Alamos, New Mexico | *Fission and Stability in the Heavy-Element Region in the Macroscopic-Microscopic Approach* |
| November 9 | Dr. René Steinbrügge, Max Planck Institute für Kernphysik, Heidelberg, Germany | *Investigating Highly Charged Ions with Ultrabrilliant Light Sources* |
| December 8 | Dr. V.Z. Goldberg, Cyclotron Institute, Texas A&M University, College Station, Texas | *Mystery of $^{9}$He and Very Exotic Neutron Rich Light Nuclei* |

## **2016**

| | | |
|---|---|---|
| January 11 | Prof. Wladyslaw Trzaska, Department of Physics, University of Jyvaskyla, Finland | *The Hunt for Neutrino Mass Hierarchy and CP Violation* |
| January 26 | Dr. Cheuk-Yin Wong, Oak Ridge National Laboratory, Oak Ridge, Tennessee | *Wheeler's Toroidal Nuclei and Light-Mass Toroidal High-Spin Isomers* |
| February 2 | Dr. Evgeny Tereshatov, Cyclotron Institute, Texas A&M University, College Station, Texas | *Cyclotron Institute Opportunities in Chemical Studies of Super Heavy Elements* |
| February 8 | Dr. Shea Mosby, Nuclear Astrophysics and Structure, LANL, Los Alamos, New Mexico | *Neutron Capture by Any Means Necessary* |
| February 23 | Prof. Sanjay Reddy, Institute for Nuclear Theory, University of Washington, Seattle, Washington | *Nuclear Astrophysics in the Multi-Messenger Era* |
| March 8 | Prof. Jorge Piekarewicz, Department of Physics, Florida State University, Tallahassee, Florida | *Information and Statistics: A New Paradigm in the Study of Neutron Stars* |

| | | |
|---|---|---|
| March 22 | Prof. Anatoli Afanasjev, Department of Physics and Astronomy, Mississippi State University, Mississippi | *Covariant Density Functional Theory: Nuclei at the Extremes of Nuclear Landscape* |
| March 24 | Dr. A. Wakhle, National Superconducting Cyclotron Laboratory, Michigan State University, East Lansing, Michigan | *Heavy-Ion Fusion Reactions with Neutron-Rich Radioactive Ion Beams* |